Observation of Spin Correlations in $t\bar{t}$ events at $\sqrt{s} = 7$ TeV using the ATLAS detector.

A thesis submitted to the University of Manchester for the degree of Doctor of Philosophy in the Faculty of Engineering and Physical Sciences

2013

J.W. Howarth

Particle Physics Group
School of Physics and Astronomy

Abstract

This thesis presents measurements of the the spin correlation strength in top anti-top quark pair production at the LHC using the ATLAS detector. The data used corresponds to 4.6 fb^{-1} of integrated luminosity taken during 2011 at the LHC at a center of mass energy of 7 TeV. The spin correlation is studied utilising different observables with different sensitivities to the production mechanism, in particular to gluon-gluon fusion in the like or unlike helicity state, quark anti-quark annihilation in the unlike helicity state, or a combination of the three. In addition cuts are made on the invariant mass of the $t\bar{t}$ system to enhance or suppress contributions from different initial state production mechanisms. The analysis presented is a precision test of both $t\bar{t}$ production and decay in the SM. These measurements are compared to the most current theoretical predictions. No deviation from the SM expectation was observed. In a subset of the data, corresponding to an integrated luminosity of 2.1 fb^{-1}, the hypothesis of zero spin correlation is excluded at 5.1 standard deviations.

Contents

Total word count: 29421

Declaration

No portion of the work referred to in the thesis has been submitted in support of an application for another degree or qualification of this or any other university or other institute of learning.

Copyright

1. The author of this thesis (including any appendices and/or schedules to this thesis) owns certain copyrights or related rights in it (the "Copyright"(and he has given The University of Manchester certain rights to use such Copyright, including for administrative purposes.

2. Copies of the thesis, either in full or in extracts and whether in hard or electronic copy, may be made only in accordance with the Copyright, Designs and Patents Act 1988 (as amended) and regulations issued under it or, where appropriate, in accordance with licensing agreements which the University has from time to time. This page must for part of any such copied made.

3. The ownership of certain Copyright, patents, designs, trade marks and other intellectual property (the "Intellectual Property") and any reproductions of copyright works in the thesis, for example graphs and tables ("Reproductions"), which may be described in this thesis, may not be owned by the author and may be owned by third parties. Such Intellectual Property and reproductions cannot and must not be made available for use without the prior written permission of the owner(s) of the relevant Intellectual Property and/or Reproductions.

4. Further information on the conditions under which disclosure, publication and commercialisation of this thesis, the Copyright and any Intellectual Property and/or Reproductions described in it may take place is available in the University IP Policy [1], in any relevant Thesis restriction declarations deposited in the University Library, The University Library's regulations [2] and in The University's policy on presentation of Theses.

---

[1]See http://www.campus.manchester.ac.uk/medialibrary/policies/intellectual-property.pdf
[2]See http://www.manchester.ac.uk/library/aboutus/regulation

Acknowledgements

Firstly, I would like to thank all of my family who have supported me throughout my education. Especially my parents; Kim, Jason, and Brian, and my grandparents; Don and Cynthia.

I am very grateful to the many staff and students at The University of Manchester, in particular Prof Schwanenberger and Dr Wengler for supervising me, Mark and Yvonne for teaching me, and Fred for giving me a chance in the first place. Thanks to Sabah and Anne, without whom I would have probably fallen at every technical or administrative hurdle!

Thanks to everyone on the LTA for making two years at CERN feel more like a holiday than work, for the poker nights, for Mario Kart, for wine, and for skiing!

Finally I would like to thank Joe. Your love and support was a constant crutch on which I leaned heavily and without which this thesis might never have been written.

HOLA SWAMPY

Chapter 1

Introduction

The top quark is a versatile tool for testing the Standard Model. Due to its short lifetime, many properties that would normally be diluted by the confined nature of quarks are accessible experimentally. Properties such as spin, charge, and mass, provide avenues through which the Standard Model can be rigorously tested. As the heaviest known particle in the Standard Model, the top quark is also an ideal candidate for searches for new physics. Pair production of top quarks at the Large Hadron Collider provide striking experimental signals at rates never before observed in experimental particle physics. A thorough understanding of the top-quark pair-production process is a crucial goal of the LHC program. The process is not only a sensitive test of the Standard Model. Top quark pair production is an important experimental background in the $t\bar{t}H$ process and in searches for physics beyond the Standard Model.

A measurement of spin correlation between pair-produced top and anti-top quarks probes the full production and decay chain of the $t\bar{t}$ process. The spin correlation in $t\bar{t}$ production, in both gluon-gluon fusion and $q\bar{q}$ annihilation, is known at next-to-leading order in the SM. This property was previously studied at the Tevatron collider but these studies were limited in their sensitivity. Spin correlation is an ideal property for testing if the predictions of the SM are correct.

This thesis describes the first observation of non-vanishing spin correlation in $t\bar{t}$ production on a sub-set of ATLAS data taken during LHC operation in 2011. An extension of this analysis is also presented using the full 2011 ATLAS data. The spin correlation is probed in experimental observables that are sensitive to different linear combinations of the coefficients of the spin-density matrix for both gluon-gluon and $q\bar{q}$ produced $t\bar{t}$ pairs and is also sensitive to possible contributions from new physics in both $t\bar{t}$ production and decay.

The dileptonic decay of $t\bar{t}$ pairs are an excellent tool for probing the Standard

Model. However, reconstruction of the final state requires special consideration due to the presence of the two neutrinos in the dileptonic decay mode. The effectiveness of the method of reconstruction can have a large effect on the resulting sensitivity of the analysis. In this thesis a previously developed method, called Neutrino Weighting, is improved upon and adapted to reconstruct data from ATLAS.

In Chapter 2 a brief theoretical overview of the Standard Model, $t\bar{t}$ production and spin correlation is presented. Chapter 3 describes the LHC machine and the ATLAS detector, including a discussion of the performance and resolution of these machines in 2011 and 2012. Chapter 4 details the extraction of trigger efficiencies and performance for 2011 and 2012 data. Chapter 5 describes the object reconstruction and selection cuts used in this analysis to select events. Chapter 6 details the procedure used to reconstruct the $t\bar{t}$ system, including comparisons between other procedures and a discussion of the performance of the reconstruction on data. Chapter 7 explains the method by which the spin correlation is extracted from the data and the estimation of sources of systematic uncertainty. Finally Chapter 8 reports the results of the analysis and compares these to theoretical predictions.

Chapter 2

Theoretical Overview

2.1 The Standard Model

The Standard Model (SM) of particle physics is a theory that describes fundamental particles and their interactions. It is the most accurate scientific theory ever developed and, so far, describes all observed experimental particle-physics data with astounding accuracy. Particles in the SM are categorised into two basic types: fermions and bosons. Fermions are particles with one-half spin, whereas bosons are particles with integer spin. Fermions are responsible for most of the observable stable matter in the universe and bosons are the particles which mediate interactions between fermions. Fermions are divided into two sub-sets: quarks (those with fractional electric charge and colour charge) and leptons (those with integer electric charge and no colour charge). The theory describes three of the four fundamental forces: electromagnetism, the weak force and the strong force. These forces are mediated by integer-spin particles called bosons. The range of these forces and their mediating bosons are listed in Table. 2.1.

The particles of the SM are summarised in Fig. 2.1. Each particle (matter) has a corresponding anti-particle (anti-matter). These particles have identical quantum numbers except for opposite-sign charge. For neutral particles, the Z and γ bosons are their own anti-particles whereas the neutrinos and anti-neutrinos are distinct particles.

The Standard Model is a gauge theory composed of the products of the $SU(3)_C \oplus SU(2)_L \oplus U(1)_Y$ groups. These groups are often evaluated by separate parts of the theory. The $SU(3)_C$ group describes the strong interaction through the conserved colour charge (C) and is evaluated using Quantum Chromo Dynamics (QCD). The $SU(2)_L \oplus U(1)_Y$ describes the electromagnetic and weak interactions, collectively referred to in a form as "Electro-Weak" (EW), through

Force	Range	Boson
Electromagnetic	∞	Photon
Weak	10^{-18}	$W^{\pm}$ and Z
Strong	10^{-15}	gluon
Gravity	∞	graviton (postulated)

Table 2.1: Fundamental forces and their range.

the conserved weak charge and hypercharge. EW interactions are described using Quantum Electrodynamics (QED).

Quarks and gluons carry colour charge and, unlike leptons, cannot exist as free particles. Quarks form composite bound states, called hadrons, with integer electric charge. Two types of hadrons are known to exist: Baryons and Mesons. Baryons consist of three bound quarks and Mesons are composed of a bound quark and anti-quark pair. Bound states of only gluons are also possible but these have not been observed.

Despite its success, the SM remains an incomplete theory. The interactions of particles are only described for the EW and strong forces and gravity is notably absent. Also, the model cannot fully describe the abundance of matter over anti-matter in the universe, nor does it provide candidates for dark matter.

The Higgs boson is the most recently discovered particle [1] in the SM and is responsible for mediating interactions with the Higgs field, imbuing fermions and the W and Z bosons with mass. The discovery of the Higgs boson was a triumph for the SM, which had long predicted its existence. The measured mass of the Higgs from the ATLAS experiment is 125.5 GeV [2] making it almost the heaviest particle in the SM, with the exception of the top quark.

Figure 2.1: Particles of the SM. For each particle the observed mass is indicated in the top left. Below this is the particle's electric charge and then the particle's spin. Other quantum numbers, such as colour charge, are not included. Values are taken from the Particle Data Group (PDG) [3] 2013 summary tables and particle listings.
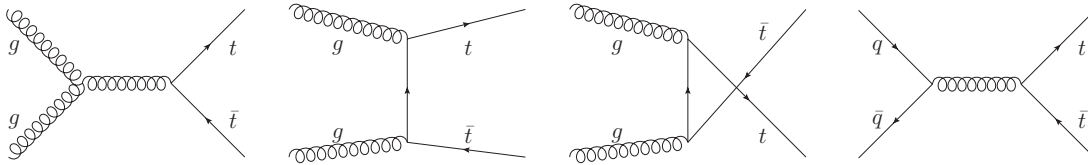
Figure 2.2: Leading order diagrams for $t\bar{t}$ production.

2.2   The Top Quark

The top quark was theorised, along with the b quark, to explain charge-parity (CP) violation in Kaon decay [4] via the introduction of a new quark doublet. After the discovery of the b quark [5] a hunt began for its isospin partner. The top quark was discovered in 1995 by the D0 and CDF collaborations at the Tevatron collider [6, 7].

The top quark has a very high mass, higher than any other known fundamental particle. The most recent experimental results find the mass to be 173.2 GeV [8, 9]. As a consequence of this high mass, the top quark has a very short lifetime of order $5 \cdot 10^{-25}$s. This is an order of magnitude shorter than the time scale for strong interactions. Hence, the top quark decays before it can hadronise. This rapid decay means that the spin information of the top quark is not diluted by hadronisation effects and is transferred to its decay particles, allowing for direct measurements of properties associated with the top quark spin.

2.2.1   Top quark pairs at the LHC

Pair production of top quarks at the LHC occurs via the strong force. At LHC energies, the production is dominated by the gluon-gluon fusion process (90%) with a small contribution from the annihilation of a quark and an anti-quark (10%). The leading-order Feynman diagrams for these processes are shown in Fig. 2.2.

Top quarks decay almost exclusively to a W boson and a b-quark. Subsequently, the W decays into either a pair of quarks ("hadronically") or into a lepton and a neutrino ("leptonically"). In $t\bar{t}$ production, there are two W's. One W from the top quark decay and one from the anti-top quark decay. Top pair decays are categorised by the decay modes of these W bosons. If both decay hadronically then the decay is said to be "all hadronic", if one decays hadronically and the other decays leptonically then the decay is said to be "semi-leptonic". If both decay leptonically then the decay is referred to as "dileptonic". The branching ratios for these decay modes are shown in Fig. 2.3. The dileptonic mode has

Top Pair Branching Fractions
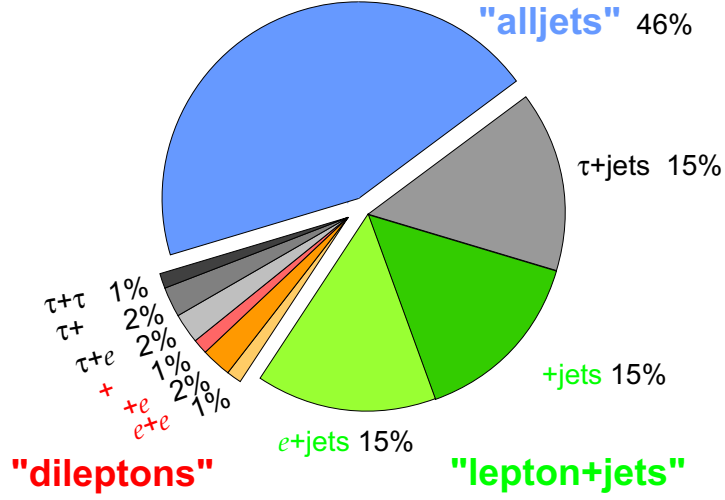
Figure 2.3: Branching fractions for $t\bar{t}$ decays, categorised by the decay modes of the W bosons [10].

the smallest branching ratio of the three but it also provides the cleanest experimental signal due to the two leptons in the decay. In addition, the LHC is a top-quark factory and this reduces the effect of the lower branching ratio of the dilepton channel. The semi-leptonic channel has a high branching ratio and also has a lepton from the leptonic decay of one of the W bosons that can be used to trigger these events. However, the channel suffers more from backgrounds from other SM processes than the dilepton channel. For example, the production of a W boson with associated jets.

2.2.2 Spin correlations

The degree to which the spin of the top quark is aligned to the spin of the anti-top quark, in $t\bar{t}$ pair production, is known as the "spin correlation". It may be expressed as the ratio of the difference of spin-aligned pairs (N_{like}) and spin anti-aligned pairs (N_{unlike}) in a given frame of reference:

$$C = \frac{N_{like} - N_{unlike}}{N_{like} + N_{unlike}} = \frac{N(\uparrow\uparrow) + N(\downarrow\downarrow) - N(\uparrow\downarrow) - N(\downarrow\uparrow)}{N(\uparrow\uparrow) + N(\downarrow\downarrow) + N(\uparrow\downarrow) + N(\downarrow\uparrow)}. \tag{2.1}$$

This parameter is dependent upon the reference direction that is used to quantify the top and the anti-top spin direction, commonly called the "spin-analysing basis" or the "spin-quantisation axis". The parameter C is predicted by the SM

to NLO accuracy for a number of given spin-quantisation axes [11, 12, 13] and a measurement of it is a precision test of the SM.

The spin-correlation information in $t\bar{t}$ events are encoded in the squared matrix elements for the 2→2 production via gluon-gluon fusion or $q\bar{q}$ annihilation:

$$|M|^2 \propto X + \mathbf{B^+} \cdot \mathbf{s_1} + \mathbf{B^-} \cdot \mathbf{s_2} + C_{ij}s_{1i}s_{2i}, \qquad (2.2)$$

where X determines the cross section and all distributions that are independent of the top and anti-top quark spin. For example, the transverse momentum distribution of the top quark is encoded in X. The notation $\mathbf{s_1}$ and $\mathbf{s_2}$ are the spin vectors of the t and $\bar{t}$ in the t and $\bar{t}$ rest frames, respectively, and are unit vectors in the directions chosen as the spin-quantisation axis. The $\mathbf{B^+}$ and $\mathbf{B^-}$ are vectors that describe the longitudinal and transverse polarisation of the top quark and the anti-top quark, relative to the production plane, and are equal to zero at LO in the SM. The longitudinal polarisations of the top and anti-top were recently measured by ATLAS and CMS and no deviation from the zero hypothesis was observed [14, 15]. The individual polarisations of the t and $\bar{t}$ are assumed to be zero from this point onwards. Similarly, the components of the production that are not sensitive to spin correlation (those encoded in X) are not discussed further.

The matrix C_{ij} encodes the spin-correlation information and is described with six independent coefficients[1]:

$$C_{ij} = c_1\delta_{ij} + c_2\hat{p}_i\hat{p}_j + c_3\hat{k}_i\hat{k}_j + c_4(\hat{p}_i\hat{k}_j + \hat{k}_i\hat{p}_j) + c_5\epsilon^{ijk}\hat{p}_l + c_6\epsilon^{ijk}\hat{k}_l, \qquad (2.3)$$

where $\hat{p}_i, \hat{p}_j$ describe the directions of the incoming quarks or gluons and $\hat{k}_i, \hat{k}_j$ are the momentum directions of the top quark and the anti-top quark in the zero-momentum-frame (ZMF), respectively. The Kronecker delta and the permutation tensor are denoted by the symbols δ_{ij} and ϵ^{ijk}, respectively. The coefficients c_5 and c_6 are zero in the SM and would require non-SM charge-parity (CP) symmetry violation in order to have a sizeable effect [16]. The coefficients $c_1 \rightarrow c_4$ are all C-even and P-even and describe the spin correlation at LO in the SM [16]. It is possible (and desirable) to construct experimental observables that differ in their sensitivity to each of these co-efficients. By investigating multiple observables (see Section 2.3), each of these coefficients can be probed and their agreement with the SM predictions can be investigated. By investigating spin correlation in

---

[1]The convention for the numbering of these coefficients in this thesis is different from the examples given in [13] but their forms are the same.

different regions of $t\bar{t}$ invariant mass, it is possible to shift the contributions of each coefficient to the overall spin correlation and to maximise the sensitivity of the experimental observables.

2.2.3 Invariant mass regimes

Production at the LHC at LO is dominated by the gluon-gluon fusion process (90%), with small contributions arising from $q\bar{q}$ annihilation (10%). In this simplified picture, it is also possible to further divide these processes by their helicity structure, resulting in four possibilities for $t\bar{t}$ production;

1. $q_{\mathbf{L}}\bar{q}_{\mathbf{R}}$ and $q_{\mathbf{R}}\bar{q}_{\mathbf{L}}$: Opposite-helicity quark anti-quark annihilation.

2. $q_{\mathbf{R}}\bar{q}_{\mathbf{R}}$ and $q_{\mathbf{L}}\bar{q}_{\mathbf{L}}$: Like-helicity quark anti-quark annihilation.

3. $g_{\mathbf{L}}g_{\mathbf{R}}$ and $g_{\mathbf{R}}g_{\mathbf{L}}$: Opposite-helicity gluon fusion.

4. $g_{\mathbf{L}}g_{\mathbf{L}}$ and $g_{\mathbf{R}}g_{\mathbf{R}}$: Like-helicity gluon fusion.

The relative contributions of like-helicity to unlike-helicity gluons is approximately 65% vs 35% [17]. The $q\bar{q}$ production process is dominated almost entirely by the opposite-helicity case. The annihilation in the like-helicity case results in a system with zero total angular momentum which results in a highly virtual intermediate gluon. Therefore, this production mode is highly suppressed compared to the others.

The contributions of the different initial states can be suppressed or enhanced by the introduction of a cut on the invariant mass of the resultant $t\bar{t}$ pair. Like-helicity-gluon-gluon fusion tends to result in $t\bar{t}$ pairs with a lower invariant mass than unlike-helicity-gluon-gluon fusion or $q\bar{q}$-annihilation-produced pairs. By only considering low invariant mass $t\bar{t}$ pairs, a sample can be selected to have an enhanced contribution from like-helicity-gluon-gluon fusion. Similarly, by only choosing high mass $t\bar{t}$ pairs, a sample may be selected to have an enhanced contribution from unlike-helicity initial states, both gluon-gluon and $q\bar{q}$.

The contributions of the coefficients $c_1 \rightarrow c_4$ to the resulting spin correlation are not independent of the initial-state production mechanism and it is advantageous to probe the spin correlation differentially in terms of the resulting invariant mass of the $t\bar{t}$ system in order to probe these effects. A cut of 450 GeV on the $t\bar{t}$ invariant mass is used to create two regions of phase space. The cut value that is used to define these regions ensures roughly equal statistics in both (at truth
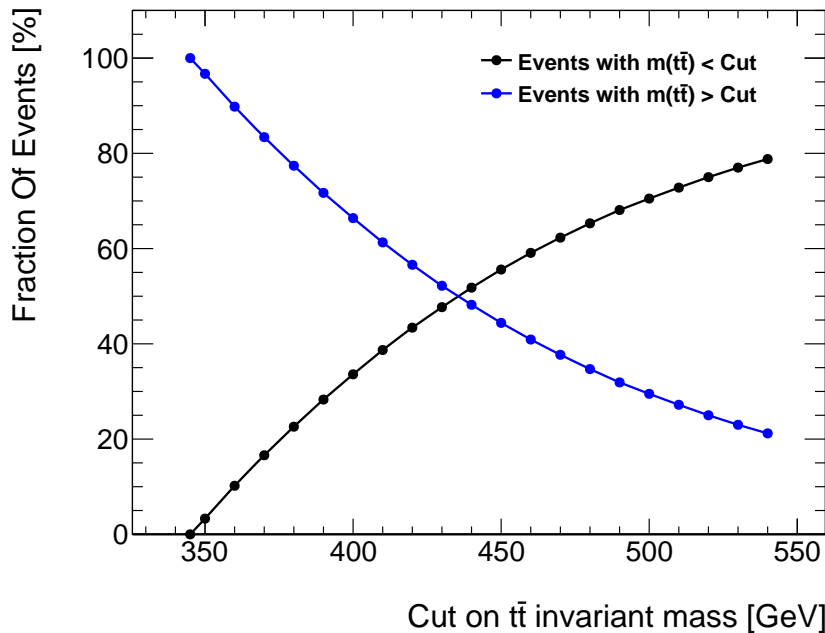
Figure 2.4: Fraction of $t\bar{t}$ MC truth events passing a cut on $t\bar{t}$ invariant mass. At 440 GeV, roughly half of the events have a $t\bar{t}$ invariant mass above this value and half below it. A cut is placed at 450 GeV to coincide with other differential top-quark analyses that use 450 GeV to separate between the high and low invariant-mass regions.

level before detector acceptance and resolution effects). This is the same definition that was used in top-quark charge asymmetry analyses [18, 19, 20]. The effect of this cut on the sample statistics is illustrated in Fig. 2.4 for 15 million $t\bar{t}$ Monte Carlo events. A cut of 450 GeV appears to slightly bias the low invariant mass region to more statistics, however this value is retained to facilitate comparisons to other top-quark properties analyses that utilise this cut. The same behaviour with respect to the invariant-mass cut is observed in MC samples that include SM spin correlations and MC that do not.

2.2.4 Spin analysing power

During decay, the spin information of the top quark is transferred directly to the W boson and the b quark. The degree to which these particles, and the subsequent daughters of the W boson, retain sensitivity to the spin information of their parent top quark is known as the particles' "spin-analysing power" (α) and is defined between the values of -1 and 1. The α parameters correct the spin correlation that is measured, using a given decay particle, to the true spin

	b-quark	W^+	l^+	$\bar{d}$-quark or $\bar{s}$-quark	u-quark or c-quark
α_i (LO)	-0.410	0.410	1.000	1.000	-0.310
α_i (NLO)	-0.390	0.390	0.998	0.930	-0.310

Table 2.2: Spin-analysing power at leading order and next-to-leading order for the decay products of the top quark (with a mass of 172.5 GeV) from the decay $t \to bW^+$. The decay products of the W boson can be used as spin analysers and their spin-analysing powers are also listed [21, 22, 23].

correlation between the top and the anti-top via the linear correction;

$$C = \alpha_+\alpha_-A. \tag{2.4}$$

For decay particles with $\alpha = 1$, the measured spin correlation would correspond to the true spin correlation. If a decay particle had $\alpha = 0$, then the spin information would be lost.

The values for the spin-analysing power of particles in a top-quark decay event are shown in Table 2.2. The b-quark and W boson do not carry the full spin information of the top quark. The reason for this is that the b and W are both massive particles and it is always possible to define a frame of reference where the direction of the spins of these particles are flipped, diluting their spin-analysing power. Charged leptons and lighter quarks can be approximated as massless in this case and the full spin information can be recovered. However, up-flavour quarks and neutrinos introduce an additional complication. The calculations for these processes cannot be factorised into separate angular and momentum-dependent parts and the spin information is diluted by this effect. The same is not true for down-type quarks and charged leptons, where the calculation can be factorised into only the angular dependent parts and the full spin information is available at LO. The spin-analysing power of the neutrinos, b-quarks and up-flavour quarks have a small dependence on the mass of the top quark and the mass of the W. The down-type quarks from the W decay and the charged leptons have no dependence on the mass of the top. The spin-analysing power of all of the decay particles is independent of the degree of spin correlation between the t and the $\bar{t}$.

When considering the decay modes of $t\bar{t}$ pairs, the dilepton and semi-leptonic channels have the highest spin-analysing power. These decay modes contain particles from both the top and the anti-top with $\alpha = 1$ and hence have access to the full spin information. However, it is experimentally difficult to distinguish

between particle jets arising from down-flavour quarks from those arising from up-flavour quarks. Therefore, the dilepton channel has the highest overall sensitivity to spin correlation out of all of the $t\bar{t}$ decay modes. For the remainder of the thesis only the spin-analysing powers of the two charged leptons in the dilepton channel are considered (α_+, α_-), where the sign indicates the sign of the electric charge of the lepton.

2.3 Spin Correlation Observables

The spin information of the top quark can be accessed through the angular distributions of its decay particles. Observable quantities that are sensitive to spin correlation in $t\bar{t}$ events are constructed using the angular distributions of these decay particles. The particular angles that are used, and the reference frames in which they are measured, determines the degree to which the observable quantity probes the coefficients c_1, c_2, c_3, and c_4 and how they behave with respect to the $t\bar{t}$ invariant mass.

No variable exists that is maximally sensitive to spin correlation (i.e. there is no frame of reference or angular definition that results in an observable spin correlation of $C = 1$) but it is possible to investigate several variables that are each differently sensitive to c_1, c_2, c_3 and c_4 and to fully probe the spin correlation. These variables are investigated in an inclusive $t\bar{t}$ invariant mass selection and also in two regions of $t\bar{t}$ invariant mass, below 450 GeV and above 450 GeV.

Helicity basis

It is possible to directly measure A (and therefore C) using the angles of the leptons, relative to their parent top quarks. The double-differential angular distribution for $t\bar{t}$ decay can be described as:

$$\frac{1}{\sigma}\frac{d\sigma}{d\cos(\theta_+)d\cos(\theta_-)} = \frac{1}{4}(1 - \alpha_+\alpha_- A\cos(\theta_+)\cos(\theta_-)) \, , \tag{2.5}$$

where θ is the angle between the charged lepton and some chosen spin-quantisation axis in the ZMF of the parent top quark, and σ denotes the cross section of the channel under consideration. θ_+ (θ_-) describes the angle between the direction of flight of the lepton ℓ^+ (ℓ'^-) in the t ($\bar{t}$) rest frame and a reference direction $\hat{\mathbf{a}}$ ($\hat{\mathbf{b}}$). The distribution of $\cos(\theta_+)\cos(\theta_-)$ is something that can be observed experimentally, provided the top quarks are reconstructed and a suitable spin-quantisation axis is chosen as the reference direction. The parameter C could be

directly extracted by taking the average of this distribution over many events:

$$C = \alpha_+ \alpha_- A = -9 \langle \cos(\theta_+) \cos(\theta_-) \rangle. \tag{2.6}$$

However, in this thesis the distribution of $\cos(\theta_+) \cos(\theta_-)$ is used in a template method to extract the $t\bar{t}$ spin correlation to increases the statistical sensitivity. This is discussed further in Section 7.1.

The "Helicity" basis defines the spin-quantisation axis that is used to measure θ to be the direction of the parent top quark in the $t\bar{t}$ ZMF. This basis has consistent sensitivity over the whole $t\bar{t}$ invariant-mass range and is sensitive to a linear combination of c_1, c_2, c_2, and c_4. Spin correlation creates an asymmetry in the otherwise symmetrical $cos(\theta_+)cos(\theta_-)$ distribution. In terms of these coefficients, the asymmetry of this variable, which can be observed as a non-zero $< \cos(\theta_+) \cos(\theta_-) >$, is generated by:

$$[c_1^a + y^2 c_2^a + c_3^a + 2y c_4^a], \qquad y = \hat{p}.\hat{k}, \tag{2.7}$$

where $a = q, g$ depending on the initial state production. The Helicity basis has been studied in the context of spin correlation by the ATLAS collaboration previously [24, 25], though this thesis represents the first time that it has been used for spin-correlation measurements with real data. The truth-level distribution for the $cos(\theta_+)cos(\theta_-)$ variable, using the Helicity basis, is shown in Fig. 2.5. Two hypotheses for the value of A are shown: $t\bar{t}$ events with SM spin correlation ($A = SM$) and $t\bar{t}$ events with no spin correlation ($A = 0$). The variable is shown in an inclusive selection and also for high and low $t\bar{t}$ invariant mass selection. Similar separation between the SM and uncorrelated case is observed in all distributions.

Maximal basis

The $cos(\theta_+)cos(\theta_-)$ variable can be measured with other spin-quantisation axes than the Helicity basis. The "Maximal" basis [13] is derived directly from the eigenvectors of the spin-density matrix for gluon-gluon-fusion production at the LHC (c_1^g, c_2^g, c_3^g, and c_4^g) and, by definition, is sensitive to all non-zero coefficients for the gluon-gluon fusion process. This basis is, by construction, the basis which yields the highest absolute value for C in the SM. The distributions for this observable at truth level for SM correlated and for uncorrelated $t\bar{t}$ events is shown in Fig. 2.6 in three different $t\bar{t}$ invariant mass regimes: inclusive, high mass, and low mass. Similar separation between the correlated and uncorrelated case is seen

in all three regimes.

In order to calculate the $\cos(\theta_+)\cos(\theta_-)$ variables, in either the Helicity or Maximal basis, the following procedure is used [26]:

- The top and anti-top 4 momenta must be reconstructed in the laboratory frame.

- A rotation-free boost into the $t\bar{t}$ zero-momentum frame is performed, such that the co-ordinate system between the lab frame and the ZMF have parallel axes. The spin-quantisation axes $\hat{\mathbf{a}}$ and $\hat{\mathbf{b}}$ are calculated in this frame.

- A second rotation-free boost is performed into the t and $\bar{t}$ rest frames.

- The direction $\hat{\mathbf{q}}_+$ ($\hat{\mathbf{q}}_-$) is calculated, which is the direction of the spin analyser ℓ_+ (ℓ_-) in the t ($\bar{t}$) rest frame.

- The angles $\cos(\theta_+) = \hat{\mathbf{a}} \cdot \hat{\mathbf{q}}_+$ and, $\cos(\theta_-) = \hat{\mathbf{b}} \cdot \hat{\mathbf{q}}_-$ are calculated.

Both the Maximal basis and the Helicity basis, when used with the $cos(\theta_+)cos(\theta_-)$ variable, are said to be "directly sensitive" to spin correlation, meaning that the spin correlation may be directly extracted from the average of the distribution. The observables that follow are said to be "indirectly sensitive", meaning that the effect of spin correlation affects the shapes of the distributions, but that it is not possible to directly extract the spin-correlation value from the distribution alone. This terminology is purely for illustrative purposes as, in this thesis, the spin correlation is extracted in the same manner for each of the variables by means of a template fit. This extraction is discussed further in Section 7.1.

S-Ratio

Another experimental observable that is sensitive to a linear combination of the non-zero-spin-correlation coefficients is the "S-Ratio" [17], though the exact degree of dependence on each coefficient is still being calculated by the theory community. The observable is constructed by taking a ratio of the correlated and uncorrelated matrix elements in the gluon-gluon-fusion process, using the Helicity basis to define the θ angles:

$$S = \frac{(|M^g|^2_{\mathbf{RR}} + |M^g|^2_{\mathbf{LL}})_{corr}}{(|M^g|^2_{\mathbf{RR}} + |M^g|^2_{\mathbf{LL}})_{uncorr}} = \frac{m_t^2\{(t \cdot l^+)(t \cdot l^-) + (\bar{t} \cdot l^+)(\bar{t} \cdot l^-) - m_t^2(l^+ \cdot l^-)\}}{(t \cdot l^+)(\bar{t} \cdot l^-)(t \cdot \bar{t})},$$

$$(2.8)$$

where t, $\bar{t}$, l^+ and l^- are the 4 vectors of the top quarks and the charged leptons. Unlike the $cos(\theta_+)cos(\theta_-)$ variables, the separation between the $C = SM$ and

22

$C = 0$ hypotheses for this observable is highly dependent on the invariant mass of the $t\bar{t}$ system. At low $t\bar{t}$ invariant mass, the values for S are enhanced closer to one and suppressed at lower values. At high values of invariant mass this is no longer the case and distinguishing between spin-correlated and spin-uncorrelated cases is difficult. The parton level distributions in the inclusive, high, and low $t\bar{t}$ invariant mass regimes are shown in Fig. 2.7. Good separation is observed in the inclusive region and this is enhanced in the like-helicity, gluon-gluon-fusion-rich, low invariant mass region. At high invariant mass the separation diminishes.

Delta Phi ($\Delta\phi$)

Experimentally, the $\cos(\theta_+)\cos(\theta_-)$ and S-Ratio variables both require full event reconstruction to extract the momenta of the top and anti-top quark. This procedure is susceptible to mis-modelling and combinatorics effects. It is possible to determine a variable that is sensitive to spin correlation but using objects that are observable in the lab frame. In Equation 2.8 the term $(l^+ \cdot l^-)$ appears only in the numerator. This suggests that the angular difference between the two leptons in the lab frame is sensitive to spin correlation [17]. The $\Delta\phi$ variable is defined as the absolute difference of the azimuthal angle between the two leptons in the lab frame and shares many of the same features as its "parent" variable, the S-Ratio. It is sensitive to spin correlations arising from gluon-gluon fusion and its sensitivity is highest in the low $t\bar{t}$ invariant-mass region and it has diminished sensitivity in the high-mass region, illustrated in Fig. 2.8. In addition, this variable is sensitive only to the linear combination of the c_1 and c_2 parameters, in contrast to the others which have sensitivity to all four non-zero coefficients. This variable was used in the first observation of non-zero spin correlation [27].

Summary of observables

In summary, four observables are studied in this thesis. Each observable has a different sensitivity and motivation:

1. $\cos(\theta^+)\cos(\theta^-)_{helicity}$ [24, 25]: An observable that is directly sensitive to spin correlation. The observable is sensitive to a linear combination of the $c_1^a \to c_4^a$ coefficients from both gluon-gluon fusion and $q\bar{q}$ annihilation. The dependence on the invariant mass of the $t\bar{t}$ system is small.

2. $\cos(\theta^+)\cos(\theta^-)_{maximal}$ [13]: An observable that is sensitive to production from gluon-gluon fusion in general (both like-helicity and opposite-helicity) and theoretically is the maximally sensitive observable to spin correlations

23

at the LHC, though this may be suppressed to a degree by experimental-resolution effects. By construction, the observable is sensitive to the $c_1^g \to c_4^g$ coefficients from the gluon-gluon-fusion matrix elements. The dependence on the invariant mass of the $t\bar{t}$ system is small.

3. S-Ratio [17]: An observable that is sensitive to the $c_1^g \to c_4^g$ coefficients from gluon-gluon fusion (specifically like-helicity-gluon-gluon initial states). The observable shows a large dependence on $t\bar{t}$ invariant mass, with the highest sensitivity to spin correlations in the low $t\bar{t}$ invariant-mass region.

4. $\Delta\phi$ [17]: A lab frame observable that is highly sensitive to spin correlations arising from like-helicity-gluon production and which is sensitive to a linear combination of the c_1^a and c_2^a coefficients. This observable displays a high correlation between sensitivity to spin-correlation and $t\bar{t}$ invariant mass, with the highest sensitivity shown in the low $t\bar{t}$ mass region. This observable has the added advantage of being defined in the lab frame and so it avoids experimental effects arising from the need for full $t\bar{t}$ reconstruction.

2.4   Monte Carlo Event Simulation

Monte Carlo (MC) simulations provide a calculation of the differential cross section for particle interactions. When interfaced with detector simulation, they provide a realistic simulation of the detector response to high-energy collisions. These simulations can be summarised into four parts and a brief description of each follows.

Hard process

The hard process is the calculation of the physics process of interest at a fixed order in perturbative QCD/QED. This part of the calculation models; the collision and production of new particles, the radiation of particles with high transverse momentum at large angles relative to the parent particle, and the decay of these particles that have short lifetimes (for example the t or W). The point at which the perturbative expansion is terminated (i.e. the order of the calculation) is an important point to consider in MC simulation and is often a limiting factor in the precision of the simulation. Most MC generators perform calculations of the hard process at LO. However, in the case of $t\bar{t}$ production, higher-order corrections to the cross section can be large and LO is not sufficient. Generators that operate

Figure 2.5: Distribution of $cos(\theta_+)cos(\theta_-)_{helicity}$ for parton level MC@NLO events at $\sqrt{s} = 7$ TeV for all events (top), for events with $t\bar{t}$ invariant mass less than 450 GeV (center) and invariant mass higher than 450 GeV (bottom). The histograms show the Standard Model and uncorrelated scenarios.
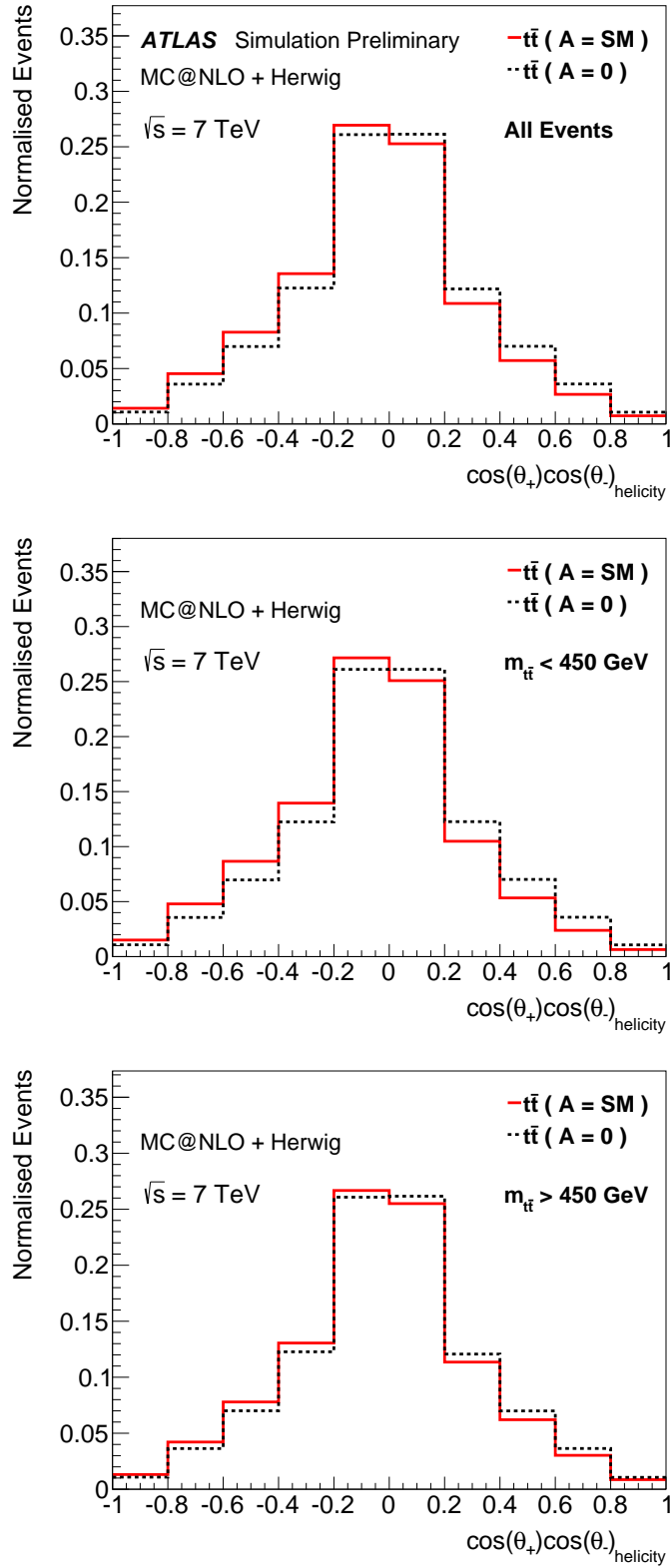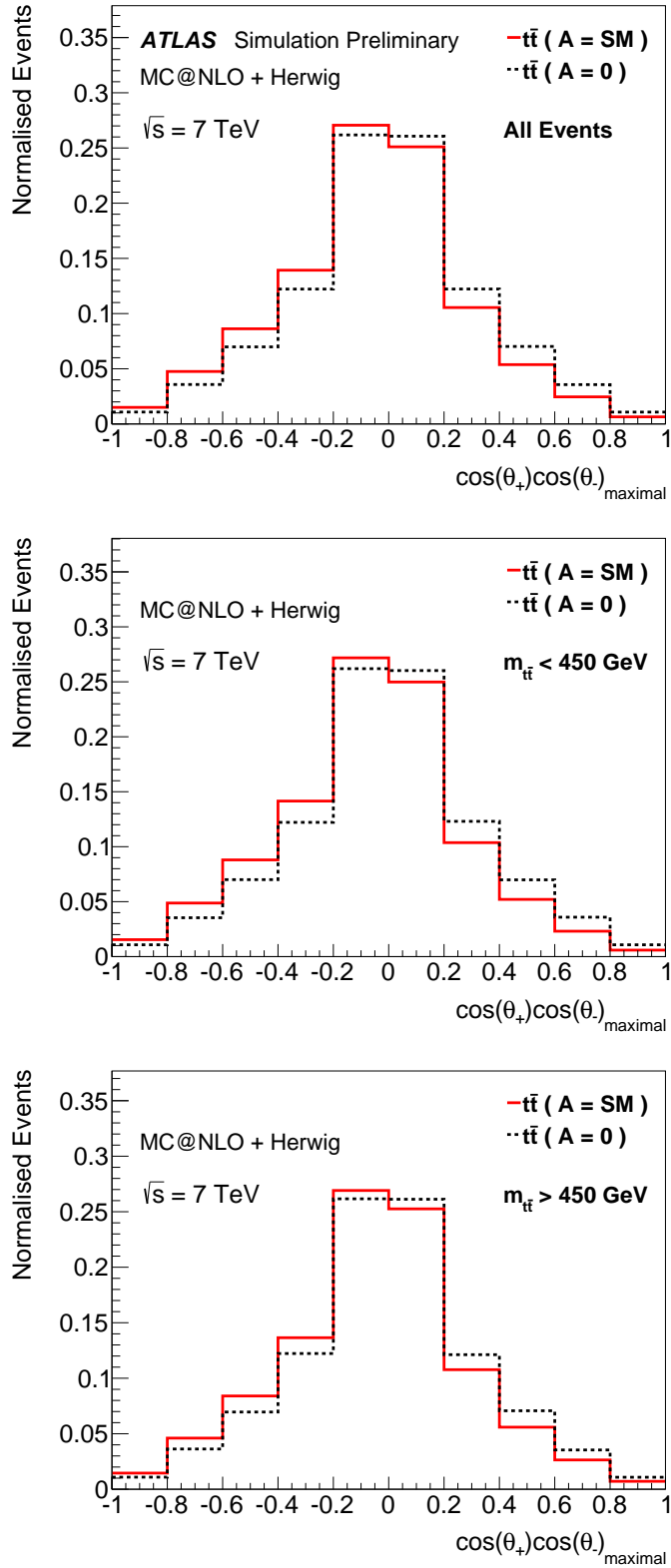
Figure 2.6: Distribution of $cos(\theta_+)cos(\theta_-)_{maximal}$ for parton level MC@NLO events at $\sqrt{s} = 7$ TeV for all events (top), for events with $t\bar{t}$ invariant mass less than 450 GeV (center) and invariant mass higher than 450 GeV (bottom). The histograms show the Standard Model and uncorrelated scenarios.
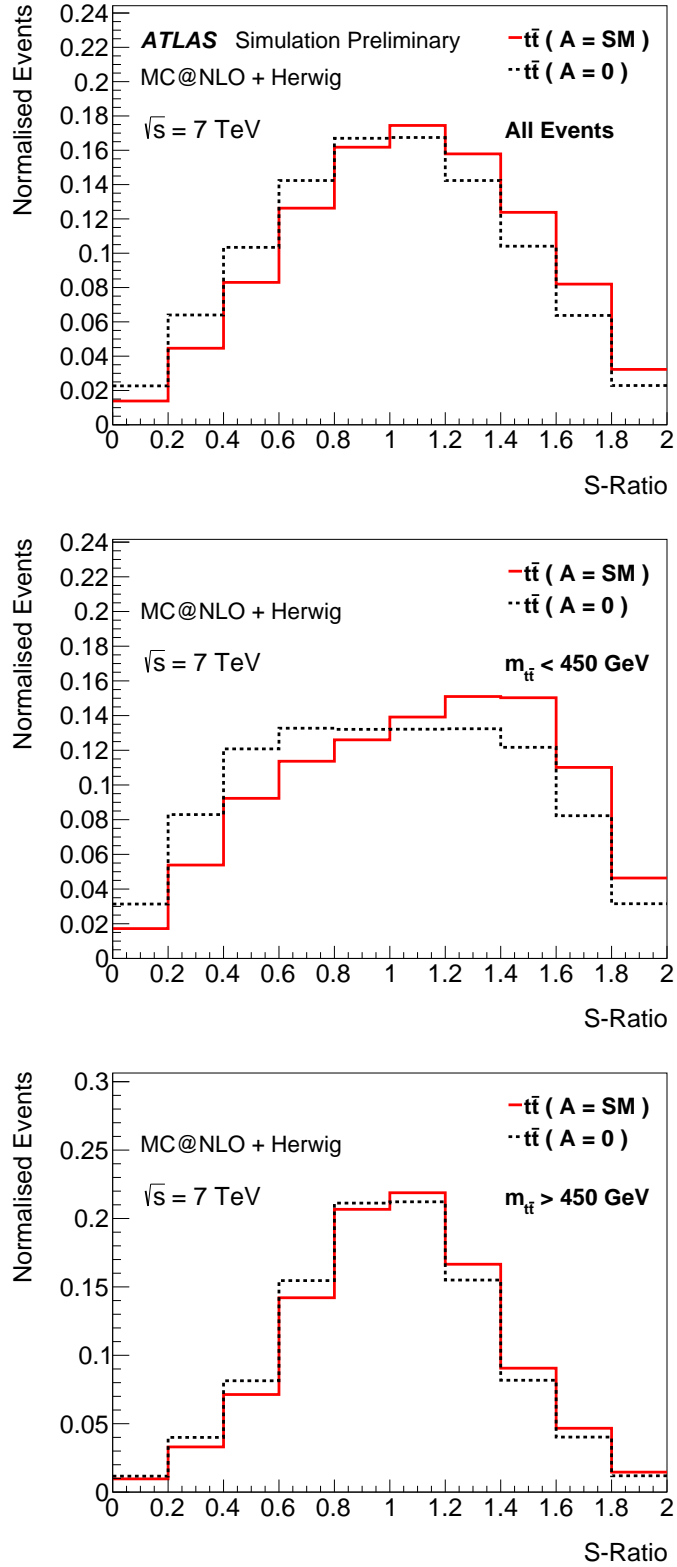
Figure 2.7: Distribution of S-Ratio for parton level MC@NLO events at $\sqrt{s} = 7$ TeV for all events (top), for events with $t\bar{t}$ invariant mass less than 450 GeV (centre) and invariant mass higher than 450 GeV (bottom). The histograms show the Standard Model and uncorrelated scenarios.

Figure 2.8: Distribution of $\Delta\phi$ for parton level MC@NLO events at $\sqrt{s} = 7$ TeV for all events (top), for events with $t\bar{t}$ invariant mass less than 450 GeV (centre) and invariant mass higher than 450 GeV (bottom). The histograms show the Standard Model and uncorrelated scenarios.
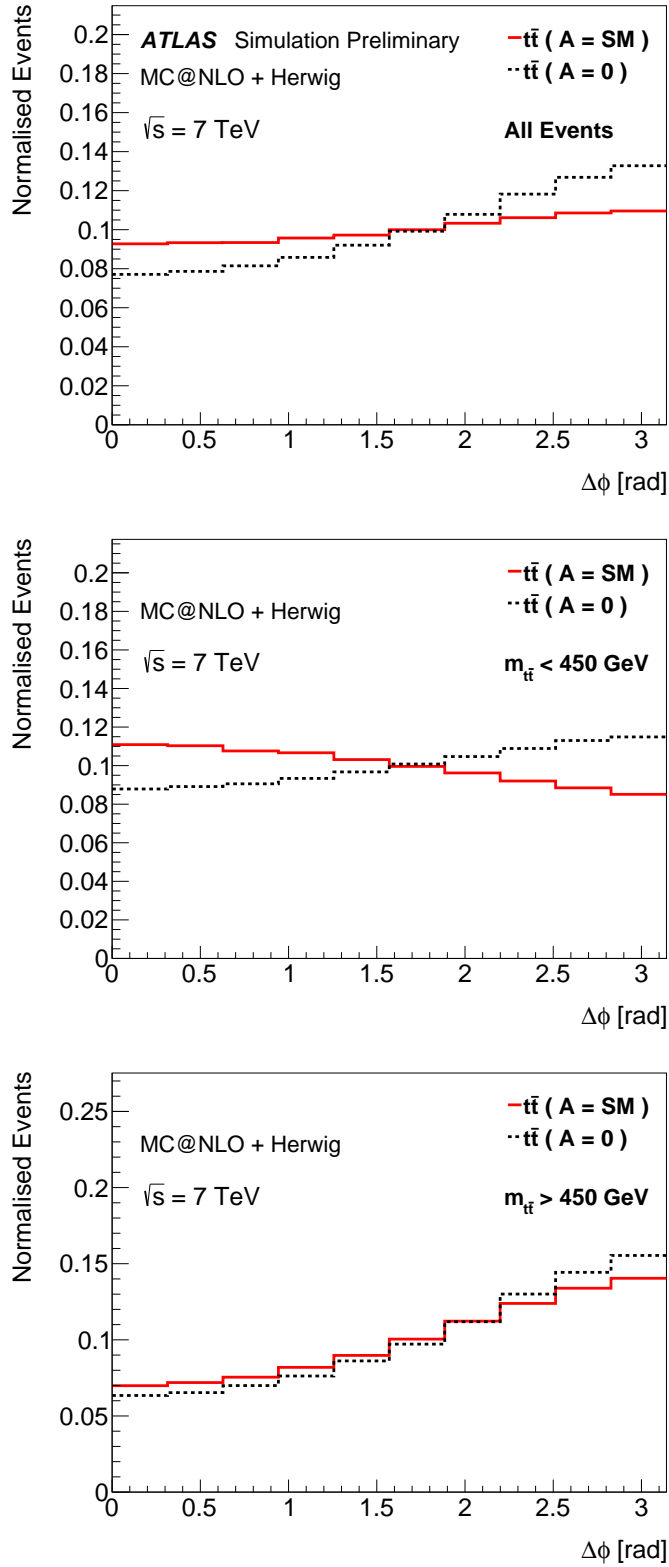
at NLO provide a better description but still underestimate the inclusive cross section observed in data. Fortunately, the $t\bar{t}$ cross section is now known at full NNLO in QCD [28] and NLO generators can be rescaled to obtain a very accurate simulation for the differential cross section of $t\bar{t}$ events.

Parton shower

Following the calculation of the hard process, soft and collinear emissions from the particles are calculated at LO in QCD. The decays of particles that are not calculated in the hard process are also performed. The PS then hadronises the resulting partons into colour-confined objects using either a string [29] fragmentation model or a cluster-fragmentation model. Parton showers (PS) describe the bulk of a collision event well, however calculation of the hard process are required to describe hard angular emissions. The modelling of these parton showers is an important consideration and can lead to sizeable systematic uncertainties. The effects on this analysis of this modelling are discussed further in Chapter 7.3.

Non-perturbative effects

The initial-state gluons or quarks that are used in the hard process are taken from the incoming protons. The subsequent evolution of these proton remnants must be accounted for in the simulation. Additional interactions can occur in each LHC event, leading to additional jets or leptons in the event, and the effects of these "pile-up" interactions must also be accounted for in the simulation. These effects fall under the definition of the "Underlying Event" and are calculated by dedicated programs such as JIMMY [30]. Finally, the resulting particles from decays and radiation in the parton shower are treated as colourless but in reality they are colour-confined objects. The effects of colour confinement must be modelled using "Colour Reconnection". Each of these modelling effects can also introduce systematic uncertainties are discussed in Chapter 7.3.

Parton Distribution Function

The initial state (i.e. the momentum distribution of the initial quarks and gluons) is described using a parton distribution function (PDF). These PDFs are expressed as the probability that a certain particle, with a given momentum fraction, will be found inside the proton. PDFs are calculated by performing global fits to experimental observations from deep-inelastic-scattering experiments or from collider experiments. Various PDFs are available that describe parton mo-

menta from protons at the energies expected at the LHC. One such example is developed and maintained by the CTEQ collaboration [31] and is used as the default for ATLAS $t\bar{t}$ MC.

2.4.1 MC Generators

In practice there are a number of ways to implement this basic framework. Many MC event generators exist; either to perform general purpose simulations of different processes, or to perform simulation of specialised cases. The matching between the matrix-element calculation and the parton shower is also an important consideration.

LO generators

ALPGEN [32] is a multi-leg generator that simulates $2 \to n$ events where n can be a large number of extra particles. This makes it an ideal generator for multi-parton final states such as $Z \to \ell\ell+$ jets. The SHERPA [33] generator is also a LO generator but one that is designed to be highly modular in it's construction. New processes are easy to include, and it is possible to interface the generator to a wide variety of external tool. As such, SHERPA is often used for simulation of BSM physics scenarios or for tests of QCD. HERWIG [34] is a LO generator that is used to perform PS calculation using an angular-ordered matching to the LO matrix elements and employing a cluster fragmentation model for hadronisation. HERWIG may also be used to calculate the hard process at LO but it is not used for this function in this analysis. The PYTHIA [63] generator performs PS calculations at LL with matching to the matrix elements achieved using energy-ordered emissions and using string fragmentation for hadronisation. Like HERWIG, PYTHIA may also be used to calculate hard proceses but the number of included processes is somewhat limited compared to other LO generators and it is only used for simulating the PS in this analysis. ACERMC [35] is LO generator that allows for tuning of the amount of initial-state and final-state radiation (ISR/FSR). It can be used to estimate uncertainties due to simulation, such as ISR/FSR systematic uncertainties and is only employed for this purpose in this analysis.

NLO generators

To perform top-quark measurements at high precision, generators that perform calculations at higher orders than LO are required. Two possible generators

are capable of such calculations. The MC@NLO generator [36] calculates $|\mathcal{M}|^2$ at NLO accuracy in $t\bar{t}$ production. However, NLO effects are not included in the decay of the $t\bar{t}$ system. The MC@NLO generator is interfaced to HERWIG to perform the PS. MC@NLO is somewhat limited in that it can only be interfaced to HERWIG to perform the PS. The POWHEG generator [37] also generates events at NLO accuracy and includes the possibility of using either angular-ordered shower matching with cluster fragmentation, via HERWIG, or momentum-ordered shower matching with string fragmentation via the PYTHIA generator. The implications of angular-ordered versus momentum-ordered PS simulation, and it's effects on $t\bar{t}$ events, are discussed further in Section 7.3.

Chapter 3

Experimental Apparatus

3.1   The Large Hadron Collider

The Large Hadron Collider (LHC) [38, 39, 40] is a proton-proton collider situated at the CERN laboratory in Geneva, Switzerland. The collider itself is a 27 km circumference ring straddling the border between France and Switzerland. There are four interaction points housing some of the most sophisticated experiments ever developed. The experiments are: ALICE (A Large Ion Collider Experiment), ATLAS (A Toroidal LHC ApparatuS), CMS (Compact Muon Solenoid) and LHCb (Large Hadron Collider Beauty). The ATLAS and CMS experiments are both general-purpose detectors. They are tasked with finding and measuring the properties of the Higgs boson, searching for possible signs of physics beyond the SM, and for precision measurements of the parameters of other SM particles; for example, the top quark. ALICE is a heavy-ion experiment, designed to investigate quark-gluon plasmas produced in special lead-ion collisions. LHCb is an experiment seeking to make precision measurements of B-meson physics and to search for sources of CP violation in the SM.

3.1.1   Injector Chain

The LHC itself does not accelerate protons from rest to collision energy. The accelerator complex at CERN is needed to successively increase the energy of the protons through four different accelerators before they reach the LHC ring.

The protons begin at a hydrogen source and are accelerated to 50 MeV by a linear accelerator called "Linac2". They are then injected into the proton source booster (PSB) where they are accelerated to 1.4 GeV. Next they enter the Proton Synchrotron and are accelerated up to 25 GeV before being injected into the Super

Accelerator	Energy (GeV)	Speed (% c)	Lorentz Factor
Linac2	0.05	31.4	1.053
PSB	1.4	91.6	2.493
PS	25	99.93	26.731
SPS	450	99.9998	500.0
LHC	3,500 / 4,000	99.99999996	35355.338

Table 3.1: Accelerators at the CERN complex and the energies to which they accelerate protons as part of the LHC program [41].
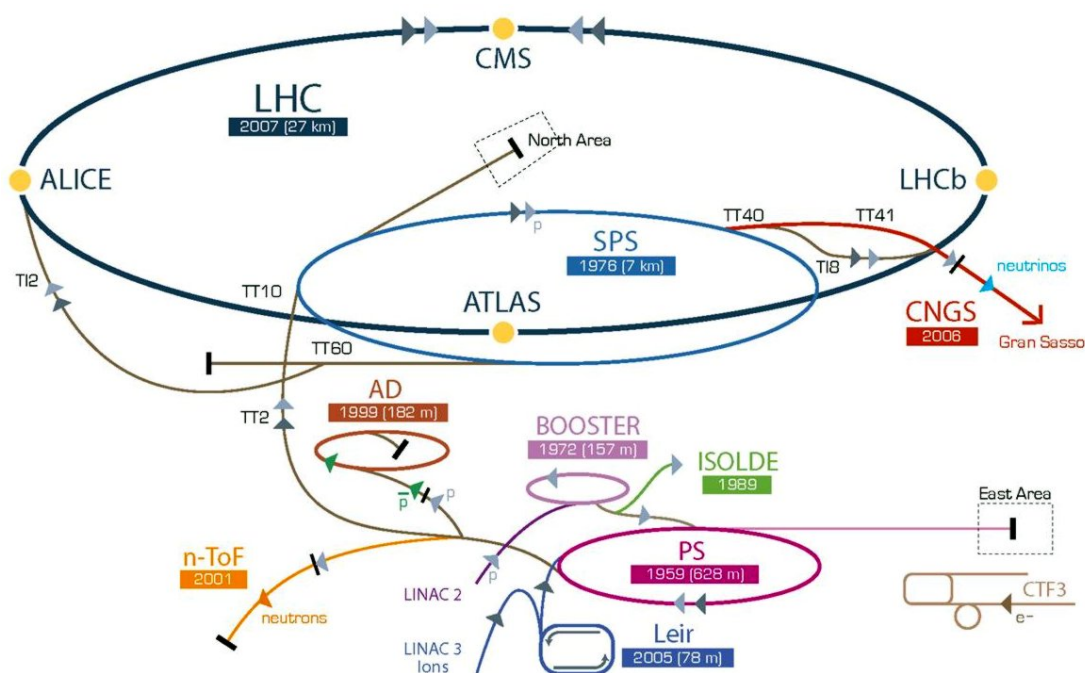
Figure 3.1: The CERN accelerator complex [42].

Proton Synchrotron (SPS). Here they are boosted to an energy of 450 GeV before finally being injected into the LHC, where they are accelerated to a collision energy of 7 TeV (in 2011) or 8 TeV (in 2012). With the exception of Linac2, which as its name suggests uses linear accelerator technology, the majority of these accelerators are based on synchrotron technology. The accelerators involved in the LHC operation are summarised in Table 3.1 and are illustrated in Fig. 3.1.

3.1.2 The LHC

The LHC is a synchrotron that uses superconducting magnet technology. It is designed to operate at a radio frequency of 40 MHz with a maximum of 2808

bunches. In practice the LHC has yet to reach such conditions and in 2011 and 2012 ran with a maximum of approximately 1800 bunches. The LHC is designed to run at a collision energy of 14 TeV. This was limited to 7 TeV in 2011 and to 8 TeV in 2012 (collectively referred to as LHC run 1) in order to provide time to correct design faults in the high-voltage connector cables used in the system for magnet-quench detection. The LHC is expected to resume operation in 2015 with a collision energy of 13 TeV.

The number of particles per unit area and unit time is called the instantaneous luminosity ($\mathcal{L}$) and is defined as:

$$\mathcal{L} = F \frac{f N_1 N_2}{4\pi \sigma_x \sigma_y}, \tag{3.1}$$

where F is a geometrical factor to account for the crossing angle of the two proton beams, f is the beam revolution frequency (nominally 11 kHz), N_1, N_2 are the number of protons in the colliding bunches and σ_x, σ_y are the beam widths transverse to their longitudinal direction (and are assumed to be the same for all colliding bunches). At design luminosity the LHC is expected to operate at an instantaneous luminosity of order $10^{34} \text{cm}^{-2}\text{s}^{-1}$. During LHC run 1 this was limited to less than $8 \cdot 10^{33} \text{cm}^{-2}\text{s}^{-1}$. In 2010 ATLAS recorded 35 pb^{-1} of data, in 2011 it recorded 4.6 fb^{-1} of data, and in 2012 it recorded 20 fb^{-1} of data. The average number of interactions per bunch crossing, instantaneous luminosity, and the number of colliding bunches are shown in Figure. 3.2. The average number of interactions per bunch crossing increased as a function of time along with the instantaneous luminosity. The number of colliding bunches increased between 2010 and 2011 from less than 400 to approximately 1800 but remained consistent for the majority of the 2011 and 2012 data-taking period.
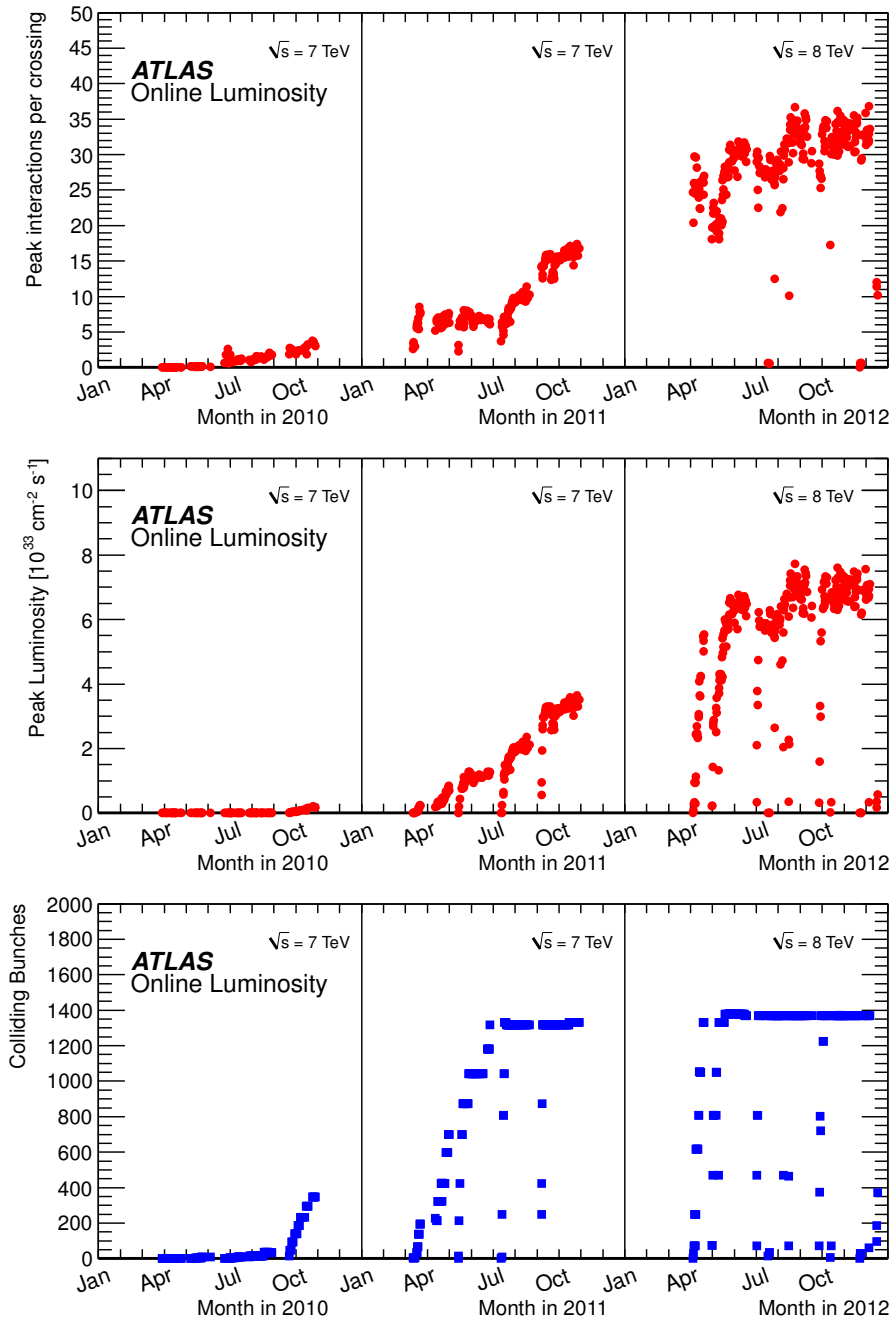
Figure 3.2: ATLAS performance plots for LHC run 1 showing the peak number of interactions per bunch crossing (top), the peak instantaneous luminosity (center) and the number of colliding bunches (bottom) [43].
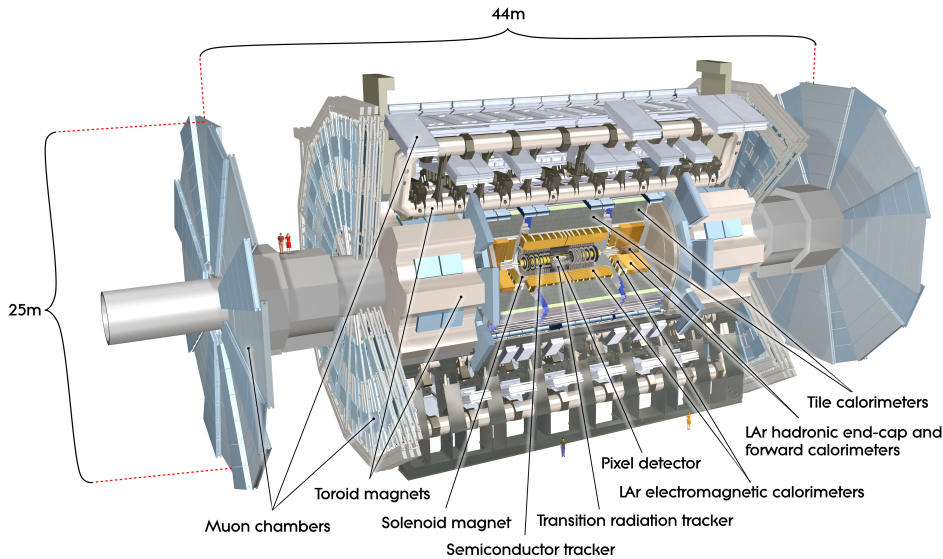
44m

25m

Tile calorimeters

LAr hadronic end-cap and
forward calorimeters

Pixel detector

LAr electromagnetic calorimeters

Toroid magnets

Solenoid magnet

Transition radiation tracker

Muon chambers

Semiconductor tracker

Figure 3.3: An overview diagram of the ATLAS detector [44].

3.2   The ATLAS Detector

The ATLAS detector [45] (Fig. 3.3) is a multi-purpose detector designed to make precision measurements of various SM phenomena, investigate the newly discovered Higgs boson, and to search for possible signals from physics beyond the SM. It is situated at interaction point 1 (IP1) in the LHC ring and is the largest of the LHC experiments.

The detector is constructed in a layered system and is split into barrel and end-cap regions with subdetectors based on different technologies. The goal of this design is to allow for precision measurements of SM particles and to be sufficiently precise so as to be able to infer the presence of neutrinos through missing transverse energy. The detector closest to the interaction point is the inner detector (ID). It is primarily a silicon detector and is designed to measure the tracks of charged particles. It consists of three subdetectors: the pixel detector, the semi-conductor tracker, and the transition radiation tracker. Surrounding the ID is a large solenoid magnet which provides a 2 T magnetic field to allow for the determination of track charge and momentum in the ID. Surrounding the solenoid magnet are two sampling-calorimeter systems. Two systems are used for EM and hadronic-shower energy measurement, respectively. In the barrel and end-cap regions, EM calorimetry is performed using a design based on a Liquid-Argon (LAr) sampling medium with lead or steel absorption. Hadronic calorimetry is achieved in the barrel region using a tile-based calorimeter, with
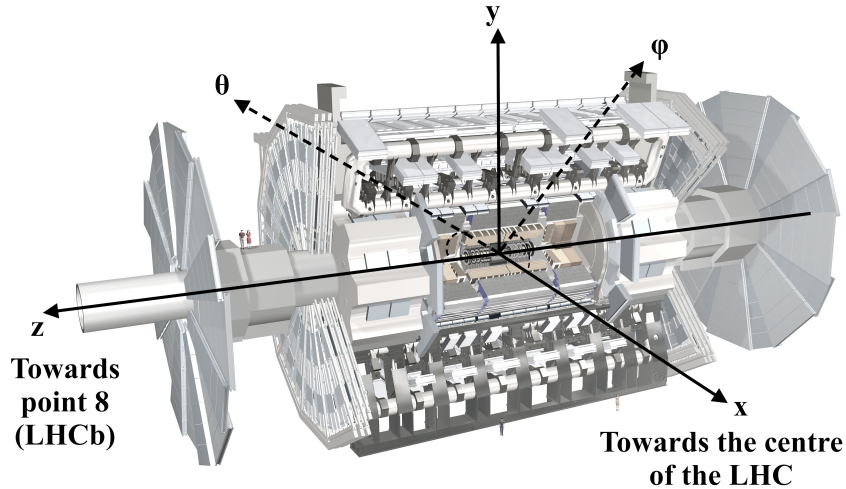
Figure 3.4: A schematic diagram illustrating the ATLAS cartesian co-ordinate system and cylindrical polar coordinate system [46].

steel absorption and scintillating tiles as the sampling medium. In the end-cap region, hadronic calorimetry also uses LAr as a sampling medium, with copper or tungsten for absorption. The outermost layer of ATLAS is the Muon Spectrometer (MS) which is used for precision measurements of muon tracks. A magnetic field in the MS is provided by a 0.5 - 1 T toroidal magnet system that straddles the entire spectrometer.

The detector itself is radiation hard (in particular the tracking systems) and highly granular in order to deal with high event rates and intense pile-up conditions at the LHC. ATLAS has coverage of almost the full 4π solid angle.

3.2.1 The ATLAS coordinate system

The ATLAS coordinate system is a right-handed coordinate system with the x direction pointing to the center of the LHC ring, the y direction pointing almost vertically upwards (due to the tilt of the LHC tunnel it is actually 0.7 degrees away from vertical) and the z direction pointing along the beam pipe in the anti-clockwise direction if viewed from above, illustrated in Fig. 3.4. Cylindrical polar coordinates are also frequently used to describe physics objects. The azimuthal angle ϕ is defined as the angle in the x-y plane and the polar angle θ defined as the angle w.r.t the positive z axis, illustrated in Fig. 3.4. Rapidity is defined as:

$$y = \frac{1}{2} \ln \left(\frac{E + p_{\mathrm{z}}}{E - p_{\mathrm{z}}} \right). \tag{3.2}$$

37

It is often useful to define the "pseudo-rapidity" of an object (η) where:

$$\eta = -\ln \tan(\theta/2). \tag{3.3}$$

The pseudo-rapidity is the rapidity for massless particles. The distance between two objects in the η-ϕ plane (ΔR) is defined as:

$$\Delta R = \sqrt{(\Delta\eta)^2 + (\Delta\phi)^2}. \tag{3.4}$$

Finally, it is convenient to describe only the transverse components of certain physical quantities (X) with the X_T subscript. For example, the transverse momenta and energy of a particle are written as p_T and E_T, respectively:

$$\begin{aligned} p_\mathrm{T} &= |p| \sin\theta \\ E_\mathrm{T} &= E \sin\theta. \end{aligned} \tag{3.5}$$
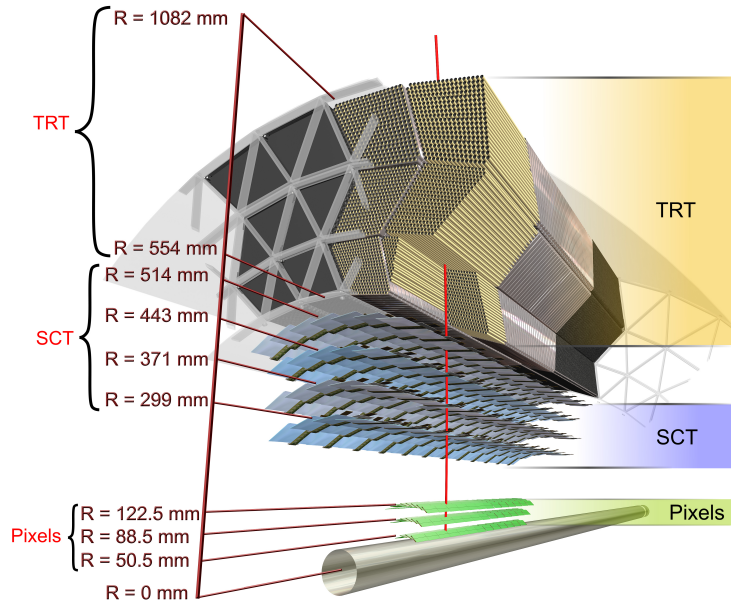
Figure 3.5: An overview diagram of the ATLAS Inner Detector tracking systems [47].

3.2.2 Inner Detector

The Inner Detector (ID) is primarily a silicon based tracking system designed to reconstruct charged particle tracks down to a p_T of 0.5 GeV. It covers the full ϕ angle and provides tracking in the region of $|\eta| < 2.5$. It is also able to provide some rudimentary particle identification information using transition radiation, thanks to the straw drift-tube technology used in the outermost layers. A schematic cross section of the detector is shown in Fig. 3.5.

The read out of information from the ID is a challenging task when compared to the other subdetectors. The combined number of read out channels of the pixel detector alone amounts to over 90% of the total number of active read-out channels for the whole ATLAS detector.

Pixel Detector

The Pixel Detector is the most central detector in ATLAS, situated just 50.5 mm away from the beam line in the innermost layer. It consists of three layers of silicon pixel modules in the central barrel, and five disk layers in the high η end-cap regions. The detector contains 1744 sensor modules, each with 46080 pixels with dimensions 50×400 μm^2 (or 50×600 μm^2 in 10% of cases). The

detector is exposed to intense radiation and must be extremely radiation hard to allow for precision tracking measurements over years of detector operation. Each layer provides an r, η, ϕ measurement for a track, called a "space point". The pixel detector has a nominal track accuracy of 10 μm by 115 μm in the $r - \phi z$ plane.

During the first ATLAS upgrade, after LHC run 1, the current pixel detector will be augmented with an additional layer called the insertable b-layer (IBL). This new layer is also based on silicon-pixel technology but it includes new three-dimensional silicon modules at high η in addition to the planar modules already in use. This upgrade will provide improved tracking accuracy which will be crucial in the harsher operating conditions expected in the second LHC run.

Semi Conductor Tracker (SCT)

Continuing outwards from the Pixel Detector, the next component of the ID is the SCT. The SCT is a silicon-based strip detector. Each module contains two strips placed at small stereo angles to provide a partial space-point measurement. The small stereo angle (16 micro radians) reduces the number of ambiguous space-point solutions. When combined with the global position of the modules, a 3D space point can be constructed just as in the Pixel detector, though the technology is cheaper and easier to scale to the large surface areas required by the SCT. The SCT is constructed in four layers of modules (8 layers total). The SCT provides up to 4 space points for track reconstruction. The SCT has a nominal track accuracy of 17 μm by 580 μm in the $r - \phi z$ plane.

Transition Radiation Tracker (TRT)

The final part of the inner detector is the Transition Radiation Tracker. Unlike the other two silicon-based layers, this layer is designed from straw-tube technology. A mix of XeO_2CO_2 gas surrounds a 4 mm wire at the centre of each tube. The gas is ionised by charged particles, providing a signal along the wire as free electrons drift towards it. The TRT is less precise when compared to the other ID components for track reconstruction. However, the difference in the transition radiation emitted by pions and electrons makes this subdetector useful for particle identification. The TRT provides tracking information in the region of $|\eta| < 2$. The TRT can provide up to 32 space points on average, per track, and has a nominal track accuracy of 130 μm in the $r - \phi$ plane.
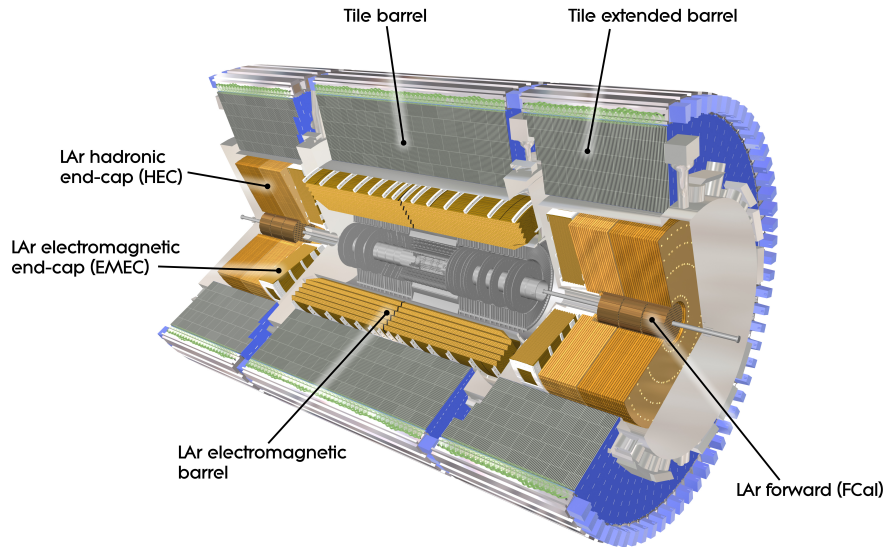
Figure 3.6: An overview diagram of the ATLAS Calorimeter systems [48].

3.2.3 The Calorimeters

Calorimetry at ATLAS is designed to measure the energies of both charged and neutral particles. The Calorimeter systems are based on two technologies: Liquid Argon active medium, with either lead or copper absorption (LAr), and scintillation tiles with steel absorbers (Tile). A schematic diagram is shown in Fig. 3.6.

ElectroMagnetic Calorimeter (EMCal)

The ElectroMagnetic Calorimeter surrounds the solenoid magnet and inner detector and is responsible for energy measurements of particles who's interactions with dense materials are dominated by electromagnetic processes, such as electrons and photons. The detector uses liquid argon as the active medium with lead absorption. There is also a pre-sampling layer situated between the main EMCal and the solenoid magnet to measure energy loss due to the material in the ID. The detector is constructed in an accordion-like design such that full coverage in ϕ is achieved and particles pass through an equivalent amount of material regardless of their direction. The detector extends up to $|\eta| = 3.2$.

The granularity of the detector is finer where it overlaps with the coverage of the inner detector, with three layers of active and absorber material in order to perform precise measurements of photons and electrons. At other regions only two layers are used with less granularity. The EMCal is designed to measure the energies of electrons and photons and to contain their particle showers within the

EMCal. It was specifically designed to provide good photon resolution, which is crucial for the $H \rightarrow \gamma\gamma$ decay channel.

Hadronic Calorimeter

The Hadronic Calorimeter (HCal) uses a combination of LAr and scintillating-tile technology. In the barrel region ($|\eta| < 1.7$) steel is used as the absorbing material and scintillating tiles are used as the active medium. In the end-cap region ($1.7 < |\eta| < 3.2$) copper is used as the absorbing material and LAr is used as the active medium. The Hadronic Calorimeter is designed to measure the energy of particles that interact via the strong force, and to completely contain their particle showers within the calorimeter system.

Forward Calorimeters

ATLAS also has the capability of performing calorimetry at very high pseudo-rapidity ($3.2 < \eta < 4.9$) which is important for the measurement of missing transverse energy ($E_{\mathrm{T}}^{\mathrm{miss}}$). Layers of copper and tungsten are used as absorbing materials and LAr is used as the active medium. This detector must withstand very high particle fluxes close to the beam line and fully contain particle energy in order to provide a good measurement of $E_{\mathrm{T}}^{\mathrm{miss}}$.
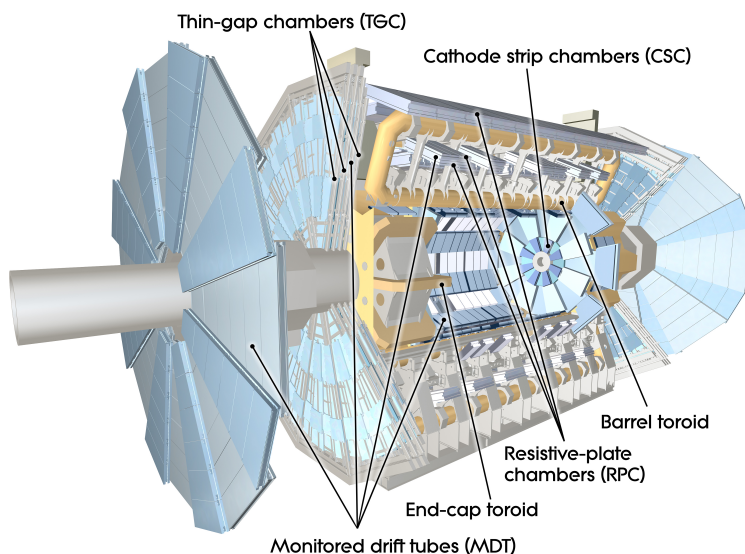
Figure 3.7: An overview diagram of the ATLAS Muon Spectrometer [49].

3.2.4   Muon Systems

The Muon Spectrometer (MS) is the largest of the sub-detectors and has four components. The MS is designed to perform measurements of only muon tracks as all other particles (with the exception of neutrinos) are absorbed by the calorimeter systems. The MS also plays a crucial role in the Trigger system and covers a pseudo-rapidity range of up to $|\eta| = 2.7$ in some cases. There are gaps in the muon spectrometer coverage due to electronics for the other internal detector components and the physical support structures, or "feet", of ATLAS itself. An illustration of the muon systems is shown in Fig. 3.7. The MS is divided into chambers for precision tracking and fast trigger chambers. Hardware triggers (see Section 3.3) are not able to use all of the available information and must rely on specialised parts of the Muon Spectrometer instead. The muon track resolution varies depending on energy and location in the detector. An example resolution for a 1 TeV muon would be $\sigma(p_{\mathrm{T}})/p_{\mathrm{T}} = 10\%$.

Precision tracking

Precision muon tracking is performed by Monitored Drift Tubes (MDTs) and Cathode Strip Chambers (CSCs). The MDTs are a straw-tube technology filled with an Argon and CO_2 gas mixture and a tungsten wire. Three or four layers of straws are collected in each module along with read out electronics and internal sensors to monitor alignment, temperature, and magnetic field. The MDTs cover an η range of up to $|\eta| = 2.7$ in the two outer most layers and $|\eta| < 2$ in the

innermost layer. The MDTs are capable of handling particle rates of up to 150 Hz per cm^2. The CSCs contain resistive strip plates, anode wires, and an ArCO$_2$ gas mixture. The resistive plates are arranged to be perpendicular to the wires for ϕ measurements or parallel to them for η measurements. The CSCs complement the MDTs as a precision detector for measuring muon tracks. They are employed in the forward region in the innermost layer $2.0 < |\eta| < 2.7$. CSCs are used in this region as they are more granular and are capable of handling a higher particle flux of up to 1000 Hz per cm^2.

Muon triggers

Triggering of muon signals is achieved through Resistive Plate Chambers (RPCs) in the barrel region and Thin Gap Chambers (TGCs) in the end-cap regions. The RPCs are two phenolic-melaminic plastic plates separated by a gas mixture of $C_2H_2F_4$, Iso-C_4H_1O and SF_6. There are three layers of RPC stations and each is capable of providing a measurement of η and ϕ. This technology is extremely fast and is crucial in the triggering of muon events early on in the trigger system. In the end-cap regions the TGCs provide trigger information. Each chamber is filled with a gas mixture of CO_2 and C_5H_10, with an anode wire placed to collect free electrons left by muon tracks. The TGCs are capable of performing trigger tracking even with extremely high rates expected in the high η regions.
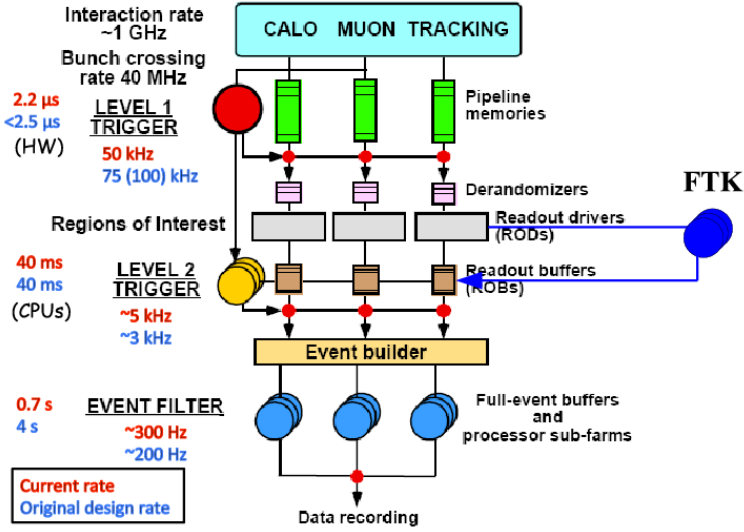
Figure 3.8: An overview diagram of the ATLAS Trigger design [50].

3.3 ATLAS Trigger System

At nominal luminosity in ATLAS, there are 40 million events every second, with each event containing multiple interactions. ATLAS has extensive computing resources but it is not possible to record every event nor would it be possible to read out the detector at this rate. The purpose of the Trigger system is to record interesting events, that contain high-momentum objects, and to reject other events.

The ATLAS trigger is divided into three levels. The first is the Level 1 (L1) trigger and is hardware based. The second and third, called the Level 2 (L2) and Event Filter (EF) respectively, are software based and are collectively referred to as the High Level Trigger (HLT). Each level imposes stricter requirements on physics objects than the preceding level, reducing the event rate.

3.3.1 Level 1

The L1 trigger uses information from the calorimeter and muon subdetectors to identify regions of interest (ROIs). The size of these regions depends on the trigger used and are defined in $\eta - \phi$ space; a common example would be $\delta\eta = \delta\phi = 0.4$. The L1 trigger is designed to make fast decisions (in less than 2.5 μs) and so only basic information from the detector is used. It is not possible to read out the ID information to and use it within the time constraints of the L1 trigger. For this reason, the ID tracking information is not used in L1 trigger decisions. The event

rate is reduced from the order of GHz to only a few hundred kHz.

3.3.2   High Level Trigger

The L2 trigger is a software-based trigger that performs more sophisticated reconstruction of physics objects than the L1 and uses information from all three main subdetectors of ATLAS: ID, Calorimeter and Muon. The software algorithms still have significant time constraints (less than 40 ms) and so the reconstruction must be optimised for speed rather than the best possible accuracy. The L2 trigger reduces the rate of events from hundreds of kHz to the order of 1kHz.

The EF is the final and most complex level of the trigger and as such is allowed a relatively long execution time to reconstruct events (1s). The full detector information is available to the EF algorithms and often the reconstruction performs comparably to the offline reconstruction algorithms. The EF reduces the trigger rate from a few kHz to a few hundred Hz; for example, 250 Hz was an average EF rate during 2011 running. Following the HLT decision the events are written to disk.

A full trigger chain is composed of an L1 trigger, an L2 trigger and an EF trigger. Each individual trigger may be prescaled by a number X such that only 1 in every X events are selected. These prescales are an essential part of controlling the overall rate of a trigger chain. Triggers in ATLAS generally follow a common naming convention. First the trigger level is specified, followed by a character or two indicating the object the trigger is designed to identify; for example, "e" refers to electron triggers, "mu" to muon triggers and "j" to jet triggers. Following this is a number indicating either an energy or transverse momentum cut and finally a string of characters to indicate any additional trigger features. A trigger chain might therefore take the form:

$$\text{L1\_e10} \rightarrow \text{L2\_e20\_medium\_IDTrkNoCut} \rightarrow \text{EF\_e20\_medium\_IDTrkNoCut} \quad (3.6)$$

where the trigger is selecting electrons with a minimum p_T of 20 GeV with medium identification cuts. The "IDTrkNoCut" indicates that this trigger did not use any tracks from the ID to make its decision.

Chapter 4

Trigger Efficiency Monitoring

The ATLAS detector is neither perfect nor constant in its operation and response. In order to effectively measure top quark properties, the detector must be well understood, calibrated and re-calibrated regularly. The performance of the trigger is an important part of the detector response and good lepton trigger identification is crucial for selecting $t\bar{t}$ events. An understanding of the efficiencies and performance of particular triggers is vital for any physics analysis.

4.1 Inner Detector Trigger efficiencies

Trigger efficiencies may be divided into two types: absolute efficiencies and relative efficiencies. Absolute efficiency directly measures the performance of the detector. An example would be how often a trigger track is found when a lepton passed through the inner detector. Relative efficiency measures parameters with respect to some other benchmark parameter. For example, comparing trigger electrons to electrons reconstructed by the offline software. These types of efficiencies avoid detector limitations in their efficiency calculation. A further benefit of such an efficiency measurement is that it can be derived directly from data without the need for MC simulation. Only relative efficiencies will be discussed in this thesis.

4.2 Regions of interest

Triggers at ATLAS use C++ algorithms to build physics objects and subsequently make trigger decisions. Limitations of the detector hardware read out and the high rate of interactions means that these algorithms must be very fast. Reconstructing trigger objects in the entire detector for each event, in order to make a

trigger decision, is not always feasible, even with algorithms optimised to only use minimal computing resources. The ATLAS HLT receives information from the L1 triggers about the location in the detector of potentially interesting physics objects. A region in $\eta - \phi$ space around the object is created, called a region of interest (ROI). The trigger algorithms are then run only on detector signatures in this ROI, vastly reducing the overall computing time in each event. All L2 and EF physics triggers use ROIs and the trigger objects reconstructed inside them are used to make their decisions and to select events. This strategy made the ATLAS trigger system highly successful in 2010, 2011 and 2012 data taking, enabling the use of single-lepton-inclusive triggers for physics analysis throughout the data-taking period. Some triggers are capable of running in a "full scan" mode where the whole detector is considered, not only ROIs. However, these triggers are limited in their implementation and the use of ROI-based triggers is far more common in 2011 and 2012 data.

4.3   Trigger Objects

Many different kinds of objects are identified or reconstructed by the L1 and HLT respectively. The identification of muons and jets is possible at all trigger levels, with increasing sophistication as the trigger moves from L1 to EF. Jets are identified at L1 by energy clusters in the calorimeter using a sliding-window algorithm, and then reconstructed from calorimeter clusters in the HLT. Muons are identified at L1 by specialised trigger chambers in the Muon Spectrometer and tracks are reconstructed in the HLT. Electrons are reconstructed in both levels of the HLT, with limited recognition at L1 from energy clusters. Trigger objects in the HLT are built using ID tracks, calorimeter clusters and muon tracks. These trigger objects are then used to make the trigger decision, based on parameters such as p_{T}.

4.4   Trigger Tracking

Trigger tracking is not possible at L1. The read out of the ID cannot be performed in the time needed for an L1 trigger decision ($<2.5~\mu$s). At L2, full read out of the inner detector is possible and trigger tracks are reconstructed. Time constraints are still substantial (40 ms) but it is possible to reconstruct tracks and use them to build electron and muon trigger objects. At EF the time restrictions are more generous and trigger tracking is almost as effective as the tracking used in offline

Signature	Uses Tracks	Primary Alg. 2011	Primary Alg. 2012
Electron	Yes	IDScan	L2Star-A
Photon	No	-	-
Muon	Yes	IDScan	L2Star-A
Tau	Yes	SiTrack	L2Star-B
$E_{\mathrm{T}}^{\mathrm{miss}}$	No	-	-
Jet	No	-	-
b-jet	Yes	SiTrack	L2Star-B
B-phys	Yes	SiTrack	L2Star-B

Table 4.1: Trigger signatures and their associated tracking algorithms in 2011 and 2012.

reconstruction.

Many physics objects use ID-trigger tracks in some form. All charged lepton signatures use ID tracks (though muons may be reconstructed using only MS tracks) as well as b-jet and B-physics signatures. It is important to optimise the performance of the ID tracking for each signature through the use of multiple track-reconstruction algorithms. Prompt leptons benefit from tracking algorithms that are optimised to find tracks originating from the primary-interaction vertex, whereas signatures with displaced vertices, such as b-jets, may require more relaxed tracking that does not include this vertex assumption. The trigger signatures that utilise ID tracks, and the algorithms that are used to reconstruct these tracks, are listed in Table 4.1.

4.4.1 Tracking algorithms

The IDScan (*"Inner Detector Scan"*) algorithm is an L2 tracking algorithm optimised for tracks originating from a primary vertex. It is well suited to the reconstruction of tracks originating from the primary vertex and is used as the primary L2 trigger algorithm for electron and muon signatures in the 2010 and 2011 triggers.

SiTrack (*"Silicon Tracker"*) is an algorithm that also operates at L2; however, unlike IDScan it is optimised to find tracks from displaced vertices rather than those originating from the primary vertex. SiTrack is used as the primary L2 tracking algorithm for b-jet signatures in 2011 triggers.

For 2012 data a new tracking algorithm was designed for L2, called "L2Star", which combines features from both IDScan and SiTrack. This algorithm has three modes; A, B and C. Mode A served a similar purpose to IDScan as the primary

algorithm for objects originating from the primary vertex. Similarly mode B served the same purpose as SiTrack as the primary algorithm for signatures that require track reconstruction from displaced vertices, such as b-jets. Mode C is designed to perform similarly to the offline tracking algorithms but is not used as a primary algorithm due to its longer execution time in comparison to A and B.

The EFID (*"Event Filter Inner Detector"*) algorithm is similar in execution to the offline track reconstruction and is used for all 2010-2012 data taking periods.

4.4.2   Relative-Efficiency Monitoring

Relative-efficiency monitoring measures how accurate a trigger algorithm is with respect to an offline algorithm, which are assumed to be a good reference. Offline algorithms have very few limitations on computing resources and time, in comparison to those imposed upon the trigger algorithms, and can be more complex. Two definitions of efficiency are considered.

The simplest relative efficiency is to compare all tracks inside an ROI, that are reconstructed by the offline algorithms, to those reconstructed by the trigger algorithms. Efficiency is defined as the number of trigger tracks that matched to tracks in the offline with a $\Delta R < 0.01$:

$$\epsilon_{ROI} = \frac{\text{online track} \in \text{offline track}}{\text{all offline tracks}}. \tag{4.1}$$

Conversely it is also possible to define a "fake" rate for tracks that are found by the trigger algorithms but not by the offline algorithms:

$$\text{fake}_{ROI} = \frac{\text{online track} \notin \text{offline track}}{\text{all offline tracks}}. \tag{4.2}$$

The advantage of using all tracks reconstructed inside an ROI is that it offers the possibility of high statistics, since more than one track can be reconstructed inside an ROI.

In order to measure trigger-tracking efficiency, triggers are required that do not base their decision on any tracking information. Such triggers are generally not of use for physics analyses, and as such they can only be assigned a limited amount of bandwidth. This limits the statistics available for assessment.

A more complex relative efficiency, called "Object-based" efficiencies, uses physics objects such as electrons and muons reconstructed by offline algorithms. An event is said to be efficient if the offline track associated with an offline physics

Trigger	L2			EF		
	Period E	Period I	Period M	Period E	Period I	Period M
Efficiency						
μ	91.6	94.5	94.5	97.8	98.7	98.4
μ (comb)	99.3	99.2	99.3	99.9	100.0	100.0
e	76.5	79.7	79.4	93.8	95.1	94.8
e (comb)	—	—	95.7	—	—	98.7
b-jet	93.2	95.6	93.3	98.9	99.3	99.1
Fake Rate						
μ	6.1	6.3	7.7	4.7	5.0	6.0
e	12.1	11.5	12.6	7.1	7.0	9.0
b-jet	4.8	4.4	5.8	3.9	3.6	4.7

Table 4.2: Efficiencies and fake rates of ATLAS triggers in 2011 data. Muon trigger efficiencies and fake rates are derived using the "mu_20_IDTrkNoCut" trigger. Object-based efficiencies are indicated with "(comb)". Electron trigger efficiencies and fake rates are derived using the "e20_medium_IDTrkNoCut" trigger, in Periods E and I, and using the "e22vh_medium_IDTrkNoCut" trigger in Period M. Object-based efficiencies are only available for the latter trigger. Efficiencies and fake rates for b-jets are estimated using the "b10_IDTrkNoCut" trigger in all periods. Object-based efficiencies are not available for this trigger.

object, such as an electron, is matched to a trigger track:

$$\epsilon_{ROI} = \frac{\text{online track} \in \text{physics object track}}{\text{all physics object tracks}}. \tag{4.3}$$

This technique suffers from fewer statistics than the first as only tracks from physics objects are considered. However, this technique provides efficiencies that are directly related to physics analyses and is more useful to monitor.

4.4.3 Relative efficiencies in 2011 data

The purpose of relative-efficiency monitoring in 2011 data is to provide run-by-run information on the performance of triggers used for physics analyses. For physics analyses such as dileptonic $t\bar{t}$ decay, single lepton triggers are crucial for selecting events. In processes with no prompt leptons; for example, in $ZH \rightarrow \nu\nu b\bar{b}$ b-jet triggers are also of interest.
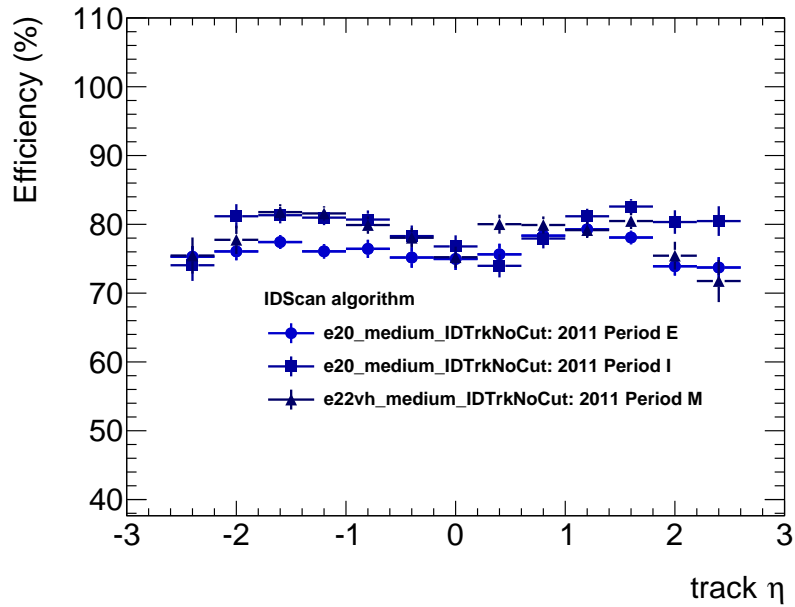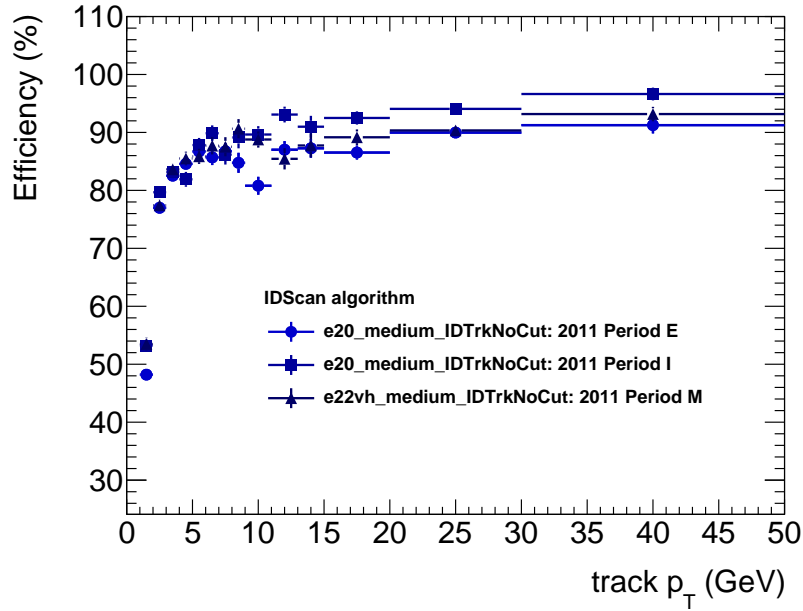
Figure 4.1: ROI-based efficiencies for electron triggers in 2011 ATLAS data for ID-Scan. The efficiency is presented as a function of the track p_{T} and (*top*) and η (*bottom*).
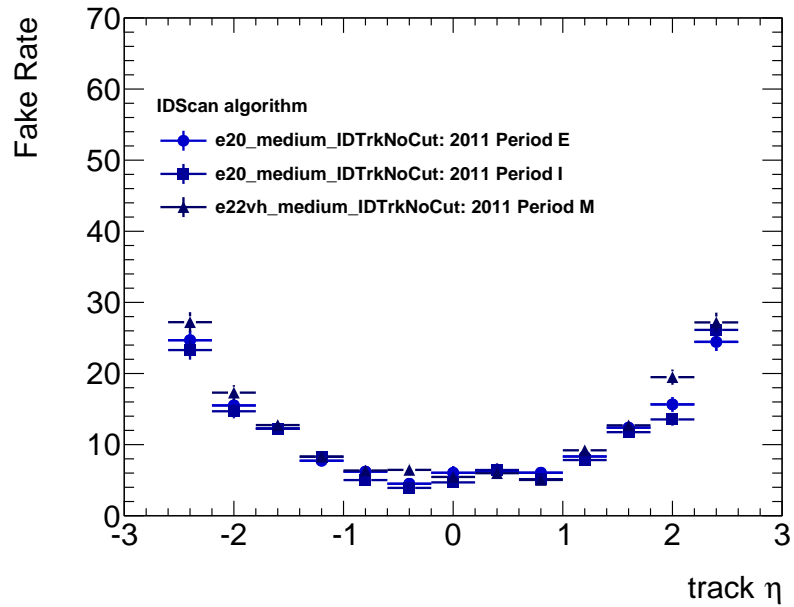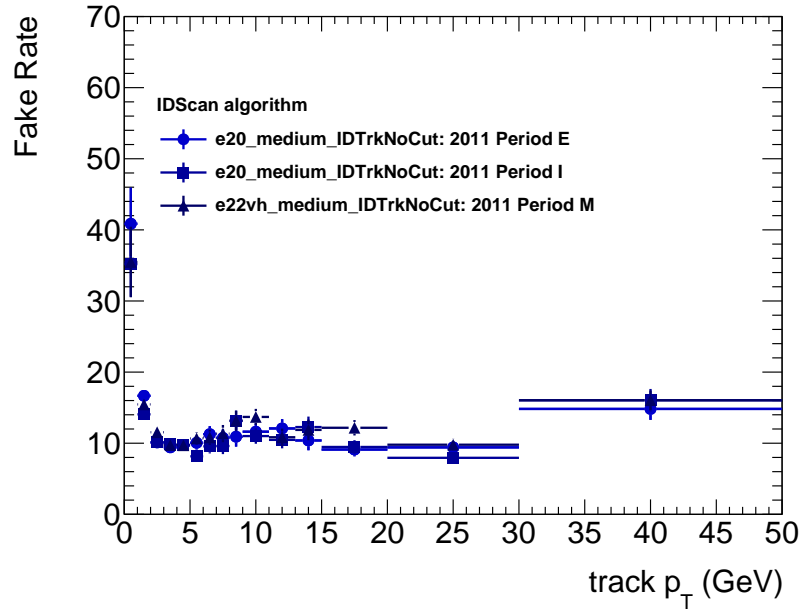
Figure 4.2: ROI-based fake rates for electron triggers in 2011 ATLAS data for IDScan. The efficiency is presented as a function of the track p_T and (*top*) and η (*bottom*).
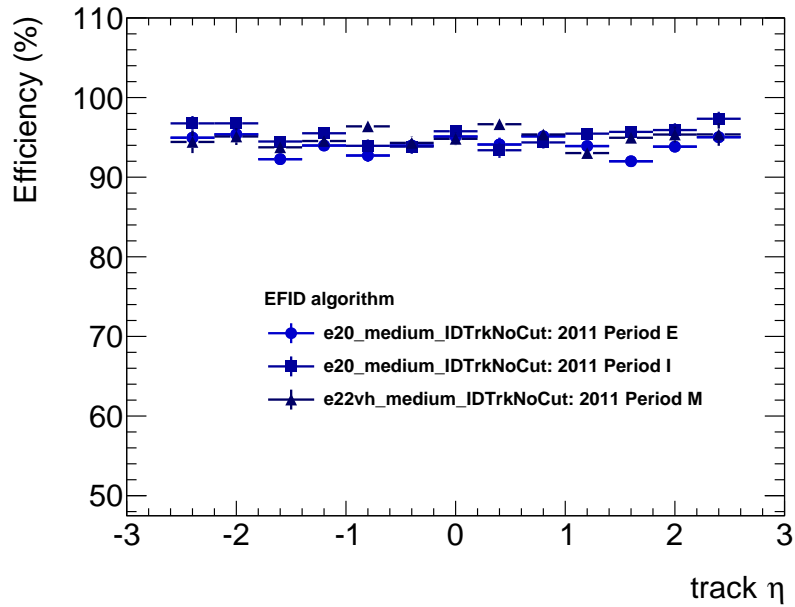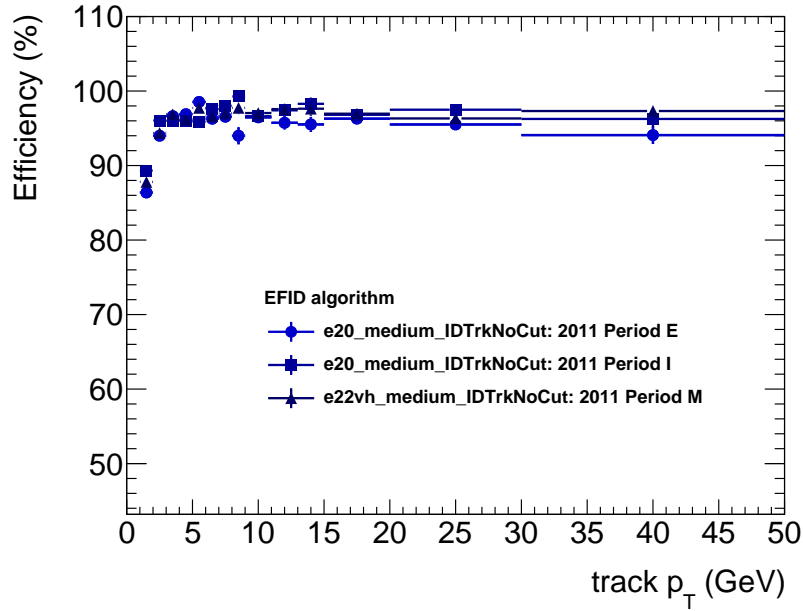
Figure 4.3: ROI-based efficiencies for electron triggers in 2011 ATLAS data for EFID. The efficiency is presented as a function of the track p_T and (*top*) and η (*bottom*).
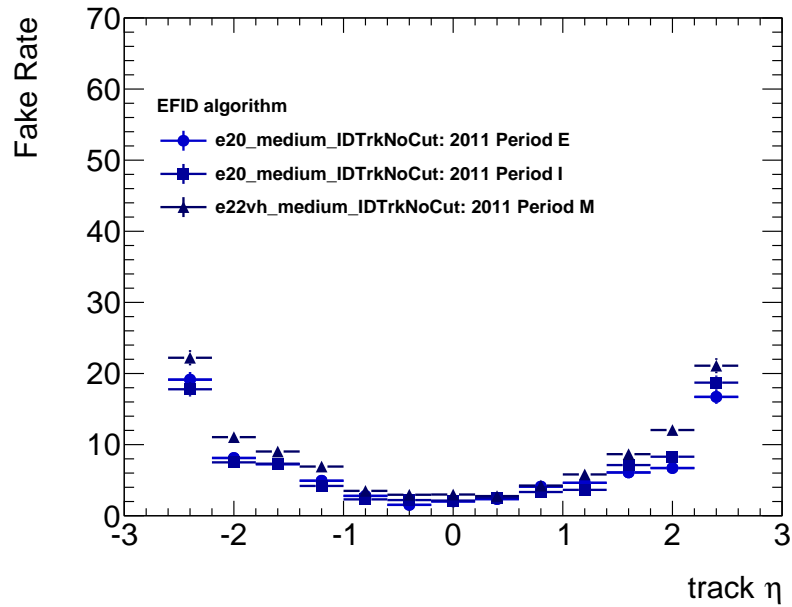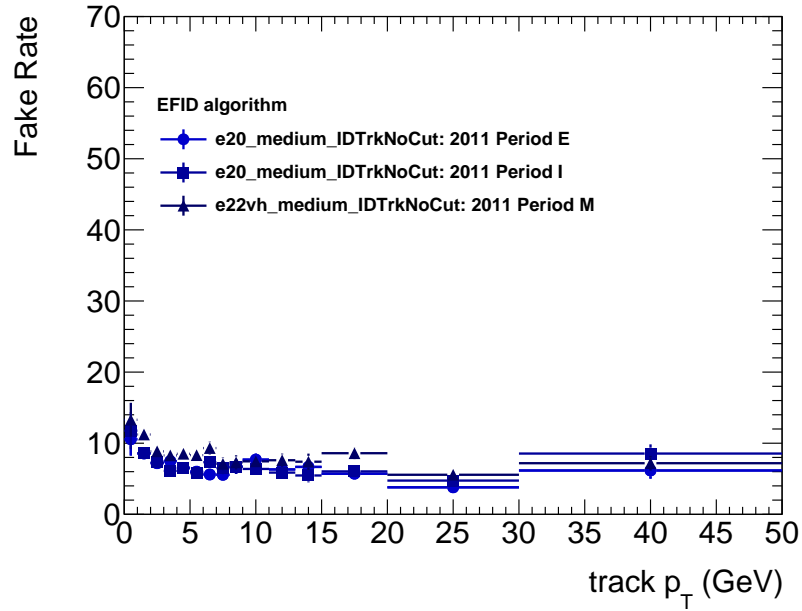
Figure 4.4: ROI-based fake rates for electron triggers in 2011 ATLAS data for EFID. The efficiency is presented as a function of the track p_T and (*top*) and η (*bottom*).

Figure 4.5: Object-based efficiencies for electron triggers in 2011 ATLAS data for IDScan. The efficiency is presented as a function of the track p_T and (*top*) and η (*bottom*).

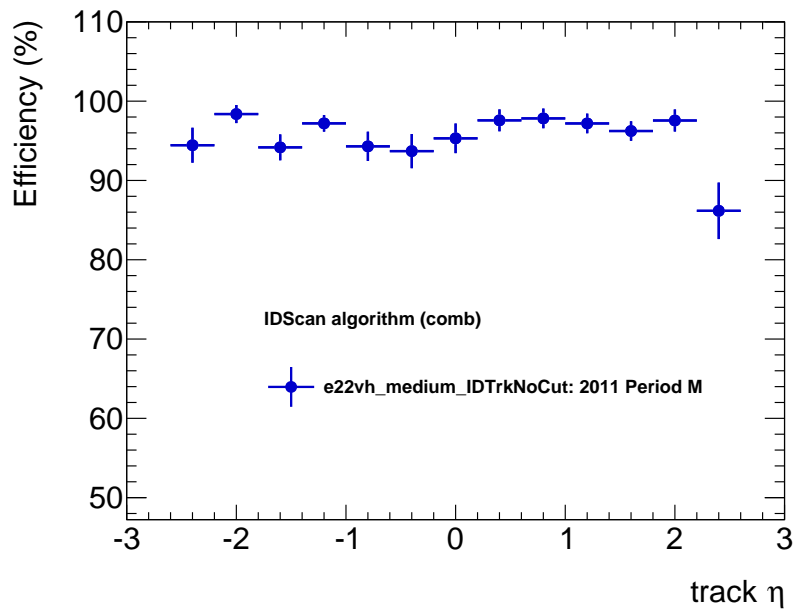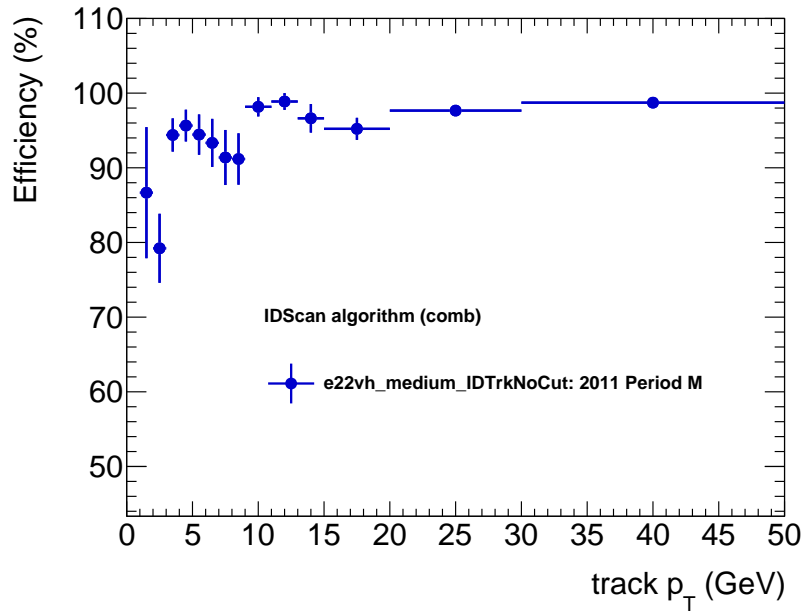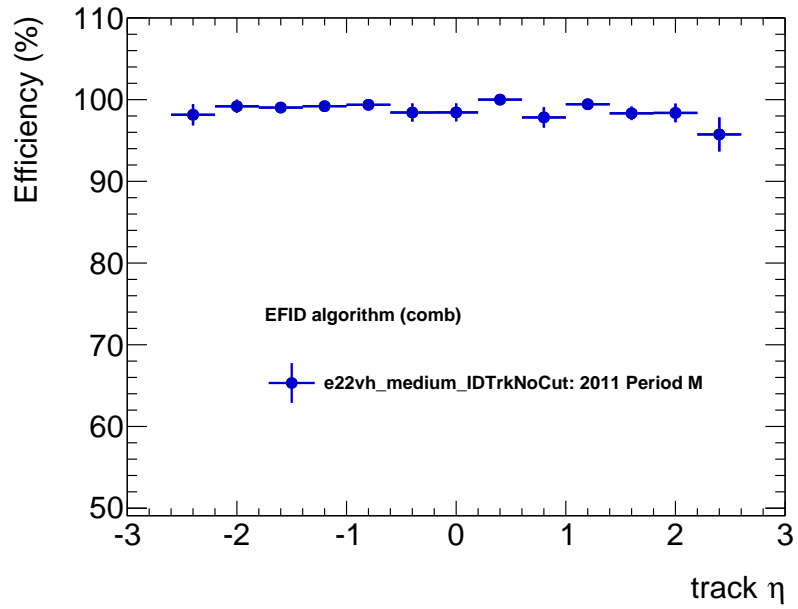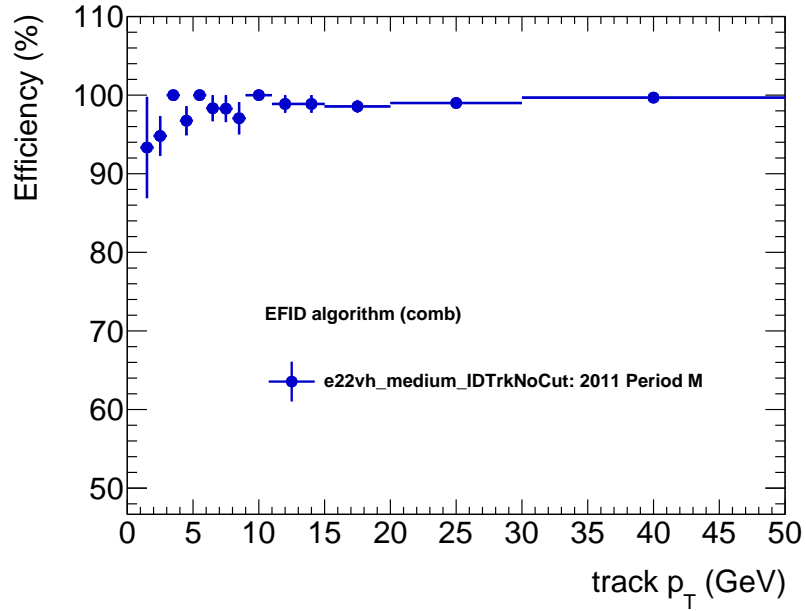**Figure 4.6:** Object-based efficiencies for electron triggers in 2011 ATLAS data for EFID. The efficiency is presented as a function of the track p_T and (*top*) and η (*bottom*).

Electron

Electron efficiencies are measured using two triggers. For earlier data periods, efficiencies are measured using the "e20_medium_IDTrkNoCut" trigger. This trigger requires electrons with $p_T > 20$ GeV and medium-quality cuts on the calorimeter clusters. No requirement is made on the ID tracks so as not to bias the tracking efficiency. In later data periods, pileup conditions require the introduction of a tighter trigger that include additional isolation requirements "e22vh_medium_IDTrkNoCut". The results for three example runs, with high statistics, at different points during the 2011 run are presented.

At L2, the ROI-based efficiency of the IDScan algorithm remained stable at approximately 80% with a fake rate of 12%. The efficiency and fake rates are presented in Fig. 4.1 and Fig. 4.2, respectively. The efficiency, as a function of p_T, rises from low to high p_T and is reasonably stable at greater than 20 GeV. The efficiency, as a function of offline track η, shows some structure. Lower efficiency is observed at higher $|\eta|$. The fake rate, as a function of offline track p_T, shows a sharp increase at low p_T. A more stable rate is observed in the efficiency plateau for this trigger. The fake rate, as a function of offline track η, shows a definite structure, with higher fake rates observed at high $|\eta|$. This is easily understood as the ID end caps have a lower resolution in the end-cap regions compared to the barrel region. For the "e20_medium_IDTrkNoCut" trigger, an improvement in efficiency is observed between early and later data periods at high track p_T. This is due to improvements that occurred in the IDScan algorithm. The "e22vh_medium_IDTrkNoCut" was implemented later in the data-taking period (replacing the "e20" trigger) and remained stable with an efficiency of approximately 80%. The efficiencies for 2011 in each data period are summarised in Table 4.2.

At EF, the ROI-based efficiency of the EFID algorithm is 94% for most of the p_T spectrum. The efficiency and fake rates are presented in Fig. 4.3 and Fig. 4.4, respectively. The efficiency as a function of track η is also more stable, being flat across the whole spectrum. The EFID tracking algorithm performs better than the IDScan algorithm because it has more generous computing time and has access to full detector read out. The fake rate for EFID shows similar features to the IDScan performance. The fake rate is observed to have a strong dependence on offline track η, with more tracks being found by the trigger algorithms at high $|\eta|$ than are found offline.

Object-based efficiencies were only implemented towards the later part of the 2011 data taking and are only available for the "e22vh_medium" trigger.

These showed an efficiency of 96% for IDScan and 99% for EFID, illustrated in Fig. 4.5 for IDScan and Fig. 4.6. The efficiency is expected to be much higher for the object-based efficiencies since these use well-reconstructed objects for their reference tracks.

Muon

Muon efficiencies are measured using the "mu20_IDTrkNoCut" trigger. This trigger requires muon spectrometer tracks of greater than 20 GeV but makes no requirements on the ID tracks in order to provide unbiased tracking efficiencies. The results for three example runs, with high statistics, at different points during the 2011 run are presented.

At L2, the ROI-based efficiency of the IDScan algorithm remained stable at approximately 97% with a fake rate of 8%. This is much higher than for electrons. Electron triggers that do not use ID track information suffer from higher fake rates than the muon case, where muon spectrometer tracks are used and have a lower fake rate. The efficiency and fake rates are presented in Fig. 4.7 and Fig. 4.8, respectively. The efficiency, as a function of p_T, rises from low to high p_T and is stable at greater than 10 GeV. The efficiency, as a function of offline track η, shows similar structure as is observed in electron triggers, with a lower efficiency observed at higher $|\eta|$. The fake rate, as a function of offline track p_T, shows a sharp increase at low p_T as is seen in electrons. The fake rate, as a function of offline track η, again shows a definite structure. The similarities in shapes of these distributions with those that are observed in electron trigger is not surprising. Both triggers use the same tracking algorithm and similar performance is to be expected. The efficiencies and fake rates for 2011 in each data period are summarised in Table 4.2.

At EF, the ROI-based efficiency of the EFID algorithm is close to 100% and is stable in both p_T and η. The fake rate is low, but still shows a noticeable shape difference between the barrel and end-cap regions. The efficiency and fake rates are presented in Fig. 4.9 and Fig. 4.10, respectively.

Object-based efficiencies for both IDScan and EF are close to 100% and no dependence on track η is observed, except perhaps for slight inefficiencies at very high $|\eta|$ for IDScan. Object based efficiencies are presented in Fig. 4.11 and Fig. 4.12 for IDScan and EFID, respectively.

Figure 4.7: ROI-based efficiencies for muon triggers in 2011 ATLAS data for IDScan. The efficiency is presented as a function of the track p_T (*top*) and η (*bottom*).

Figure 4.8: ROI-based fake rates for muon triggers in 2011 ATLAS data for IDScan. The efficiency is presented as a function of the track p_T and (*top*) and η (*bottom*).
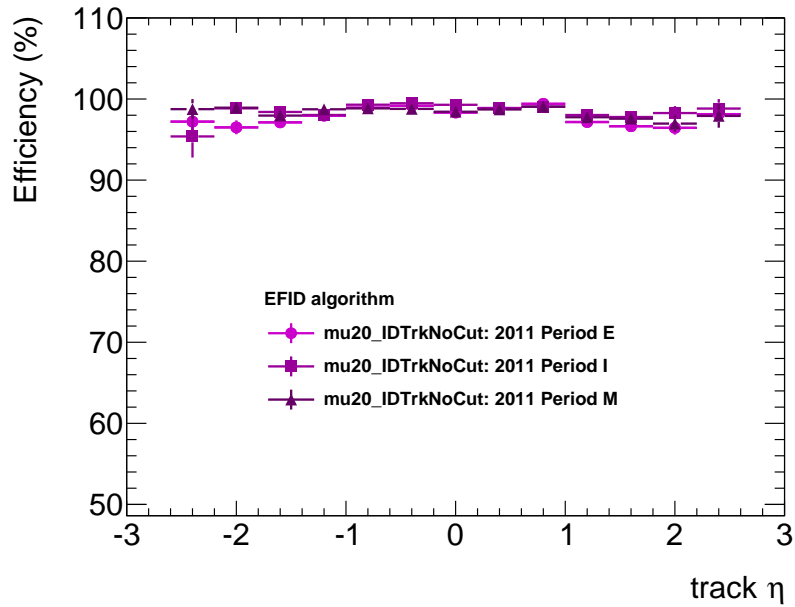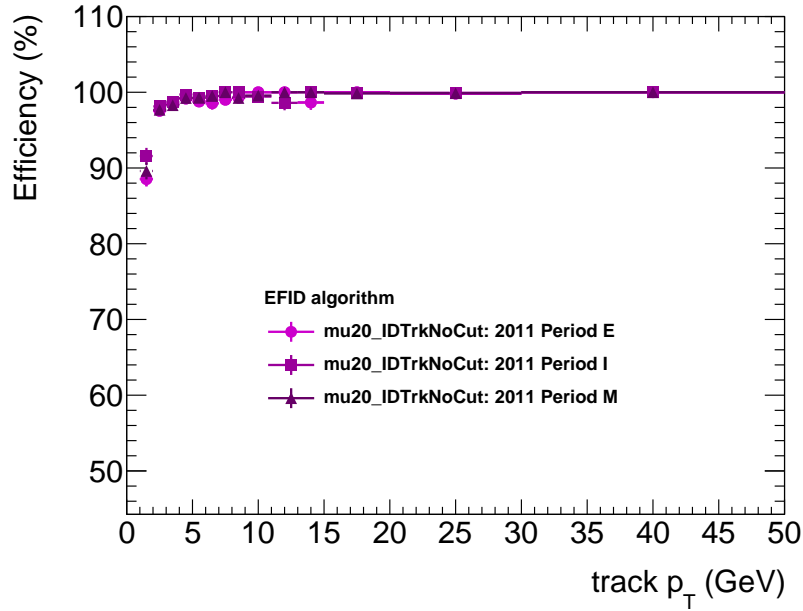
Figure 4.9: ROI-based efficiencies for muon triggers in 2011 ATLAS data for EFID. The efficiency is presented as a function of the track p_T (*top*) and η (*bottom*).
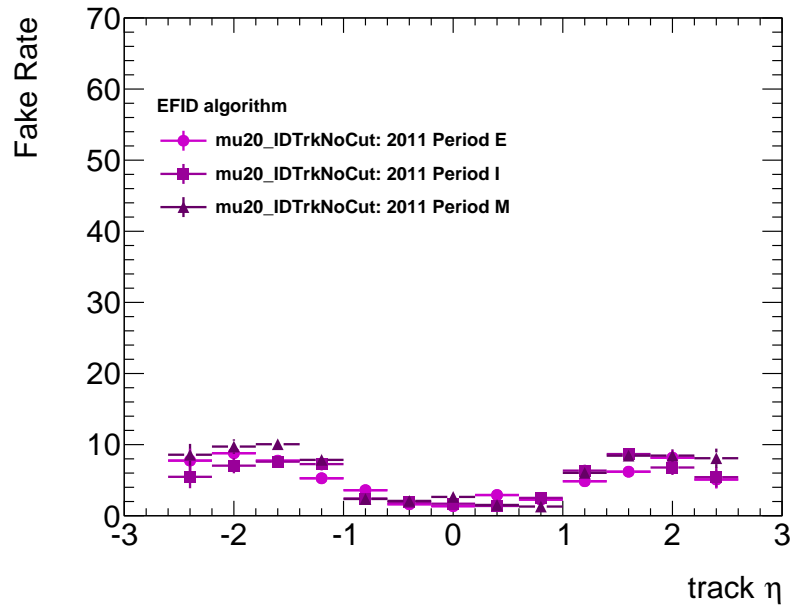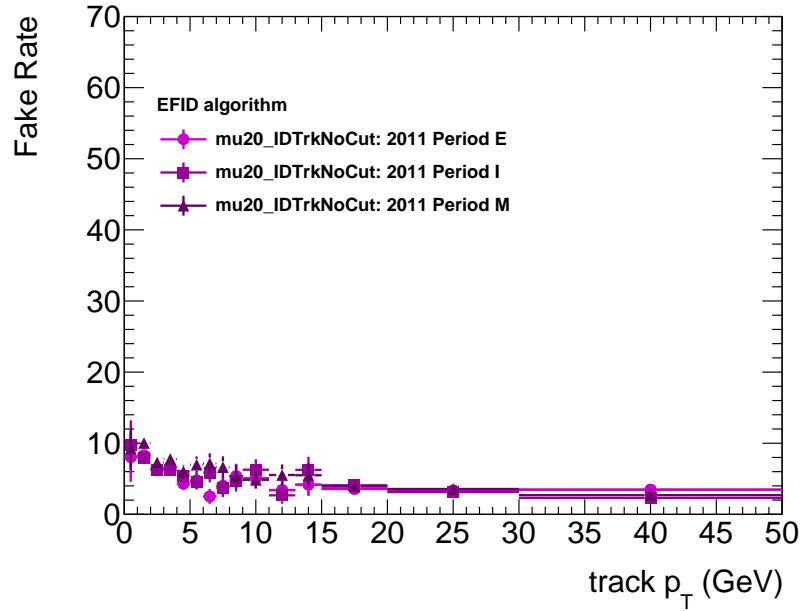
Figure 4.10: ROI-based fake rates for muon triggers in 2011 ATLAS data for EFID. The efficiency is presented as a function of the track p_T (*top*) and η (*bottom*).
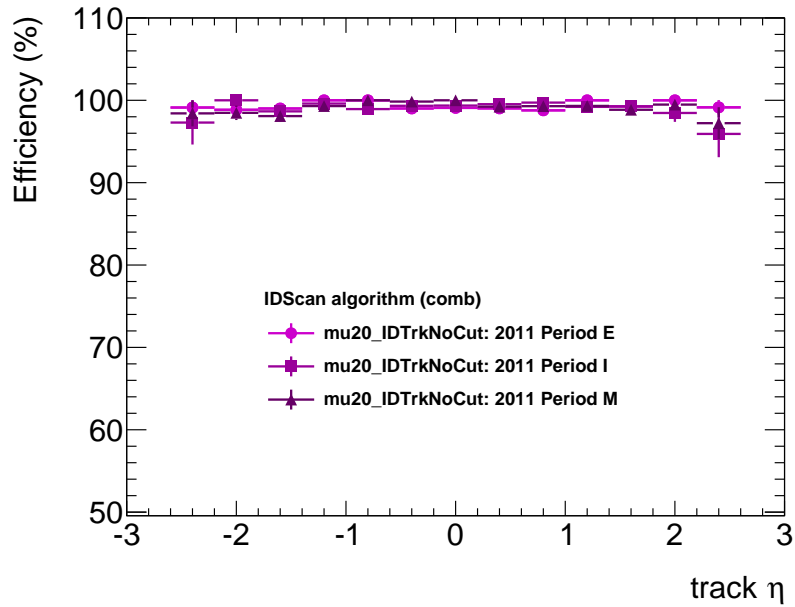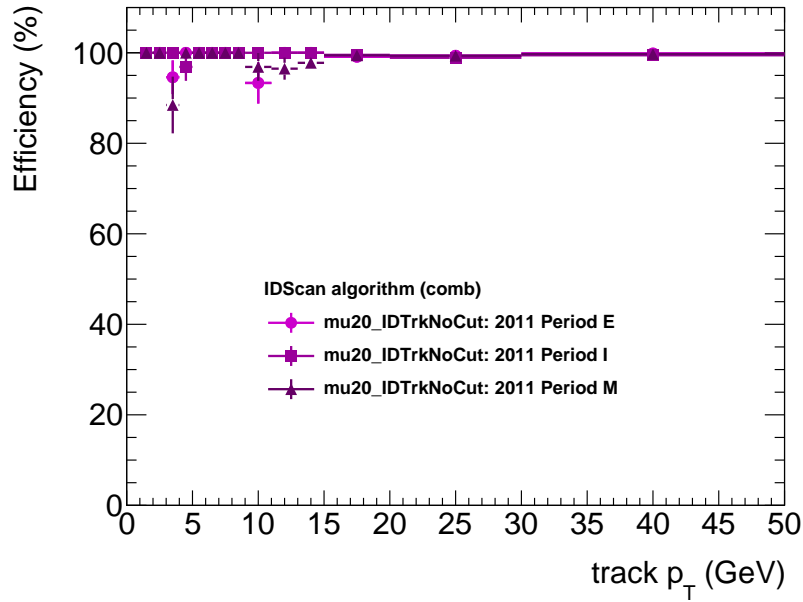
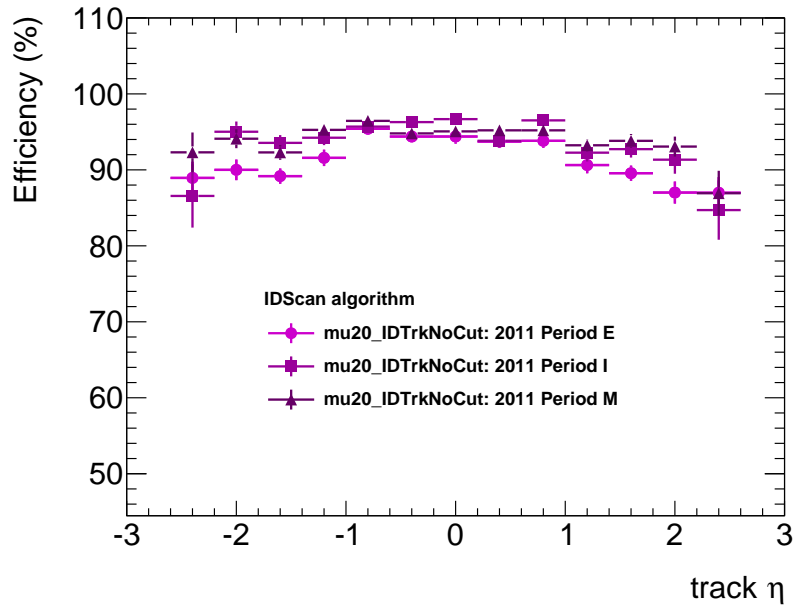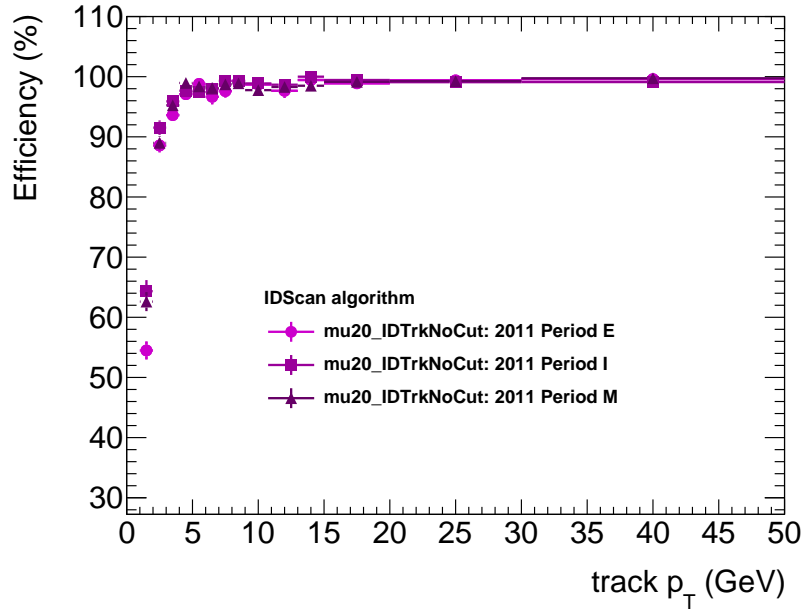**Figure 4.11:** Object-based efficiencies for muon triggers in 2011 ATLAS data for IDScan. The efficiency is presented as a function of the track p_T (*top*) and η (*bottom*).

Figure 4.12: Object-based efficiencies for muon triggers in 2011 ATLAS data for EFID. The efficiency is presented as a function of the track p_T (*top*) and η (*bottom*).
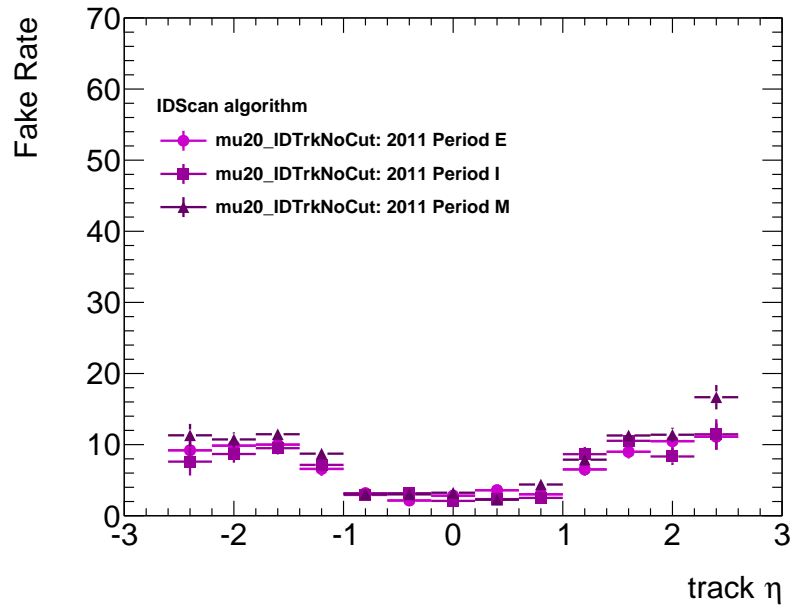
Figure 4.13: ROI-based efficiencies for *b*-jet triggers in 2011 ATLAS data for SiTrack. The efficiency is presented as a function of the track p_T (*top*) and η (*bottom*).

Figure 4.14: ROI-based fake rates for *b*-jet triggers in 2011 ATLAS data for SiTrack. The efficiency is presented as a function of the track p_T (*top*) and η (*bottom*).

Figure 4.15: ROI-based efficiencies for b-jet triggers in 2011 ATLAS data for EFID. The efficiency is presented as a function of the track p_T (*top*) and η (*bottom*).
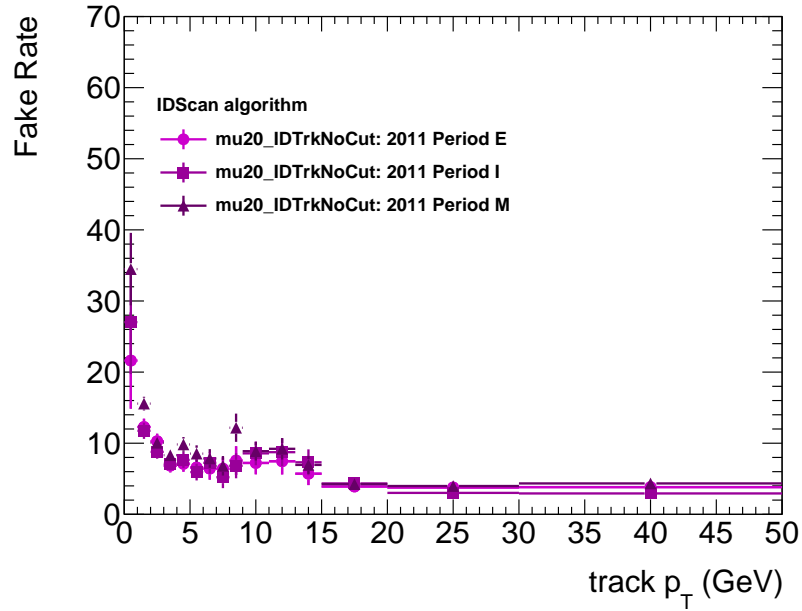
Figure 4.16: ROI-based fake rates for *b*-jet triggers in 2011 ATLAS data for EFID. The efficiency is presented as a function of the track p_T (*top*) and η (*bottom*).
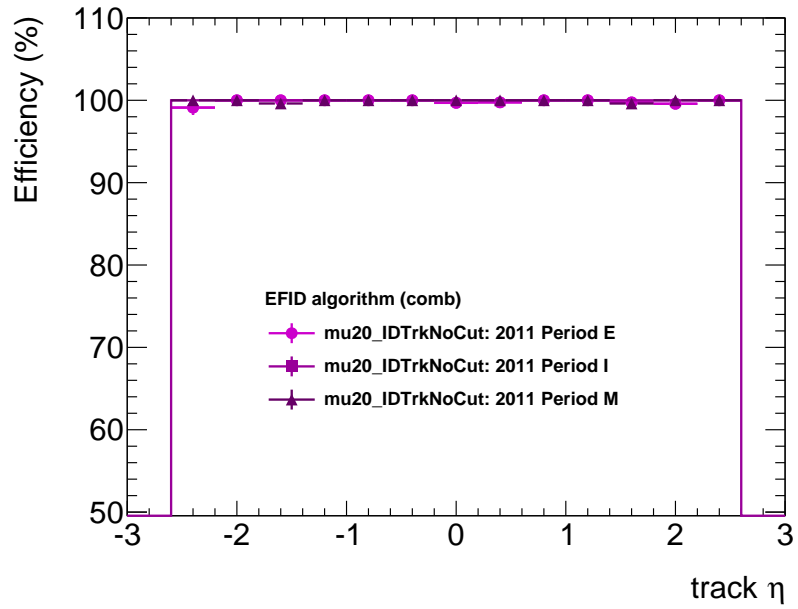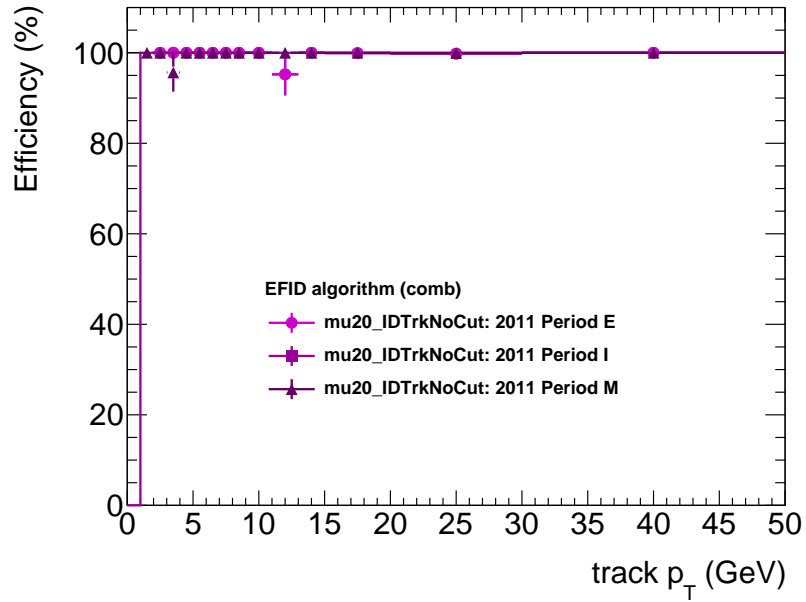
B-jet

Efficiencies of b-jet triggers are measured using the "b10_IDTrkNoCut" trigger. This trigger requires jets consistent with b-quarks with greater than 10 GeV but makes no requirements on the ID tracks. Jets are identified as being consistent with b-quarks by muon tracks in the MS, consistent with heavy-flavour decays inside the jet. The results for three example runs, with high statistics, at different points during the 2011 run are presented.

At L2, the ROI-based efficiency of the SiTrack algorithm remains stable at approximately 94% with a fake rate of 5%. The efficiency and fake rates are presented in Fig. 4.13 and Fig. 4.14, respectively. The efficiency, as a function of p_T, is stable at greater than 10 GeV. The efficiency, as a function of offline track η, shows a gradual dependence with efficiency decreasing at higher track $|\eta|$. The fake rate, as a function of offline track p_T, shows a sharp increase at low p_T as is seen in electrons and muons. The fake rate, as a function of offline track η, increases gradually with $|\eta|$. Though different in execution, the SiTrack algorithm suffers from many of the same limitations as IDScan in terms of efficiency and fake rate at low p_T or high $|\eta|$. The efficiencies and fake rates for 2011 in each data period are summarised in Table 4.2.

At EF, the ROI-based efficiency of the EFID algorithm is close to 100% and is stable in p_T, with a slightly lower efficiency at high $|\eta|$. The fake rate is low but shows the same shapes as for the SiTrack algorithm. The efficiency and fake rates are presented in Fig. 4.15 and Fig. 4.16, respectively.

Trigger	L2			EF		
	Period E5	Period J4	Period L1	Period E5	Period J4	Period L1
Efficiency						
μ	96.0	95.3	95.6	98.2	98.2	98.3
μ (comb)	99.7	99.7	99.6	99.8	100.0	99.9
e	87.6	86.9	87.9	93.9	93.9	94.5
e (comb)	95.2	95.3	95.9	96.3	96.6	97.2
b-jet	93.8	94.0	93.8	95.8	96.0	95.9
Fake Rate						
μ	16.5	17.5	16.8	5.7	6.5	5.7
e	19.5	20.2	20.7	6.0	6.5	7.0
b-jet	15.4	18.2	17.8	3.7	4.1	4.0

Table 4.3: Efficiencies and fake rates of ATLAS triggers in 2012 data. Muon trigger efficiencies and fake rates are derived using the "mu_22_IDTrkNoCut" trigger. Object-based efficiencies are indicated with "(comb)". Electron trigger efficiencies and fake rates are derived using the "e24vh_medium_IDTrkNoCut" trigger. Efficiencies and fake rates for b-jets are estimated using the "b55_NoCut_j55_a4tchad" trigger in all periods. Object-based efficiencies are not available for this trigger.

4.4.4 Relative efficiencies in 2012 data

Electron

ROI-based efficiencies for electrons are measured using the "e24vh_medium1_IDTrkNoCut" trigger. This trigger requires a trigger electron with a transverse energy of greater than 24 GeV and isolation cuts on the calorimeter clusters used to build the electron. No requirement is made on trigger tracks in order to have an unbiased trigger for measuring tracking efficiency.

At L2, the ROI-based efficiency of the L2Star-A algorithm remained stable at approximately 87%. This performance is a large improvement over the performance of IDScan in 2011 data. The L2Star algorithm uses all of the best features of the tracking algorithms used in 2011 with code optimisation to reduce execution time and improvements to the components of the algorithm that locate the tracks originating from a vertex. The same shape dependence is observed in both p_{T} and $|\eta|$. The efficiencies are presented in Fig. 4.17. The fake rate is noticeably higher due to the increased pile-up in 2012 data. The increased occupancy of the inner detector results in more possibilities for track reconstruction and causes a higher fake rate. The fake rate at L2 is approximately 20%, with a similar dependence on track $|\eta|$, similar to the 2011 result. The fake rate is presented in
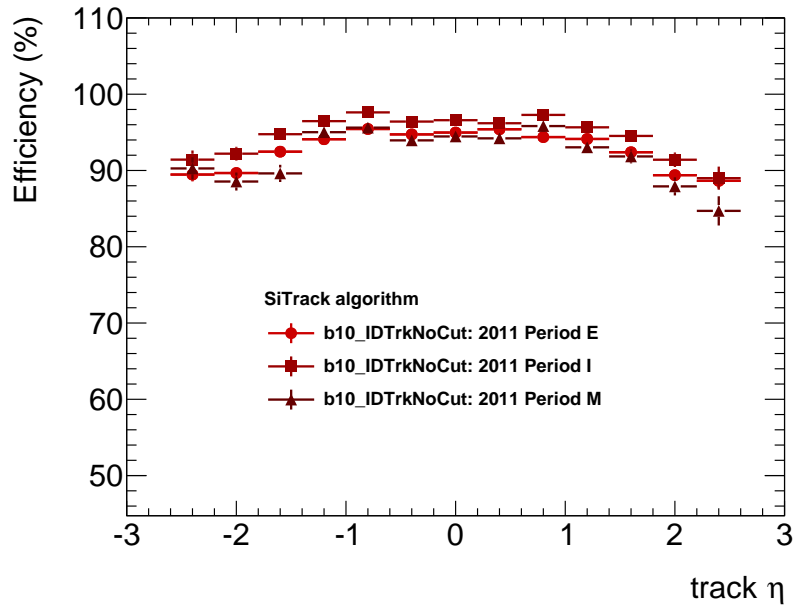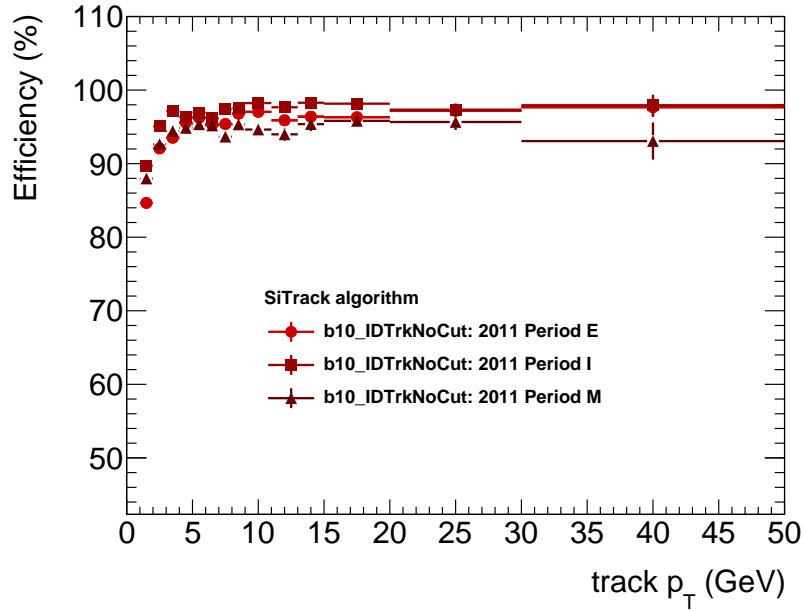
Figure 4.17: ROI-based efficiencies for electron triggers in 2012 ATLAS data for L2Star-A. The efficiency is presented as a function of the track p_{T} (*top*) and η (*bottom*).
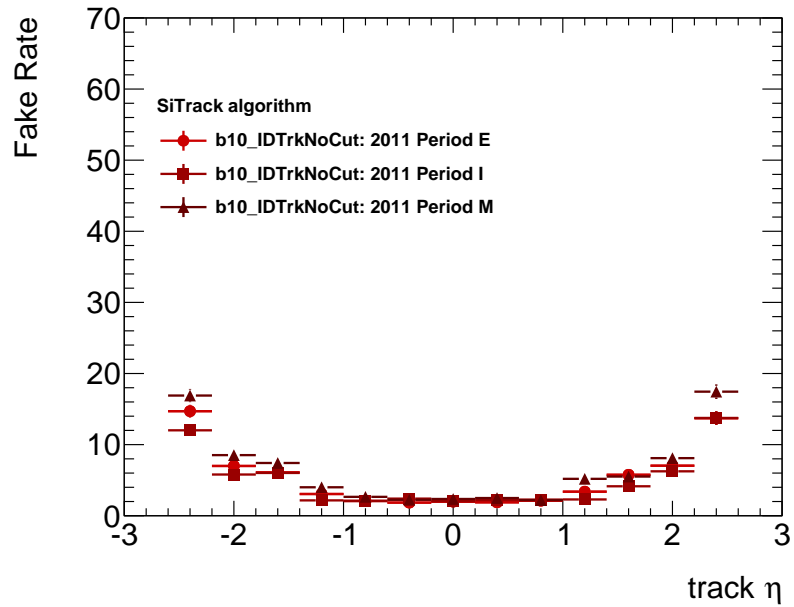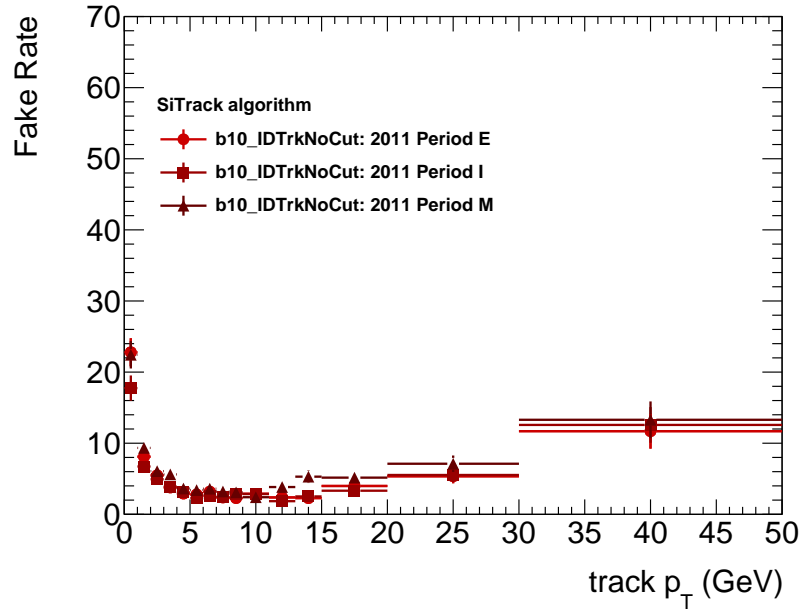
Figure 4.18: ROI-based fake rates for electron triggers in 2012 ATLAS data for L2Star-A. The efficiency is presented as a function of the track p_T (*top*) and η (*bottom*).
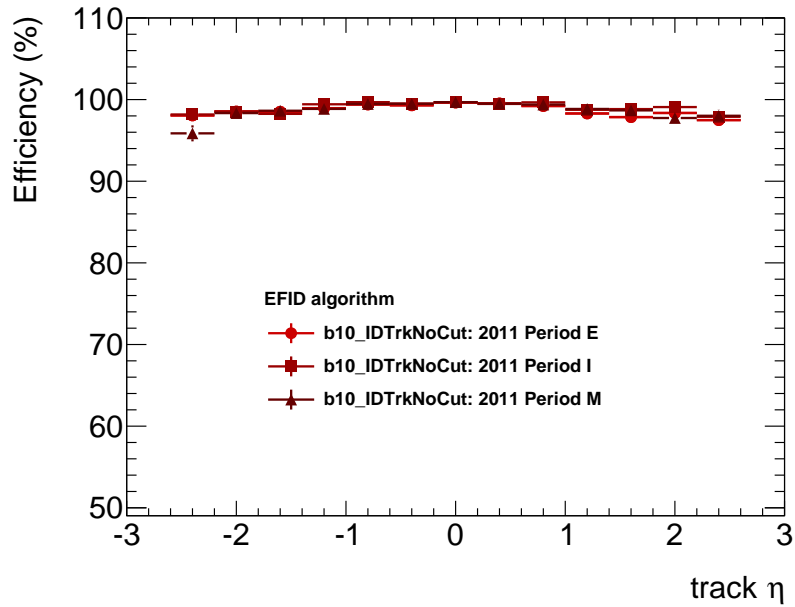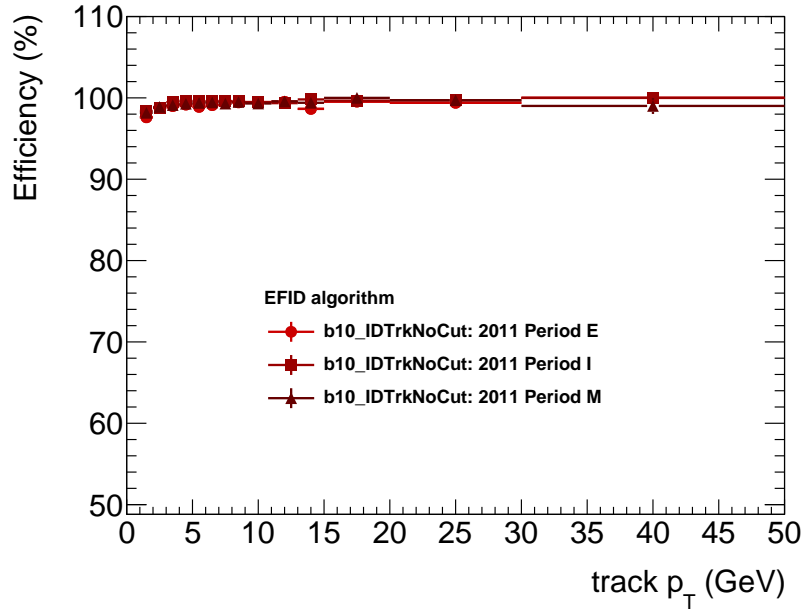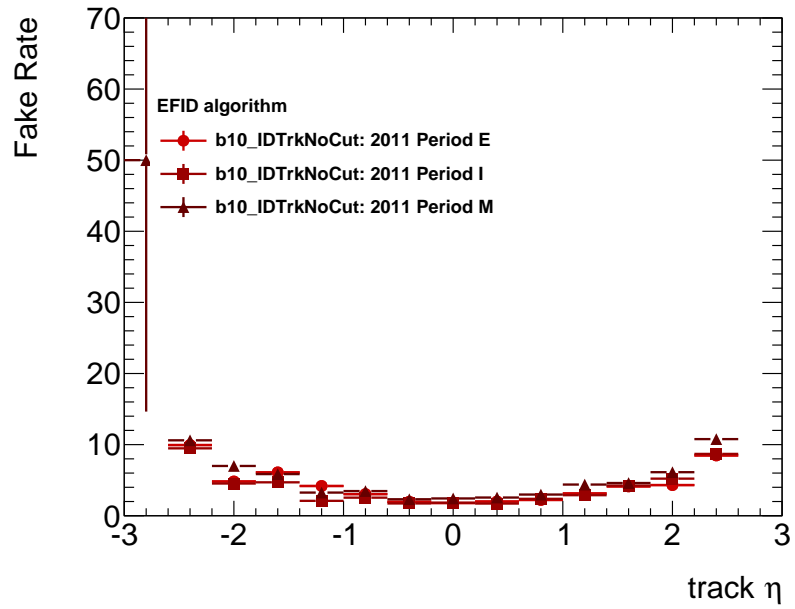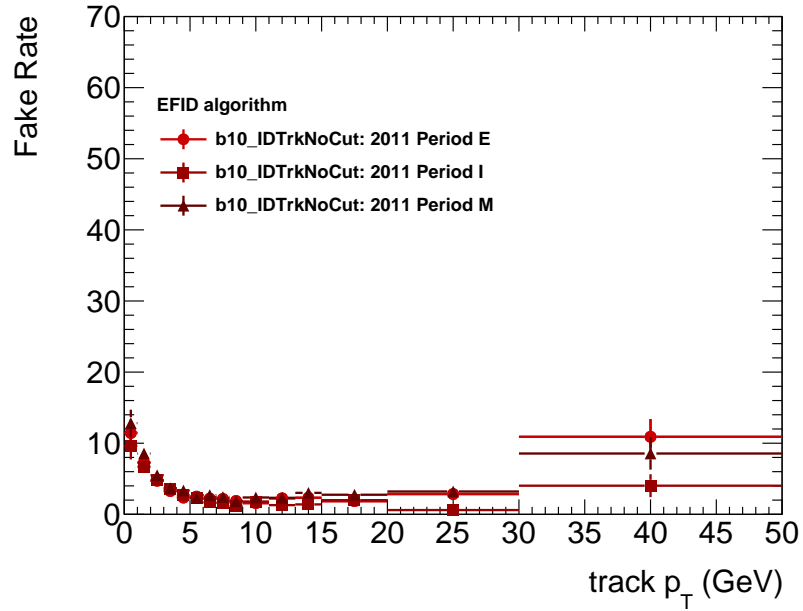
Figure 4.19: ROI-based efficiencies for electron triggers in 2012 ATLAS data for EFID. The efficiency is presented as a function of the track p_T (*top*) and η (*bottom*).

Figure 4.20: ROI-based fake rates for electron triggers in 2012 ATLAS data for EFID. The efficiency is presented as a function of the track p_T (*top*) and η (*bottom*).

Figure 4.21: Object-based efficiencies for electron triggers in 2012 ATLAS data for L2Star-A. The efficiency is presented as a function of the track p_T (*top*) and η (*bottom*).

Figure 4.22: Object-based efficiencies for electron triggers in 2012 ATLAS data for EFID. The efficiency is presented as a function of the track p_T (*top*) and η (*bottom*).

Fig. 4.18. The efficiencies and fake rates for the electron triggers are summarised in Table 4.3.

At EF, the ROI-based efficiency of the EFID algorithm is presented in Fig. 4.19. The efficiency is 94%, similar to the performance in 2011. This is expected as the EFID algorithm remained largely unchanged between 2011 and 2012. The fake rate is presented in Fig. 4.20. Considering the higher pileup, the fake rate for EFID is still quite low. Again, the rate increases with $|\eta|$.

The object-based efficiencies are presented in Fig. 4.21 and Fig. 4.22 for L2Star_A and EFID, respectively. The object based efficiencies for both algorithms are above 95%, with lower efficiency at low p_T and higher $|\eta|$.

Muon

ROI-based efficiencies for muons are measured using the "mu22_medium_IDTrkNoCut" trigger. This trigger requires a trigger muon with a transverse energy of greater than 22 GeV. No requirement is made on trigger tracks in order to have an unbiased trigger for measuring tracking efficiency.

At L2, the ROI-based efficiency of the L2Star-A algorithm remained stable at approximately 96%. This performance is a slight improvement over the performance of IDScan for muon tracks in 2011 data. The dependence of efficiency on track $|\eta|$ is small, and much less than the dependence observed for electrons. These differences are not caused by the trigger tracking algorithm, which is largely the same between electrons and muon, but by the difference in the triggers used to monitor the efficiency. Muons are seeded by tracks in the muon detector whereas electrons are seeded by jets in the calorimeter. The efficiencies are presented in Fig. 4.23. The fake rate is noticeably higher due to the increased pile-up in 2012 data, particularly at lower p_T. The fake rate at L2 is approximately 17%. The fake rate is presented in Fig. 4.24. The efficiencies and fake rates for the muon triggers are summarised in Table 4.3.

At EF, the ROI-based efficiency of the EFID algorithm for muon tracks is presented in Fig. 4.25. The efficiency is 98%, again similar to the performance in 2011 due to the similar EFID algorithm used in both periods. The fake rate is presented in Fig. 4.26. The rate increases with track $|\eta|$ and a very noticeable difference between the barrel region and end-cap region can be clearly observed.

The object-based efficiencies are presented in Fig. 4.27 and Fig. 4.28 for L2Star_A and EFID, respectively. The object based efficiencies for both algorithms are above 99%, with almost no dependency on track p_T or $|\eta|$.
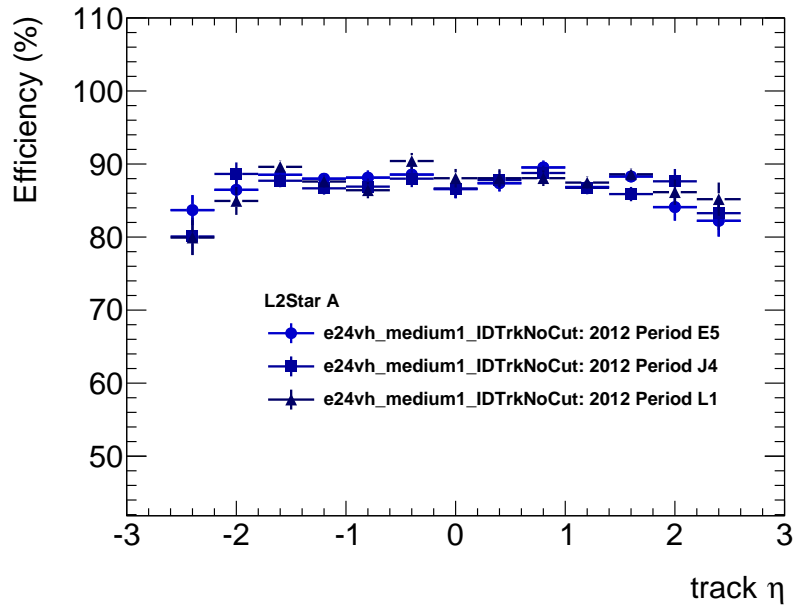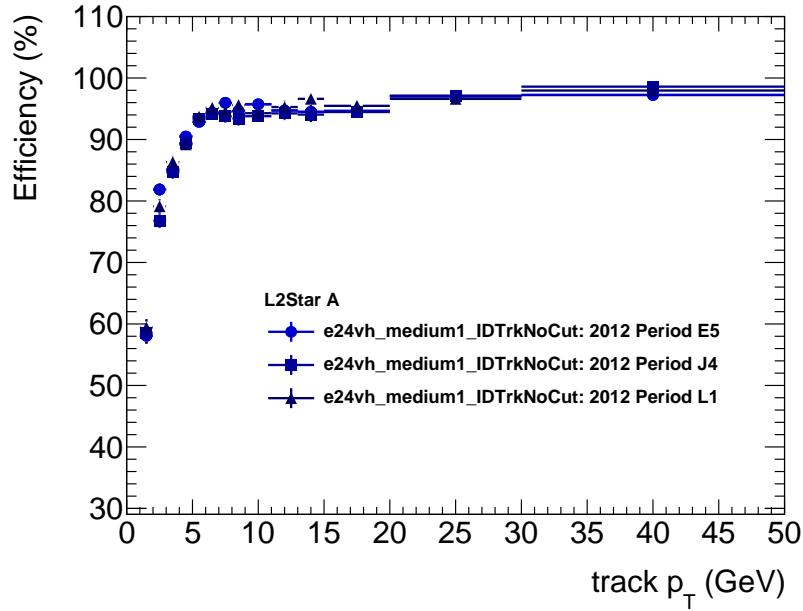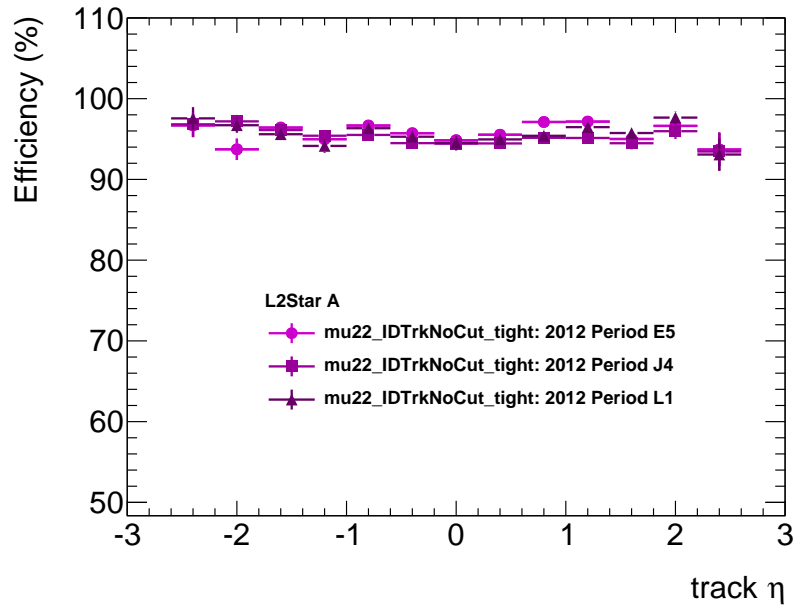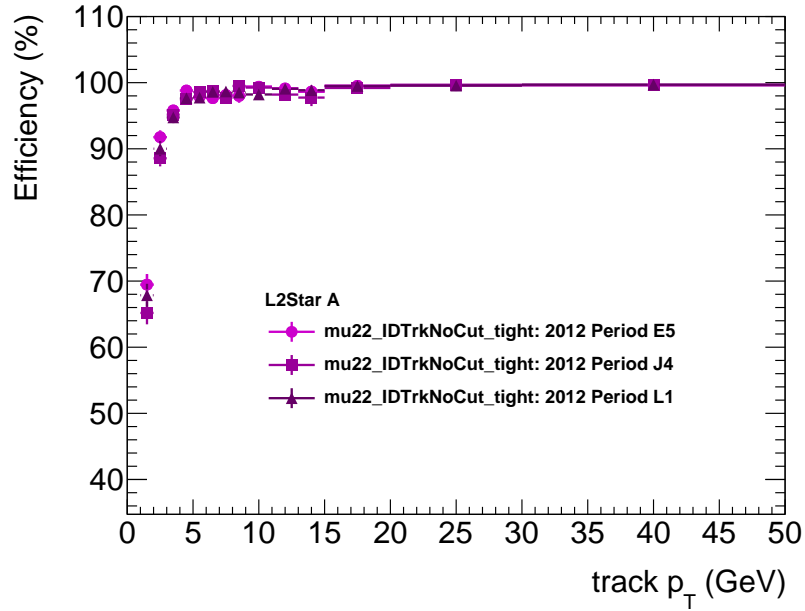
Figure 4.23: ROI-based efficiencies for muon triggers in 2012 ATLAS data for L2Star-A. The efficiency is presented as a function of the track p_T (*top*) and η (*bottom*).
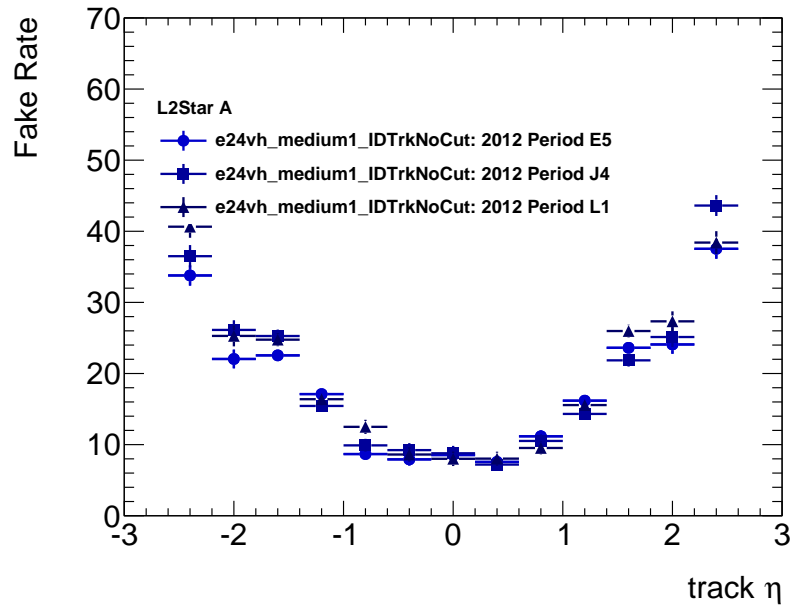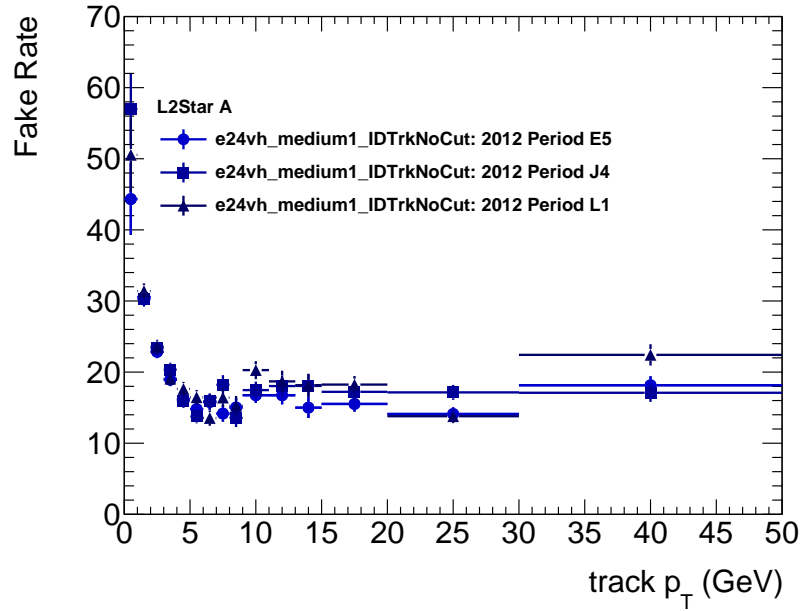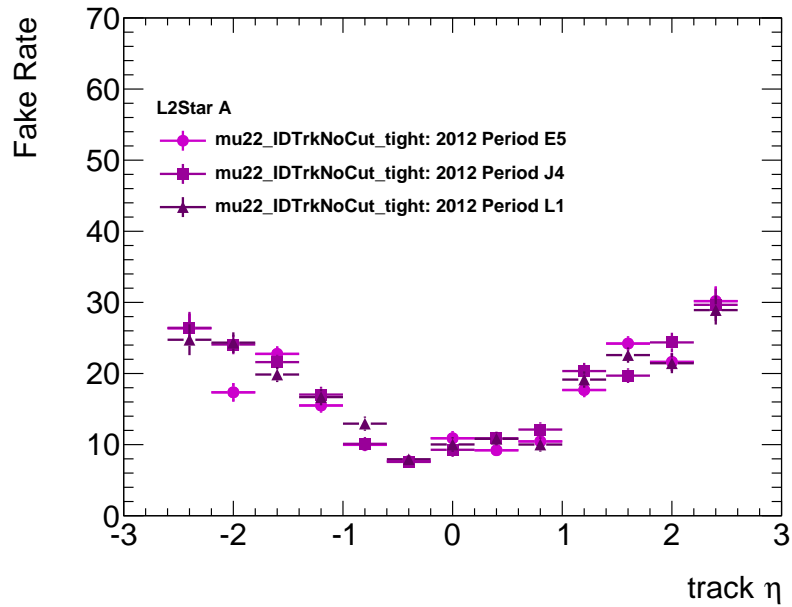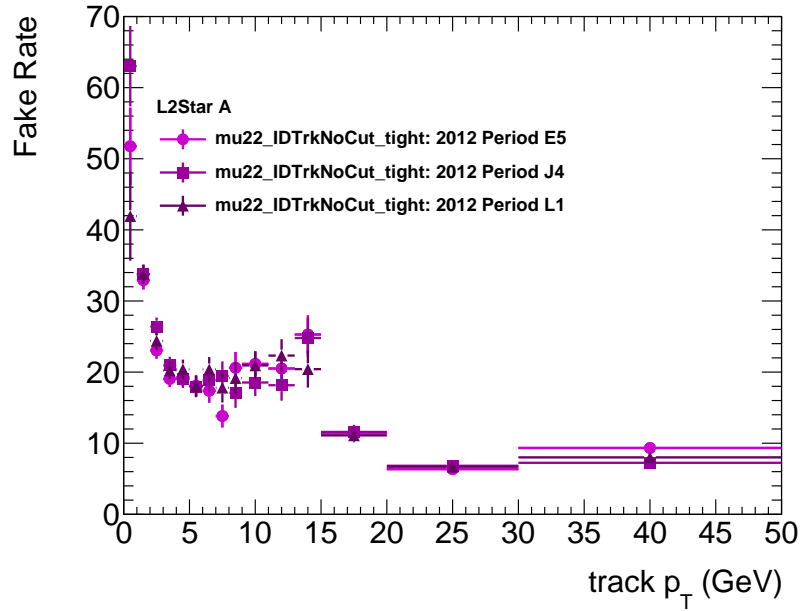
Figure 4.24: ROI-based fake rates for muon triggers in 2012 ATLAS data for L2Star-A. The efficiency is presented as a function of the track p_T (*top*) and η (*bottom*).
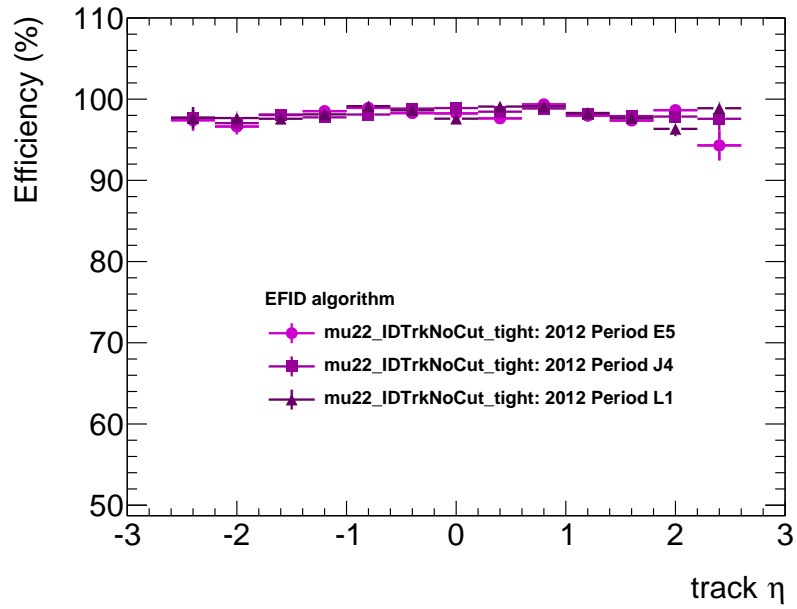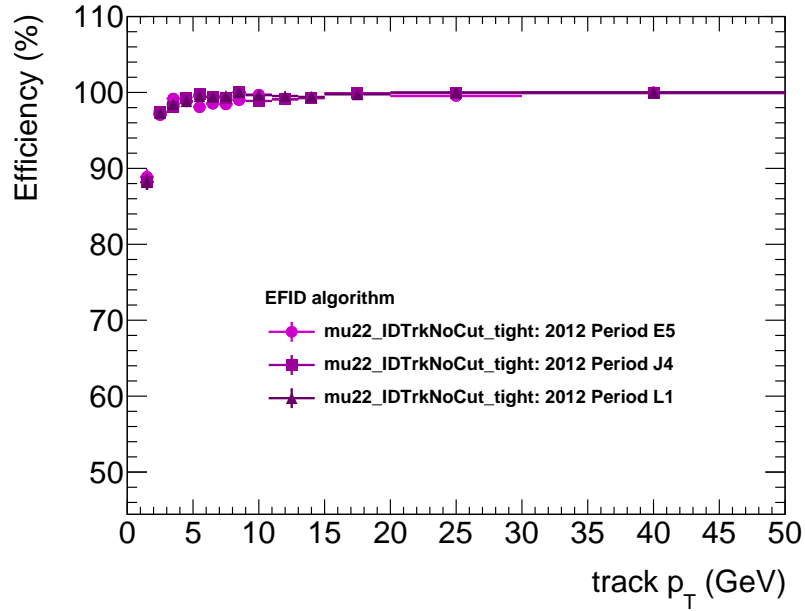
Figure 4.25: ROI-based efficiencies for muon triggers in 2012 ATLAS data for EFID. The efficiency is presented as a function of the track p_T (*top*) and η (*bottom*).
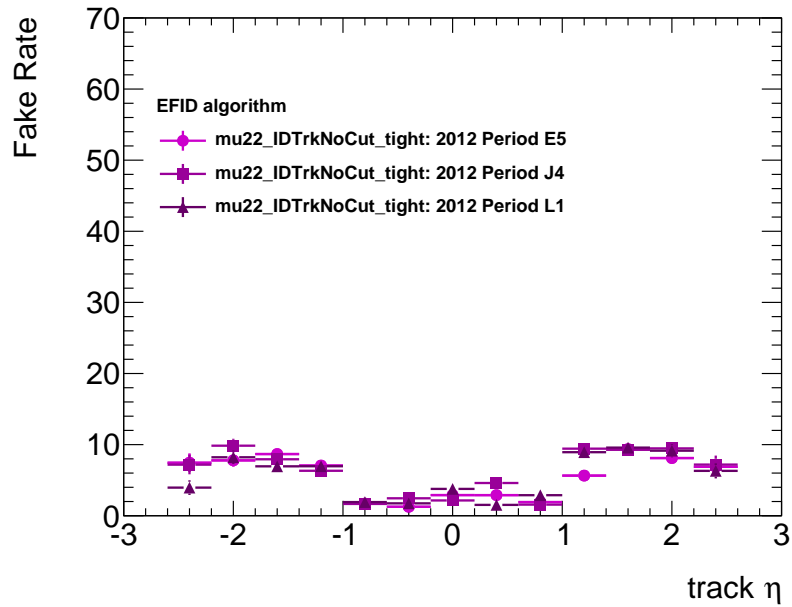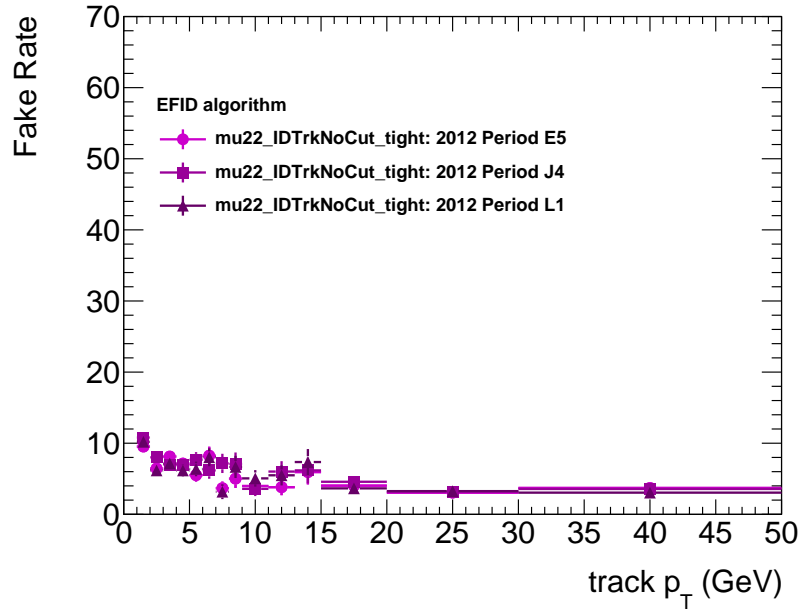
Figure 4.26: ROI-based fake rates for muon triggers in 2012 ATLAS data for EF. The efficiency is presented as a function of the track p_T (*top*) and η (*bottom*).
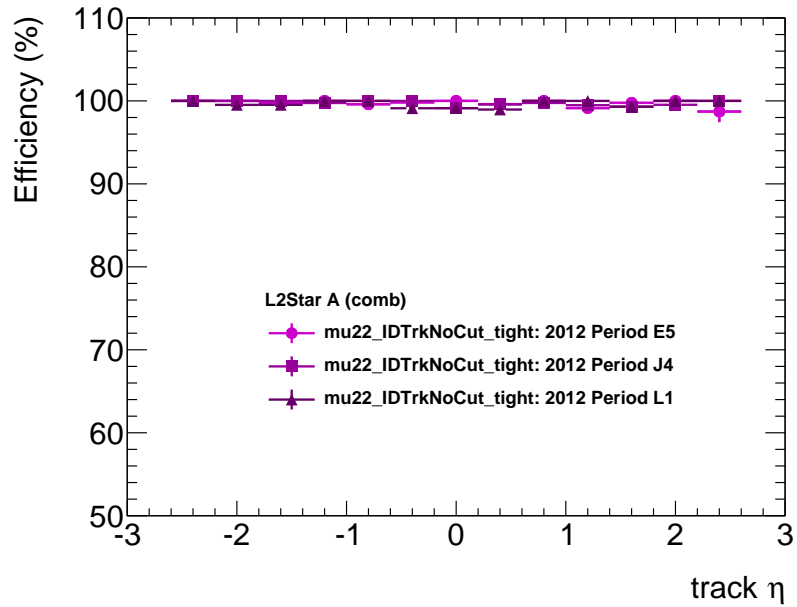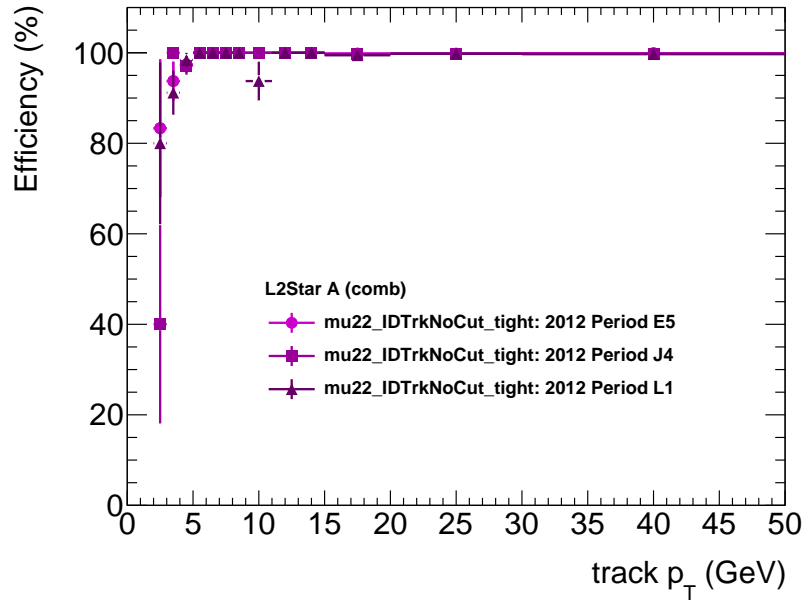
Figure 4.27: Object-based efficiencies for muon triggers in 2012 ATLAS data for L2Star-A. The efficiency is presented as a function of the track p_T (*top*) and η (*bottom*).
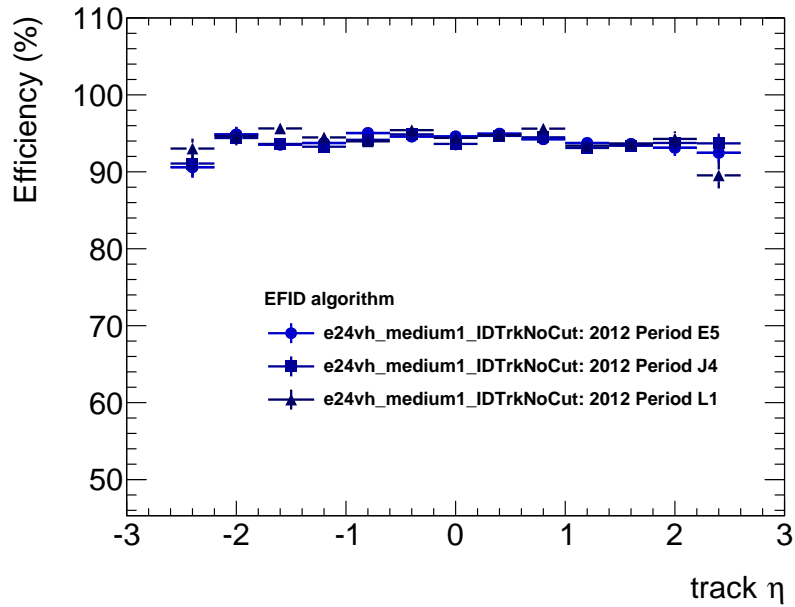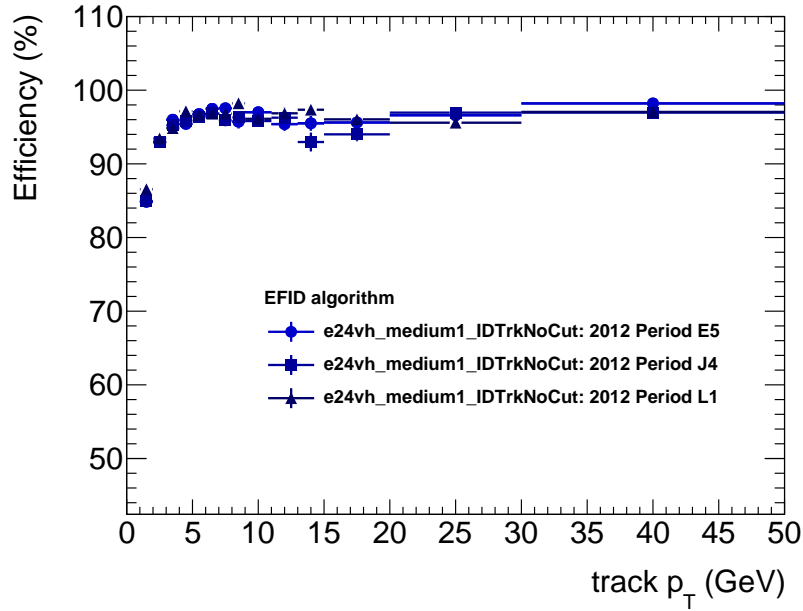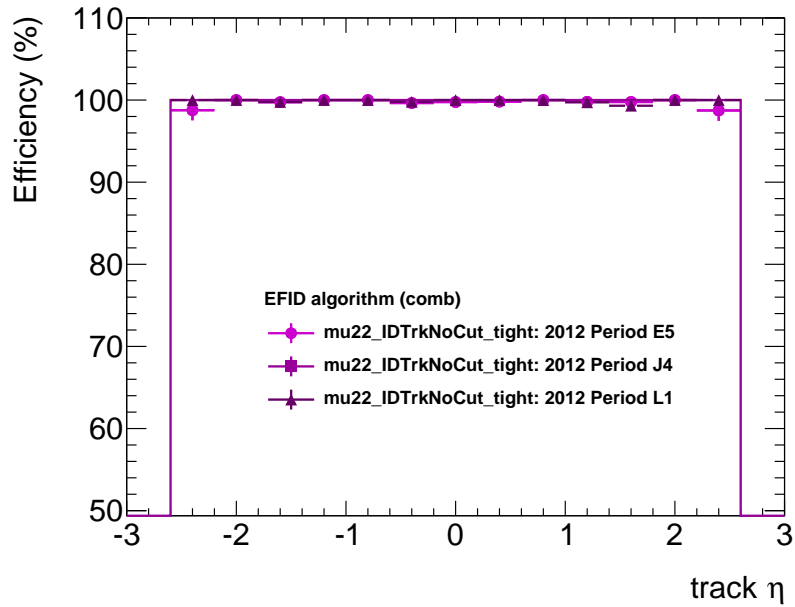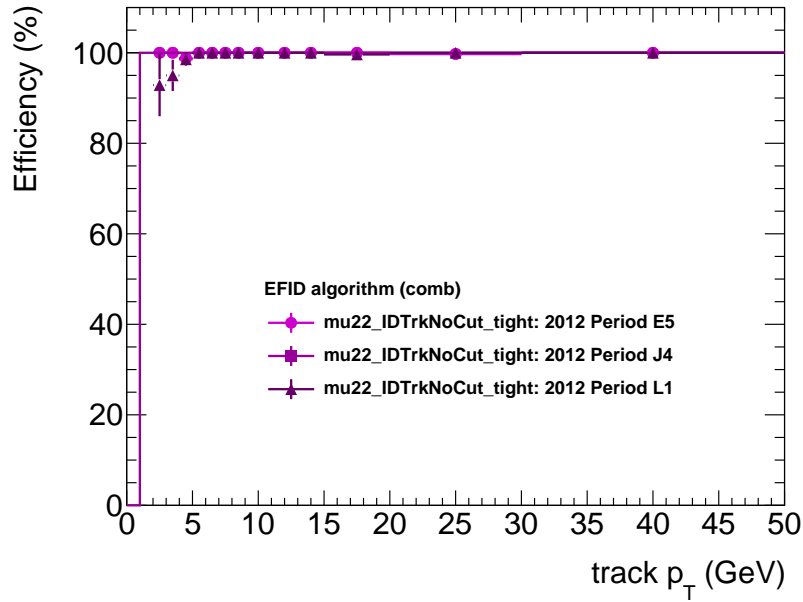
Figure 4.28: Object-based efficiencies for muon triggers in 2012 ATLAS data for EFID. The efficiency is presented as a function of the track p_T (*top*) and η (*bottom*).
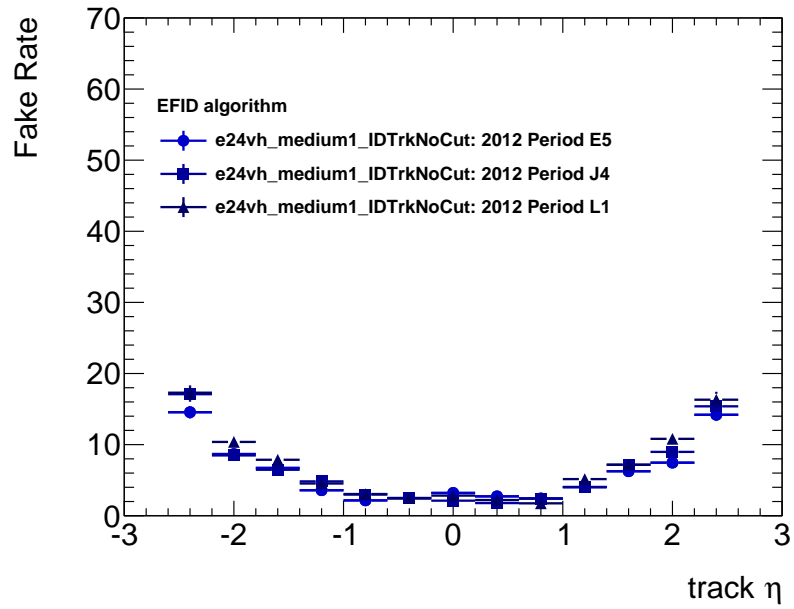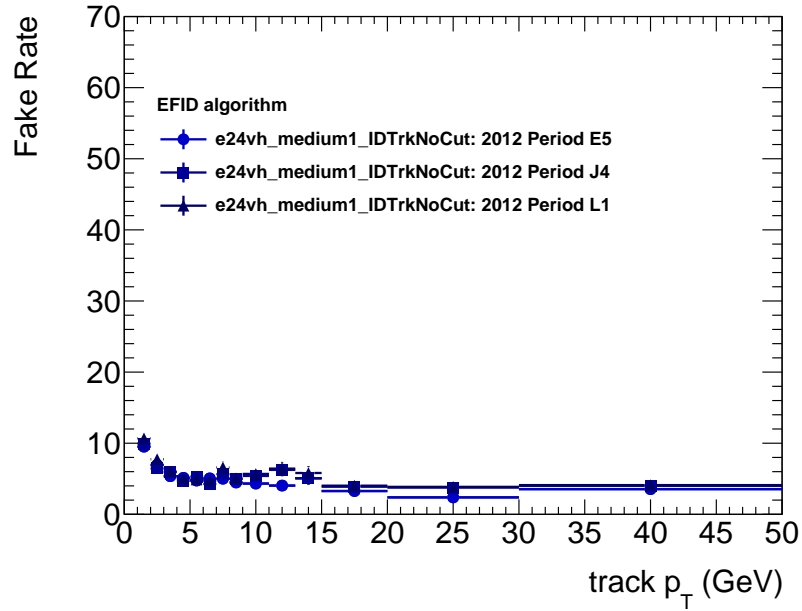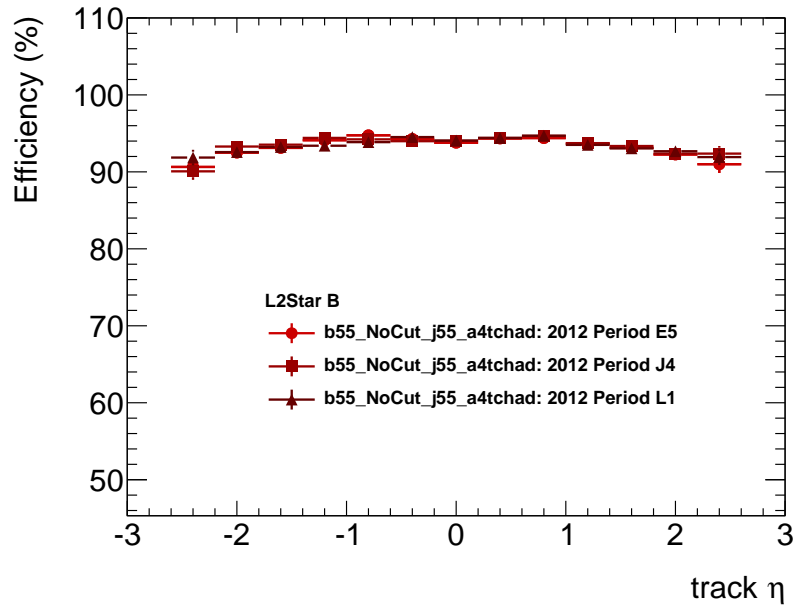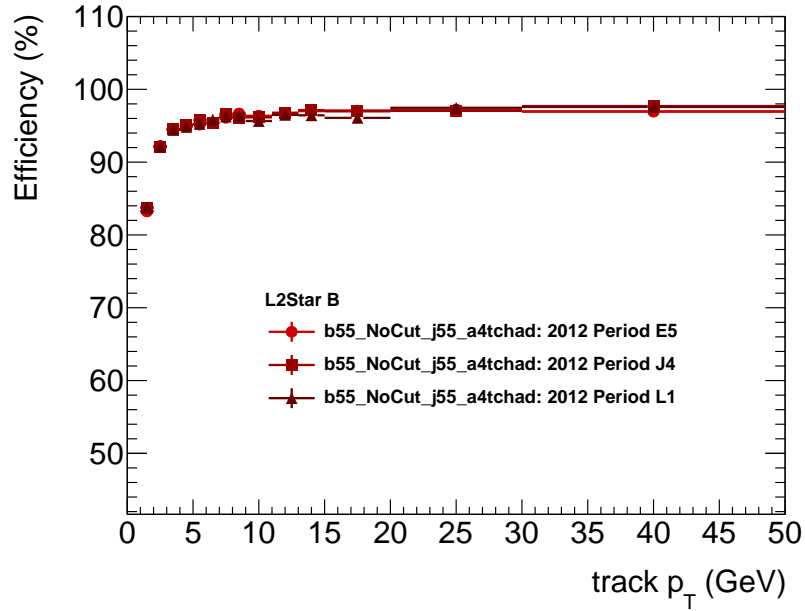
Figure 4.29: ROI-based efficiencies for b-jet triggers in 2012 ATLAS data for L2Star-B. The efficiency is presented as a function of the track p_T (*top*) and η (*bottom*).
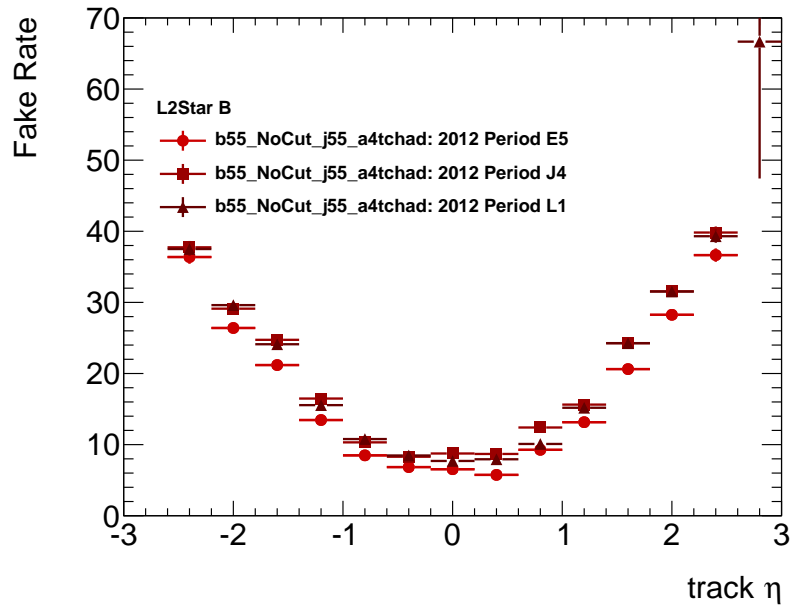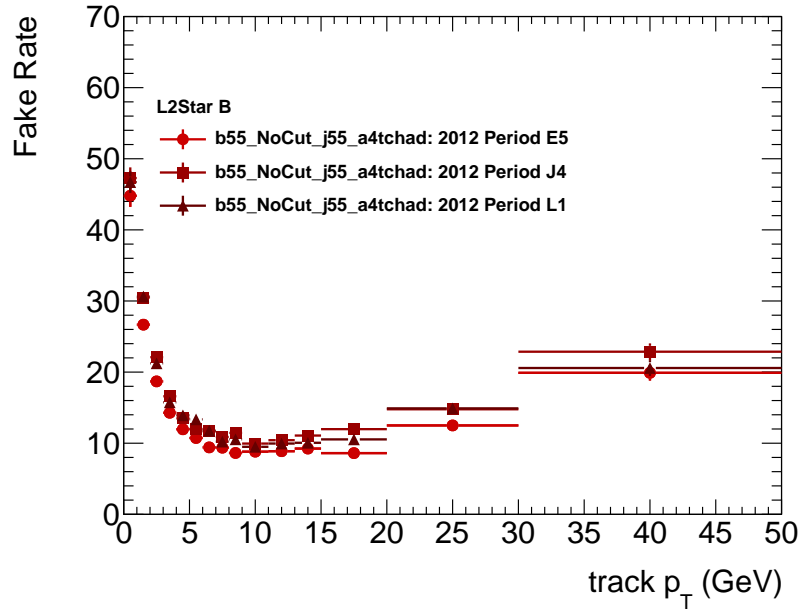
Figure 4.30: ROI-based fake rates for *b*-jet triggers in 2012 ATLAS data for L2Star-B. The efficiency is presented as a function of the track p_T (*top*) and η (*bottom*).
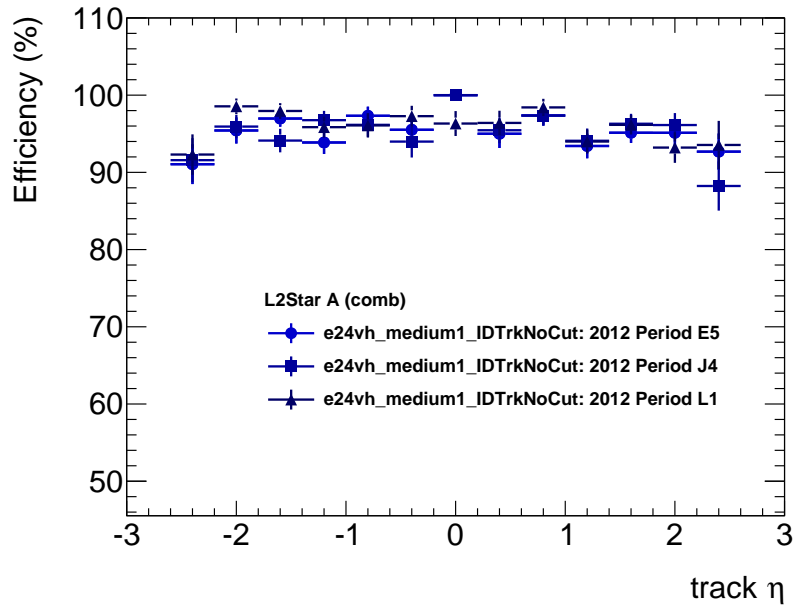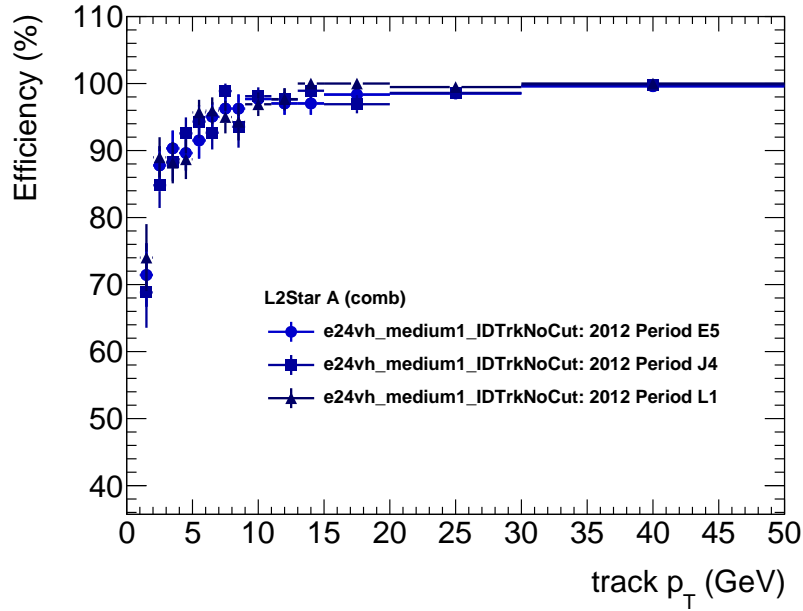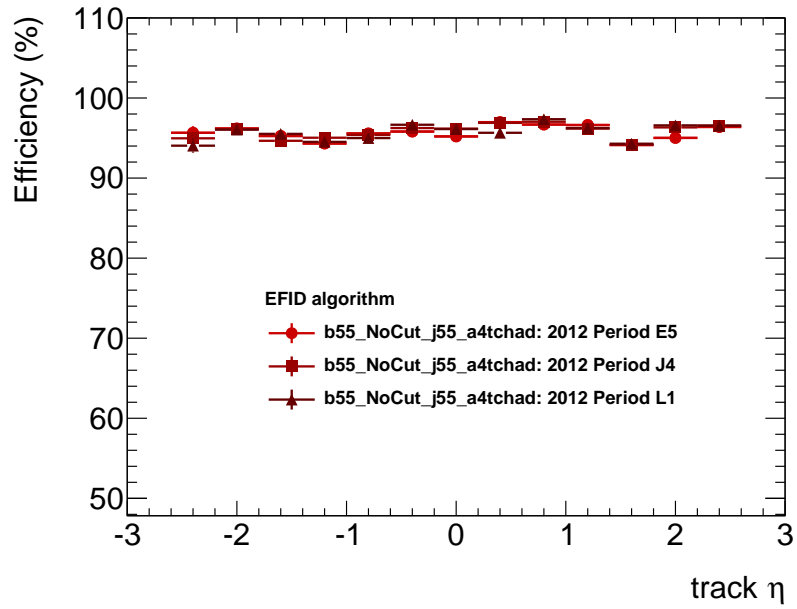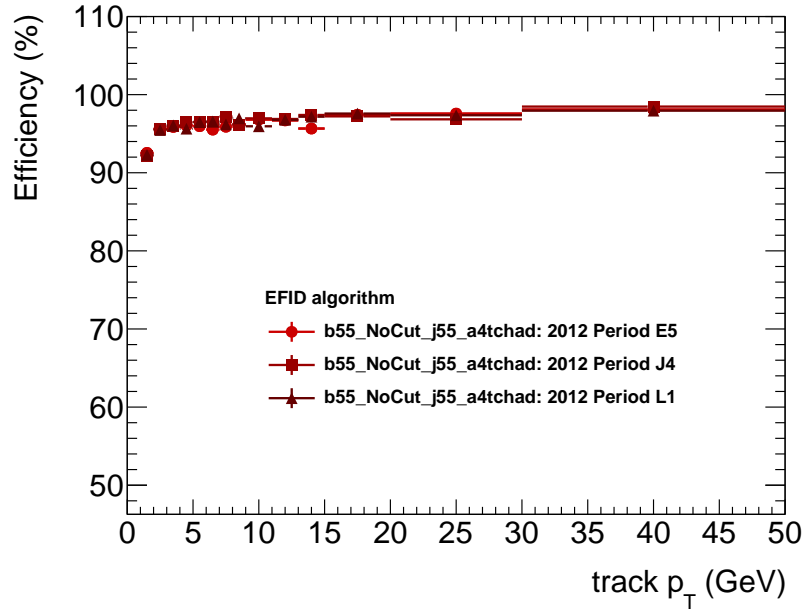
Figure 4.31: ROI-based efficiencies for b-jet triggers in 2012 ATLAS data for L2Star-B. The efficiency is presented as a function of the track p_T (*top*) and η (*bottom*).
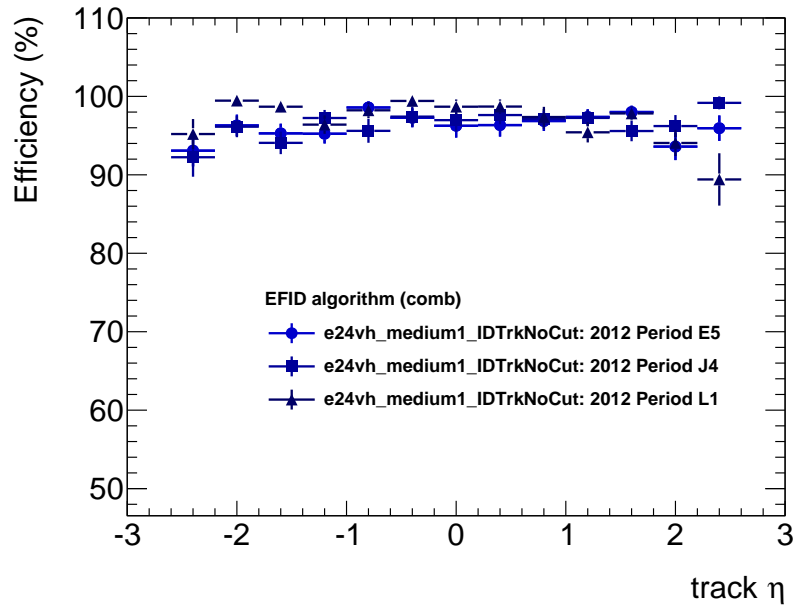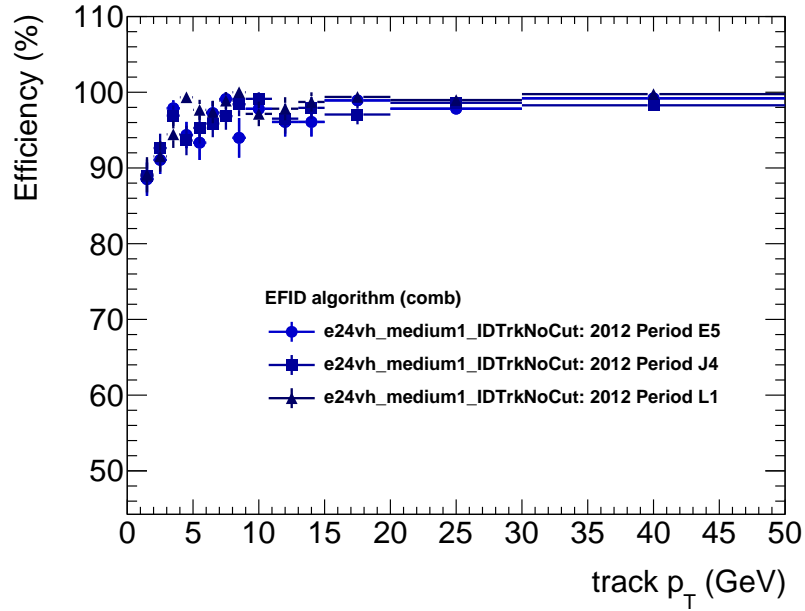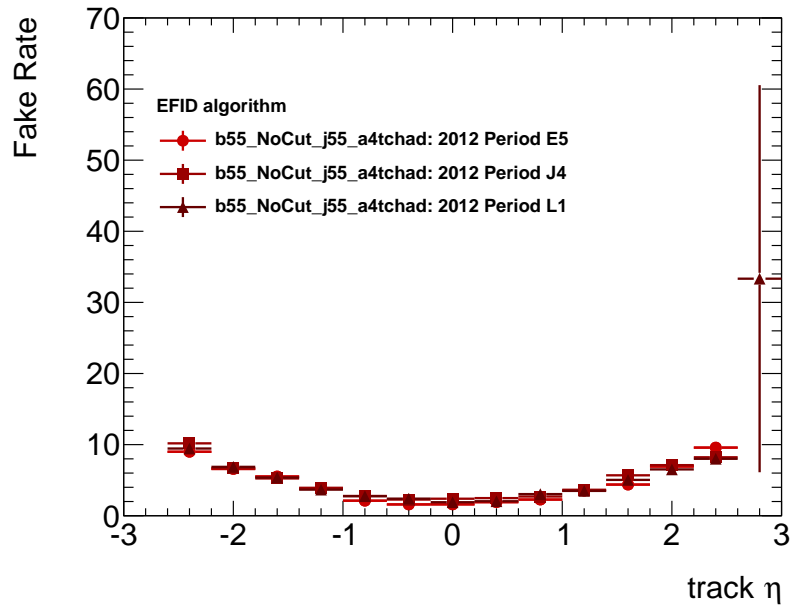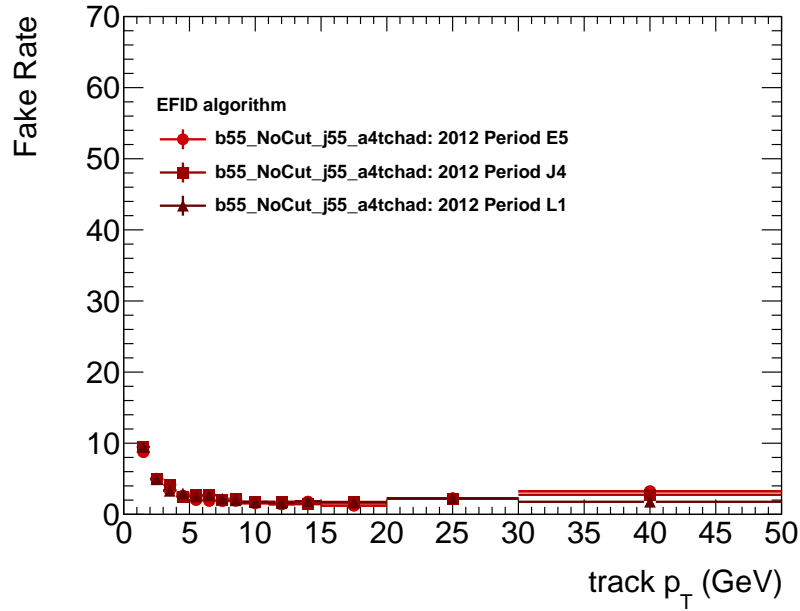
Figure 4.32: ROI-based fake rates for *b*-jet triggers in 2012 ATLAS data for EFID. The efficiency is presented as a function of the track p_{T} (*top*) and η (*bottom*).

B-jet

ROI-based efficiencies for b-jet tracks are measured using the "b55_NoCut_j55_a4tchad trigger. This trigger uses a different strategy than its 2011 counterpart. A high energy jet is required of greater than 55 GeV with calorimeter cuts to identify hadronic jets over electrons or photons. These changes were motivated by both increased pileup and development of the object identification algorithms.

At L2, the ROI-based efficiency of the L2Star-A algorithm remained stable at 94%. This performance is similar to the performance observed in 2011. A slight dependence is seen on the track $|\eta|$ but this dependence is small. The efficiencies are presented in Fig. 4.29. The fake rate is noticeably higher, higher than any other signature, due to the increased pile-up in 2012 data, particularly at high values of track $|\eta|$. The fake rate at L2 is approximately 18% and is shown in Fig. 4.30. The efficiencies and fake rates for the b-jet triggers are summarised in Table 4.3.

At EF, the ROI-based efficiency of the EFID algorithm for b-jet tracks is presented in Fig. 4.31. The efficiency is 96% and has little dependence on track p_{T} and $|\eta|$. The fake rate is presented in Fig. 4.32 and is much smaller than the fake rate observed in L2Star_B. The benefits of a longer execution time for tracking algorithms at EF is particularly apparent in this trigger. The rate increases with track $|\eta|$, as with the 2011 case.

4.4.5   Summary

The performance of the ATLAS single lepton and b-jet triggers during 2011 and 2012 was very good. In 2011 the efficiencies at L2 for muons and b-jets is over 90% in all cases. Electron efficiency is slightly lower but still good. The fake rates for all trigger signatures are small. In 2012 the efficiencies for all signatures are above 90% representing an improvement for electron signatures due to the introduction of a new L2 tracking algorithm. The fake rates also increased in all signatures due to increased contributions from pile up. The same common features are observed in many of the tracking algorithms. In general, trigger tracking efficiency drops at $|\eta|$ increases. Given the resolution of the detector in the these regions, this result is not surprising. In 2012, the pileup had a large effect on the fake rates at L2 but was controlled much better in the EFIF algorithm at EF. In both 2011 and 2012 the efficiencies for the EFID algorithm are excellent in all signatures, approaching 100% for muons.

A good understanding of the performance of the trigger algorithms is essen-

tial for effectively selecting physics events. The ATLAS trigger algorithms are executed with performance similar to the offline algorithms that are used as a reference. In efficiencies derived from physics objects very high efficiencies are observed, indicating very little efficiency loss due to the time constraints imposed on the trigger tracking. The increase in pile-up between 2011 and 2012 did not result in a loss of efficiency. Thanks to the introduction of more sophisticated trigger tracking algorithms most efficiencies increased despite the pileup.

Chapter 5

Dilepton Event selection

5.1 Data Periods

During the 2011 7 TeV LHC run, the data were split into periods corresponding
to stable detector conditions, labelled A-M. Not all periods are used for physics
analysis. A list of the integrated luminosity collected in each period that is used
for this analysis is shown in Table 5.1. A total of 4.6 fb^{-1} of data are used for
this analysis, the full data set for 2011.

5.2 Object Definitions

The physics objects used for this analysis are electrons, muons, jets and vertices.
These objects are optimised to provide the best performance possible for a dilep-
tonic $t\bar{t}$ selection. All object definitions are implemented following the standard
selection and correction criteria used by the ATLAS top group, described in de-

Data period	Int. Luminosity	Electron Trigger	Muon Trigger
period B-D	0.176 fb^{-1}	EF_e20_medium	EF_mu18
period E-H	0.938 fb^{-1}	EF_e20_medium	EF_mu18
period I	0.333 fb^{-1}	EF_e20_medium	EF_mu18
period J	0.223 fb^{-1}	EF_e20_medium	EF_mu18_medium
period K	0.583 fb^{-1}	EF_e22_medium	EF_mu18_medium
period L-M	2.402 fb^{-1}	OR EF_e22vh_medium1 EF_e45_medium1	EF_mu18_medium

Table 5.1: Table of analysis triggers used for data taking in the 7 TeV data. Note
that *medium1* and *medium* are two distinct trigger types. The letter "v" indicated
η dependent cuts in the trigger and the letter "h" refers to a veto of energy in the
hadronic calorimeter in the region around the trigger electron.

tail in Ref. [51]. A common C++ framework, implemented within ROOT, was created to provide analysers with standard energy scales, trigger scales, pileup re-weighting factors and object corrections and to implement these in a consistent way. All object scales and corrections are derived using this framework and conform to the prescriptions recommended by the ATLAS top group [52, 53].

5.2.1 Tracks and Vertices

Tracks in the ID and vertices are used in the construction of reco-level physics objects, in the case of tracks, or for performing data or object quality cuts, in the case of both vertices and tracks.

ID tracks are reconstructed within the region of $|\eta| < 2.5$ due to the acceptance constraints of the Pixel and SCT detector. Space-point measurements are used to seed tracks in a pattern-recognition algorithm. This algorithm uses a Kalman filter to reconstruct tracks in the Pixel and SCT detectors together and then projects them out into the TRT. Ideally, each track has three space-point hits in the Pixel detector and four in the SCT. If tracks were fitted with any missing Pixel space points or more than one missing SCT space point, then the physics objects to which they associate (for example, an electron) are rejected.

Vertices are constructed by grouping tracks together based on their impact parameters with the beam. Only tracks with a measured $p_{\mathrm{T}} > 400$ MeV are considered when building vertices. Tracks are compared to a vertex candidate using a χ^2 fit and are removed if they are inconsistent with the candidate vertex at greater than 7 standard deviations. The primary vertex for an event is defined as the vertex with the highest sum of associated track p_{T}^2.

5.2.2 Jets

Jets are reconstructed using the $anti-k_{\mathrm{T}}$ jet algorithm [54] with a distance parameter of $R = 0.4$ using clustered energy in the calorimeters called "topo clusters". Clusters are built by taking a calorimeter cell with a large energy deposit and by associating neighbouring cells with significant energy deposits. The $anti-k_{\mathrm{T}}$ then groups these cluster objects together to form jets. These jets are calibrated to the EM scale and then corrected for the hadronic calorimeter response. In this analysis, selected jets are required to have $p_{\mathrm{T}} > 25$ GeV and $|\eta| < 2.5$ and require $|JVF| > 0.75$ to reject jets associated with pileup, where $|JVF|$ is defined as the fraction of tracks from the inner detector that are associated with both this jet and a vertex. Cleaning cuts, shown in Table 5.2, are applied to remove jets of

Source		Cleaning Cut
EM coherent noise:	EmF	> 0.95
	|Q|	> 0.08
HEC spike (1):	Hecf	> 0.8
	n90	<=5
HEC spike (2):	Hecf	> 0.5
	|Q|	> 0.5
Cosmics/Beam (1):	|t|	> 25 ns
Cosmics/Beam (2):	Emf	< 0.05
Cosmics/Beam (3):	Fmax	> 0.99
	$|\eta|$	<2

Table 5.2: Jet cleaning cuts used in this analysis. If any of the 6 group cases are satisfied the jet fails the cleaning cuts. EmF is defined as the fraction of energy from the EM calorimeter to the total jet energy, |Q| is a quality factor based on the fraction of energy of a jet associated with a poorly modelled LAr cell, Hecf is similar to |Q| (however, in the hadronic calo endcaps only), n90 is the minimum number of calorimeter cells containing at least 90% of the jet energy, Fmax is the maximum energy fraction in one calorimeter layer and t is the jet timing [55].

poor quality and jets that are found within a $\Delta R < 0.2$ of selected electrons are removed to avoid double counting.

5.2.3 Electrons

Electrons are reconstructed from ID tracks and energy deposits in the EMCal. They are required to have $|\eta| < 2.47$ due to the η constraints of the inner detector and calorimeter. The transition region between the barrel and the calorimeter end caps, $1.37 < |\eta_{cluster}| < 1.52$, is also excluded due to reduced performance in these regions. Deposits in the EMCal from photons or from $\gamma \to e^+e^-$ conversions are rejected based on the shape of their energy deposits. Prompt electrons have a central energy deposit in a cluster whereas photons and pair conversions have a broader shape in ϕ. Electrons must pass strict cuts on track quality, calorimeter clusters, and other variables to provide good separation between jets and isolated electrons, called "Tight++" requirements [56, 57]. In addition they are required to have a direction corrected transverse energy (E_T) of greater than 25 GeV where $E_\mathrm{T} = E_{cluster}/\cosh(\eta_{track})$ which corrects the calorimeter cluster for the electron track direction. Electrons are required to be isolated from other activity in the detector. A variable p_T and E_T based isolation cut is used. The cut is a

variable cut on the amount of energy in a cone around the electron but the precise value varies so that a 90% efficiency with respect to "Tight++" across the whole $p_T > 30$ GeV and $E_T > 20$ GeV range is maintained [51]. Finally, electrons that have a $\Delta R < 0.4$ with a selected jet after electron-jet overlap removal are removed.

5.2.4 Muons

Muons are required to have been reconstructed using a combined algorithm based on tracks from the ID and the MS, described in [58]. Candidates are required to be within the ID acceptance of $|\eta| < 2.5$, to have $p_T > 20$ GeV, and to pass quality cuts on their associated ID tracks. These quality cuts are defined by the Muon Combined Performance (MCP) group [59]. Muons that overlapped with jets, where the jet satisfies $p_T > 25$ GeV and $|JVF| > 0.75$, are removed. The sum of all transverse energy in a cone around the muon candidate of radius $\Delta R = 0.2$, excluding the muon track, is required to be less than 4 GeV. The sum of all transverse momenta of ID tracks in a cone of radius $\Delta R = 0.3$ is required to be less than 2.5 GeV. The requirements on the jet overlap and jet isolation are optimised to reduce contributions from heavy-flavour decays with very little dependence on pileup [51].

5.2.5 E_T^{miss}

The sum of missing transverse momenta used for this analysis is built using all physics objects in the event[60]:

$$E_{T(x,y)}^{miss} = E_{T(x,y)}^{RefElec} + E_{T(x,y)}^{RefJet} + E_{T(x,y)}^{RefSoftJet} + E_{T(x,y)}^{RefMuon} + E_{T(x,y)}^{CellOut}, \qquad (5.1)$$

where the ordering of the terms indicates the order in which calorimeter cells are grouped to physics objects. Photons and τ objects are absent from the calculation. "RefElec" (meaning *Refined Electron*) are electrons satisfying the "Tight++" requirement and with $p_T > 10$ GeV, with all nominal scales and corrections applied with the exception of the out-of-cluster correction. "RefJets" (meaning *Refined Jets*) are jets reconstructed by the $anti - k_T$ algorithm and calibrated to EM+JES energy scale with $p_T > 20$ GeV. "RefSoftJet" are similar to "RefJets" but with 7 GeV $< p_T < 20$ GeV. The "RefMuon" term is defined using muons that are reconstructed with the "MuID" algorithm inside the Muon Spectrometer acceptance of $|\eta| < 2.7$ and from combined muons with $|\eta| < 2.5$. All calorimeter cells with energy deposits not associated to any of the other terms

are grouped as the "CellOut" collection. The final $E_{\mathrm{T}}^{\mathrm{miss}}$ value is calculated for each event using the quadrature sum of the x and y components:

$$E_{\mathrm{T}}^{\mathrm{miss}} = \sqrt{(E_x^{\mathrm{miss}})^2 + (E_y^{\mathrm{miss}})^2} \qquad (5.2)$$

5.3 Analysis Triggers

To select interesting $t\bar{t}$ like events with high efficiency, triggers are used based on single electron or muon signatures. Electron triggers are required to have a trigger electron with a minimum p_{T} of 20 GeV in periods B-J, a minimum p_{T} of 22 GeV in period K, and either 22 GeV or 45 GeV in periods L-M. Muon triggers are required to have a trigger muon with minimum p_{T} of 18 GeV in all periods.

The minimum p_T cut on electrons and muons selects objects in the plateau region of efficiency of these triggers in almost all cases, with the exception of the EF_e45_medium1 trigger. The higher threshold of 45 GeV is used to accept events that are rejected by the hadronic-core veto component (indicated by the letter "h" in the trigger name) of the lower threshold trigger in periods L-M but an event is selected if it satisfied either trigger. The hadronic-core veto rejects trigger electrons with significant energy in the hadronic calorimeter in the same region of η-ϕ as the trigger electron.

5.4 Selection

Dilepton $t\bar{t}$ events are characterised by two high p_{T} leptons, two jets from b-quarks and missing transverse energy from the two neutrinos. The cuts that are used in this analysis are derived from a previous cross-section analysis in the dilepton channel [61]. Events not originating from dileptonic $t\bar{t}$ decay are suppressed using event-level selection cuts. The list of cuts that are used in this analysis are described along with the background processes that they are designed to suppress.

- **Events must pass a single lepton trigger**: Events are required to have fired either an electron or muon trigger. The trigger that is used depends upon the data period as described in section 5.3. For the e^+e^- and $\mu^+\mu^-$ channel the corresponding lepton trigger must have fired. For the $e^{\pm}\mu^{\mp}$ channel either an electron or a muon trigger must have fired.

- **Exactly two opposite sign leptons**: Two well reconstructed leptons are required; either two electrons, two muons, or one electron and one muon. The

lepton object definitions are described in Section 5.2.3 and 5.2.4. The selected lepton pair must have opposite sign charge. This suppresses backgrounds from any SM process that does not include two prompt leptons, for example single top production in the s or t channel. In the $e^\pm\mu^\mp$ channel, the requirement of exactly one muon and one electron has the additional effect of removing $Z \to ee$ and $Z \to \mu\mu$ events. At least one lepton in the event must be matched to the trigger lepton that is used to select the event.

- **Two or more selected jets**: At least two well reconstructed jets in each event are required, though no requirement for b-tagging is made. The object cuts used on jets are described in Section 5.2.2. When combined with the lepton multiplicity requirement, this cut removes most non-$t\bar{t}$ SM physics signals from the selection. Many of the remaining backgrounds require extra jets either from pileup or radiated partons in order to imitate the signal kinematics of two oposite sign leptons and at least two jets.

- $E_T^{\mathbf{miss}} >$ **60 GeV**: (e^+e^- and $\mu^+\mu^-$ channels only) In the e^+e^- and $\mu^+\mu^-$ channels more than 60 GeV of missing transverse energy is required. This cut reduces contributions from Drell-Yan events, as in this process there are no neutrinos from the hard scatter that result in missing energy. The cut also suppresses diboson events with few or no neutrinos in their final state decay channels; for example ZZ final states where neither Z decayed to neutrinos. For $t\bar{t}$ dilepton events the efficiency of this cut is very high due to the presence of two neutrinos in the dilepton final state.

- $H_T >$ **130 GeV** : ($e^\pm\mu^\mp$ channel only) H_T is defined as the scalar sum of the transverse energy of all selected leptons and jets in the event. This cut is only applied in the $e^\pm\mu^\mp$ channel and can be interpreted as requiring a large amount of energetic activity in the event. This cut rejects background events with lower energy, for example $Z \to \tau\tau$+jets, whilst favouring $t\bar{t}$ signal events.

- Z **Veto**: (e^+e^- and $\mu^+\mu^-$ channels only) Events with an invariant mass that is less than 10 GeV away from the Z pole mass of 91 GeV are rejected. This cut reduces a large amount of the Drell-Yan $\to e^+e^-$ or $\mu^+\mu^-$ background. Events in which the Z decays to two tau leptons (that subsequently decay leptonically) have a broad invariant mass spectrum that peaks at lower values, illustrated in Fig. 5.6 and 5.7, and a similar cut to suppress this background would result in an unacceptable loss of signal statistics. This cut also introduces a difference in acceptance between the standard model spin sample and the uncorrelated

spin sample. In the uncorrelated sample the leptons typically have a larger separation in ϕ and hence a higher invariant mass. The efficiency of this cut is 3% higher for the uncorrelated sample than it is for the SM sample. This effect is accounted for in the extraction procedure and does not affect the final result.

- **Dilepton Invariant mass > 15 GeV**: (e^+e^- and $\mu^+\mu^-$ channels only) The invariant mass is defined as the invariant mass of the two selected leptons in the event. Low energy $Z\,\gamma^* \to \ell\ell$ events and meson production such as J/Ψ could enter the selection by decaying to two opposite sign leptons. These processes typically have a low invariant mass and are rejected by this cut. The invariant mass of the $t\bar{t}$ system peaks at much higher values and so this cut does not have a large effect on signal acceptance.

- **Cosmic Rejection**: Events are rejected if two muon tracks are back to back in ϕ (i.e. $\Delta\phi > 3.1$) and if the point of closest approach to the primary vertex is greater than 5 mm. Both tracks are required to have the same sign pseudorapidity.

- **Data Quality Cuts: (Good Run List)**: An event in data is required to have been included in a good run list (GRL). These GRLs are generated centrally by ATLAS and reject events where data quality is deemed to be poor. In addition to ATLAS central recommendations, physics subgroups also impose their own requirements when appropriate. In the case of a predominantly jet-based analysis, bad data quality of the inner detector may be a tolerable defect, whereas for a muon-based Drell-Yan selection the calorimeter information may not be necessary. For top analyses it is required that the entire detector was online and that the data quality is assessed to be good. An example of some of the data quality monitoring via trigger efficiencies is shown in Sect. 4. The GRL used in this analysis corresponds to an integrated luminosity of 4.7 fb^{-1}.

- **Data Quality Cuts: (Vertex)**: A reconstructed vertex with at least three tracks is required to have been identified as the primary vertex and not one originating from other pileup events.

- **Data Quality Cuts: (LAr)**: In 2011 a tower of the ATLAS Liquid Argon calorimeter was disabled creating a hole in the detector acceptance. In the portion of affected data, events are rejected where a jet is detected close to this hole and may have been mis-measured due to this fault. In addition this effect is taken into account in the detector simulation and the calculation of $E_{\mathrm{T}}^{\mathrm{miss}}$.

Parameter	Value
Top Mass	172.5 GeV
Top Width	1.320 GeV
W Mass	80.399 GeV
Z Mass	91.1876 GeV
W Width	2.085 GeV
Z Width	2.4952 GeV
u mass	0.32 GeV
d mass	0.32 GeV
s mass	0.50 GeV
c mass	1.55 GeV
b mass	4.95 GeV
g mass	0.75 GeV
W to Lepton BR	0.108
W to Hadron BR	0.338

Table 5.3: Common parameters used in MC samples. Values are taken from PDG2010 [3] values.

- **Passed Truth Cuts**: In the signal MC events it is required that the selected event be a true dilepton $t\bar{t}$ event, and that the two reconstructed leptons correspond to the true leptons from the hard process and not from a secondary process. This cut is implemented to avoid double counting contributions from non-prompt leptons, which are estimated separately using a data-driven method.

With the application of all cuts the contribution of background events to the final selection is approximately 20%. With the addition of a single b-jet requirement (b-tag) this could be reduced to 10%; however, the cost in statistics for utilising b-tagging to signal events is quite large (on the order of 20%) and would also introduce additional systematic uncertainty. For this reason b-tagging is not implemented.

5.5   Monte Carlo Simulation

5.5.1   Common Parameters

In all MC samples a common set of mass and width parameters is taken from the Particle Data Group (PDG) 2010 values [3]. These parameters are summarised in Tab. 5.3.

5.5.2 $t\bar{t}$ generators

Signal $t\bar{t}$ events are generated using version 4.01 of the MC@NLO[36] generator. MC@NLO is interfaced with HERWIG [34] (version 6.520) and JIMMY [30] (version 4.31) for parton showering (PS) and underlying event (UE) simulation respectively. MC@NLO is used to generate both top quarks, the W and b particles from top decay, and the subsequent hadronic or leptonic W decay. HERWIG then showered these particles and JIMMY simulated interactions with the underlying event. MC@NLO used ATLAS Event Tune 2 (AUET2) as well as the CT10 [31, 62] NLO PDF set.

MC@NLO includes parameters which may be adjusted to simulate uncorrelated $t\bar{t}$ events. By configuring the point at which HERWIG initiates the parton showering and decay of particles, spin correlation can effectively be removed from the MC. If HERWIG is allowed to decay the top quarks then they are treated as unpolarised, effectively removing spin correlation from the event. In this manner 15 million $t\bar{t}$ events are generated with spin correlation (semi-leptonic and dileptonic) and 10 million events without spin correlation using the same tunes and PDF settings as the signal $t\bar{t}$ events. This technique causes the top quarks in the uncorrelated case to have no intrinsic width as they are treated as being on shell. This effect is considered as a source of systematic uncertainty but is found to be negligible.

Signal events are also generated with POWHEG [37] (version heavy vector quark (hvq) patch 4 or powheg box 1.0) interfaced to either HERWIG or PYTHIA [63] to perform showering and using either the Perugia2011C tune [64] or AUET2 and JIMMY to simulate the underling event.

Both POWHEG versions included a bug that resulted in an incorrect calculation for $t\bar{t}$ spin correlation at higher orders. These POWHEG samples are only used in the estimation of systematic uncertainties independent to these bugs (for example colour reconnection) and are never compared to other generators directly. In more recent versions of POWHEG this bug is corrected; however, it was not possible to generate samples for 7 TeV in time for the submission of this thesis.

Additionally, $t\bar{t}$ events are generated with ACERMC [35] for initial state and final state radiation systematic uncertainties, detailed in Sect. 7.1, using JIMMY for underlying event simulation.

The Tauola program [65] is used to decay tau particles in HERWIG. In some cases, if the polarisation is not considered correctly, tau decays can be treated as unpolarised, effectively making an event with SM spin correlations and a tau

Process	Generator	$\sigma\cdot$BR	k-factor	Events (10^3)
A=SM	MC@NLO + HERWIG	79.01	1.125	15,000
A=0	MC@NLO + HERWIG	79.01	1.125	10,000
μ scale up	MC@NLO + HERWIG	89.47	1.012	10,000
μ scale down	MC@NLO + HERWIG	68.51	1.322	10,000
Mass = 165 GeV	MC@NLO + HERWIG	100.53	1.120	5,000
Mass = 170 GeV	MC@NLO + HERWIG	85.99	1.120	5,000
Mass = 172.5 GeV	MC@NLO + HERWIG	80.85	1.120	1,000
Mass = 175 GeV	MC@NLO + HERWIG	74.30	1.120	5,000
Mass = 180 GeV	MC@NLO + HERWIG	63.34	1.143	5,000
Baseline (hvq patch 4)	POWHEG + PYTHIA	80.07	1.131	10,000
No colour reconnection	POWHEG + PYTHIA	80.06	1.131	10,000
Underlying event tune	POWHEG + PYTHIA	80.07	1.131	10,000
Parton Shower (box v1)	POWHEG + PYTHIA	80.85	1.191	10,000
Parton Shower (box v1)	POWHEG + HERWIG	80.07	1.202	3,000
ISR/FSR Up	ACERMC	41.01	2.208	10,000
ISR/FSR Down	ACERMC	41.01	2.209	10,000

Table 5.4: MC $t\bar{t}$ samples used for signal templates and generator systematics uncertainties. All samples used fast detector simulation with the exception of the A=SM and A=0 samples which used full detector simulation. The k-factor is a correction factor for the $\sigma\cdot$BR to the NNLO calculation [28].

decay appear the same as an uncorrelated $t\bar{t}$ event. This is accounted for in all ATLAS MC samples and was only present in the POWHEG + HERWIG implementation. When comparing POWHEG samples interfaced with different showers in this analysis, tau decay events are excluded to account for this problem. In a similar analysis performed by the CMS collaboration this effect was not accounted for in the signal MC and was the dominant source of systematic uncertainty [66].

All $t\bar{t}$ samples that are used in this analysis are summarised in Tab. 5.4.

5.5.3 Comparison to theory predictions

The truth information of various generators is also compared to theory predictions [12], with results given in Tables 5.5, 5.6 and 5.7. For the MC, the true spin information is extracted directly using the $\cos(\theta^+)\cos(\theta^-)$ variable in the Helicity basis on the generator level truth particles. The theoretical predictions are calculated at full NLO and include corrections for EW effects. The MC@NLO generator is only NLO in the production but not in the decay of the $t\bar{t}$ pairs and does not include EW corrections. Therefore, a complete agreement of the

predictions from MC@NLO and these theoretical predictions is not expected. Nevertheless MC@NLO agreed with theory predictions within the theory uncertainties for the inclusive regime. Small deviations are observed in the high and low $t\bar{t}$ invariant mass regions with a split at 450 GeV on truth level. A POWHEG sample that included the bug in spin correlation is also included for reference and deviates noticeably from the theory predictions, far more than would be expected due to NLO or EW effects.

5.5.4 Background MC generators

The single top background process is estimated using MC@NLO interfaced to HERWIG and using the same versions and parameters as for the $t\bar{t}$ samples. Only single top production in association with a W boson is considered. Contributions of this nature are considered using a data-driven approach described in Sect. 5.6.1. The background diboson processes are generated using the ALPGEN [32] generator interfaced to HERWIG with 0, 1, 2 or 3 (incl.) additional partons. Drell-Yan events are also generated using ALPGEN + HERWIG for 0 - 5 (incl.) additional partons in both the high dilepton invariant mass regime ($40 \rightarrow 2000$ GeV) and the low invariant mass regime (between $10 \rightarrow 40$ GeV). The $Z \rightarrow \tau^+\tau^-$ MC is used directly as the background model; however, the normalisation of the $Z \rightarrow ee$ and $Z \rightarrow \mu\mu$ is taken from data, described in Sect. 5.6.2. A summary of these samples is presented in Tables 5.8 and 5.9.

MC Sample	$\ell^+ : \ell^-$	$b : \bar{b}$	$\ell^+ : b$	$\bar{b} : \ell^-$
THEORY	0.310 ± 0.006	0.047	-0.121	-0.121
MC@NLO A=SM	0.313 ± 0.002	0.043 ± 0.002	-0.121 ± 0.002	-0.120 ± 0.002
MC@NLO A=0	0.002 ± 0.003	0.001 ± 0.003	0.003 ± 0.003	-0.002 ± 0.003
POWHEG	0.194 ± 0.004	0.037 ± 0.004	-0.085 ± 0.004	-0.094 ± 0.004

Table 5.5: Comparison between theory predictions [12] and values derived from AT-LAS MC samples with the MC@NLO generator and POWHEG generator which contains a bug in the spin correlation calculation. The theory predictions are extrapolated by assuming a spin analysing power of the b quark to be -0.390 at NLO for a top mass of 172.5 GeV and performing a linear transformation from the lepton-lepton theoretical predication.

MC Sample	$\ell^+ : \ell^-$	$b : \bar{b}$	$\ell^+ : b$	$\bar{b} : \ell^-$
THEORY	0.203 ± 0.008	0.031	-0.079	-0.079
MC@NLO A=SM	0.157 ± 0.003	0.016 ± 0.003	-0.059 ± 0.003	-0.061 ± 0.003
MC@NLO A=0	0.008 ± 0.004	0.008 ± 0.004	-0.005 ± 0.004	0.001 ± 0.004
POWHEG	0.050 ± 0.005	0.007 ± 0.006	-0.018 ± 0.006	-0.037 ± 0.006

Table 5.6: Comparison between theory predictions [12]and values derived from AT-LAS MC samples with the MC@NLO generator and POWHEG generator, which contains a bug in the spin correlation calculation, in the events with $t\bar{t}$ invariant mass > 450 GeV. The theory predictions are extrapolated by assuming a spin analysing power of the b quark to be -0.390 at NLO for a top mass of 172.5 GeV and performing a linear transformation from the lepton-lepton theoretical predication.

MC Sample	$\ell^+ : \ell^-$	$b : \bar{b}$	$\ell^+ : b$	$\bar{b} : \ell^-$
THEORY	0.422 ± 0.002	0.064	-0.165	-0.165
MC@NLO A=SM	0.453 ± 0.003	0.066 ± 0.003	-0.176 ± 0.003	-0.173 ± 0.003
MC@NLO A=0	-0.003 ± 0.004	-0.005 ± 0.004	0.002 ± 0.004	0.006 ± 0.004
POWHEG	0.335 ± 0.006	0.066 ± 0.006	-0.152 ± 0.006	-0.151 ± 0.006

Table 5.7: Comparison between theory predictions [12] and values derived from AT-LAS MC samples with the MC@NLO generator and POWHEG generator, which contains a bug in the spin correlation calculation, in the events with $t\bar{t}$ invariant mass < 450 GeV. The theory predictions are extrapolated by assuming a spin analysing power of the b quark to be -0.390 at NLO for a top mass of 172.5 GeV and performing a linear transformation from the lepton-lepton theoretical predication.

Process	Generator	$\sigma \cdot$BR	k-factor	Events (10^3)
$Z \to ee + 0$	ALPGEN + HERWIG	668.32	1.25	6618
$Z \to ee + 1$	ALPGEN + HERWIG	134.36	1.25	133.5
$Z \to ee + 2$	ALPGEN + HERWIG	40.54	1.25	200.4
$Z \to ee + 3$	ALPGEN + HERWIG	11.16	1.25	500
$Z \to ee + 4$	ALPGEN + HERWIG	2.88	1.25	150
$Z \to ee + 5$	ALPGEN + HERWIG	0.83	1.25	50
$Z \to \mu\mu + 0$	ALPGEN + HERWIG	668.68	1.25	6615
$Z \to \mu\mu + 1$	ALPGEN + HERWIG	134.14	1.25	133.4
$Z \to \mu\mu + 2$	ALPGEN + HERWIG	40.33	1.25	200
$Z \to \mu\mu + 3$	ALPGEN + HERWIG	11.19	1.25	550
$Z \to \mu\mu + 4$	ALPGEN + HERWIG	2.75	1.25	150
$Z \to \mu\mu + 5$	ALPGEN + HERWIG	0.77	1.25	50
$Z \to \tau\tau + 0$	ALPGEN + HERWIG	668.40	1.25	10613
$Z \to \tau\tau + 1$	ALPGEN + HERWIG	134.81	1.25	333.4
$Z \to \tau\tau + 2$	ALPGEN + HERWIG	40.36	1.25	100.5
$Z \to \tau\tau + 3$	ALPGEN + HERWIG	11.25	1.25	510
$Z \to \tau\tau + 4$	ALPGEN + HERWIG	2.79	1.25	145
$Z \to \tau\tau + 5$	ALPGEN + HERWIG	0.77	1.25	45
$Z \to ee + 0$ (low mass)	ALPGEN + HERWIG	3055.20	1.25	995
$Z \to ee + 1$ (low mass)	ALPGEN + HERWIG	84.92	1.25	300
$Z \to ee + 2$ (low mass)	ALPGEN + HERWIG	41.40	1.25	1000
$Z \to ee + 3$ (low mass)	ALPGEN + HERWIG	8.38	1.25	150
$Z \to ee + 4$ (low mass)	ALPGEN + HERWIG	1.85	1.25	40
$Z \to ee + 5$ (low mass)	ALPGEN + HERWIG	0.46	1.25	10
$Z \to \mu\mu + 0$ (low mass)	ALPGEN + HERWIG	3054.90	1.25	1000
$Z \to \mu\mu + 1$ (low mass)	ALPGEN + HERWIG	84.87	1.25	300
$Z \to \mu\mu + 2$ (low mass)	ALPGEN + HERWIG	41.45	1.25	1000
$Z \to \mu\mu + 3$ (low mass)	ALPGEN + HERWIG	8.38	1.25	150
$Z \to \mu\mu + 4$ (low mass)	ALPGEN + HERWIG	1.85	1.25	40
$Z \to \mu\mu + 5$ (low mass)	ALPGEN + HERWIG	0.46	1.25	10
$Z \to \tau\tau + 0$ (low mass)	ALPGEN + HERWIG	3055.10	1.25	1000
$Z \to \tau\tau + 1$ (low mass)	ALPGEN + HERWIG	84.93	1.25	300
$Z \to \tau\tau + 2$ (low mass)	ALPGEN + HERWIG	41.47	1.25	500
$Z \to \tau\tau + 3$ (low mass)	ALPGEN + HERWIG	8.36	1.25	150
$Z \to \tau\tau + 4$ (low mass)	ALPGEN + HERWIG	1.85	1.25	40
$Z \to \tau\tau + 5$ (low mass)	ALPGEN + HERWIG	0.46	1.25	10

Table 5.8: Drell-Yan MC samples used for background shape modelling. The number of extra radiated jets simulated by ALPGEN are listed next to the underlying process. Two groups are listed; the first simulated $Z/\gamma*$ with an invariant mass in the range 40 GeV <mass < 2000 GeV, the second in a lower mass range 10 GeV <mass < 40 GeV.

Process	Generator	$\sigma\cdot$BR	k-factor	Events (10^3)
Wt	MC@NLO + HERWIG	14.59	1.079	900
$WW + 0$	ALPGEN + HERWIG	2.095	1.26	200
$WW + 1$	ALPGEN + HERWIG	0.996	1.26	100
$WW + 2$	ALPGEN + HERWIG	0.455	1.26	60
$WW + 3+$	ALPGEN + HERWIG	0.176	1.26	40
$WZ + 0$	ALPGEN + HERWIG	0.672	1.28	60
$WZ + 1$	ALPGEN + HERWIG	0.414	1.28	40
$WZ + 2$	ALPGEN + HERWIG	0.225	1.28	20
$WZ + 3+$	ALPGEN + HERWIG	0.095	1.28	20
$ZZ + 0$	ALPGEN + HERWIG	0.509	1.30	40
$ZZ + 1$	ALPGEN + HERWIG	0.234	1.30	20
$ZZ + 2$	ALPGEN + HERWIG	0.089	1.30	20
$ZZ + 3+$	ALPGEN + HERWIG	0.031	1.30	10

Table 5.9: Single top and diboson MC samples used for background modelling.

5.6 Data-driven background estimation

Data-driven background estimates offer an advantage over MC only estimates. They can be tuned or constrained using observations from data and either do not suffer, or suffer to a lesser degree, from theoretical uncertainties. The normalisation of Drell-Yan MC is derived by comparing the normalisation of MC with data in a Drell-Yan dominated selection. Non-prompt leptons (fake leptons) are also estimated using a data-driven technique.

5.6.1 Matrix Method for determining fake lepton background

Fake leptons can arise from many processes. The dominant sources are categorised as jets incorrectly identified as leptons, photon conversions or non-prompt leptons arising from heavy flavour decays. The main SM processes that contributed to this background are W production in association with jets, single top production in the s or t channel, and single lepton $t\bar{t}$ decays. Leptons arising from prompt leptonic tau decay are not considered as fakes.

A matrix method is used to determine the shape and normalisation of backgrounds due to fake leptons [51][67]. The method uses the rate at which a reconstructed lepton passes isolation cuts to estimate the number of fake leptons contaminating the data selection. Two lepton definitions are defined: *loose* and *tight*. The *tight* selection is the standard selection used for this analysis. The *loose* selection is the same as the *tight* selection but with either the isolation requirements relaxed (in the case of electrons) or removed (in the case of muons). The number of leptons that pass the loose and tight requirements are quantities that may be observed directly in data.

Two efficiencies are defined: the rate at which a real lepton that has passed the loose selection also passes the tight selection ϵ_{real} and the rate at which a fake lepton that has passed the loose selection also passes the tight selection ϵ_{fake}:

$$\mathbf{r_i} = \epsilon_{real} = \frac{N_{\text{real}}^{\text{tight}}}{N_{\text{real}}^{\text{loose}}} \quad \& \quad \mathbf{f_i} = \epsilon_{\text{fake}} = \frac{N_{\text{fake}}^{\text{tight}}}{N_{\text{fake}}^{\text{loose}}}. \tag{5.3}$$

The ϵ_{real} for both electrons and muons is measured using a tag and probe technique in Z boson events where a tight lepton is selected as the tag and a loose lepton is probed for tightness.

For electrons the fake efficiency is measured in a QCD enriched sample by selecting events with exactly one loose lepton and at least one jet with $p_{\text{T}} > 25$ GeV. The leading jet is required to be separated from the electron with $\Delta R > 0.7$. Events are required to have $E_{\text{T}}^{\text{miss}} < 20$ GeV to increase the contributions from QCD events. The fake efficiency is defined as the fraction of loose probe electrons that pass the tight selection.

For muons two methods are used to estimate the fake efficiency, parameterised in both muon η and p_T. In both methods events are selected where a single muon is required without isolation cuts. The selection requires a low transverse mass of the reconstructed leptonic W, $M_T(W) < 20$ GeV and a triangular cut on the sum of this mass with the observed missing transverse energy, $E_T^{miss} + M_T(W) < 60$ GeV. In the first method, ϵ_{fake} is extracted by subtracting W and Z MC from data in this selection and measuring the ratio between the loose and tight muons. In the second method, a measurement based on impact parameters of muon tracks is used [51]. For the fake estimates in the signal region, the muon contribution is taken to be the average of the two methods.

The number of events with different lepton quality definitions may be expressed in matrix form:

$$
\begin{bmatrix} N^{tt} \\ N^{tL} \\ N^{Lt} \\ N^{LL} \end{bmatrix} = \mathbf{M} \begin{bmatrix} N^{ll}_{r_1 r_2} \\ N^{ll}_{r_1 f_2} \\ N^{ll}_{f_1 r_2} \\ N^{ll}_{f_1 f_2 ,} \end{bmatrix}
\tag{5.4}
$$

where:

$$
\mathbf{M} = \begin{bmatrix} r_1 r_2 & r_1 f_2 & f_1 r_2 & f_1 f_2 \\ r_1(1-r_2) & r_1(1-f_2) & f_1(1-r_2) & f_1(1-f_2) \\ (1-r_1)r_2 & (1-r_1)f_2 & (1-f_1)r_2 & (1-f_1)f_2 \\ (1-r_1)(1-r_2) & (1-r_1)(1-f_2) & (1-f_1)(1-r_2) & (1-f_1)(1-f_2) \end{bmatrix} ,
\tag{5.5}
$$

and N is the number of events passing the selection. The upper index notation indicates the tightness of the selection for each lepton (t = *tight*, L = *loose*) and the lower index notation indicates if the lepton is real or fake. The loose definition here is different from that defined as the inclusive loose selection (l). An upper case **L** indicates an exclusive loose selection that does not include a tight lepton. For the estimate of the fake contribution to the signal region the parameter of interest is the number of events with at least one fake lepton that contaminates the N^{tt} selection. By using ϵ_{real}, ϵ_{fake} and the number of events with leptons passing *tight* or *loose* selections in data, it is possible to extract N^{tt}. By inverting the matrix $\mathbf{M}$ and rearranging equation 5.4, N^{tt} can be expressed as:

$$
N^{tt}_{fake} = N^{tt}_{rf} + N^{tt}_{fr} + N^{tt}_{ff}
\tag{5.6}
$$

$$
= r_1 f_2 N^{ll}_{rf} + f_1 r_2 N^{ll}_{fr} + f_1 f_2 N^{ll}_{ff}
\tag{5.7}
$$

$$
= \alpha r_1 f_2 [(f_1 - 1)(1 - r_2) N^{tt} + (1 - f_1) r_2 N^{tl} + f_1(1 - r_2) N^{lt} - f_1 r_2 N^{ll}]
$$
$$
+ \alpha f_1 r_2 [(r_1 - 1)(1 - f_2) N^{tt} + (1 - r_1) f_2 N^{tl} + r_1(1 - f_2) N^{lt} - r_1 f_2 N^{ll}]
$$
$$
+ \alpha f_1 f_2 [(1 - r_1)(1 - r_2) N^{tt} + (r_1 - 1) r_2 N^{tl} + r_1(r_2 - 1) N^{lt} + r_1 r_2 N^{ll}],
$$
$$
\tag{5.8}
$$

where

$$\alpha = \frac{1}{(\mathbf{r_1 - f_1})(\mathbf{r_2 - f_2})}. \tag{5.9}$$

Using the values for $N^{\mathbf{tt}}$, $N^{\mathbf{tl}}$, and $N^{\mathbf{ll}}$ observed in the data and the derived real and fake efficiencies, the number of fake leptons in the signal selection can be extracted.

In the data the observed fake contributions in the signal region are small. These estimation methods represent a significant improvement over a previous ATLAS spin correlation result where the systematic contributions from fake lepton estimates were a dominant source of systematic uncertainty [27]. In the previous result the estimation was performed on only 0.7 fb^{-1} of data and then scaled to 2 fb^{-1}, increasing the uncertainty on the method. For this result the full 4.6 fb^{-1} of data are used.

5.6.2 Normalisation of Drell-Yan MC using data

In the e^+e^- and $\mu^+\mu^-$ channels the shape of background contributions from $Z \to ee$ or $Z \to \mu\mu$ events is taken from Monte Carlo. Theoretical uncertainties on the cross sections of inclusive Z boson production are small; however, in this analysis events must have at least an additional two jets which increases the theoretical uncertainty on the process. In addition the $E_{\mathrm{T}}^{\mathrm{miss}}$ modelling can be challenging in the Z + jets sample and the resulting normalisation after selections is not well described by MC. A data-driven method is used to correct the normalisation to data in a control region. The normalisation is derived by comparing data events to MC events in a region dominated by $Z \to \ell\ell$ events:

$$N_{Z/\gamma^*+jets} = \frac{Data^{(CR)} - MC_{other}^{(CR)}}{MC_{Z/\gamma^*+jets}^{(CR)}} \times MC_{Z/\gamma^*+jets}^{(SR)}. \tag{5.10}$$

Events in this control region are selected using the described dilepton selection but with the Z veto cut reversed (i.e. the invariant mass of the dilepton system is required to be within 10 GeV of the Z pole mass) and the missing transverse energy cut loosened to $E_{\mathrm{T}}^{\mathrm{miss}} > 30$ GeV. In this control region non Drell-Yan backgrounds is subtracted from the data to approximate the number of $Z/\gamma^* \to ee$ or $Z/\gamma^* \to \mu\mu$ events. Non Drell-Yan contributions are taken from single top, $t\bar{t}$ diboson and $Z \to \tau^+\tau^-$ MC, as well as from fake leptons. Distributions for this control region are shown in Fig. 5.2 and 5.3. The components of the Drell-Yan scale factors and the resulting scale factors are presented in Tab. 5.10.

After background subtraction a discrepancy between the background subtracted data and the Drell-Yan MC is observed in the dilepton p_{T} distribution. This is discussed in greater detail in Sect. 7.3.

	e^+e^-	$\mu^+\mu^-$
Data (CR)	3149 ± 56.1	9116 ± 95.5
MC$_{DY}$ (CR)	2691.3 ± 21.4	7446.8 ± 36.4
MC$_{Other}$ (CR)	382.2 ± 18.6	730.6 ± 8.7
Scale Factor	1.03	1.13
MC$_{DY}$ (SR)	20.2 ± 1.8	73.3 ± 3.8
Scaled MC	20.7 ± 1.8	82.6 ± 4.2

Table 5.10: Expected and observed events for the estimates of the Z/γ^*+jets background. Yields are presented in the Z dominated control region (CR) and in the signal region (SR). All errors are statistical only.

5.7 Performance on 7 TeV data

—— $t\bar{t}$ (with A = SM)

·········· $t\bar{t}$ (with A = 0)

$Z/\gamma^* \to e^+e^-/\mu^+\mu^-$ Events

$Z/\gamma^* \to \tau\tau$ Events

Single Top Events

Diboson Events

Fake Lepton Events

Normalisation Uncertainty
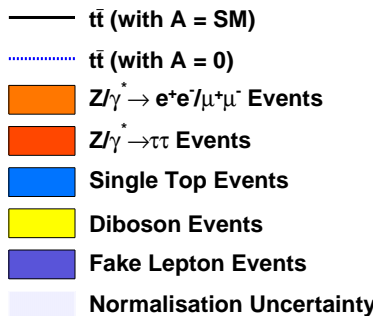
Figure 5.1: Labeling convention that is used in all Data/MC comparison plots.

5.7.1 Drell-Yan control region

Figures 5.2 to 5.5 show comparisons between simulated events and observed events in the Drell-Yan control region. In all figures, the colour and style convention for the various processes are described using the convention in Fig. 5.1. Legends are not included in most figures to aid in their readability. Figure 5.2 shows the distribution of the jet multiplicity, missing transverse energy, invariant mass of the two leptons, and the p_{T} of the dilepton pair in the e^+e^- channel. The jet multiplicity shows excellent agreement between the prediction and the data. The $E_{\mathrm{T}}^{\mathrm{miss}}$ distribution shows good agreement at low $E_{\mathrm{T}}^{\mathrm{miss}}$ and reasonable agreement at high $E_{\mathrm{T}}^{\mathrm{miss}}$, though statistical uncertainties on the data in this control region at high $E_{\mathrm{T}}^{\mathrm{miss}}$ are large. The invariant-mass distribution of the two leptons (where the requirement for the dilepton pair to have an invariant mass within 10 GeV of the Z pole mass for this control region has been relaxed) shows good agreement between data and simulation, with the peak region dominated by events from Z/γ^* as expected. The p_{T} distribution of the e^+e^- pair, after non-Z background and $t\bar{t}$ subtraction, shows very good agreement between data
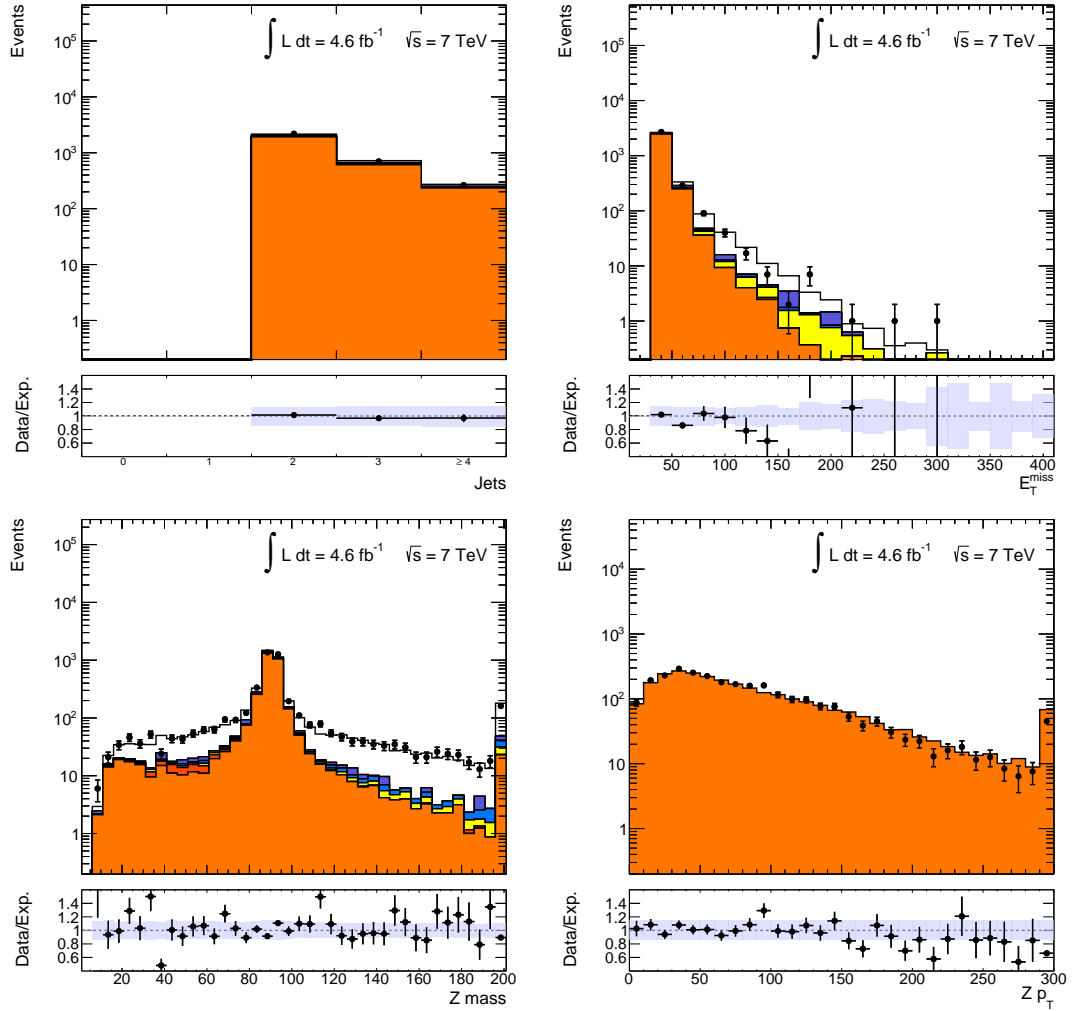
Figure 5.2: Distributions for the e^+e^- channel showing the jet multiplicity, E_T^{miss}, dilepton invariant mass and reconstructed Z boson p_T in regions dominated by $Z/\gamma^* \to e^+e^-$ events. In all distributions exactly two electrons of same flavour and oposite sign are required, as well as at least two jets. At least 30 GeV of E_T^{miss} is required and (with the exception of the invariant mass distribution) events are required to have a dilepton invariant mass between 81 GeV and 101 GeV. In the p_T distribution the single top, diboson, fake lepton, $Z \to \tau^+\tau^-$ and $t\bar{t}$ contributions have been subtracted from the data in order to compare the prediction of the Zp_T shape with the observed shape in data, directly.
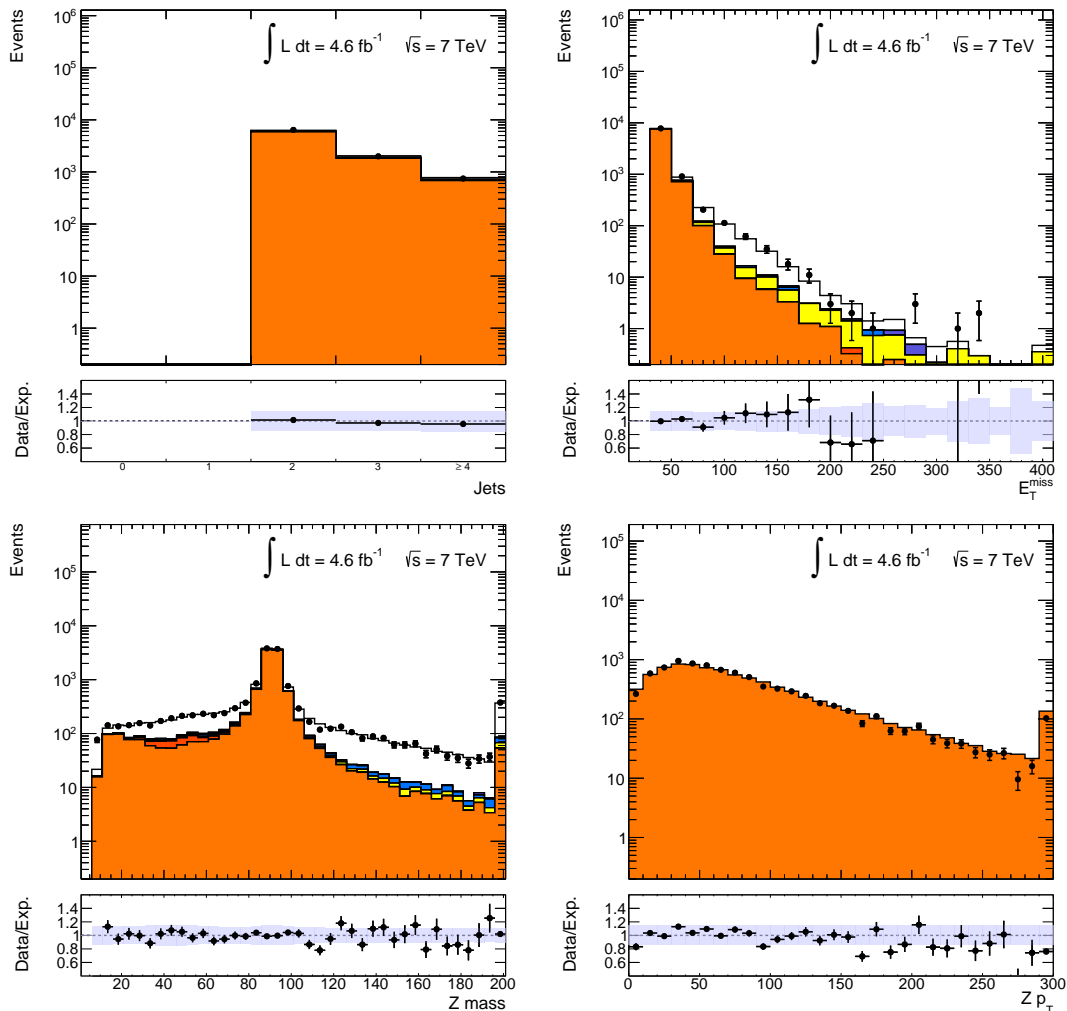
Figure 5.3: Distributions for the e^+e^- channel showing the jet multiplicity, $E_{\mathrm{T}}^{\mathrm{miss}}$, dilepton invariant mass and reconstructed Z boson p_{T} in regions dominated by $Z/\gamma^* \to \mu^+\mu^-$ events. In all distributions exactly two muons of same flavour and oposite sign are required, as well as at least two jets. At least 30 GeV of $E_{\mathrm{T}}^{\mathrm{miss}}$ is required and (with the exception of the invariant mass distribution) events are required to have a dilepton invariant mass between 81 GeV and 101 GeV. In the p_{T} distribution the single top, diboson, fake lepton, $Z \to \tau^+\tau^-$ and $t\bar{t}$ contributions have been subtracted from the data in order to compare the prediction of the Zp_{T} shape with the observed shape in data, directly.

110
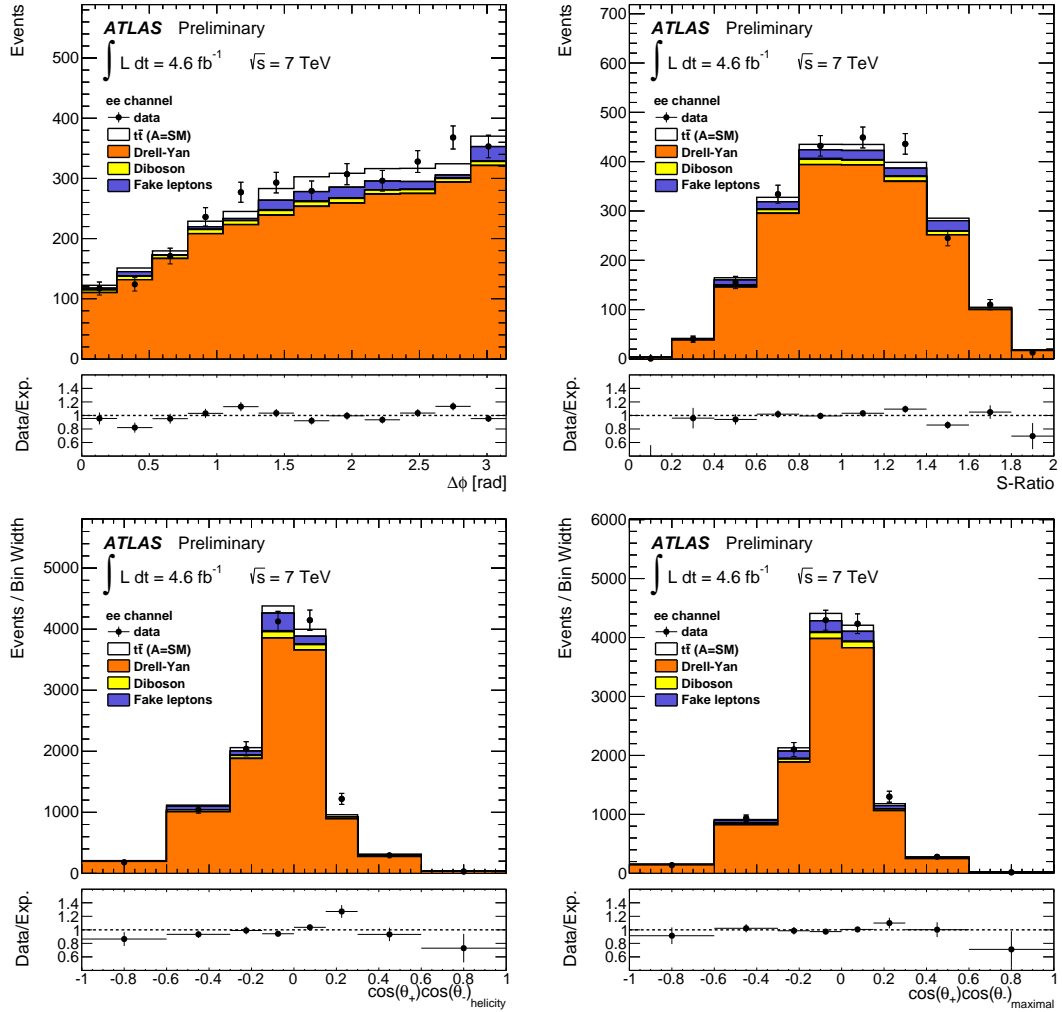
Figure 5.4: Distributions for the e^+e^- channel showing the spin-correlation analysis observables in the Drell-Yan control region. The selection cuts for this region are described in Section 5.7.1.
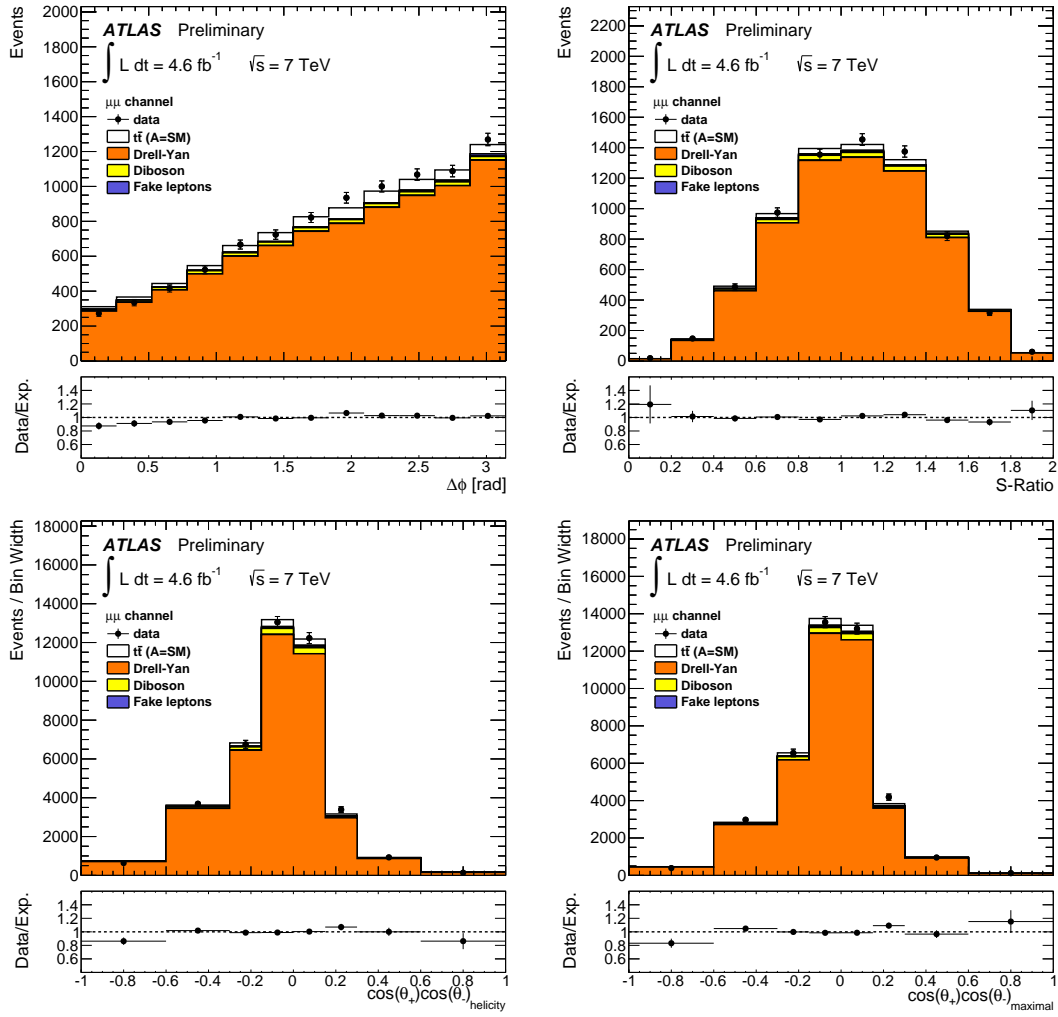
Figure 5.5: Distributions for the $\mu^+\mu^-$ channel showing the spin-correlation analysis observables in the Drell-Yan control region. The selection cuts for this region are described in Section 5.7.1.

	e^+e^-	$\mu^+\mu^-$	$e^\pm\mu^\mp$
Z+jets (DD)	20.7 ± 1.8	82.6 ± 4.2	-
$Z(\to \tau\tau)$+jets (MC)	18.1 ± 1.8	67.2 ± 3.8	172.1 ± 5.8
Fake leptons (DD)	19.8 ± 7.2	29.2 ± 3.5	100.6 ± 14.9
Single top (MC)	30.6 ± 1.9	82.5 ± 3.1	224.3 ± 5.1
Diboson (MC)	22.5 ± 1.0	60.3 ± 1.6	174.3 ± 2.8
Total (non-$t\bar{t}$)	111.7 ± 7.9	321.8 ± 7.5	671.3 ± 17.0
$t\bar{t}$ (MC)	609.6 ± 5.8	1747.3 ± 9.7	4608.6 ± 15.8
Expected	721.3 ± 9.8	2069.1 ± 12.3	5279.9 ± 16.3
Observed	736	2057	5320

Table 5.11: Number of observed events in Data and MC in the dilepton $t\bar{t}$ selection after Top Root Core update. Backgrounds estimated from Monte Carlo are indicated with (MC), whereas backgrounds estimated by data-driven techniques are indicated with (DD). Quoted uncertainties are the quadrature sum of statistical uncertainties on the yield.

and prediction. Figure 5.3 presentes the same distributions but in the $\mu^+\mu^-$ channel. The observed performance is the same as for the e^+e^- channel. All distributions in data are described well by the prediction.

In Figs. 5.4 and 5.5, the experimental observables that are sensitive to spin correlation are presented in this control region[1]. In Fig. 5.4 the distributions for the $\Delta\phi$, S-Ratio, $cos(\theta_+)cos(\theta_-)_{helicity}$, and $cos(\theta_+)cos(\theta_-)_{maximal}$ are presented in the e^+e^- channel. The observables in this control region are well described by the prediction and no significant deviations between the expected and observed shapes are seen. In Fig 5.5 the same experimental observables are shown in the $\mu^+\mu^-$ channel. As for the e^+e^- case, the data are well described by the prediction and no significant deviations are observed.

In summary, the predictions in the control region agree well with the observed data. The dominant $Z/\gamma^* \to \ell^+\ell^-$ process in this control region is well modelled in both kinematic distributions of the event and in the experimental observables themselves.

5.7.2 $t\bar{t}$ Signal region

Figures 5.6 to 5.12 show comparisons between simulated events and observed events in the signal region. In all figures, the colour and style convention for the various processes are described using the convention in Fig. 5.1.

Figure 5.6 shows a comparison between expected and observed events for the dis-

---

[1]The presentation of experimental observables in the Drell-Yan control region differs slightly from the others. Those distributions that are publicly available outside of the ATLAS collaboration are presented in the same style in which they appear in the public document. Such distributions include the title "ATLAS Preliminary". The selections for these plots are identical to those without the "ATLAS" title. They only differ in the style of their presentation.
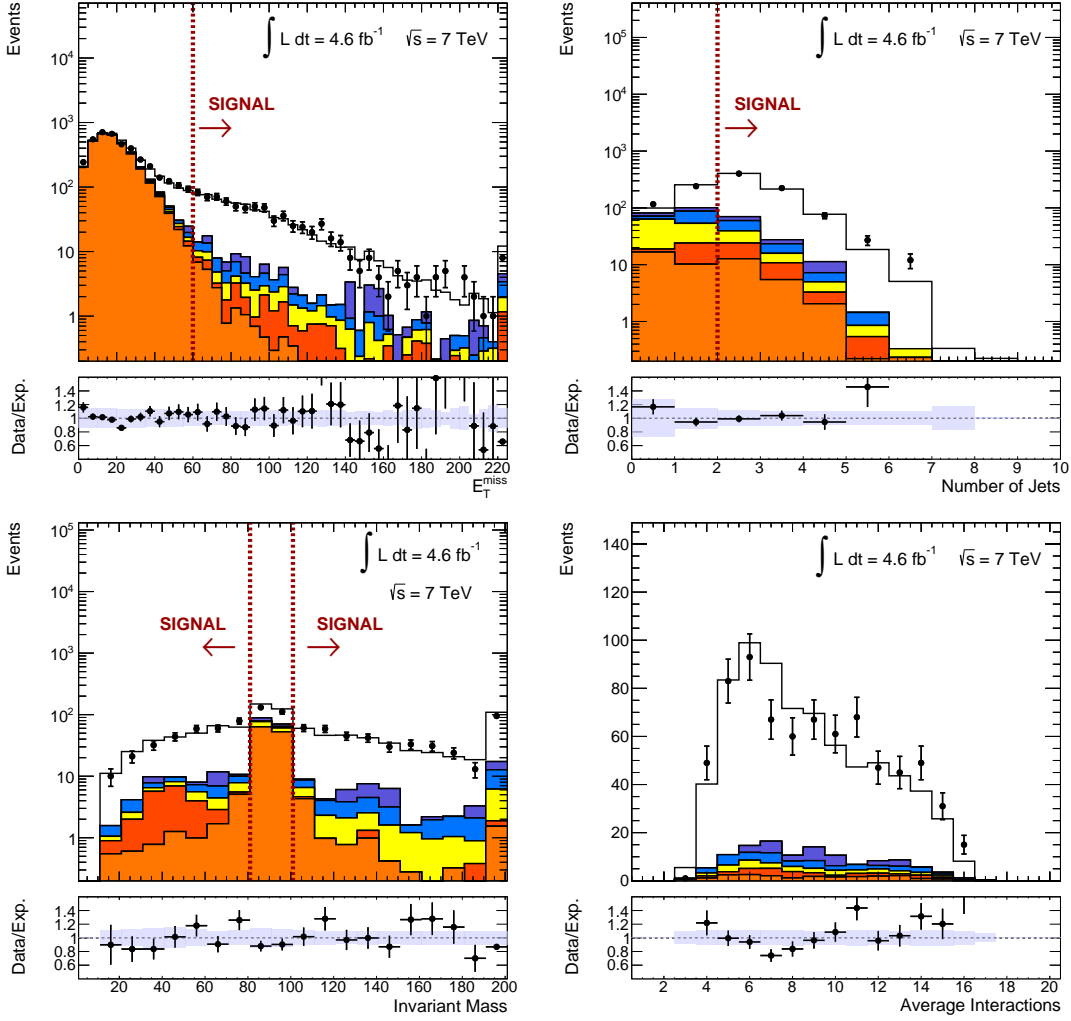
Figure 5.6: Simulation compared to data in the signal region, described in Section 5.4 for the e^+e^- channel. The distributions for E_T^{miss}, jet multiplicity, dilepton invariant mass and the average number of interactions per bunch crossing (μ) are shown *top left*, *top right*, *bottom left* and *bottom right*, respectively. In the distributions for E_T^{miss} jet multiplicity and dilepton invariant mass, the cuts that are usually applied to these variables in the signal region have been removed to illustrate their effect. The events that would normally be selected in the signal region are indicated with the red dashed lines and arrows.
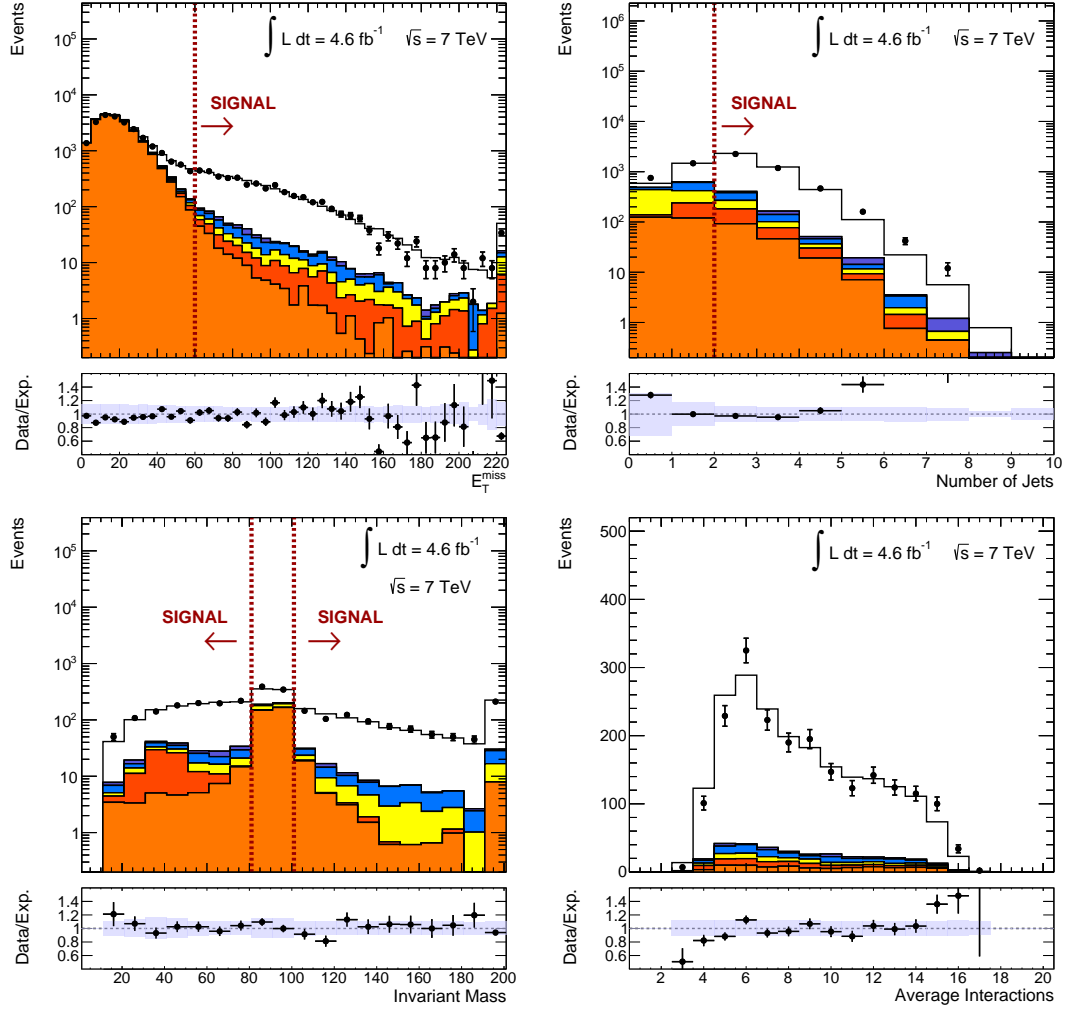
Figure 5.7: Simulation compared to data in the signal region, described in Section 5.4 for the $\mu^+\mu^-$ channel. The distributions for $E_{\mathrm{T}}^{\mathrm{miss}}$, jet multiplicity, dilepton invariant mass and the average number of interactions per bunch crossing (μ) are shown *top left, top right, bottom left* and *bottom right*, respectively. In the distributions for $E_{\mathrm{T}}^{\mathrm{miss}}$ jet multiplicity and dilepton invariant mass, the cuts that are usually applied to these variables in the signal region have been removed to illustrate their effect. The events that would normally be selected in the signal region are indicated with the red dashed lines and arrows.
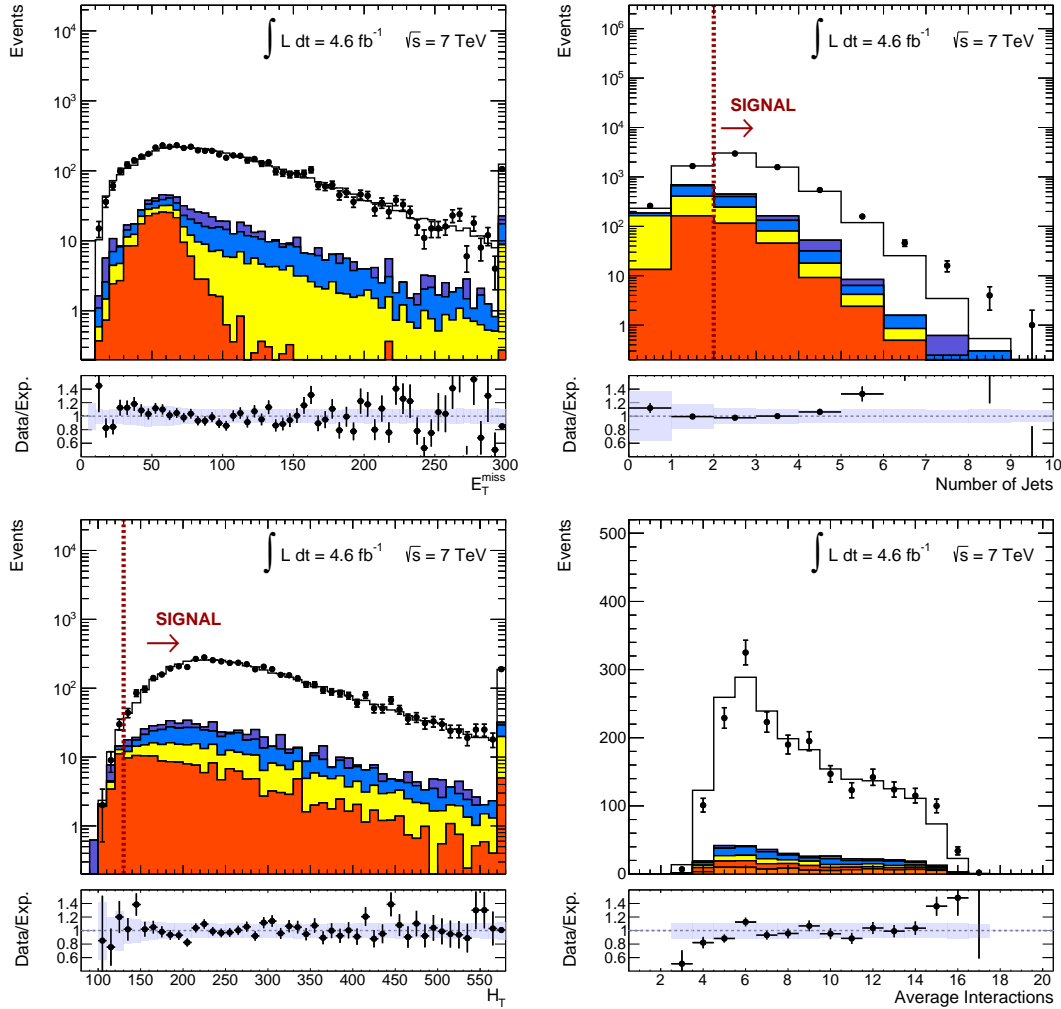
Figure 5.8: Simulation compared to data in the signal region, described in Section 5.4 for the $e^{\pm}\mu^{\mp}$ channel. The distributions for E_T^{miss}, jet multiplicity, H_T and the average number of interactions per bunch crossing (μ) are shown *top left, top right, bottom left* and *bottom right*, respectively. In the distributions for jet multiplicity and H_T, the cuts that are usually applied to these variables in the signal region have been removed to illustrate their effect. The events that would normally be selected in the signal region are indicated with the red dashed lines and arrows.
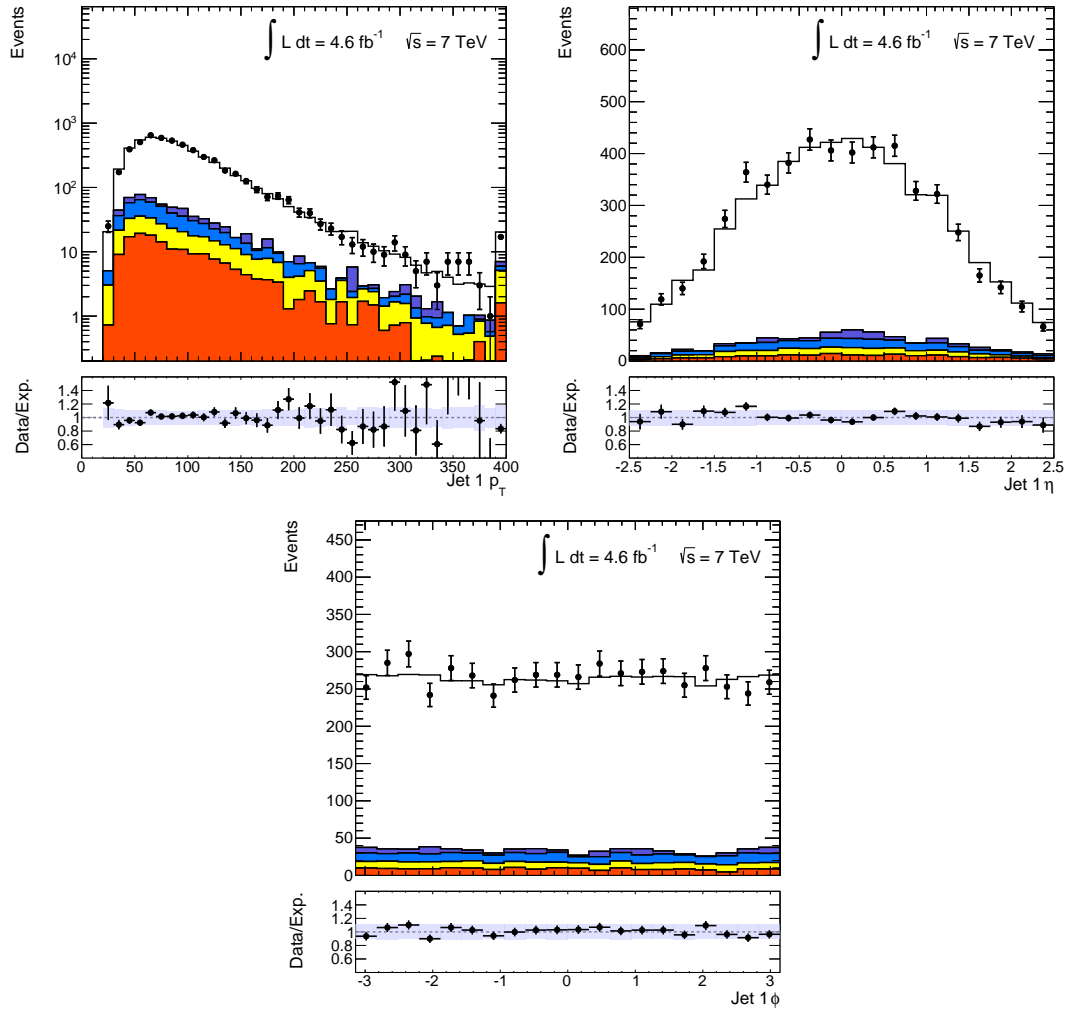
Figure 5.9: Distribution of the leading jet p_T, η, and ϕ distributions in the $e^{\pm}\mu^{\mp}$ channel in the signal region, described in Section 5.4.
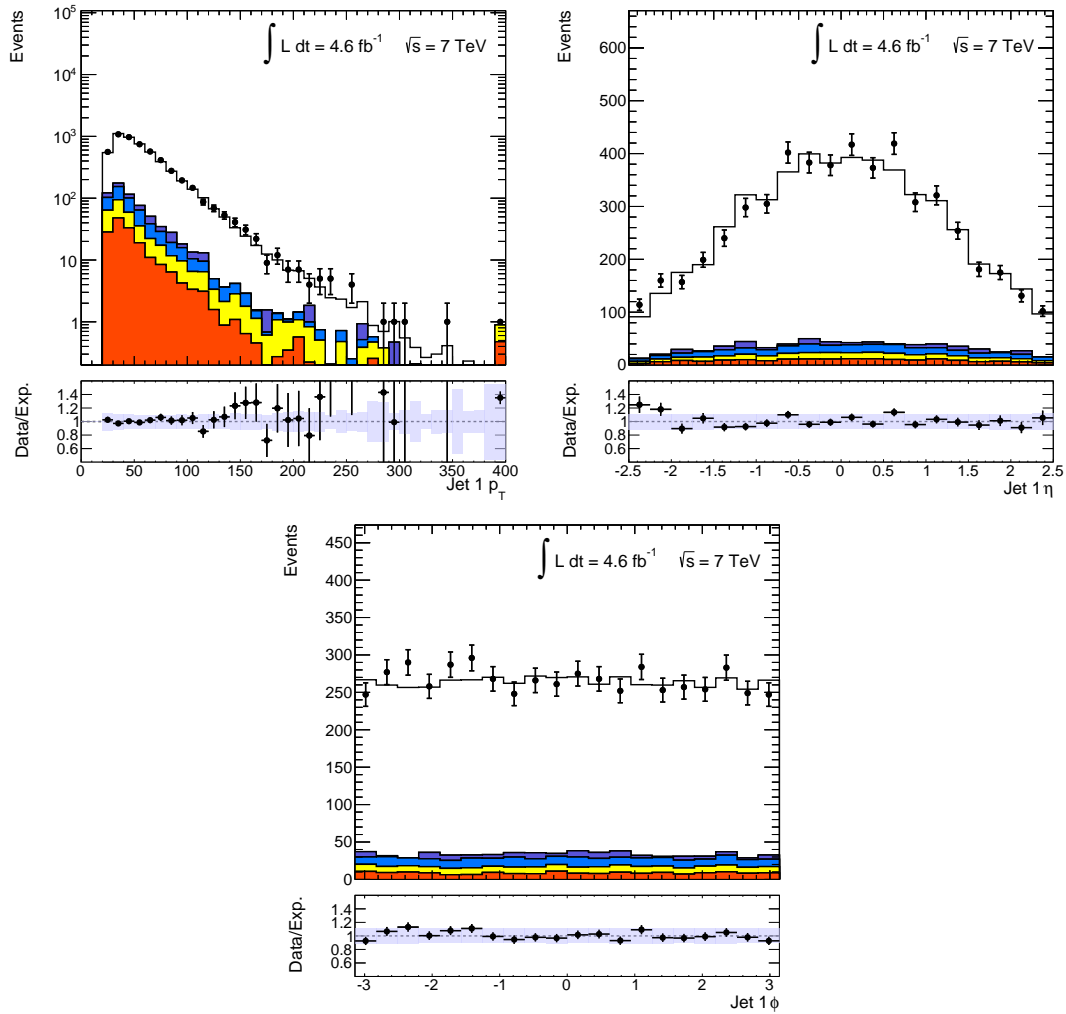
Figure 5.10: Distribution of the sub leading jet p_T, η, and ϕ distributions in the $e^{\pm}\mu^{\mp}$ channel in the signal region, described in Section 5.4.
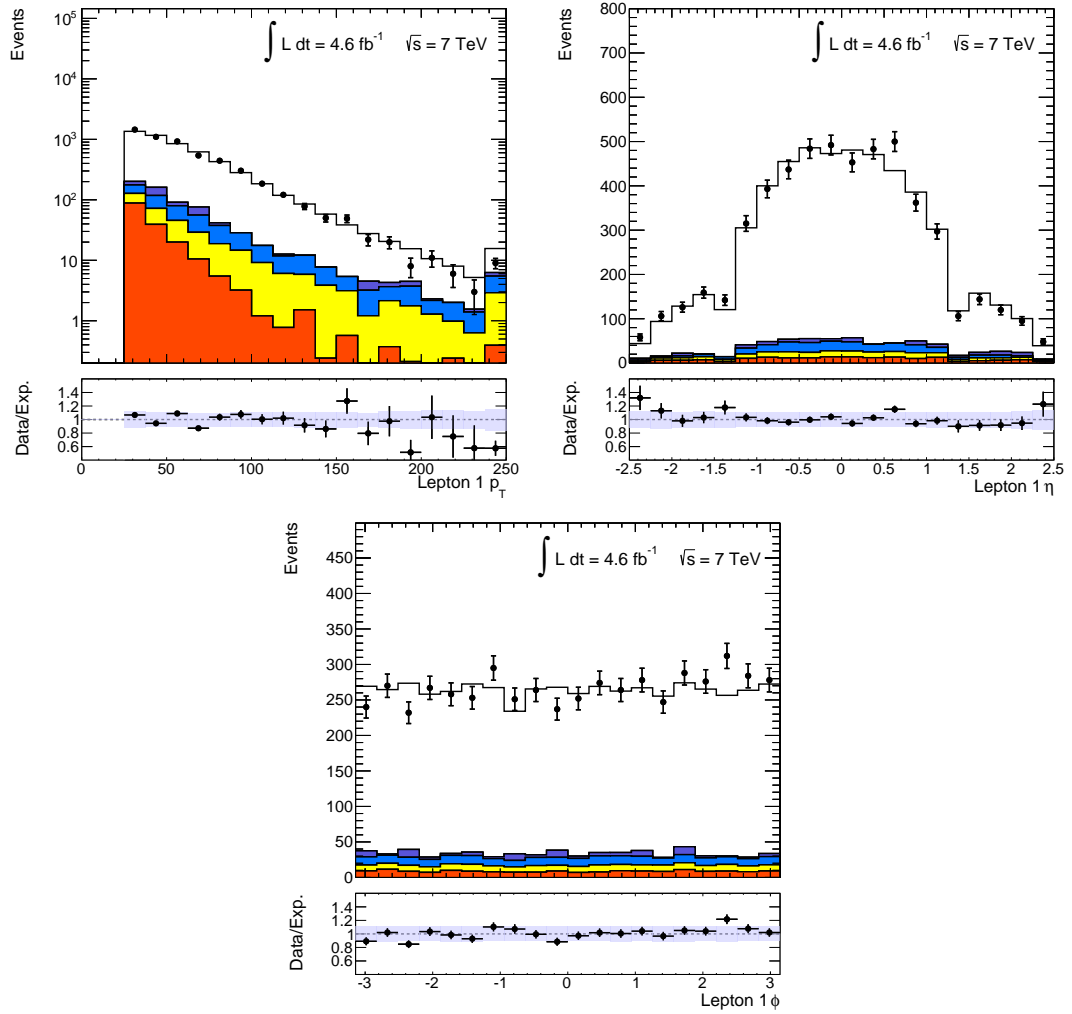
Figure 5.11: Distribution of the electron p_T, η, and ϕ distributions in the $e^{\pm}\mu^{\mp}$ channel in the signal region, described in Section 5.4.
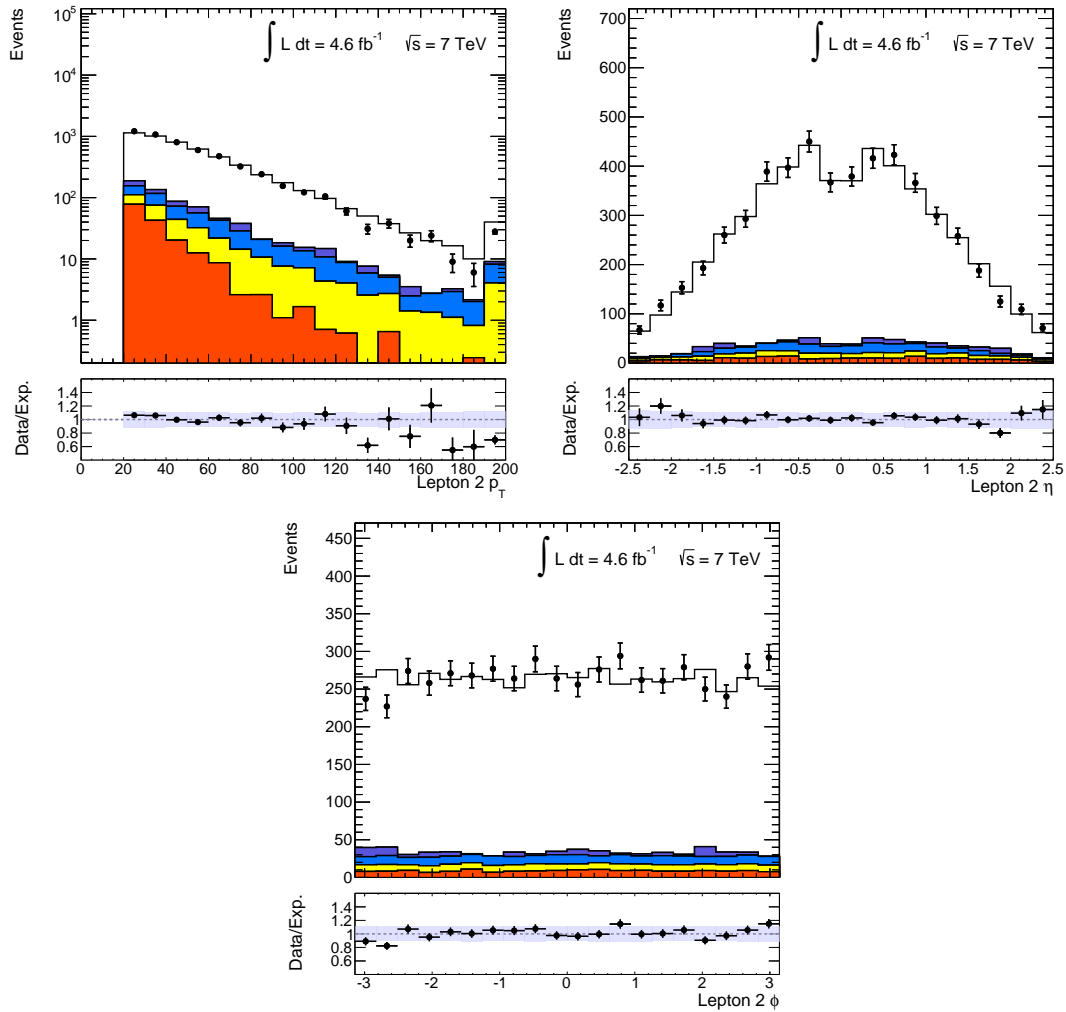
Figure 5.12: Distribution of the muon p_T, η, and ϕ distributions in the $e^{\pm}\mu^{\mp}$ channel in the signal region, described in Section 5.4.

tributions of E_T^{miss}, jet multiplicity, the invariant mass of the dilepton pair, and the number of average interactions per bunch crossing. For each of these distributions, with the exception of the average number of interactions per bunch crossing, the cut used to select signal events in that distribution has been relaxed to indicate the effectiveness of the cut. For example, in the distribution of dilepton invariant mass, it is clear that the signal cut is highly efficient and removes a large amount of Z/γ^* events at only a small cost in signal events. Similar behaviour is observed in the jet multiplicity and E_T^{miss} distributions. In the jet-multiplicity distribution, a deviation between the observed data and prediction can be seen at five or more jets. This feature is found to be caused by the MC@NLO generator, which underestimates the number of jets. The effect of this underestimation is quite mild and the bulk of the data is well described by the prediction. The expected number of events and observed number of events for this channel are presented in Table 5.11 along with their associated normalisation uncertainties. The expected number of events agrees with the observed within the quoted uncertainties. With the exception of the high jet multiplicity, the e^+e^- channel appears to be well described by the prediction.

Figure 5.7 shows the same distributions as for the e^+e^- channel in the $\mu^+\mu^-$ channel, where the signal region is indicated in distributions where a particular selection cut has been relaxed. The observed and expected events agree very well in the E_T^{miss} dilepton invariant mass and average number of interactions per bunch crossing distributions. In the jet multiplicity distribution the data at five or more jets is, once again, poorly described. The number of observed events in this region is small compared to the channel overall and the effect on the general modelling of the channel appears to be minimal. The expected number of events and observed number of events for the $\mu^+\mu^-$ channel are presented in Table 5.11 along with their associated normalisation uncertainties. Once again, the expected number of events agrees well with the observed to within the quoted uncertainties. With the exception of the high jet multiplicity, the $\mu^+\mu^-$ channel also appears to be well described by the prediction.

Figure 5.8 shows the distributions of E_T^{miss}, jet multiplicity, H_T and the average number of interactions per bunch crossing in the $e^\pm\mu^\mp$ channel in data and simulation. In the case of the $e^\pm\mu^\mp$ channel, there is no selection cut on the E_T^{miss} and the entire distribution corresponds to the signal region. The E_T^{miss} is well described in this channel with no contribution form $Z/\gamma^* \rightarrow e^+e^-$ or $\mu^+\mu^-$ and only a small contribution from $Z/\gamma^* \rightarrow \tau^+\tau^-$ in the E_T^{miss} region. The H_T distribution also shows good agreement between observed and expected events. The cut applied to define the signal region for H_T is highly efficient, removing only a small number $t\bar{t}$ events whilst suppressing some contributions from $Z/\gamma^* \rightarrow \tau^+\tau^-$ and fake leptons. As with the e^+e^- and $\mu^+\mu^-$ channel, MC@NLO fails to describe the high jet multiplicities. However, this remains a mild effect in only a small fraction of events. The expected number of events and observed number of events for the $e^\pm\mu^\mp$ channel are presented in Table 5.11 along

with their associated normalisation uncertainties. As with the other two channels, the expected number of events agrees well with the observed to within the quoted uncertainties.

Figures 5.9 and 5.9 show the distributions in the $e^{\pm}\mu^{\mp}$ channel of the leading and sub-leading jet p_T, η, and ϕ, respectively. The modelling of the jets appears to be very well described by simulation and no deviations between observed and expected distributions are observed. Similarly, Figs 5.11 and 5.12 show the distributions in the $e^{\pm}\mu^{\mp}$ channel of the electron and muon p_T, η, and ϕ, respectively. Excellent agreement between data and expectation is observed for both electrons and muons. The difference between the η modelling for electrons and muons can also be seen, and is described well by the simulation.

Table 5.11 shows the expected number of events compared to the observed number of events. The $e^{\pm}\mu^{\mp}$ channel had the highest selection statistics, followed by $\mu^{+}\mu^{-}$ and finally the $e^{+}e^{-}$ channel. The different statistical power of the channels occurs because the $e^{+}e^{-}$ and $\mu^{+}\mu^{-}$ channel included cuts to suppress Drell-Yan background that are not needed in the $e^{\pm}\mu^{\mp}$ channel. Hence, the $e^{+}e^{-}$ and $\mu^{+}\mu^{-}$ channel have lower statistics than the $e^{\pm}\mu^{\mp}$ channel. The $e^{+}e^{-}$ channel also has much lower statistics than the $\mu^{+}\mu^{-}$ channel. This is caused by the isolation cuts for electrons, which are much tighter than those for muons, in order to suppress fake electrons. The result is lower statistics for the $e^{+}e^{-}$ channel when compared to the $\mu^{+}\mu^{-}$ channel.

In summary, in the signal region, the data is well described by the simulation in all three channels. Small effects due to the choice of signal generator are observed in the jet multiplicity distributions, but the effect is negligible on overall agreement between the observed and the expected distributions.

Chapter 6

Full kinematic reconstruction

The goal of the kinematic reconstruction is to find the top and anti-top four vectors in order to build the S-Ratio and $cos(\theta_+)cos(\theta_-)$ variables. We use the decay products of the top quarks that are observable in each event, the leptons and b-jets. The neutrinos cannot be observed directly and this must be accounted for in some way in the reconstruction method. An additional uncertainty arises due to the lack of jet charge information. It is not possible to know if a jet comes from the top or the anti-top which much also be accounted for in some way. Dilepton $t\bar{t}$ events contain two neutrinos from the W boson decays. These neutrinos do not interact with the detector; however, their presence is inferred by missing transverse energy in the event. This quantity can only be measured in the transverse direction, $E_{\mathrm{T}}^{\mathrm{miss}}$, and the neutrinos momenta in the z direction must be derived by other means. In the dilepton channel there are two neutrinos but only one measurement for the sum of their transverse momenta, leading to an under-constrained system. One may define a number of kinematic constraints on the properties of the $t\bar{t}$ system using measured values and physical assumptions and use these to solve the under-constrained system. The dilepton final state has 16 observable quantities relevant to reconstruction; the reconstructed four momenta of the charged leptons and b quark jets,

$$
\begin{aligned}
m_W &= (p^l + p^\nu)^2 \\
m_t &= (p^l + p^\nu + p^b)^2
\end{aligned}
\tag{6.1}
$$

and the following quantities are also known;

$$
\begin{aligned}
m_b &= 4.5 \text{ GeV} \\
m_W &= 80.4 \text{ GeV} \\
m_t &= 172.5 \text{ GeV} \\
m_l &\approx 0.0 \text{ GeV} \\
m_\nu &\approx 0.0 \text{ GeV} \\
p_T(\nu_1) + p_T(\nu_2) &= E_T^{\text{miss}}
\end{aligned}
\tag{6.2}
$$

There are a total of 24 unknowns arising from the dilepton final state: the four vectors of the six particles. The masses of each of these particles are known and the momentum of the jets and leptons are measured. The neutrinos are undetected, leaving 8 unknown parameters. However, the sum of their transverse momenta is measured as missing transverse energy in the event, leaving only four undetermined quantities. By introducing assumptions on the mass of the top quark and W boson it is possible to solve the system. Further complications arise from the lack of jet charge information, without which a two-fold ambiguity in the pairing of the leptons and jets is introduced. It is also possible not to use the observed sum of the missing transverse energy but instead to use assumed values for η_ν which also allows the system to be solved. Two algorithms are investigated implementing both methods. The Neutrino Weighting algorithm uses assumptions on η_ν and was implemented and developed as part of this Thesis. The Topology method uses the E_T^{miss} directly to solve the system and is investigated for comparison.

6.1 Neutrino Weighting

Neutrino Weighting is a reconstruction algorithm designed to resolve ambiguities inherent to $t\bar{t}$ events with two neutrinos in the final state. It provides the user with reconstructed top quark and neutrino four momenta [68]. The algorithm uses the measured four vectors of the leptons and jets but not the observed E_T^{miss}. To solve the system, the neutrino pseudo-rapidities are assigned assumed values taken from MC simulations.

Figure 6.1 shows the neutrino pseudo-rapidity in $t\bar{t}$ MC. The distribution can be well modelled with a Gaussian distribution with a mean of zero and unit width. The distribution of the neutrino pseudo-rapidities is found to be independent of spin correlation. By rearranging Equation 6.1 and using the assumptions in Equation 6.2 it is possible to derive two polynomial equations that describe the neutrino four momenta, one for each neutrino. In the Neutrino Weighting algorithm the equations for the neu-
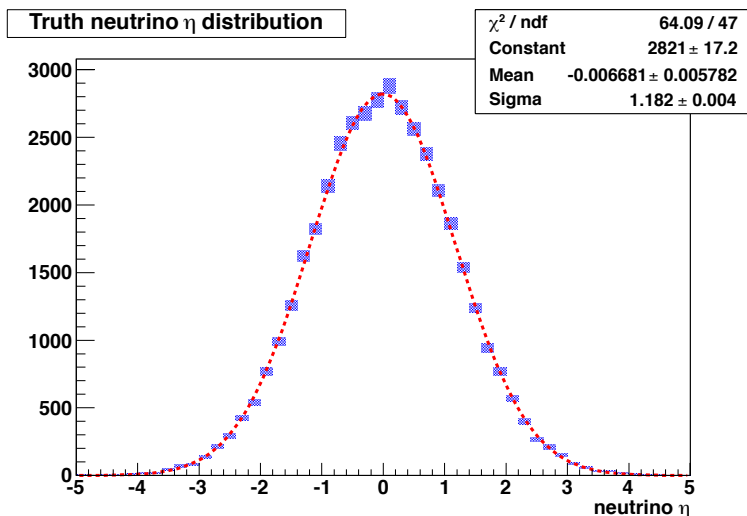
Figure 6.1: Distribution of neutrino pseudo-rapidities in MC@NLO $t\bar{t}$ with a fitted Gaussian distribution.

trino four vectors are solved many times for many different assumptions of neutrino η. In each event, a random η is generated for each neutrino using the Gaussian distribution derived from Monte Carlo in the range $-4.0 < \eta < 4.0$. This procedure is repeated 50 times per event and is found to be more effective than previous methods of performing a linear scan of fixed points [**?**]. Using these assumptions, the number of solutions per neutrino η_1, η_2 is 8: two from the ambiguity of the lepton-jet pairing and four (per pairing) from quadratic terms in the neutrino solution. Summing over the 50 solutions per neutrino gives a total of 400 solutions per event.

Thus far, the measured E_T^{miss} has not been used in the reconstruction and 400 solutions have been obtained with no information on which solution most accurately reflects the true neutrino four vectors. The measured E_T^{miss} may now be utilised as a way to weight each solution based on how well the reconstructed neutrinos agree with the observed E_T^{miss} using the weighting function:

$$ w = \sum_{\eta_1, \eta_2} \sum_{solutions} \exp\left(-\frac{\left(\not{E}_x^{calc} - \not{E}_x^{obs}\right)^2}{2\sigma_{\not{E}_{x/y}}^2}\right) \exp\left(-\frac{\left(\not{E}_y^{calc} - \not{E}_y^{obs}\right)^2}{2\sigma_{\not{E}_{x/y}}^2}\right), \qquad (6.3) $$

where $\sigma_{\not{E}_{x/y}}$ is the resolution of the x or y component of missing transverse energy [69], $\not{E}_x^{calc}$ and $\not{E}_y^{calc}$ are the missing transverse energies in the x/y direction, calculated in the solution by taking the transverse momenta of the two neutrino solutions. $\not{E}_x^{obs}$, $\not{E}_y^{obs}$ are the observed missing transverse energies observed in the event in the x and y directions. The resolution is the same for the x and y direction and is measured in 7 TeV data and MC [70]. From these studies, the resolution is chosen to be $0.66\sqrt{\Sigma E_T}$ in both data and MC, where ΣE_T is the sum of all transverse energy in the event, and is shown in Fig. 6.2. In a test performed where this resolution is varied by 10% to

account for the differences observed in MC compared to data, no significant effect is noted in the reconstruction. The weight distribution for an example event is shown in Fig. 6.3. The weight distribution peaks close to the true values for two neutrino η's in well reconstructed events.

Two methods are investigated for selecting the final neutrino four momenta. Either the solution with the highest weight is chosen or the weighted average of all solutions is taken; the latter typically performed better in expected statistical sensitivity studies. An incorrect lepton-jet pairing or neutrino η assumption can give a very high weight for a given solution. When taking only the highest weighted solution, information from other solutions that may more accurately reflect the true neutrino η's are discarded, even if their weights are almost as high as the highest weighted solution. When taking the weighted average of all solutions, the other solutions help to obtain a better estimate of the true kinematics. A study of the expected sensitivity of the analysis variables is presented in Tab. 6.1 where it is clear that the weighted average of all solutions outperformed the solution with the highest weight.

In the case where there are more than two selected jets in an event, all possible lepton-jet pairings are considered and the weighted average of all solutions is taken.

6.1.1   Jet Smearing

In approximately 15% of $t\bar{t}$ events it is not possible to find a non-complex solution to the polynomials describing the neutrino p_z. This is caused by the finite η sampling for the neutrinos and the resolution of the reconstructed objects. Smearing is performed on the jet energies to account for these resolution effects. Jet energies are smeared fifty times for each assumption of $\eta_1\eta_2$ within the measured energy resolution of the jet [71] and for each smearing the neutrino weight is recalculated. The same could be considered for leptons, but at ATLAS the lepton energy resolution is orders of magnitude better than the jet energy resolution and this is not considered. This smearing is performed for each neutrino η assumption, not only for those in which a non-complex solution could be found. By smearing the jets, the number of unsolvable events drops from 15% to less than 5%.
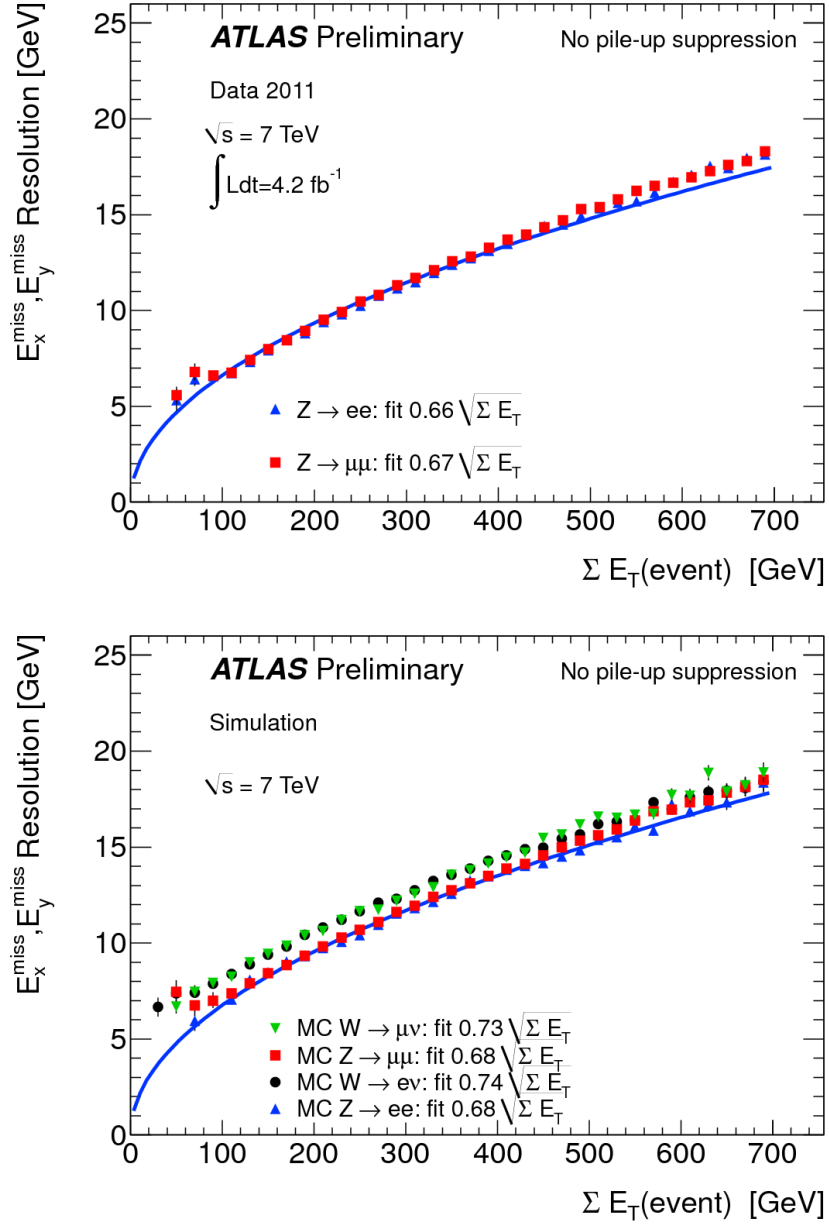
Figure 6.2: E_T^{miss} resolution in 2011 data at 7 TeV *(top)* and in MC *(bottom)* [70]. In data the resolution is measured using $Z \rightarrow e^+e^-$ and $Z \rightarrow \mu^+\mu^-$ events. In MC the resolution is measured in leptonically decaying Z events and also in leptonically decaying W events.
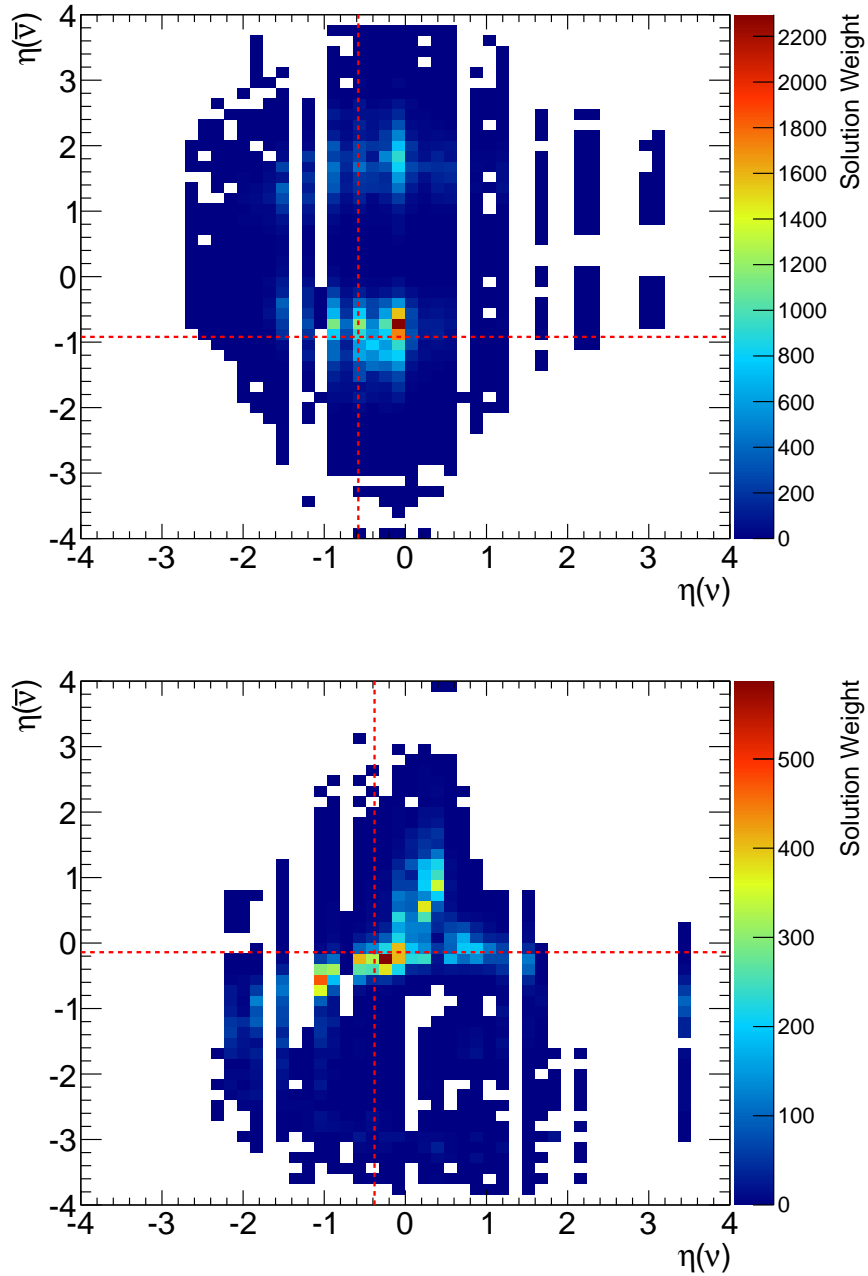
Figure 6.3: Weight distributions for neutrino weighting solutions for two example events. True values for the neutrino η are indicated with the red dashed lines. The x and y axis are the neutrino η used in the solution and the colour corresponds to the weight of the solution found at a particular point. Bins with weights less than 10^{-6} are shown as empty.

Variable	Weighted average	Maximum weight
$\Delta\phi$	0.080	n/a
S-Ratio	0.102	0.121
$cos(\theta_+)cos(\theta_-)_{helicity}$	0.199	0.269
$cos(\theta_+)cos(\theta_-)_{maximal}$	0.132	0.211

Table 6.1: Expected Statistical uncertainty of the weighted average analysis variables compared to the maximal weighted solution analysis variables. The sensitivity is calculated using 1000 pseudo experiments in the combined channel fit described in Section 7.1

.

6.2 Topology

Topology uses the E_T^{miss} in the reconstruction directly, using similar constraints as Neutrino Weighting, leading to only 8 possible solutions per event. Leptons are paired to jets based on the combination that gives the lowest invariant mass for the lepton-jet pair as this has been shown to be the most likely pairing, illustrated in Fig. 6.4. Using the E_T^{miss} and assumptions on the top and W mass, the system is solved for both neutrino and anti-neutrino four vectors. If there are multiple real solutions then the result is chosen that minimises the neutrino and anti-neutrino transverse momentum. If there are no possible real solutions the top mass assumption is varied between 157.5 GeV and 187.5 GeV in steps of 1.5 GeV. If there are still no non-complex solutions then other lepton-jet pairs are tested [72] [68].

The Topology reconstruction algorithm is optimised for a two jet exclusive selection; however, the algorithm was extended for this thesis to consider the two or more jets inclusive scenario.
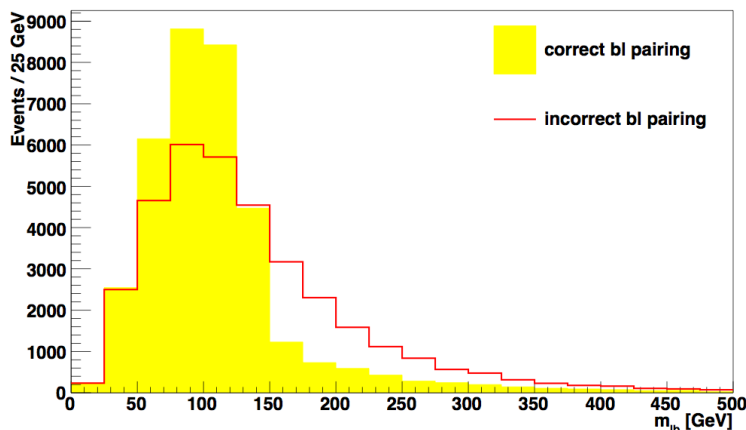
Figure 6.4: Invariant mass distribution for lepton-jet pairings. The correct pairing is shown in yellow, the incorrect pairing is shown in red.

6.3 Performance

In order to compare the advantages and disadvantages of Neutrino Weighting with other reconstruction algorithms a set of parameters is defined that are common to each. The parameters are expressed as efficiencies based on how well the reconstructed particles describe the underlying truth particles in Monte Carlo simulation. These efficiencies are used to categorise events where the reconstruction describes the underlying truth information well (matched) and events where the reconstruction describes the truth information poorly (unmatched).

130

In this analysis the direction of the top quarks is the most crucial reconstructed quantity and events are categorised as matched and unmatched based on how well the top directions are described by the reconstruction. The variable;

$$\Delta R(t\bar{t}) = \sqrt{\Delta\phi(t\bar{t})^2 + \Delta\eta(t\bar{t})^2} \qquad (6.4)$$

is defined to be the distance in $\eta - \phi$ space of the reconstructed top and anti-top four vectors and the true four vectors in the MC. If this value is less than 0.4 for both the reconstructed top and reconstructed anti-top the event is said to be matched and if not it is categorised as un-matched. The purpose of the ΔR variable is to define a parameter with which to compare different reconstruction methods in a consistent way.

In addition to the $\Delta R(t\bar{t})$ variable, the absolute reconstruction efficiency is also studied, defined as the number of events where at least one non-complex solution could be found out of the total number of selected events.

The efficiencies are measured using the nominal $t\bar{t}$ MC@NLO sample described in Section 5.5.2 and are presented with different choices of denominator in the efficiency calculation; firstly as a fraction of the total dilepton selection before $t\bar{t}$ reconstruction (total events) and secondly as a fraction of events with at least one solution after reconstruction (solved events). The efficiencies are independent of spin correlation and agree in both MC@NLO correlated and uncorrelated samples within the statistical uncertainties.

The efficiencies for both Neutrino Weighting and Topology are shown in in Table 6.2. Neutrino Weighting had the highest reconstruction efficiency and the highest matching efficiency and is chosen as the reconstruction algorithm for this analysis.

6.4 Performance on Data

In this section the performance of the reconstruction method on the full 7 TeV dilepton sample is described in detail. In Tab. 6.3 the yields for the data, signal and background samples after full reconstruction are shown. A small suppression of backgrounds is

Efficiency	Neutrino Weighting	Topology
Total events		
Reconstruction Efficiency	96.0	82.3
$\Delta R(t\bar{t}) < 0.4$	28.5	16.1
Solved events		
$\Delta R(t\bar{t}) < 0.4$	29.7	19.6

Table 6.2: Table of Neutrino weighting and Topology reconstruction efficiencies as a function of the total number of reconstructed events and of events with at least one solution.

observed due to the reconstruction, illustrated in the efficiencies shown in Table 6.4. This suppression is not unexpected as the assumptions used in Neutrino Weighting are based on $t\bar{t}$ parameters. Distributions for the reconstructed $t\bar{t}$ system are presented in Figs. 6.5, Fig. 6.6 and Fig. 6.7. In the distribution for $t\bar{t}$ invariant mass a small fraction of events appear in the bins below 350 GeV. These are events where Neutrino Weighting incorrectly reconstructs the system at an invariant mass that is incompatible with the initial assumption of the top mass due to the smearing. Good data MC agreement is observed in all distributions.

The resolution of the analysis variables are shown in Fig. 6.8 to Fig. 6.12. Two variables are used; the difference between the truth and reconstructed variable and the normalised migration matrix where in both cases truth is defined to be the variable as measured at parton level. The migration matrix shows the percentage of events from a given truth bin in the reconstructed bin. Excellent resolution is observed in the $\Delta\phi$ variable. This is expected as this variable only depends on the lepton resolution, which is typically very good at ATLAS, and does not require full $t\bar{t}$ reconstruction. The resolution of the S-Ratio variable and the $t\bar{t}$ invariant mass is also good, with a slight tendency for very high or very low values of the S-Ratio to shift closer to 1 during the reconstruction. The resolution of the $\cos(\theta_+)\cos(\theta_-)$ variables in the Helicity and Maximal bases are not as good as for the S-Ratio or $\Delta\phi$ variable. However, these variables are much more difficult to reconstruct and have a higher dependency on good resolution of the top and anti-top four vectors. The resolution of all variables is sufficient to distinguish SM spin correlations from the uncorrelated hypothesis. This is illustrated further by the expected statistical uncertainty in Sect. 7.1.

	e^+e^-	$\mu^+\mu^-$	$e^\pm\mu^\mp$
Z+jets (DD)	9.9 ± 1.2	41.4 ± 3.1	-
$Z(\to \tau\tau)$+jets (MC)	11.3 ± 1.4	51.0 ± 3.2	148.1 ± 5.4
Fake leptons (DD)	11.1 ± 6.5	25.8 ± 3.3	92.6 ± 14.4
Single top (MC)	23.8 ± 1.7	66.7 ± 2.8	185.7 ± 4.6
Diboson (MC)	14.7 ± 0.8	40.9 ± 1.3	126.8 ± 2.4
Total (non-$t\bar{t}$)	70.8 ± 7.0	225.8 ± 6.3	553.2 ± 16.2
$t\bar{t}$ (MC)	572.9 ± 5.6	1651.1 ± 9.4	4397.6 ± 15.4
Expected	643.7 ± 9.0	1876.9 ± 1.3	4960.8 ± 22.4
Observed	668	1871	4962

Table 6.3: Yields in Data and MC in the dilepton $t\bar{t}$ selection after reconstruction. Backgrounds estimated from Monte Carlo are indicated with the (MC) suffix, whereas backgrounds estimated by data driven techniques are indicated with a (DD) suffix. Quoted uncertainties are the quadrature sum of statistical uncertainty on the yield and the normalisation uncertainty on the cross section of MC samples. The $t\bar{t}$ MC is normalised to the full NNLO cross section. The uncertainty on the DD Z+jets is fixed at $\pm$ 10%. The uncertainty on the DD Fake Leptons is only statistical.

	e^+e^-		$\mu^+\mu^-$		$e^\pm\mu^\mp$		All Channels	
	Before	After	Before	After	Before	After	Before	After
Z+jets (DD)	2.9	1.5	4.0	2.2	n/a	n/a	1.3	0.7
$Z(\to \tau\tau)$+jets (MC)	2.5	1.8	3.2	2.7	3.3	3.0	3.2	2.8
Fake Leptons (DD)	2.7	1.7	1.4	1.4	1.9	1.9	1.9	1.7
Single top (MC)	4.2	3.7	4.0	3.6	4.2	3.8	4.2	3.7
Diboson (MC)	3.1	2.3	2.9	2.2	3.3	2.6	3.2	2.4
$t\bar{t}$	84.5	89.0	84.4	88.0	87.3	88.8	86.3	88.6

Table 6.4: Percentage of selected number of events for each modelled process before and after full $t\bar{t}$ reconstruction. The percentage is calculated by normalising expected events out of the total expected events. A suppression of background contributions is observed after reconstruction.
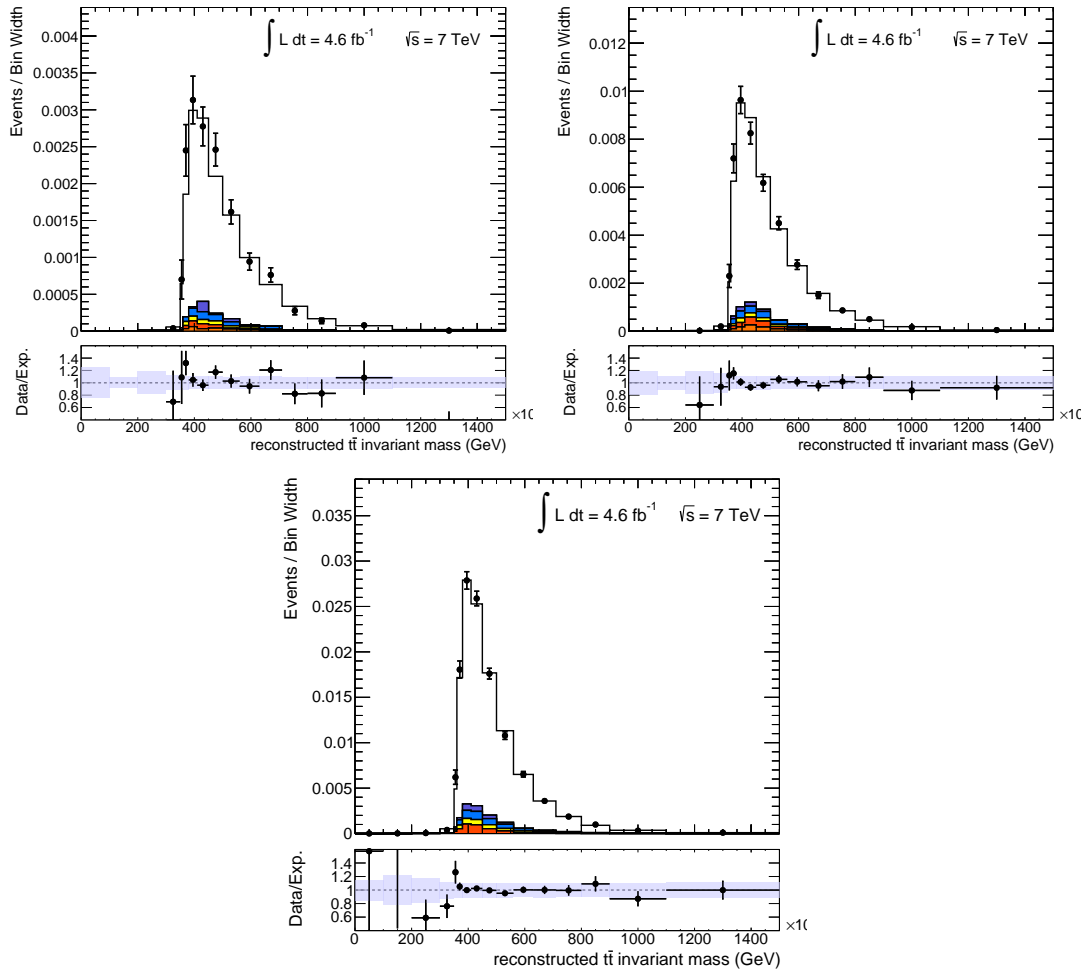
Figure 6.5: Reconstructed $t\bar{t}$ invariant mass in the e^+e^- channel *(left)*, $\mu^+\mu^-$ channel *(centre)*, and $e^{\pm}\mu^{\mp}$ channel *(right)*. The distributions use the same colour conventions as are described in Fig. 5.1.
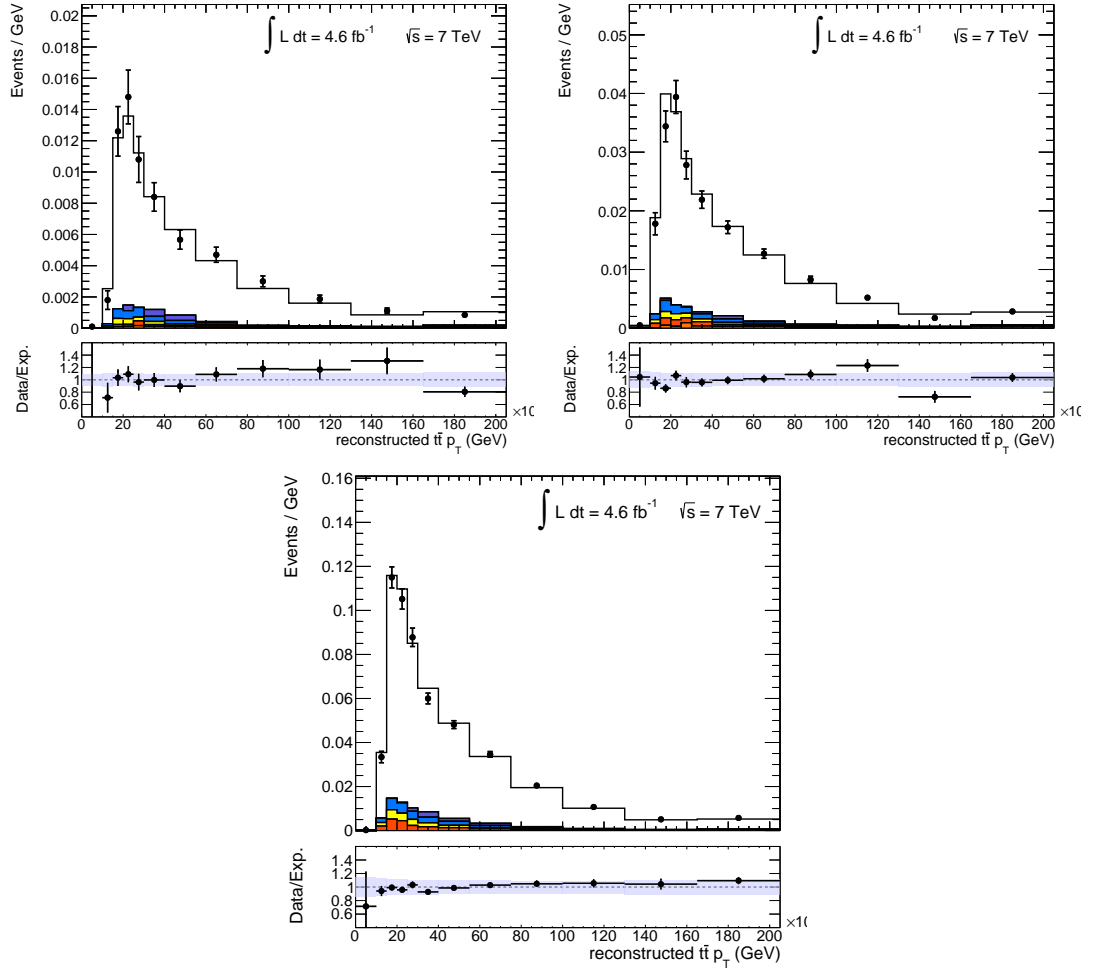
Figure 6.6: Reconstructed $t\bar{t}$ transverse momentum in the e^+e^- channel *(left)*, $\mu^+\mu^-$ channel *(centre)*, and $e^\pm\mu^\mp$ channel *(right)*. The distributions use the same colour conventions as are described in Fig. 5.1.
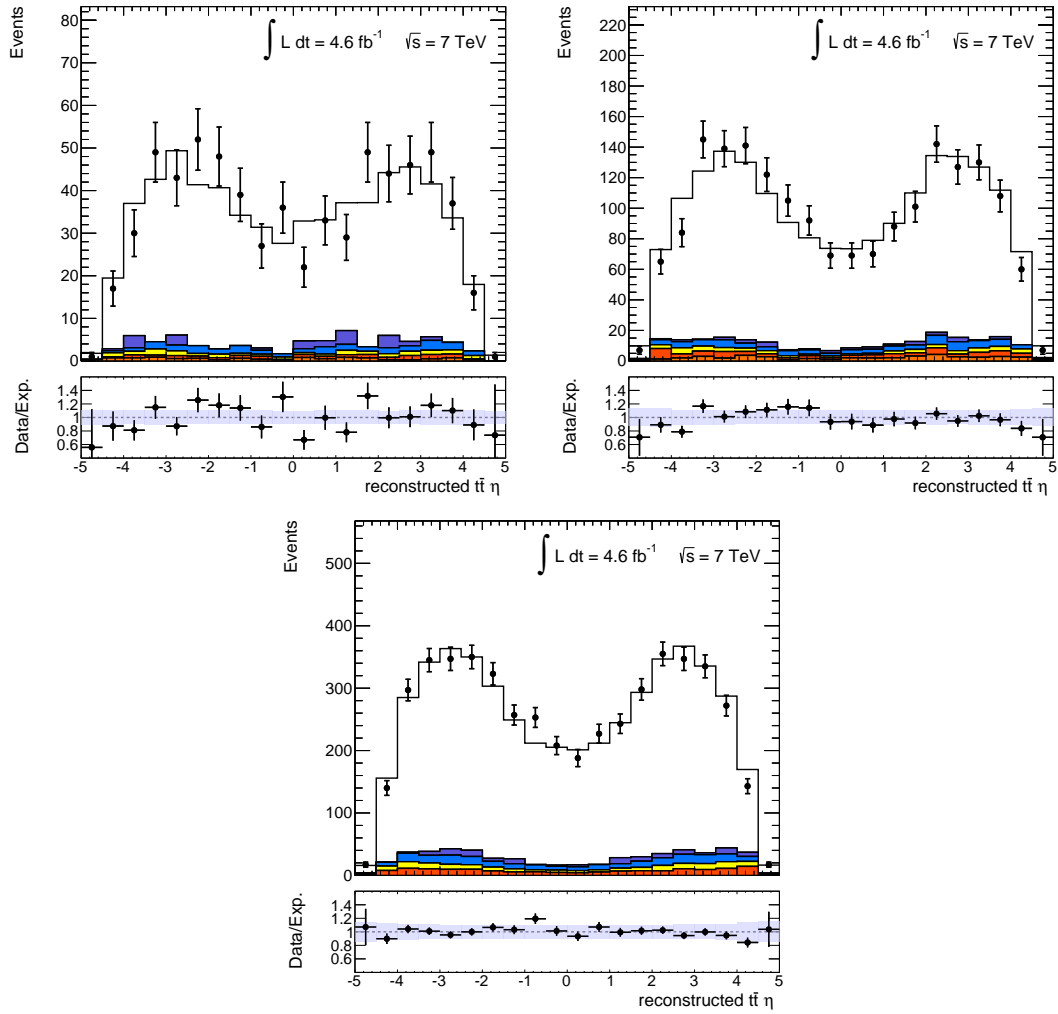
Figure 6.7: Reconstructed $t\bar{t}$ η in the e^+e^- channel *(left)*, $\mu^+\mu^-$ channel *(centre)*, and $e^\pm\mu^\mp$ channel *(right)*. The distributions use the same colour conventions as are described in Fig. 5.1.
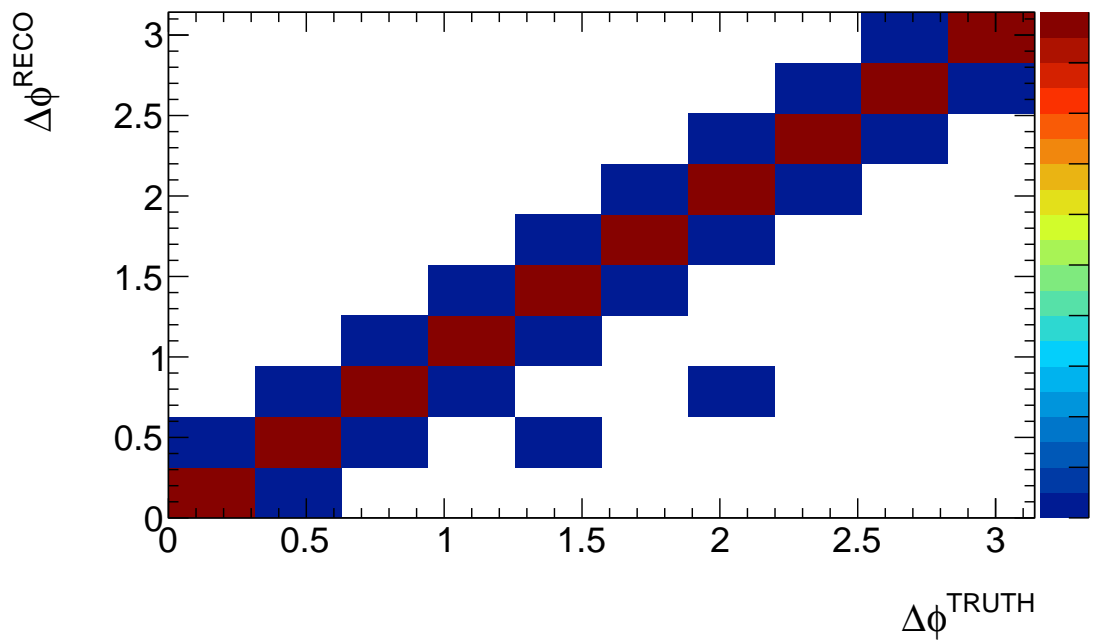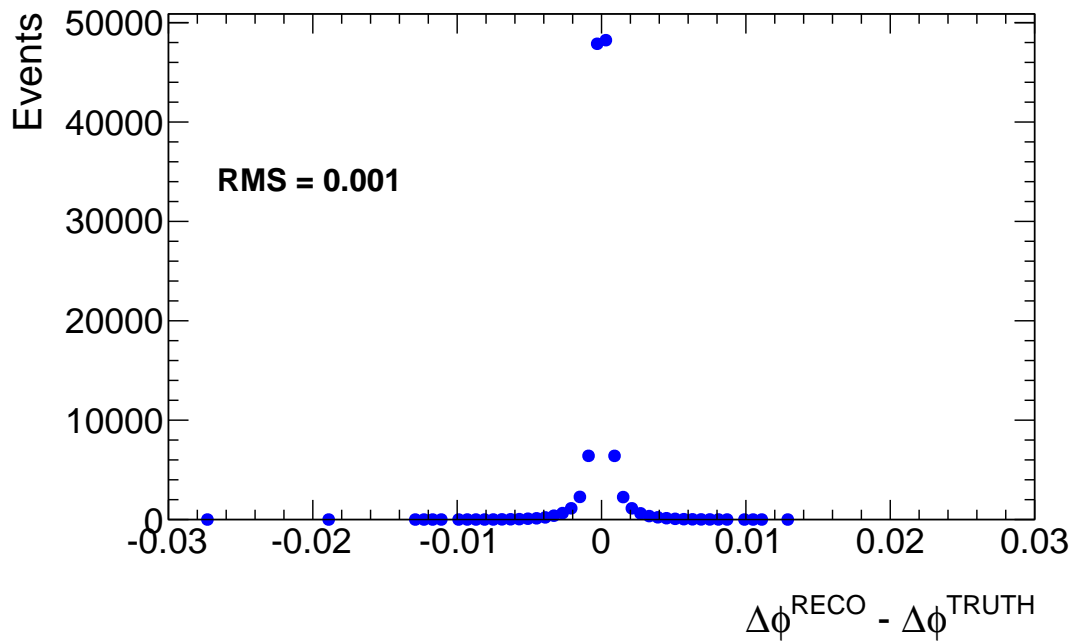
Figure 6.8: Resolution of the $\Delta\phi$ variable *(top)* and the normalised migration matrix for the $\Delta\phi$ variable *(bottom)*.
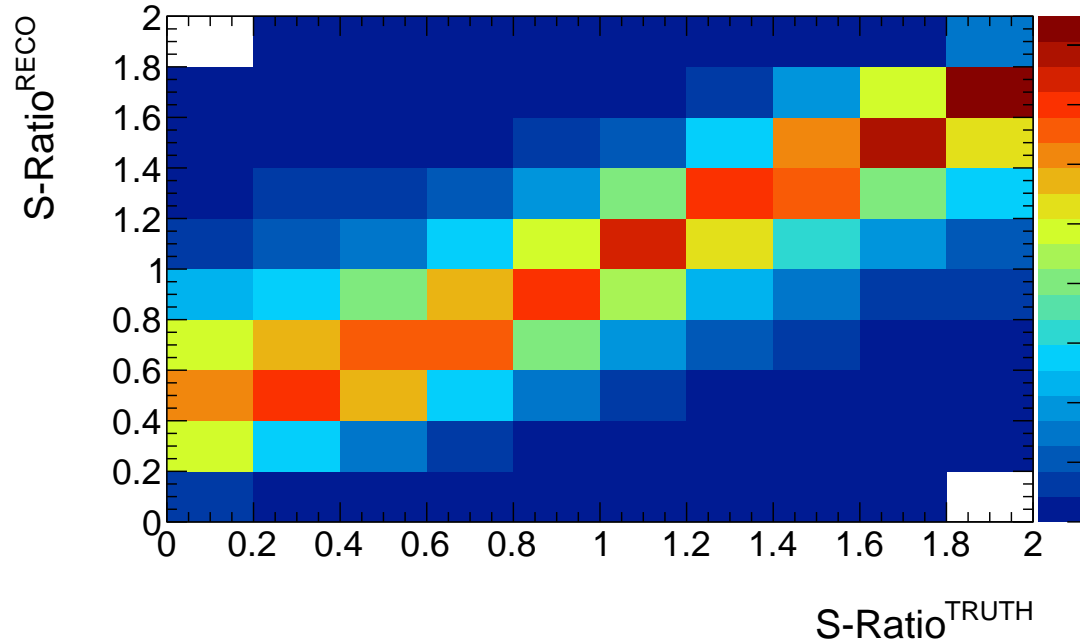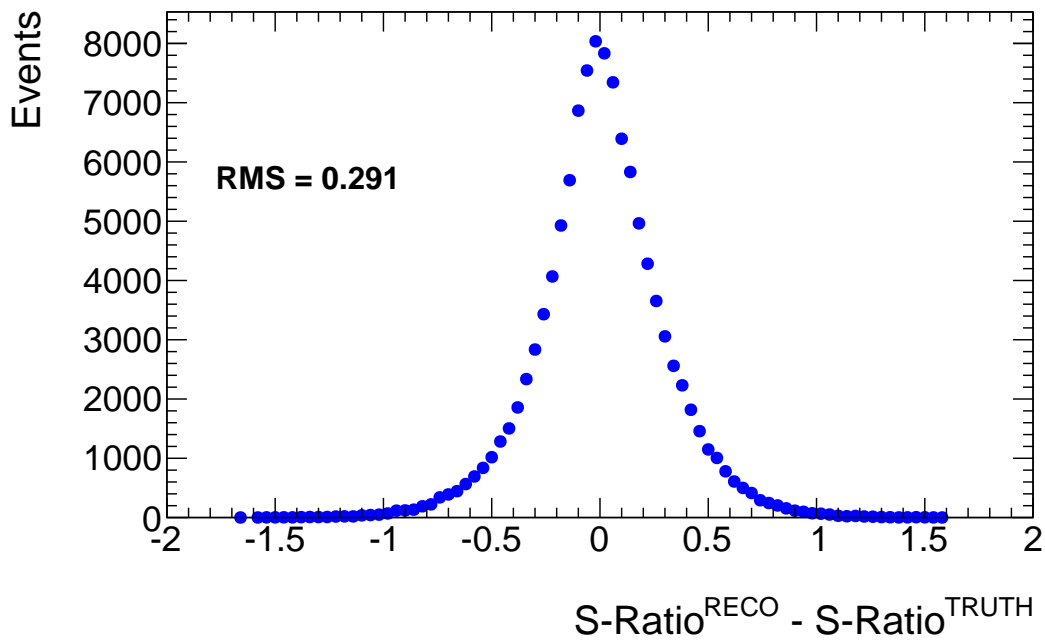
Figure 6.9: Resolution of the *S*-Ratio variable *(top)* and the normalised migration matrix for the *S*-Ratio variable *(bottom).*
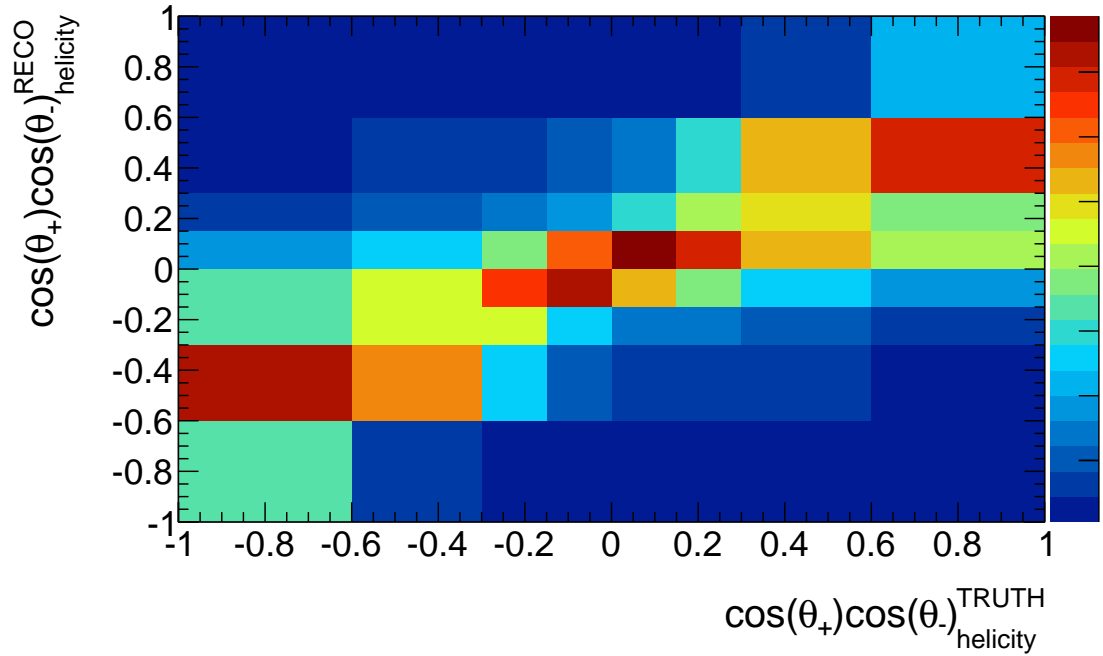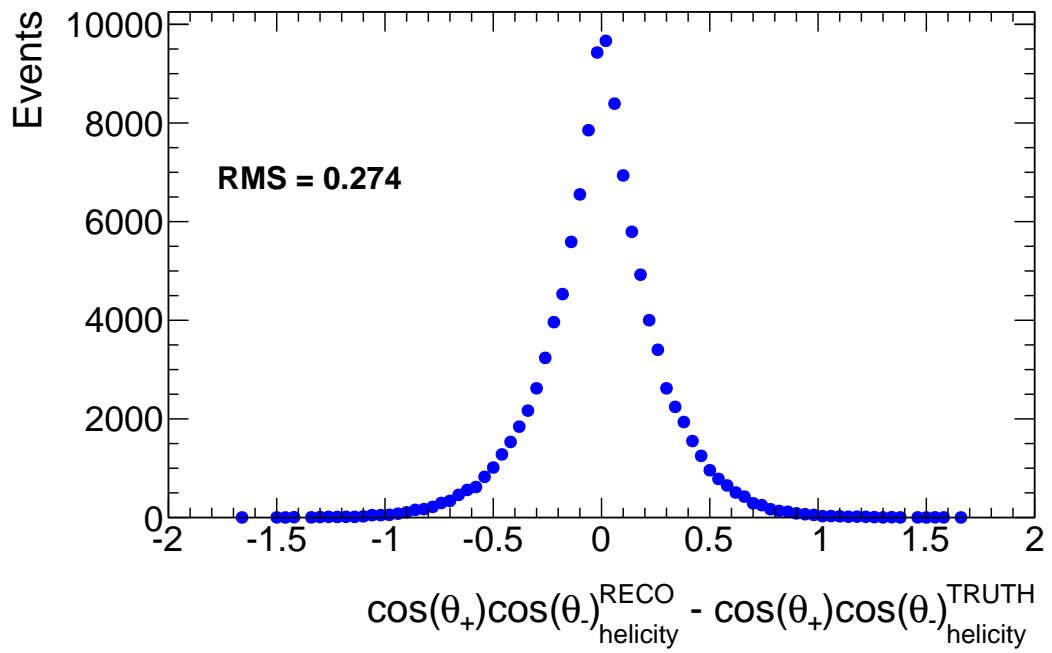
Figure 6.10: Resolution of the Helicity basis *(top)* and the normalised migration matrix for the Helicity basis *(bottom)*.
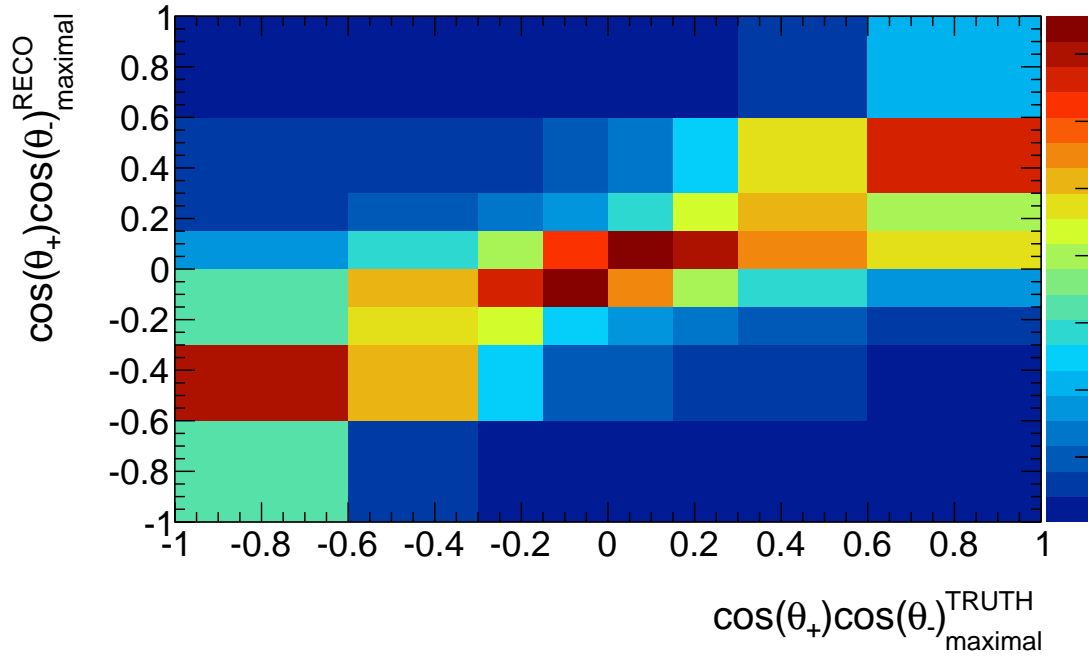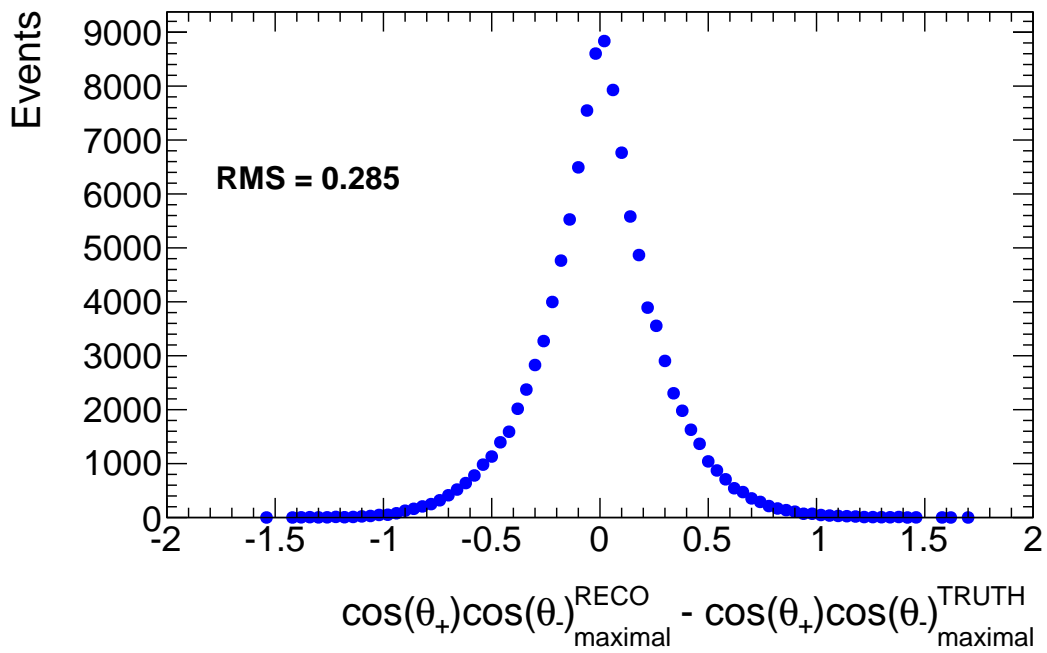
Figure 6.11: Resolution of the Maximal basis *(top)* and the normalised migration matrix for the Maximal basis *(bottom)*.
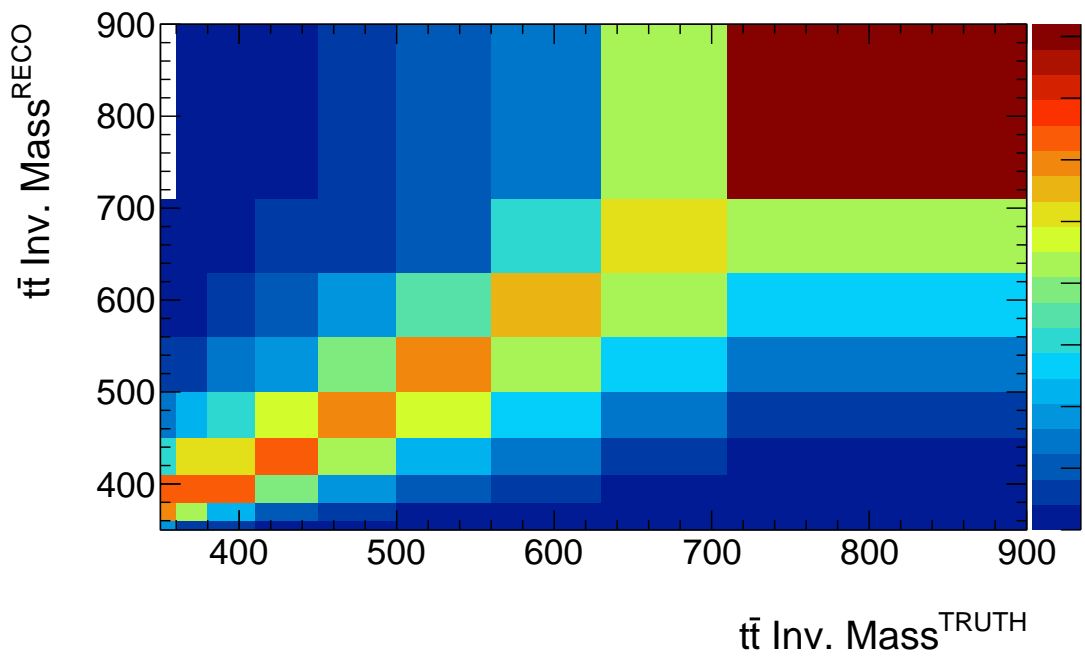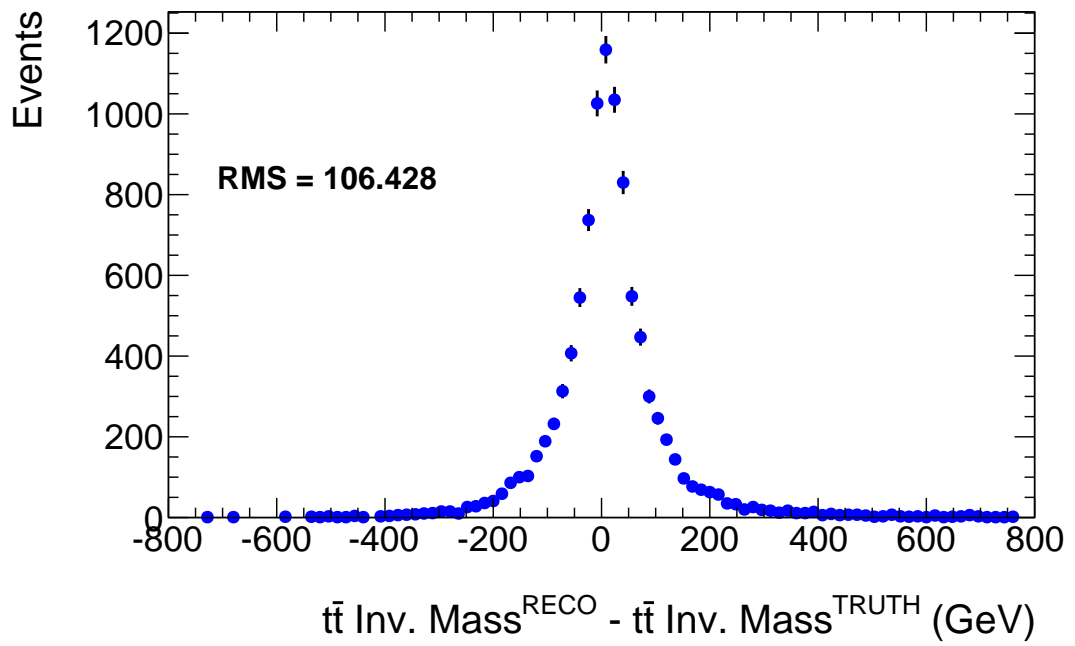
Figure 6.12: Resolution of the reconstructed $t\bar{t}$ invariant mass *(top)* and the normalised migration matrix for the reconstructed $t\bar{t}$ invariant mass *(bottom).*

Chapter 7

Extraction of spin correlation

Measurements of variables at reconstruction level suffer from biases due to detector resolution and acceptance. To extract the true spin correlation in the data these effects must be accounted for. This is achieved using a template fit to the data and a binned-maximum-likelihood method to extract the spin correlation. Two templates are constructed; one with SM $t\bar{t}$ spin correlation and one with no $t\bar{t}$ spin correlation, using the method described in Sect. 5. Each template is a histogram containing the expected shape of the signal and background processes, normalised to their theoretical cross sections (or to a data-driven estimate). In one template, the signal is described by $t\bar{t}$ MC which includes spin correlation. In the other, the signal is described by $t\bar{t}$ MC with no included spin correlation. In both templates, the background processes are identical in both shape and normalisation. The templates are fit to the data and the degree to which the data fits the SM case is extracted (f_{SM}). The normalisation of the two $t\bar{t}$ templates (signal + background) taken together is also extracted ($n_{t\bar{t}}$). The detector resolution and acceptance effects should be identical in each template and the data and are removed by this method. The same method is used for each observable.

7.1 Likelihood Fit

The likelihood function that is used in this analysis for each variable and each channel (e^+e^-, $\mu^+\mu^-$, $e^{\pm}\mu^{\mp}$) may be written as:

$$-\log(L) = \prod_{i=1}^{N} \mathcal{P}(n^i, m^i), \tag{7.1}$$

where the likelihood function (L) is maximised and the probability to observe n^i events in the data with the expected number of events m^i derived from the two templates is described by Poisson statistics ($\mathcal{P}$). The expected number of events for a given bin (i) are described using the spin correlated (S) and uncorrelated templates (U) and the

background prediction (B) using:

$$m^i = n_{t\bar{t}}(f_{SM}S^i + (1 - f_{SM})U^i) + B^i. \tag{7.2}$$

The likelihood function is minimised with respect to f_{SM} and $n_{t\bar{t}}$. The $n_{t\bar{t}}$ parameter is allowed to float in order to reduce the influence of normalisation uncertainties on the result of f_{SM}. Boundary conditions of $0.8 < n_{t\bar{t}} < 1.2$ are imposed such that the fitted normalisation is within the uncertainties of the measured $t\bar{t}$ cross section [61] [73]. The maximisation procedure is implemented using the SIMPLEX and MIGRAD algorithms in the TMinuit package [74] with the MINOS algorithm used as a consistency check between the symmetric quadratic errors provided by MIGRAD and the independent errors provided by MINOS in order to correctly extract the observed statistical uncertainty.

All of the analysis channels (e^+e^- $\mu^+\mu^-$ $e^{\pm}\mu^{\mp}$) are constructed to be mutually exclusive, due to the lepton-flavour selection, and the log likelihoods for each channel are calculated separately using templates for each from the respective channel to extract f_{SM}. They are also summed together to perform an extraction of f_{SM} in all channels simultaneously. This result is referred to as the *"combined"* channel.

7.2 Linearity Check

The extraction procedure is validated using a linearity check. The correlated and uncorrelated templates are mixed to create a new model with simulated spin correlation in the range $f_{SM} = -1 \rightarrow +2$. 1000 pseudo-data sets are generated by Poisson fluctuating each bin individually and the spin correlation and $t\bar{t}$ normalisation are extracted and compared to the input values. An example of the results for observables in the $e^{\pm}\mu^{\mp}$ channel fit are shown in Fig. 7.1. No bias is observed in the extraction procedure in the quoted range in any of the variables.

7.3 Systematic Uncertainties

The degree to which the systematic uncertainties affect the result are quoted within a 68% confidence interval (1σ deviation). Ensemble tests are used to estimate the effect of each source of systematic uncertainty. New templates are generated using the 1σ shift in the source of uncertainty for both the spin correlated template (spin) and the uncorrelated (nospin) template. Pseudo-data sets are created by mixing these templates to the observed f_{SM} in the data to create a new model and then Poisson fluctuating each bin of this model independently 1000 times. The nominal templates are then fit to the pseudo-data. In addition, the systematically shifted templates are fit to the same pseudo-data and the difference between the two fits is taken as the
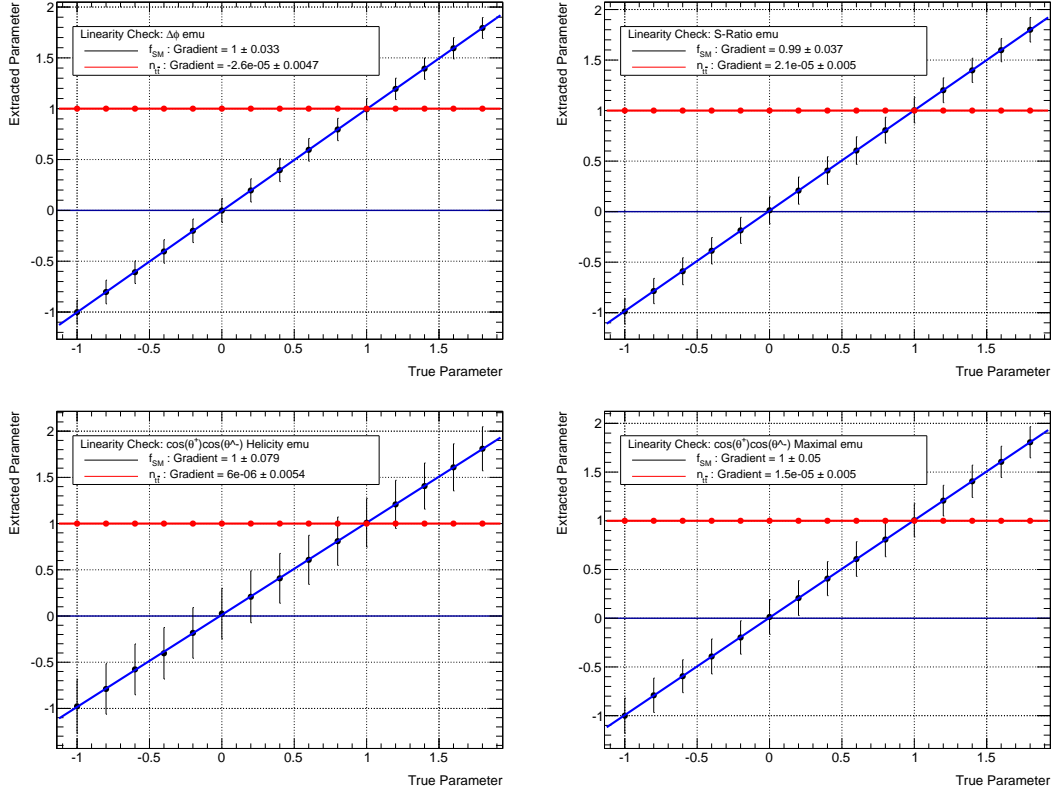
Figure 7.1: Linearity check comparing different values of input f_{SM} and $n_{t\bar{t}}$ to those extracted by the fit in the $e^{\pm}\mu^{\mp}$ channel. The results are presented for the $\Delta\phi$ observable ("top left"), the S-Ratio ("top right"), the $\cos(\theta_+)\cos(\theta_-)$ observable in the Helicity basis ("bottom left"), and the $\cos(\theta_+)\cos(\theta_-)$ observable in the Maximal basis ("bottom right"). No bias is observed in any of the observables for f_{SM} or $n_{t\bar{t}}$.

uncertainty. This procedure is performed 1000 times for each systematic uncertainty, and the final uncertainty is quoted as the mean of the difference between the two fits. The motivation for simultaneously fitting the shifted and the nominal templates is to remove statistical fluctuations inherent in the generation of the pseudo-data. When fitting the shifted templates to pseudo-data (that has been created from these same templates) any deviation from the input spin correlation would be caused by statistical fluctuations introduced in the creation of the pseudo-data, and should be identical when the nominal templates are also fitted to this pseudo-data. By taking the difference between both fits this statistical fluctuation is removed and only the shift due to the source of the systematic uncertainty is retained. The step by step procedure for the fitting is summarised below:

1. The nominal correlated and uncorrelated templates ($\mathbf{T}_{spin}$, $\mathbf{T}_{nospin}$) are fit to the data ($\mathbf{D}$) to obtain the nominal fit value ($f_{SM}^{nominal}$).

2. New templates for spin and nospin are created including a systematic shift ($\mathbf{X}$),

$\mathbf{T}^{\mathbf{X}}_{spin}$, $\mathbf{T}^{\mathbf{X}}_{nospin}$.

3. A new model is created ($\mathbf{M}$) by mixing $\mathbf{T}^{\mathbf{X}}_{spin}$ and $\mathbf{T}^{\mathbf{X}}_{nospin}$ to the observed $f^{nominal}_{SM}$.

4. Pseudo data are constructed ($\mathbf{D}'$) by independently Poisson fluctuating each bin of ($\mathbf{M}$) using the bin content as the mean.

5. The $\mathbf{T}_{spin}$ and $\mathbf{T}_{nospin}$ templates are fit to $\mathbf{D}'$ to obtain the fit value of the shifted pseudo data (f'_{SM}).

6. The $\mathbf{T}^{\mathbf{X}}_{spin}$ and $\mathbf{T}^{\mathbf{X}}_{nospin}$ templates are fit to $\mathbf{D}'$ to obtain the fit value of the shifted pseudo data to the shifted templates ($f^{\mathbf{X}}_{SM}$).

7. The difference between the two pseudo-data fits ($f^{\mathbf{X}}_{SM}$ - f'_{SM}) is taken and saved.

8. Steps $4 \rightarrow 7$ is repeated 1000 times.

9. The average of the difference in the fits ($< f^{\mathbf{X}}_{SM}$ - $f'_{SM} >$) is taken as the systematic uncertainty due to $\mathbf{X}$.

The same procedure is simultaneously used in the estimation of systematic uncertainties on the normalisation of the templates.

7.4 Sources Of Uncertainty

Systematic sources are categorised into two types:

- "Detector uncertainties": sources which affect the modelling of the physical objects in some way (for example, jet energy scale).

- "Generator uncertainties": sources which affect the modelling of the $t\bar{t}$ system itself (for example, effects due to hadronisation simulation) or that affect the background modelling.

Generator uncertainties typically have a large effect on the analysis, whereas effects from detector modelling are comparatively small. Detector uncertainties are unique to each detector whereas generator uncertainties are not. Grouping the systematic uncertainties is done in this way to facilitate comparisons of results with other experiments. Each source of systematic uncertainty is assumed to be uncorrelated with the other sources, except when stated otherwise in the following section. The total systematic uncertainty is taken to be the sum of all of the individual sources added in quadrature.

In the tables presented in Section 8.3 each source of generator uncertainty is listed individually. Sources of detector-modelling uncertainty are grouped together based on the physics objects to which they relate. For example, all uncertainties related to electron modelling, such as energy resolution or energy scale, are grouped together as

"electron modelling". All prescriptions conform to the ATLAS Top group common prescriptions [75] and a brief description of each follows.

7.4.1   Detector uncertainties

Luminosity:

- For data taken in the 7 TeV LHC running period, the Luminosity systematic uncertainty is ± 1.8 %; established primarily through Van-De-Meer scans performed during data taking and comparisons with the CMS detector. The systematic uncertainty is estimated by scaling the normalisation of both the signal and all MC derived background samples simultaneously by this value [76]. The systematic uncertainty due to luminosity is not a dominant source for any observable.

Electrons:

- Energy Scale: Systematic shifts from the nominal energy scale are derived based on the uncertainties in the method used to estimate the nominal scaling (statistics, analysis method, MC generator) [56, 77].

- Trigger Scale Factor: The scale factors are varied from the default scale factor within uncertainties derived using $Z \to ee$ events in MC [78, 79].

- Energy Resolution: The Monte Carlo is smeared by default to correct for the difference in the modelling of electron energy resolution with that observed in data. Additional smearing is performed to estimate the uncertainty [56].

The systematic uncertainties due to electron modelling are small and are typically a 1% or less effect in the observables with the highest sensitivity to spin correlations. The effects for each variable are different and are summarised in Section 8.3.

Muons:

- Muon Trigger Scale Factor: The trigger scale factors are varied according to uncertainties in the tag and probe $Z \to \mu\mu$ method used to derive the nominal scale factor.

- Momentum Scale and Resolution: Systematics due to scaling are derived by disabling momentum scaling in MC. Effects from resolution are derived from differences observed between data and MC in the dimuon invariant mass peak in $Z \to \mu\mu$ events [80, 59].

- Reconstruction Scale Factor: Scale factors are adjusted based on disagreement observed in a tag and probe method using Z Bosons decaying to two muons [81].

- Isolation Efficiency Scale Factor: The scale factor are varied $\pm 2\%$ per muon to account for observed data and MC differences in $Z \to \mu\mu$ events.

The systematic uncertainties due to muon modelling are small, similar to the case for electrons, and are typically a 1% or less effect in the observables with the highest sensitivity to spin correlations; however, they can be as large as 10% in the $\mu^+\mu^-$ channel in some cases. The effects for each variable are different and are summarised in Section 8.3. Correlations between the muon momentum scale and resolution are accounted for by deriving the full covariance matrix between the uncertainties that are correlated.

Jets:

- Jet Energy Scale (JES): Systematics are estimated using 21 different sources of Jet Energy Scale uncertainty [82] [83]. Typically, those related to jet flavour and neighbouring jets have the largest systematic uncertainty.

- Jet Energy Resolution (JER): The total systematic uncertainties on the 2011 data, described in [84], are used to smear jet resolution in order to estimate the systematic uncertainty.

- Jet Reconstruction Efficiency: The calorimeter jet reconstruction efficiency are derived using a tag and probe technique, comparing calorimeter jets to jets built from tracks in the inner detector [85]. The observed efficiency difference between data and MC is used to discard a fraction of jets. This fraction is taken at random, from within the observed inefficiency range, event by event and the shift observed between the nominal fit and the systematic shift is symmetrised.

Systematic uncertainties arising from jet modelling are the largest source of detector-related uncertainty in most observables, with the exception of the inclusive $\Delta\phi$ variable where the observable depends only upon leptons. The size of the uncertainty varies between each observable but is usually on the order of 4% or more.

$E_\mathrm{T}^\mathbf{miss}$:

- Pileup: The value for $E_\mathrm{T}^\mathrm{miss}$ is scaled up and down by a 6.6% uncertainty. This uncertainty is derived by re-weighting events in MC based on the number of reconstructed vertices in the event in order to simulate varying degrees of pileup.

- Soft Jet - Cell Out Correction: The systematics due to energy in calorimeter cells not associated to a physics object ("Cell out") and soft jets used in the calculation of the $E_\mathrm{T}^\mathrm{miss}$ are assumed to be 100% correlated and are evaluated together. The uncertainties due to the Cell Out component are derived using PYTHIA multi-jet samples with varied parameters for detector simulation, underlying event and

shower models. Soft Jet uncertainty shifts are derived using jets with 7 GeV $< p_\mathrm{T} < 20$ GeV.

- Physics Objects: All uncertainties that affect the component objects (e.g. jet energy scale) used to derive $E_\mathrm{T}^\mathrm{miss}$ are propagated to the $E_\mathrm{T}^\mathrm{miss}$ at the event level and no dedicated uncertainty is required to account for these shifts.

Modelling of the missing transverse energy is not a dominant source of systematic uncertainty for any analysis observable.

Fake Leptons:
The uncertainty due to non-prompt leptons differs depending on lepton flavour. Each source is measured separately and in the case of the $e^\pm\mu^\mp$ channel are combined in quadrature. The size of this systematic uncertainty varies depending on the contribution of fake leptons to the observable and the shape of the estimation.

- Electrons: For non-prompt electrons the dominant uncertainty is due to the different sources of misidentification, or "flavour fraction". This predominantly affects the fake efficiency used in the matrix method. The flavour fractions are varied, resulting in a shift of the fake efficiency. There is also a small contribution to the real efficiency used in the method and these are also shifted up and down. All four shifts are treated independently, with the largest shift taken as the final systematic uncertainty.

- Muons: The dominant uncertainty for the muon fake rate is the method used to estimate them. Two different methods are available, and the average is used to estimate the nominal background due to fake muons. For the systematic uncertainty, the difference between the two methods is taken (rather than the average) and the resulting estimate is normalised to the nominal fake normalisation.

Drell-Yan:

- Normalisation: The normalisation is shifted up and down by 10%. This was shown to adequately cover the uncertainty range in a similar analysis [15].

- Shape: The distribution of the Z p_T (where the Z is assumed to be the sum of the two leptons) in the Drell-Yan control region is found to be poorly modelled by the MC. The Z p_T directly affects the lepton kinematics and hence, the analysis observables. The systematic uncertainty caused by this mis-modelling is derived by re-weighting the Z boson p_T distribution in the MC to the distribution observed in the data in the Drell-Yan control region. A comparison between the MC estimate for Zp_T and the data, after background subtraction, is shown in Fig. 7.2. The weight functions are shown in Fig. 7.3. The systematic uncertainty is derived as the symmetrised difference between the result using the nominal (unweighted) Z estimate and using the re-weighted Z p_T distribution.
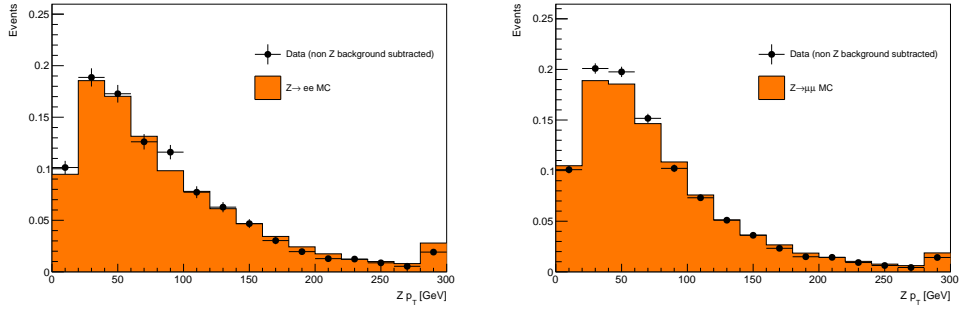
Figure 7.2: Comparison between background subtracted data and Z boson MC for the dilepton p_T spectrum for the e^+e^- channel *(left)* and $\mu^+\mu^-$ channel *(right)*.
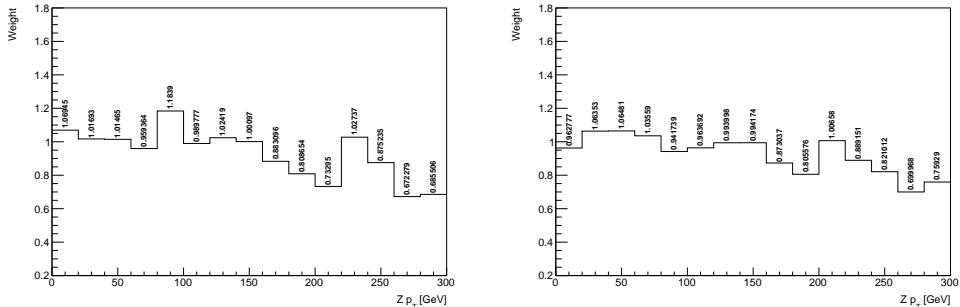
Figure 7.3: Reweighting function used to correct events due to mis-modelling of the Z boson p_T in the MC.

Monte Carlo Backgrounds:

- Single top normalisation: The systematic uncertainties associated with the single top MC in the Wt channel is derived from theory uncertainties [86]. Shifts of +0.7% / -0.8% are imposed on the single top MC to estimate the uncertainty.

- Single top shape: The single top MC used in the analysis has overlapping diagrams with $t\bar{t}$ states at higher orders. In order to estimate the magnitude of this effect a new sample is generated with these diagrams removed [87].

- Diboson normalisation: The uncertainty of the normalisation of the diboson MC shapes is determined individually for the WW, WZ and ZZ channels. For the WZ and ZZ channels, a flat uncertainty of $\pm 5\%$ is applied corresponding to the theory uncertainties on the cross section of the processes. For the WW channel an additional uncertainty of 11.52% is applied due to the inclusion of additional jets in the WW sample that did not originate from the hard process [88].

- $(Z/\gamma^* \to \tau\tau)$: A flat uncertainty of 4% is applied with an additional 24% uncertainty added in quadrature for each final state jet in the selection [88].

The systematic uncertainty due to the MC backgrounds is on the order of 2% or 3% for most of the observables, with the largest contributions arising from the uncertainty on the $Z/\gamma^* \to \tau\tau$ background estimate.

7.4.2 Generator uncertainties

Systematic uncertainties due to the $t\bar{t}$ modelling are, collectively, the dominant source of systematic uncertainty for all observables. The size and overall contribution of each source cannot be readily summarised and is highly dependent on the shape of the observable in question and the relative separation between the spin-correlated template and the uncorrelated template. The contribution of these uncertainties to the overall results are discussed in detail for each observable in Section 8.3. In general, the combined uncertainties on signal modelling are on the order of 10% for the observables most sensitive to spin correlation.

Scale Variation: Samples are generated with MC@NLO [36] in which the nominal factorisation and renormalisation scale (μ) are increased by a factor of two and reduced by a factor of a half $(2\mu, 0.5\mu)$.

Parton Shower / Fragmentation model: POWHEG samples interfaced to HERWIG are compared to the same POWHEG sample interfaced with PYTHIA. The POWHEG + HERWIG implementation suffers from the inclusion of unpolarised tau lepton decay, decreasing the spin correlation in this sample. In order to safely compare

the HERWIG shower to the PYTHIA shower, all dilepton events with tau decays at truth level are rejected for these samples only. Spin correlation is also simulated incorrectly in these samples at higher orders; however, taking the difference between the fits of the two samples as the uncertainty mitigates this effect.

ISR/FSR: The effect of initial-state and final-state radiation is estimated by taking two ACER [35] MC samples with the same matrix elements and interfacing them with PYTHIA to perform showering. The amount of showering is scaled up and down by a factor of 2 to simulate more or less initial and final state radiation. An analysis sensitive to jet radiation modelling determined that this procedure overestimated the observed jet radiation in data [89]. The systematic shift is taken as half of the difference between the two samples instead of the full difference, to account for the overestimation observed in [89].

Colour Reconnection: The effect of colour reconnection applied in MC is estimated by comparing two POWHEG $t\bar{t}$ samples using different tunes for colour reconnection; one with nominal colour reconnection parameters (Perugia2011C) and the other with no colour reconnection (Perugia2011C NOCR) [64].

Underlying event: The effect of underlying-event modelling is estimated by comparing two POWHEG $t\bar{t}$ samples each with different tunes for the underlying-event model; one with nominal underlying-event parameters (Perugia2011C) and the other with a shifted tune (Perugia2011C mpiHI) [64].

Template Statistics: The effect of limited template statistics in the signal MC is estimated by fluctuating each bin in the nominal templates for spin and uncorrelated $t\bar{t}$ within their uncertainties and fitting to the observed data. The width of the resulting distributions for f_{SM} and $n_{t\bar{t}}$ is taken as the systematic uncertainty. In general, the template statistics of the signal MC are not a limiting systematic in this analysis.

Top Mass: Samples are generated for different top masses and the fit is re-performed. The dependence of f_{SM} and $t\bar{t}$ normalisation is then extracted by a linear fit to these samples. The uncertainty of ±1.4 GeV from the nominal top mass (172.5 GeV) is taken as the uncertainty at the 1 σ level. 1.4 GeV is chosen to ensure coverage of the world average observed top mass [8]. An example of this linear fit can be seen in Fig. 7.4. The gradient of the fitted first order polynomial for each parameter is shown on the figures. A small dependence on the extracted f_{SM} on the input top mass is observed and a large dependence on the $t\bar{t}$ normalisation is observed.

PDF: The analysis is repeated with different PDF sets. The nominal PDF set, CTEQ10, is compared to NNPDF2.3 and MSTW2008nlo68cl. Each PDF set provides

151

uncertainties due to the global fit or scale choice and the effect of these are evaluated at the 1 σ level. The PDF systematic uncertainties are only available for the inclusive variables and not for the high and low $t\bar{t}$ invariant mass region.

- Intra PDF Uncertainty: Each NLO PDF set used in this analysis has an associated number of systematic shifts due to various sources provided by the various PDF collaborations. The analysis is repeated with the templates re-weighted to these shifted PDF values and the f_{SM} extracted. An uncertainty band is calculated based on the recommendations of each PDF group: CTEQ uses a symmetric hessian method, NNPDF uses a root mean squared, and MSTW2008 uses an asymmetric hessian.

- Inter PDF Uncertainty: To calculate the overall effect of the choice of PDF set, an envelope method is used. The uncertainty is taken to be the largest deviation in the intra-pdf uncertainties from the central f_{SM} value.

top p_T reweighting: The top p_T generated by MC@NLO is known to have small disagreement with unfolded data at truth level [90]. In order to estimate the effect of this mis-modelling, a reweighting is applied to each event using one of the leptonically decaying truth tops with HERWIG status code 155 (indicating a top quark before decay after parton shower). The values used for the reweighting are shown in Tab. 7.1.

top p_T	weight
0→50	1.032
50→100	1.018
100→150	0.996
150→200	0.937
200→250	0.902
250→350	0.884

Table 7.1: Reweighting function applied to events to correct for top p_T mis-modelling in MC@NLO using results obtained from [90].
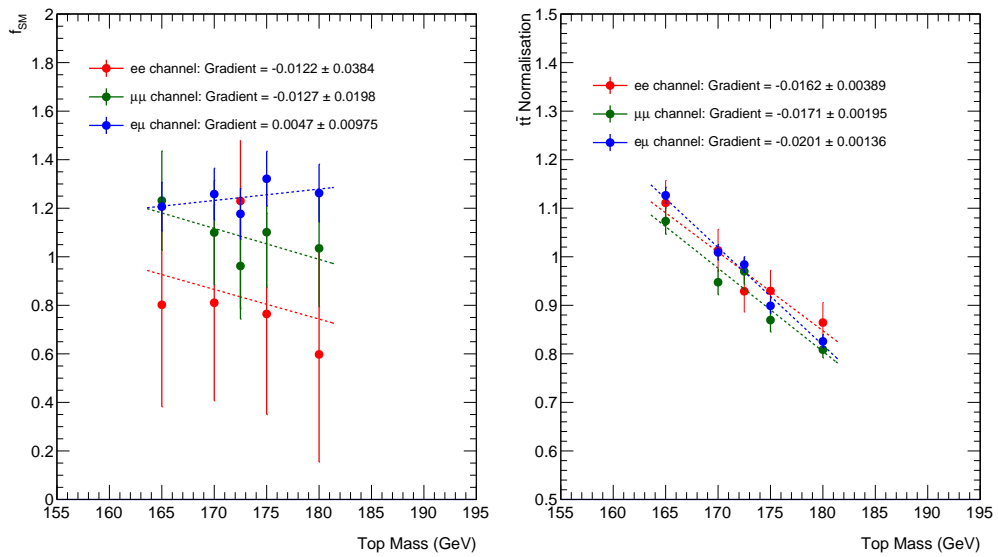
Figure 7.4: Linear fit for f_{SM} *(left)* and $t\bar{t}$ *(right)* normalisation as a function of the top mass in the template for the e^+e^- (green), $\mu^+\mu^-$ (red), and $e^\pm\mu^\mp$ (blue) channels for the $\Delta\phi$ variable.

Chapter 8

Results

In the following chapter the results for the different spin observables in each channel $(e^+e^-$, $\mu^+\mu^-$, $e^\pm\mu^\mp$, and combined) are presented. First, previous results are presented for a subset of the full 2011 data, corresponding to 2.1 fb^{-1} of integrated luminosity. Next the results on the full 4.6 fb^{-1} data are presented as well as the results for the extraction of spin correlation. Finally results are compared to theory predictions. All data-expectation figures use the common legend convention shown in Fig. 5.1. The figure is shown again for convenience in Fig. 8.1.

8.1 Performance on 7 TeV data
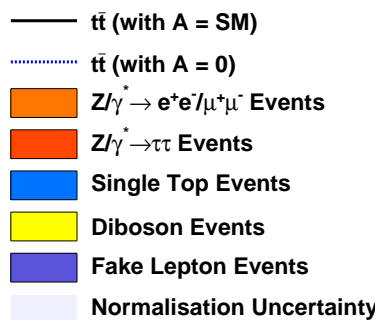
Figure 8.1: Labeling convention that is used in all Data/MC comparison plots.

8.2 Results using 2.1 fb^{-1}

An observation of $t\bar{t}$ spin correlation was previously reported in the dilepton channel using a subset of the full ATLAS 2011 data, corresponding to 2.1 fb^{-1} of data [27]. The result used the same template fit as the one described in Section 7.1, performed in the $\Delta\phi$ variable. The extracted value for the spin correlation strength is f_{SM} =1.30
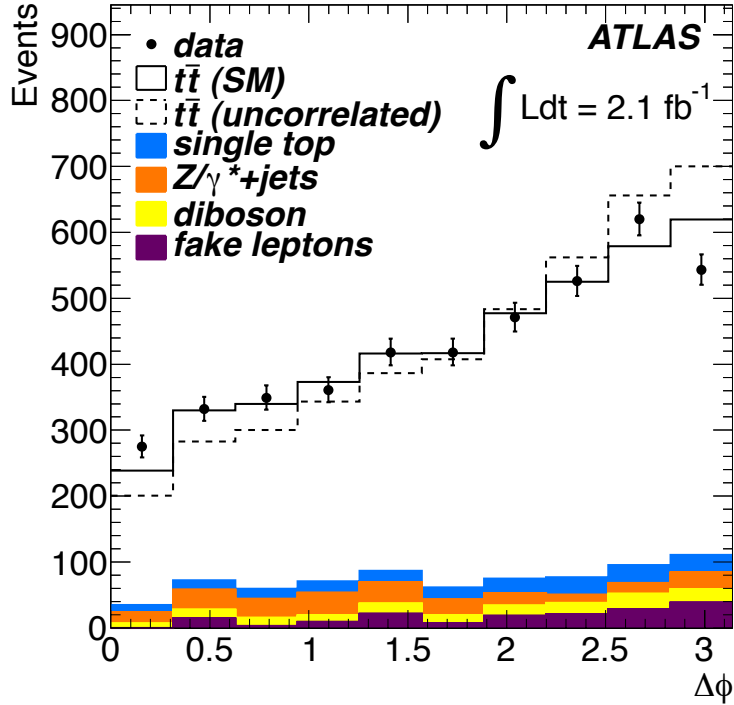
Figure 8.2: Reconstructed $\Delta\phi$ distribution for the sum of the e^+e^- $\mu^+\mu^-$ and $e^\pm\mu^\mp$ channels. The integrated number of events for both the SM and the uncorrelated $t\bar{t}$ samples is fixed to the value extracted from the fit. MC background samples are normalised using their predicted cross sections and the DD method in the case of Z/γ^*+jets. The fake lepton background is evaluated from data [27].

$\pm$ 0.14 (stat) $^{+0.27}_{-0.22}$ (syst), consistent with the prediction of the SM. The sum of the e^+e^- $\mu^+\mu^-$ and $e^\pm\mu^\mp$ channels in data is shown in Fig. 8.2. The templates for the SM hypothesis and the uncorrelated hypothesis are overlaid on the data, along with the expected background. The data are inconsistent with the uncorrelated template and the uncorrelated hypothesis was excluded at 5.1 standard deviations.

8.3 Analysis variables performance on data using 4.6 fb^{-1}

Performance of the $\Delta\phi$ observable

The observed data and expectations for the $\Delta\phi$ variable in the inclusive, low and high $t\bar{t}$ invariant-mass regions for the e^+e^- $\mu^+\mu^-$ and $e^\pm\mu^\mp$ channels are presented in Figs. 8.3, 8.4 and 8.5. Good separation between the correlated and uncorrelated $t\bar{t}$ hypotheses is observed in the inclusive and low invariant-mass regions, where this variable is expected to have high sensitivity. Separation in the high mass region is typically poor. This feature is not unexpected, as the $\Delta\phi$ variable is most sensitive to
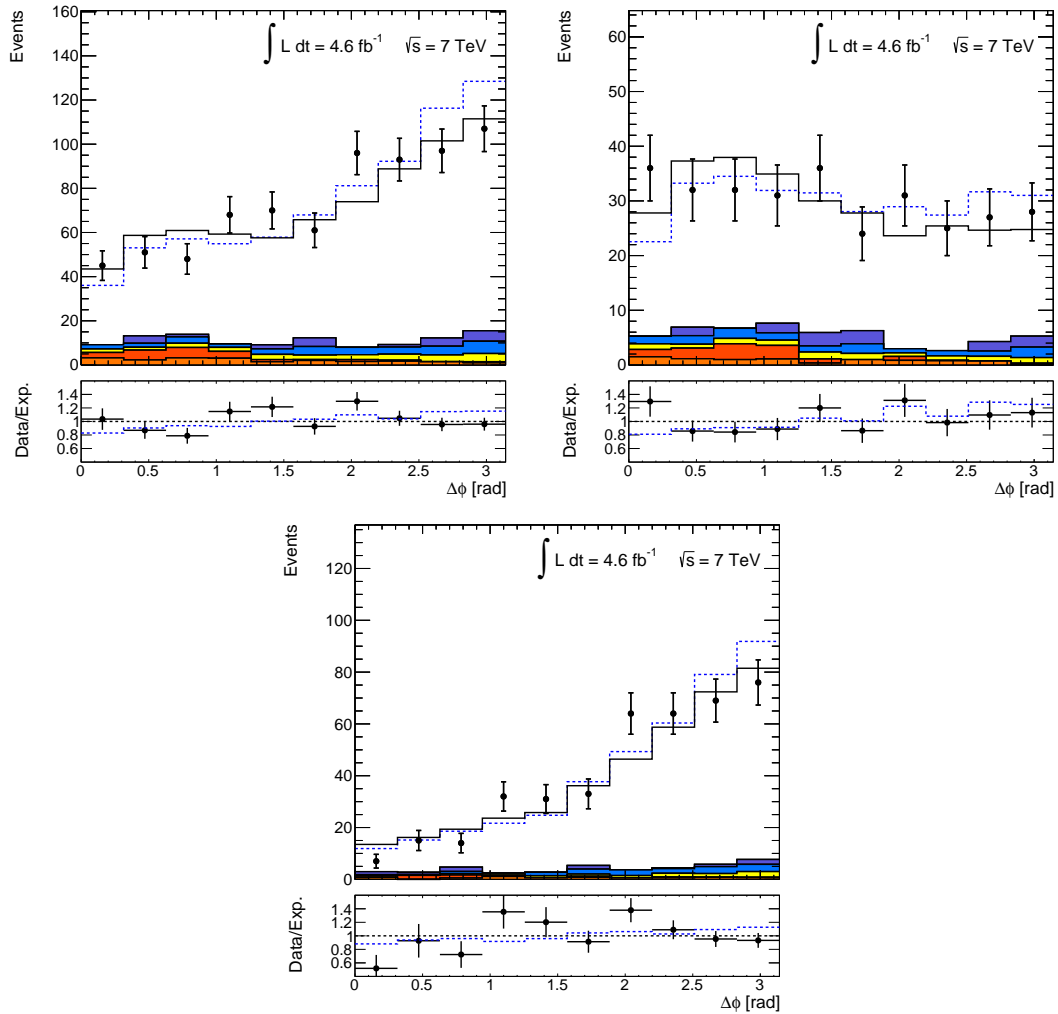
Figure 8.3: Distribution of the $\Delta\phi$ variable in the e^+e^- channel in the inclusive $t\bar{t}$ region *(top-left)*, the low $t\bar{t}$ invariant-mass region *(top-right)* and the high $t\bar{t}$ invariant-mass region *(bottom)*.
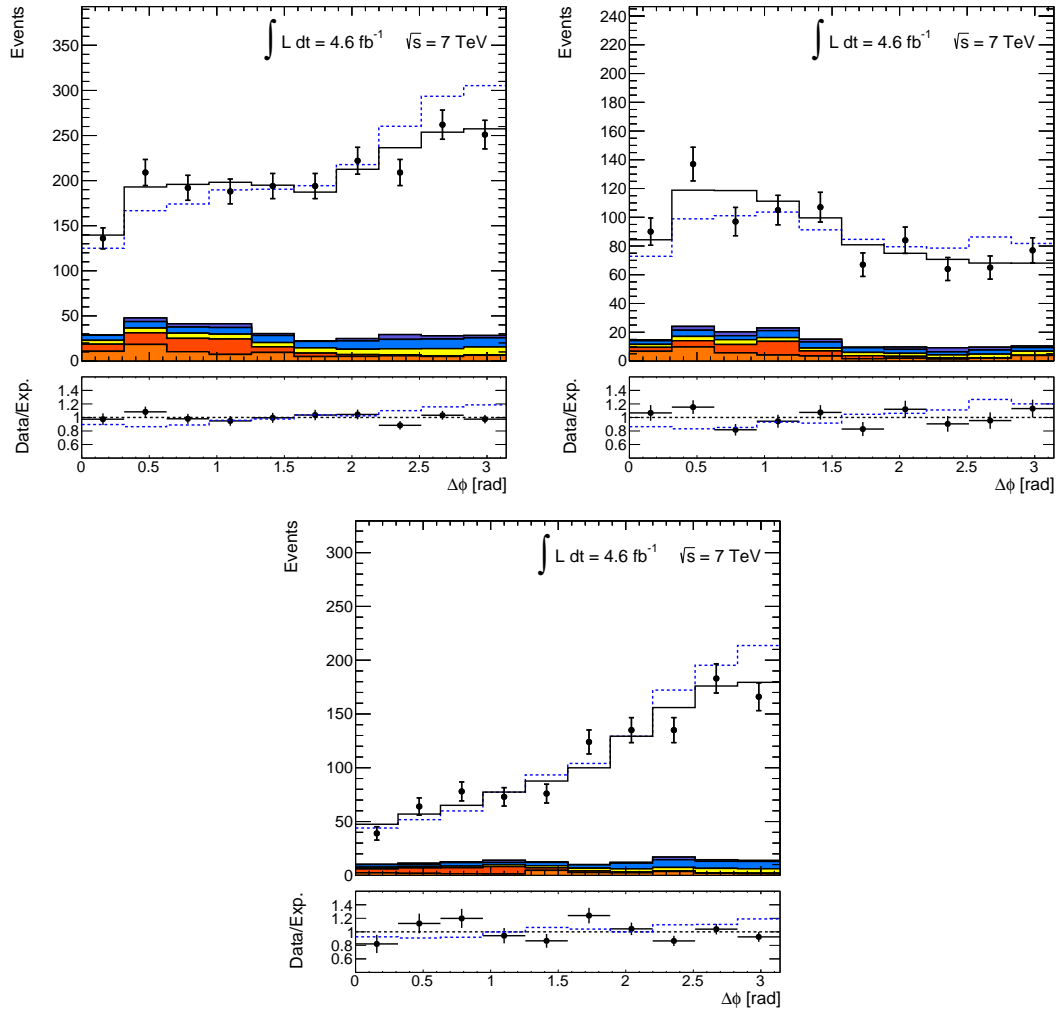
Figure 8.4: Distribution of the $\Delta\phi$ variable in the $\mu^+\mu^-$ channel in the inclusive $t\bar{t}$ region *(top-left)*, the low $t\bar{t}$ invariant-mass region *(top-right)* and the high $t\bar{t}$ invariant-mass region *(bottom)*.
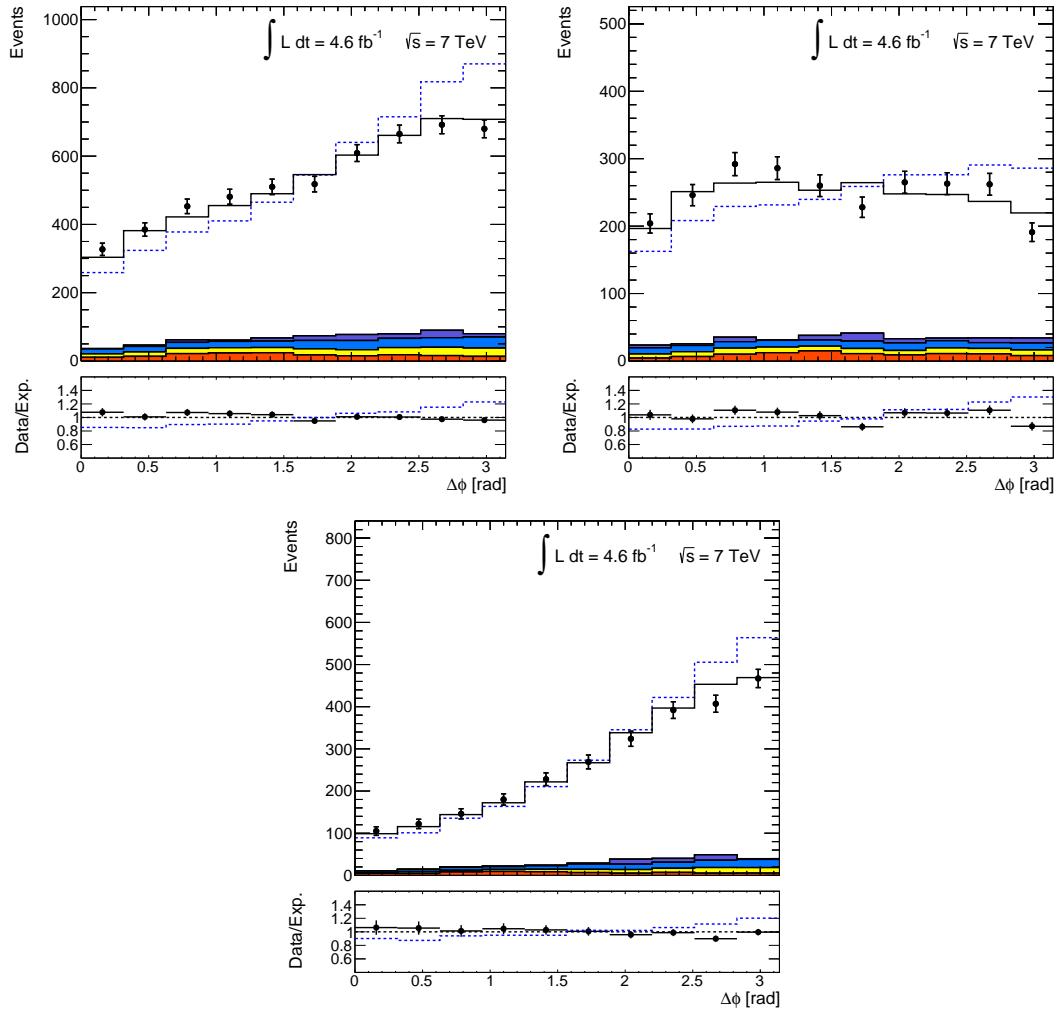
Figure 8.5: Distribution of the $\Delta\phi$ variable in the $e^{\pm}\mu^{\mp}$ channel in the inclusive $t\bar{t}$ region *(top-left)*, the low $t\bar{t}$ invariant-mass region *(top-right)* and the high $t\bar{t}$ invariant-mass region *(bottom)*.
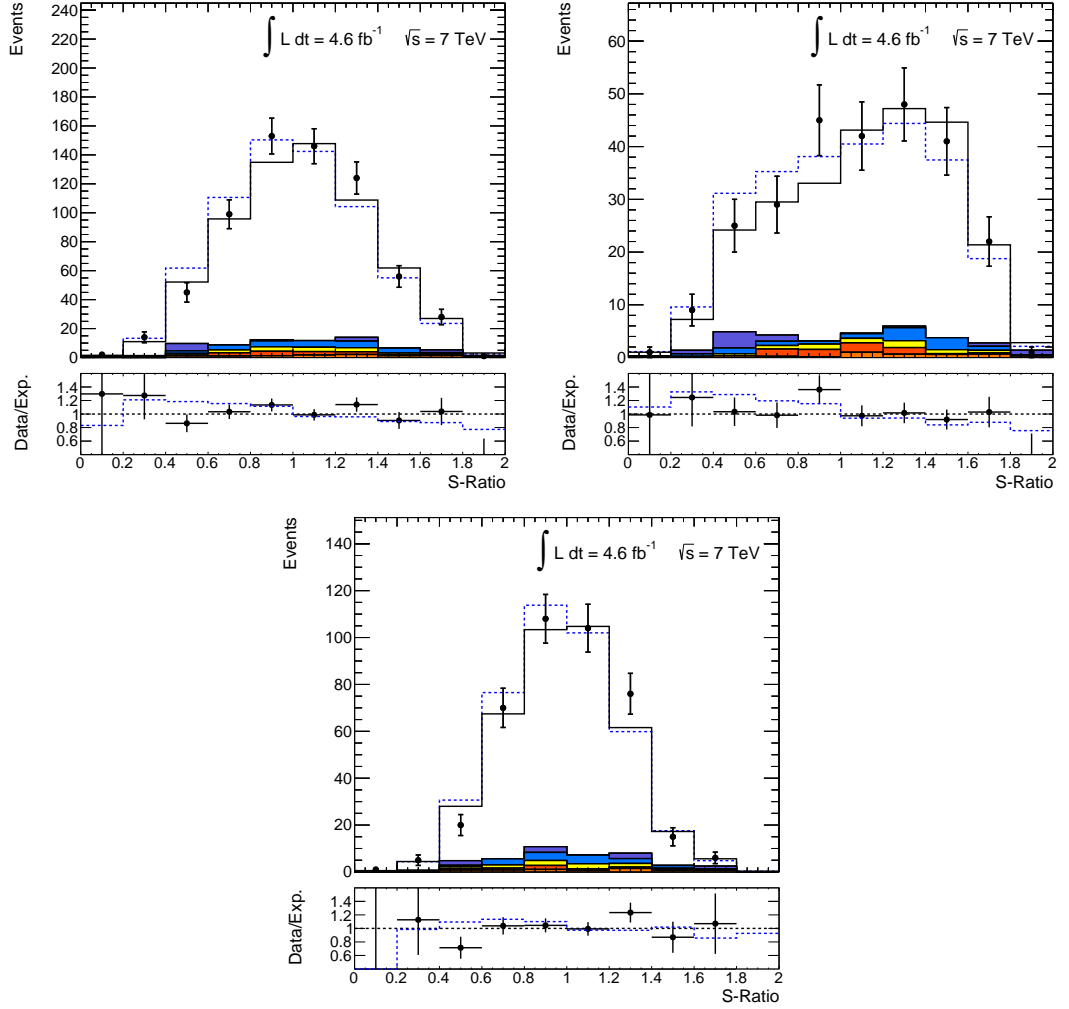
Figure 8.6: Distribution of the S-Ratio variable in the e^+e^- channel in the inclusive $t\bar{t}$ region *(top-left)*, the low $t\bar{t}$ invariant-mass region *(top-right)* and the high $t\bar{t}$ invariant-mass region *(bottom)*.

$t\bar{t}$ pairs arising from like-helicity gluon-gluon fusion which dominate at low $t\bar{t}$ invariant mass but are suppressed at high $t\bar{t}$ invariant mass in favour of oposite-helicity gluon-gluon fusion. This can be seen in the change of shape that is observed between the low and high invariant-mass regimes and the decrease in separation between the spin correlated and uncorrelated hypotheses in the high mass region.

Performance of the S-Ratio observable

The observed data and expectations for the S-Ratio variable in the inclusive, low and high $t\bar{t}$ invariant-mass regions for the e^+e^- $\mu^+\mu^-$ and $e^\pm\mu^\mp$ channels are presented in Figs. 8.6, 8.7 and 8.8. As is the case for the $\Delta\phi$ variable, good separation between the two hypothesis templates is observed in the inclusive and low invariant-mass re-
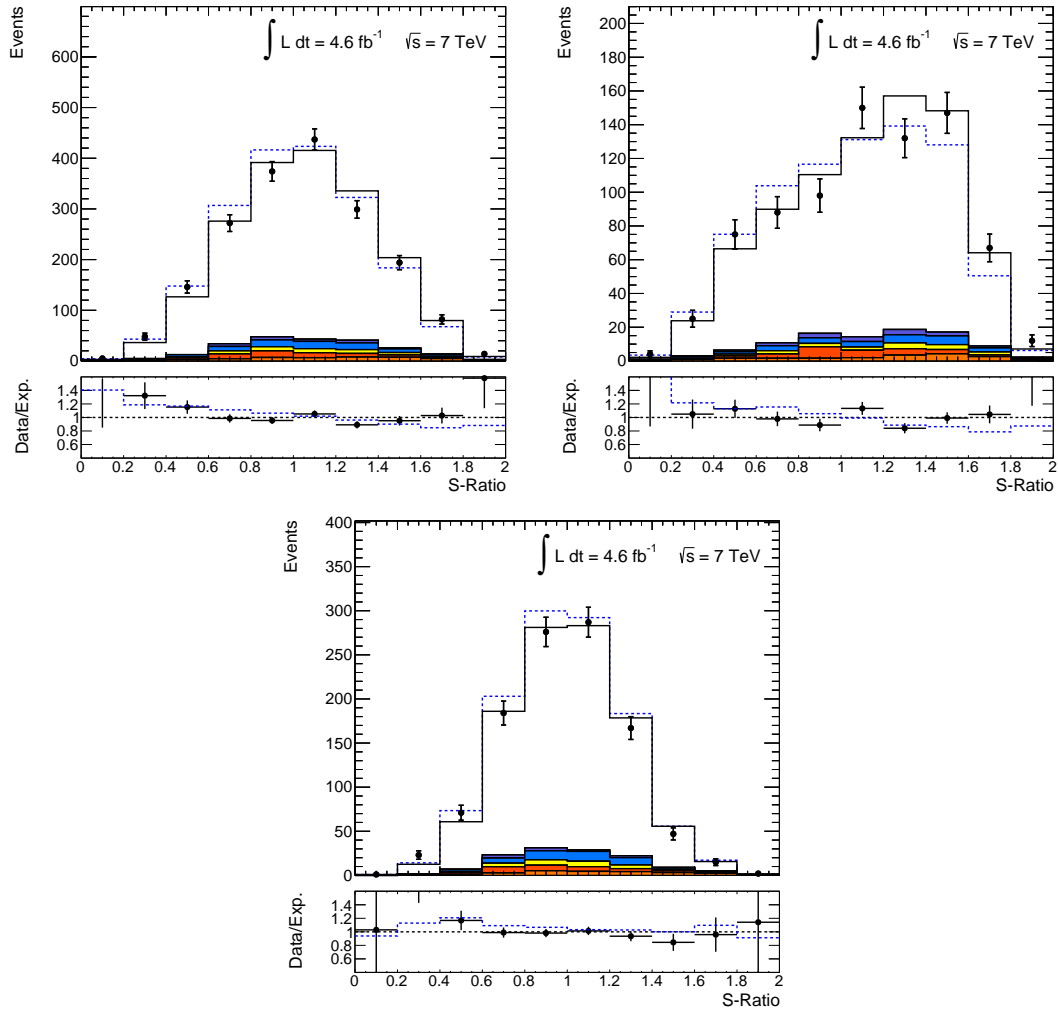
Figure 8.7: Distribution of the S-Ratio variable in the $\mu^+\mu^-$ channel in the inclusive $t\bar{t}$ region *(top-left)*, the low $t\bar{t}$ invariant-mass region *(top-right)* and the high $t\bar{t}$ invariant-mass region *(bottom)*.
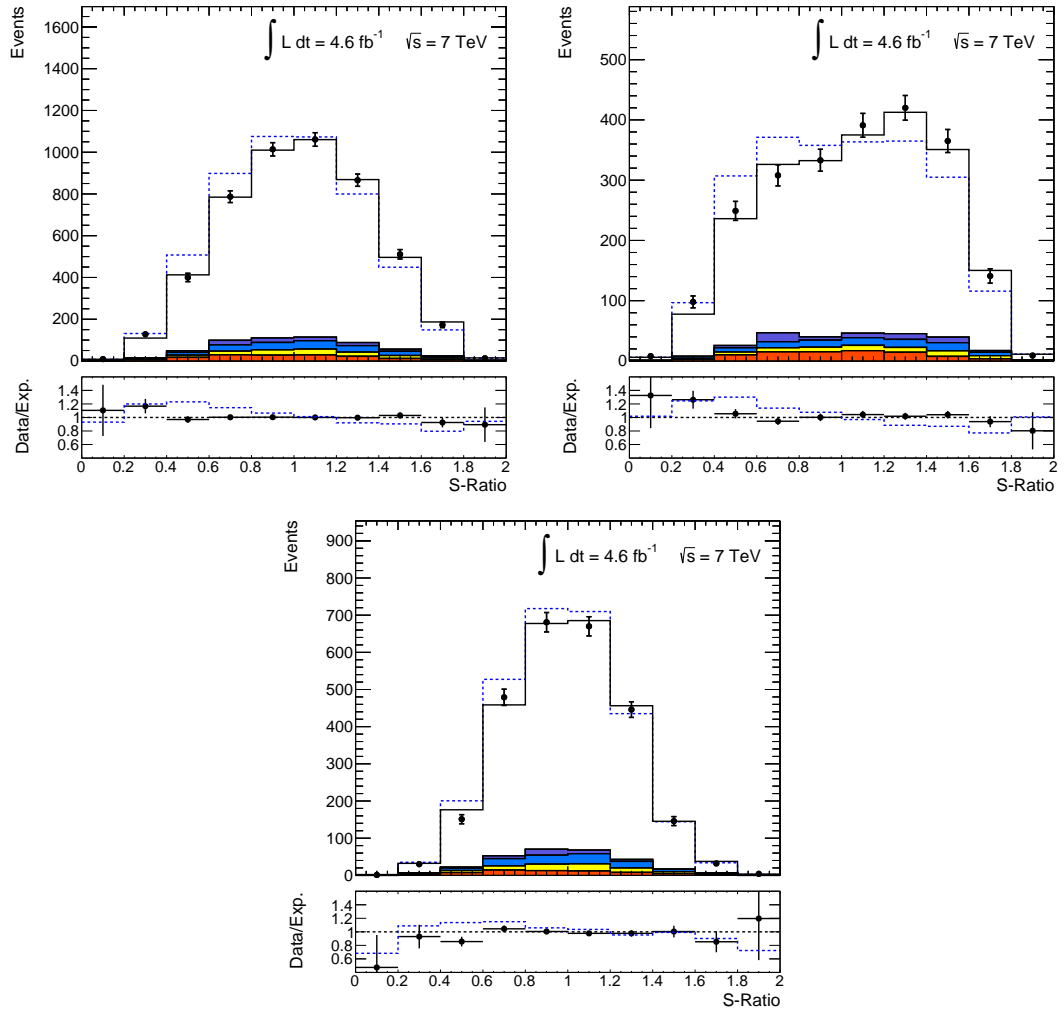
Figure 8.8: Distribution of the S-Ratio variable in the $e^{\pm}\mu^{\mp}$ channel in the inclusive $t\bar{t}$ region *(top-left)*, the low $t\bar{t}$ invariant-mass region *(top-right)* and the high $t\bar{t}$ invariant-mass region *(bottom)*.
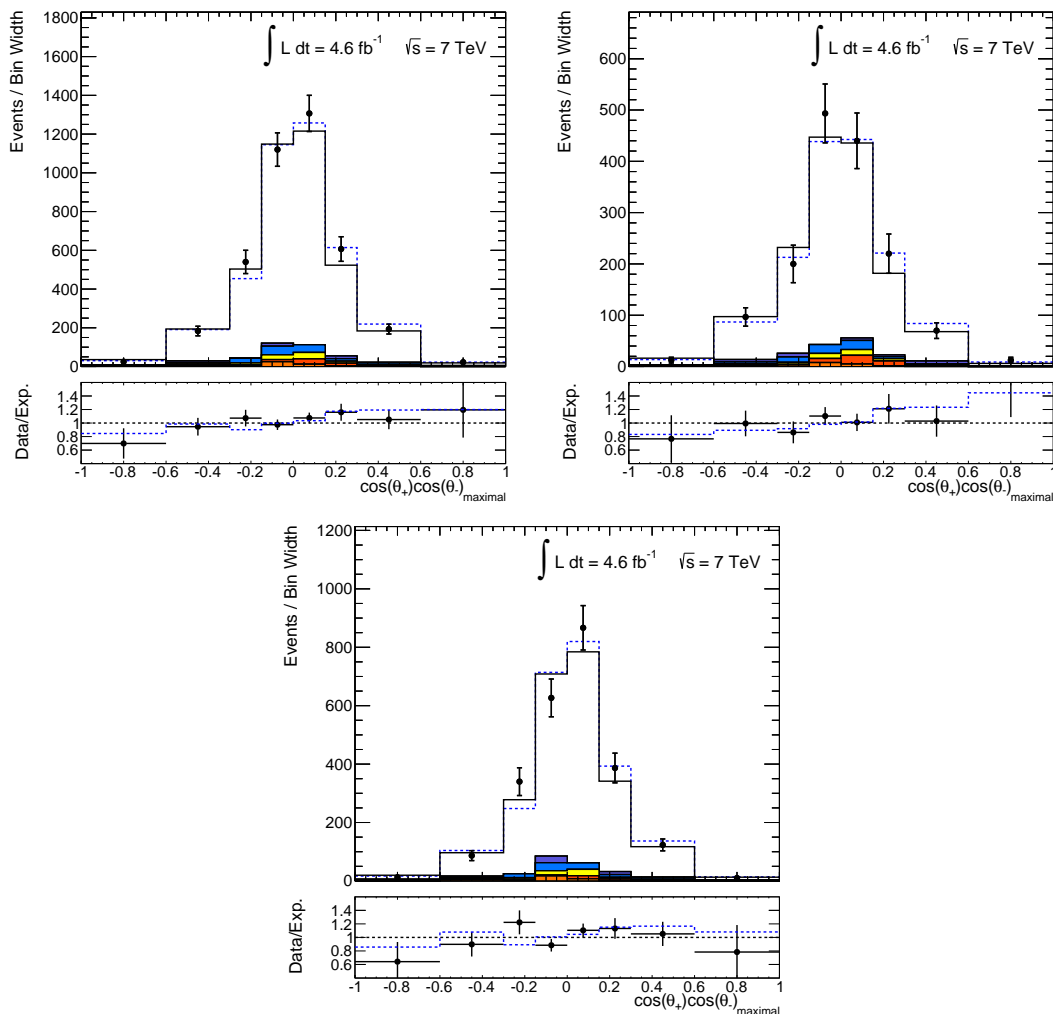
Figure 8.9: Distribution of the $cos(\theta_+)cos(\theta_-)$ observable in the Maximal basis in the e^+e^- channel in the inclusive $t\bar{t}$ region *(top-left)*, the low $t\bar{t}$ invariant-mass region *(top-right)* and the high $t\bar{t}$ invariant-mass region *(bottom)*.

gions. Separation in the high mass region is again poor; however, this is also expected behaviour for this variable for the same reason as for the $\Delta\phi$ variable. The S-Ratio variable is, by construction, most sensitive to spin correlations arising from like-helicity gluon-gluon fusion and has the highest separation power between the spin correlated and uncorrelated cases in the low $t\bar{t}$ invariant-mass regimes.

Performance of the $cos(\theta_+)cos(\theta_-)$ observable in the Maximal and Helicity basis

The observed data and expectations for the $cos(\theta_+)cos(\theta_-)_{maximal}$ observable in the inclusive, low, and high $t\bar{t}$ invariant-mass regions for the e^+e^- $\mu^+\mu^-$ and $e^\pm\mu^\mp$ channels are presented in Figs. 8.9, 8.10 and 8.11. Good separation between the two hypotheses
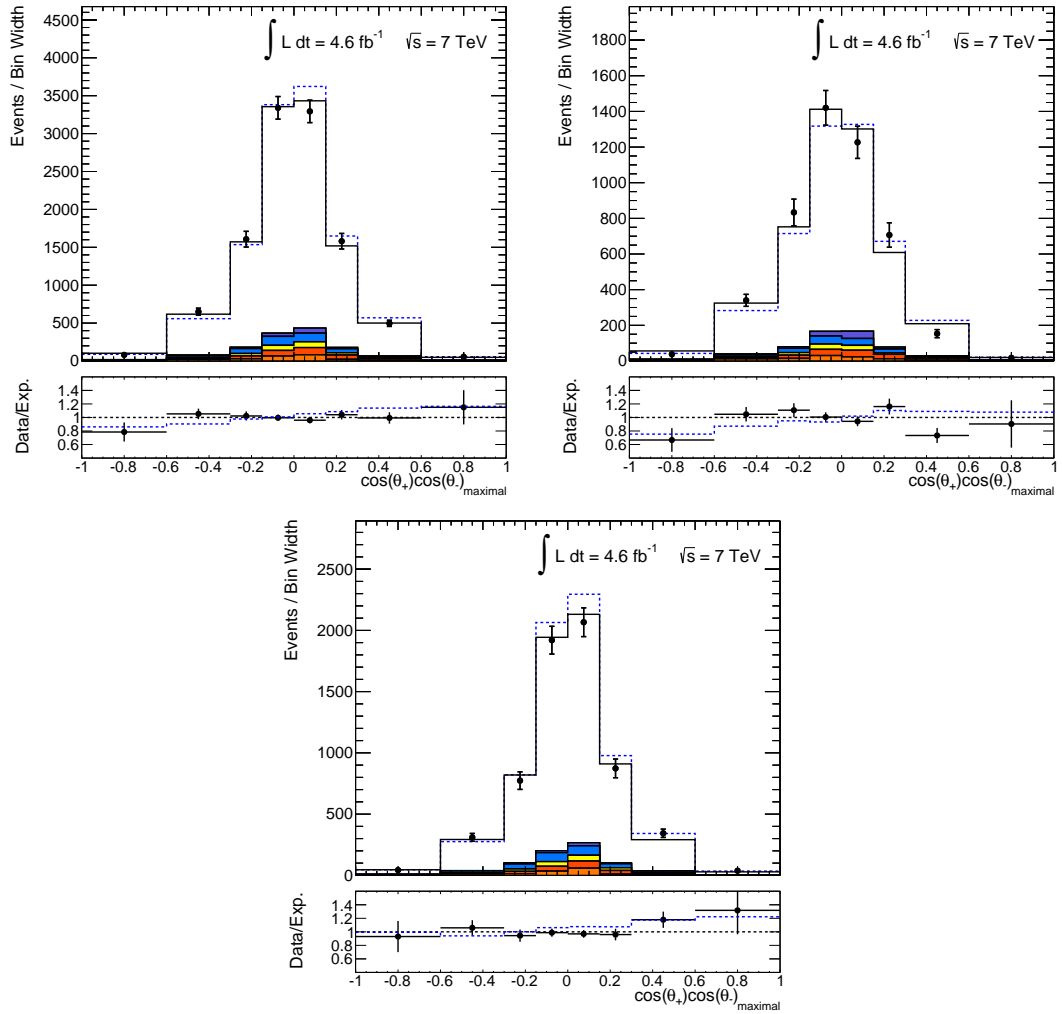
Figure 8.10: Distribution of the $cos(\theta_+)cos(\theta_-)$ observable in the Maximal basis in the $\mu^+\mu^-$ channel in the inclusive $t\bar{t}$ region *(top-left)*, the low $t\bar{t}$ invariant-mass region *(top-right)* and the high $t\bar{t}$ invariant-mass region *(bottom)*.
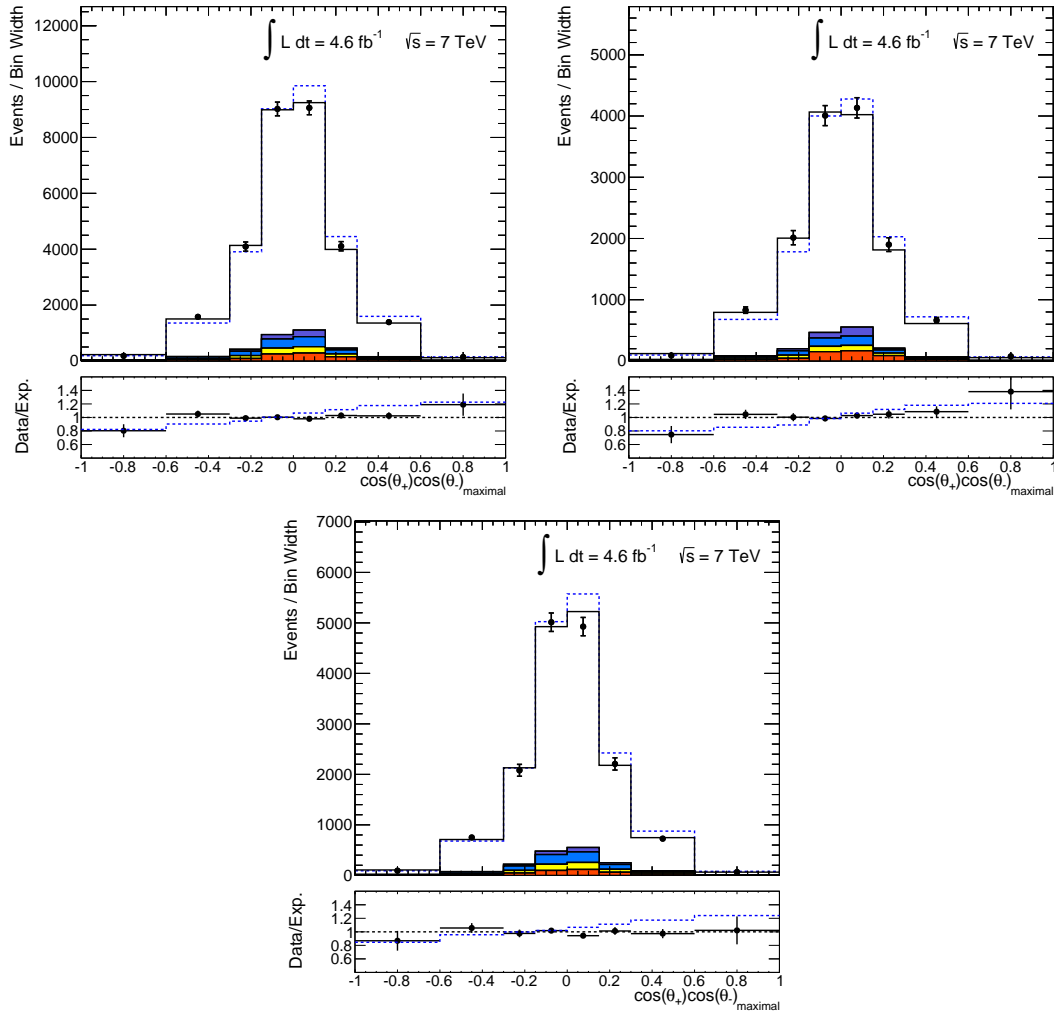
Figure 8.11: Distribution of the $cos(\theta_+)cos(\theta_-)$ observable in the Maximal basis in the $e^\pm\mu^\mp$ channel in the inclusive $t\bar{t}$ region *(top-left)*, the low $t\bar{t}$ invariant-mass region *(top-right)* and the high $t\bar{t}$ invariant-mass region *(bottom)*.
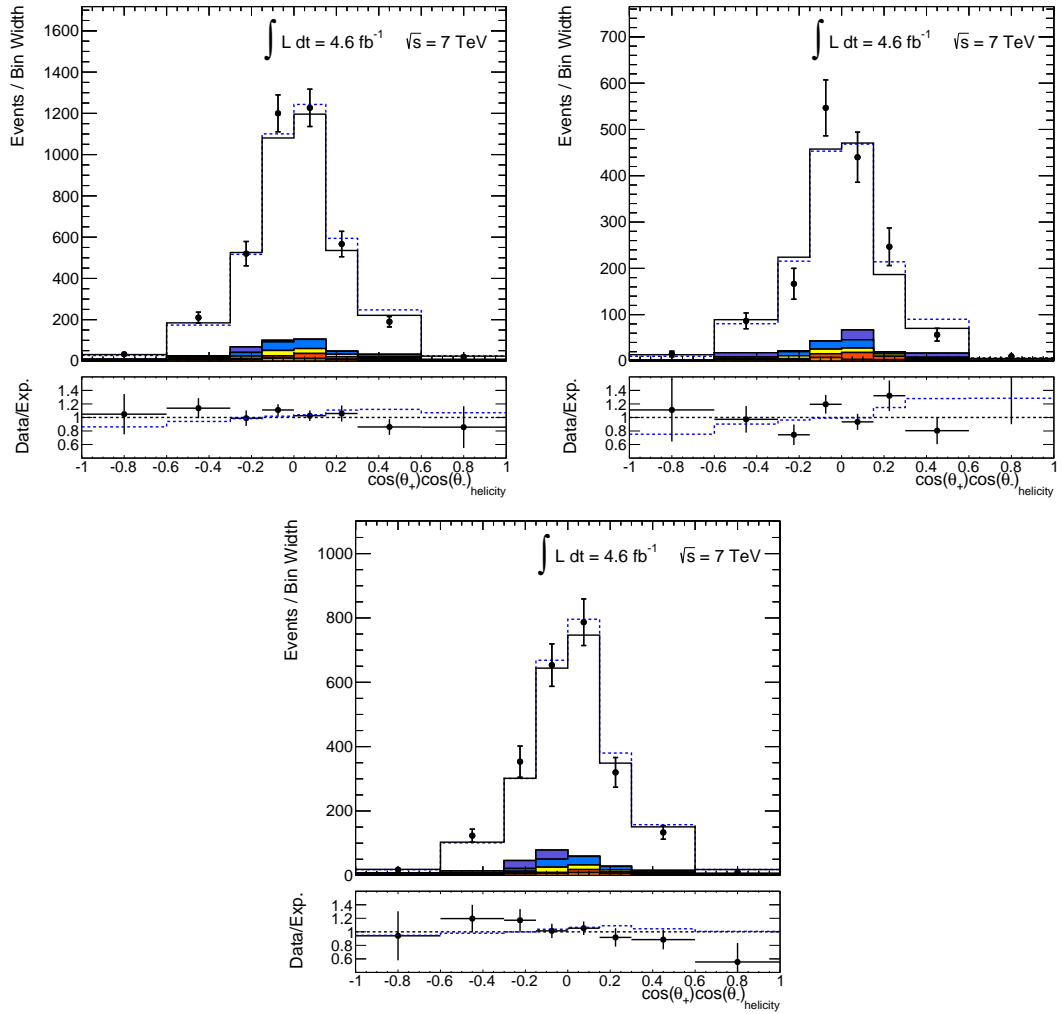
Figure 8.12: Distribution of the $cos(\theta_+)cos(\theta_-)$ observable in the Helicity basis in the e^+e^- channel in the inclusive $t\bar{t}$ region *(top-left)*, the low $t\bar{t}$ invariant-mass region *(top-right)* and the high $t\bar{t}$ invariant-mass region *(bottom)*.
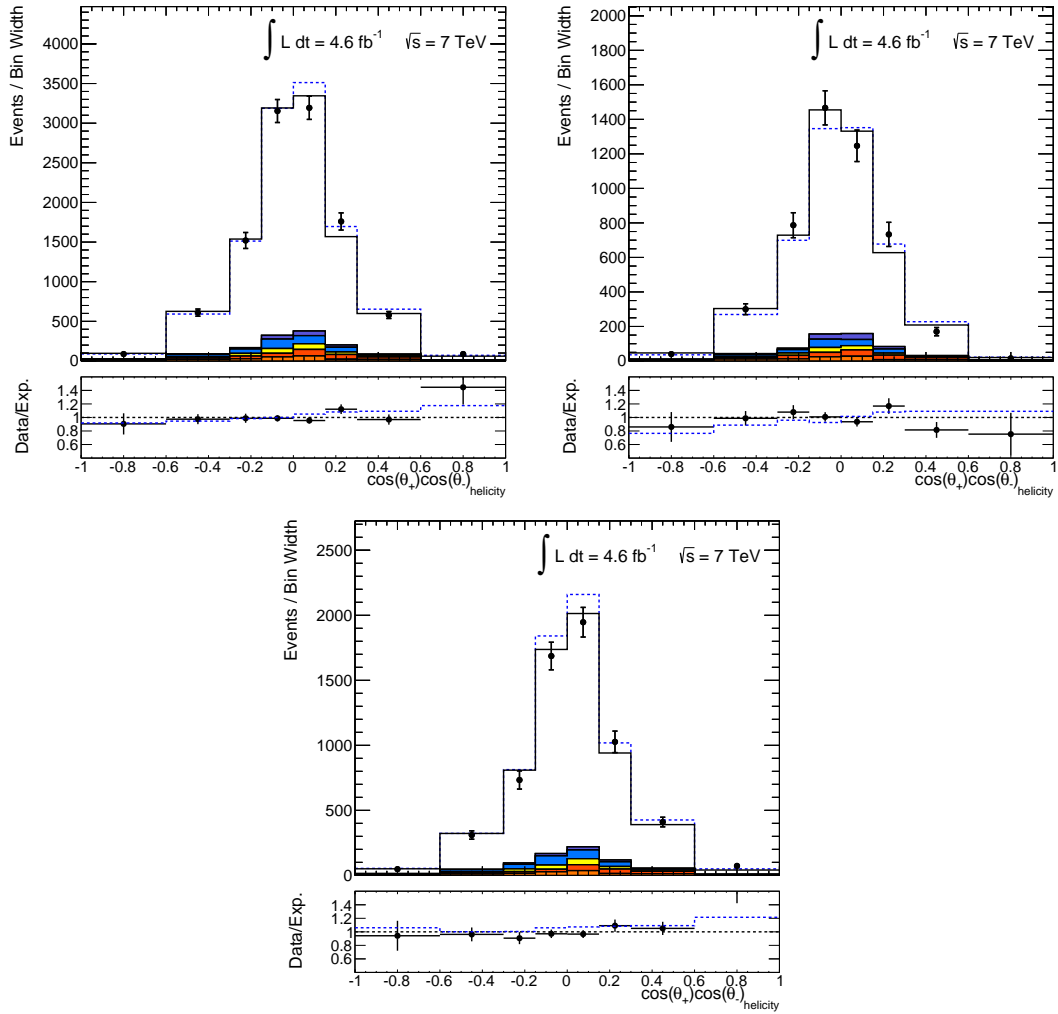
Figure 8.13: Distribution of the $cos(\theta_+)cos(\theta_-)$ observable in the Helicity basis in the $\mu^+\mu^-$ channel in the inclusive $t\bar{t}$ region *(top-left)*, the low $t\bar{t}$ invariant-mass region *(top-right)* and the high $t\bar{t}$ invariant-mass region *(bottom)*.
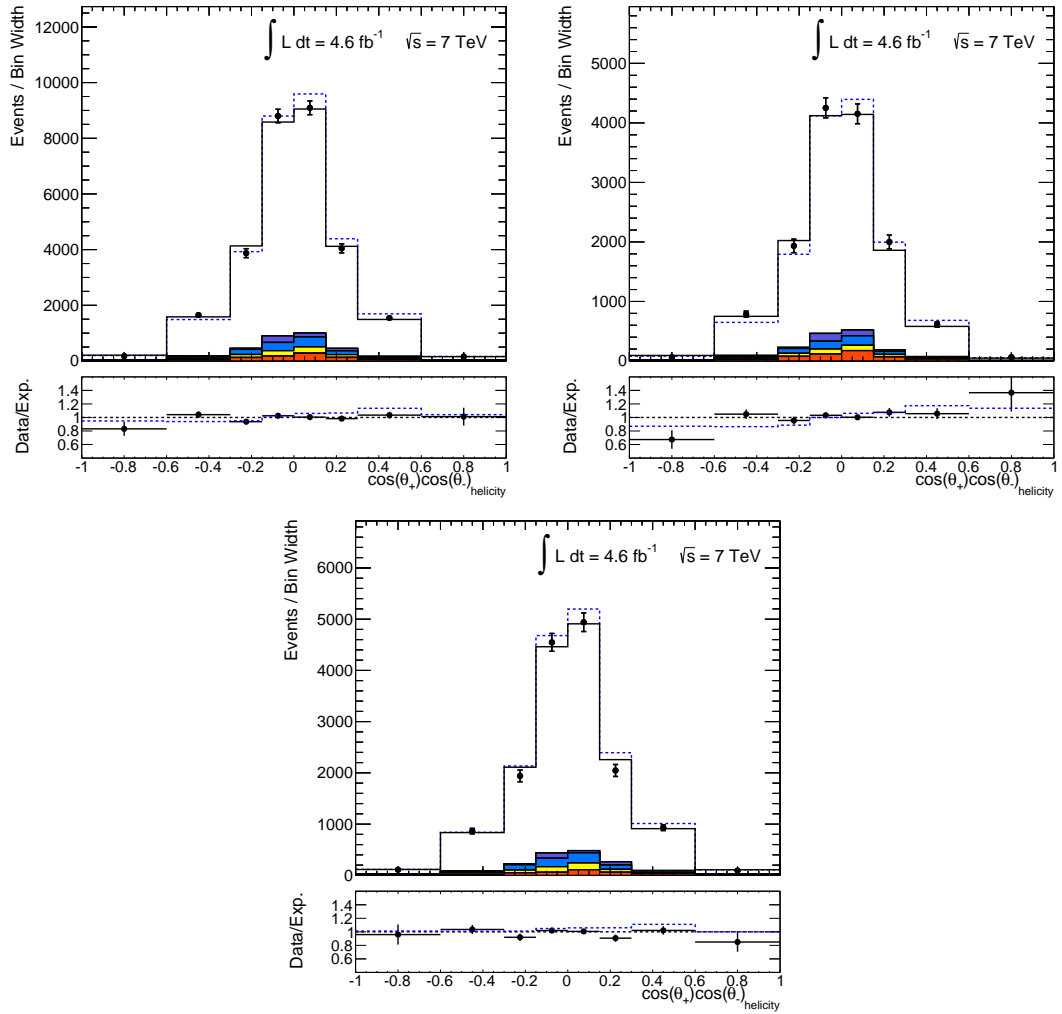
Figure 8.14: Distribution of the $cos(\theta_+)cos(\theta_-)$ observable in the Helicity basis in the $e^{\pm}\mu^{\mp}$ channel in the inclusive $t\bar{t}$ region *(top-left)*, the low $t\bar{t}$ invariant-mass region *(top-right)* and the high $t\bar{t}$ invariant-mass region *(bottom)*.

is seen in all invariant-mass regions but to lesser degree than with the $\Delta\phi$ or S-Ratio variables. The Maximal basis is expected to be sensitive to spin correlation arising from gluon-gluon fusion in general and the sensitivity is expected to be similar in all mass regions.

The same distributions for the $cos(\theta_+)cos(\theta_-)_{helicity}$ variable are presented in Figs. 8.12, 8.13 and 8.14. Good separation between the two hypotheses is observed in all three invariant-mass regions but to lesser degree than with the $\Delta\phi$, S-Ratio or $cos(\theta_+)cos(\theta_-)_{maximal}$ observables. Overall, the Helicity basis shows the least separation between the correlated and uncorrelated hypotheses out of all observables.

The e^+e^- channel is statistically limited compared to the $\mu^+\mu^-$ and $e^\pm\mu^\mp$ channels, and the $e^\pm\mu^\mp$ channel dominates in statistical sensitivity in all variables and invariant-mass regions. A higher acceptance can be observed in the uncorrelated hypothesis in the e^+e^- and $\mu^+\mu^-$ channel distributions. The uncorrelated $t\bar{t}$ sample has a higher average invariant mass distribution as the leptons tend to have a larger $\Delta\phi$ angle. The cut on the dilepton invariant mass that is used to suppress Z background in this channel affected both hypotheses differently. This is accounted for in the extraction by fixing the relative difference between the two hypotheses whilst allowing the overall normalisation to float.
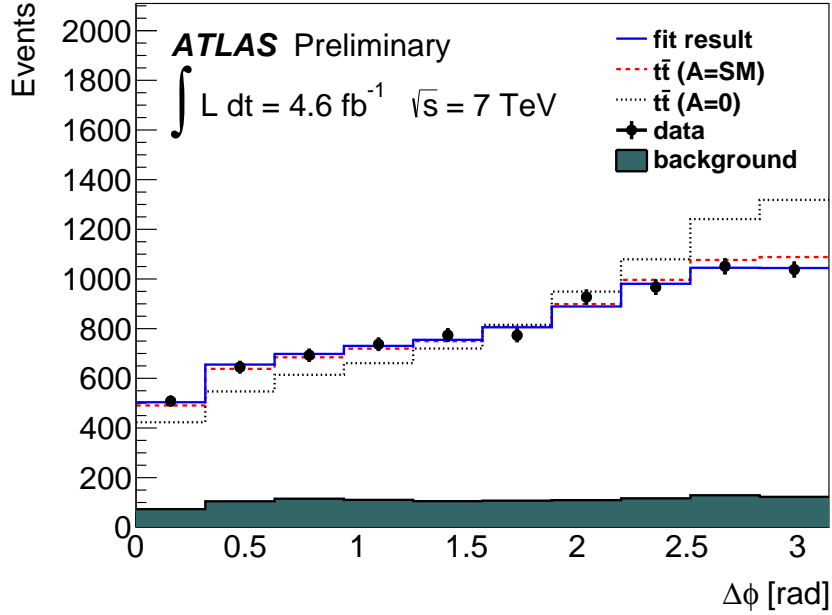
Figure 8.15: Fit results for the $\Delta\phi$ variable in the inclusive $t\bar{t}$ invariant-mass region.

8.4 Extraction of results

8.4.1 $\Delta\phi$ Results

The results for the extraction of f_{SM} in the $\Delta\phi$ variable for the inclusive, low, and high $t\bar{t}$ invariant-mass regimes are presented. The result of the fit, described in Section 7.1, for the inclusive result in the combined channel is shown in Fig. 8.15. By eye it is clear that the data favour the correlated hypothesis rather than the uncorrelated hypothesis. The results for the low and high invariant-mass regimes in the combined channel are shown in Fig. 8.16 and Fig. 8.17, respectively. In both cases, the data clearly tend toward the spin-correlated hypothesis. In both of these figures, the expected behaviour of the observable in different regions of invariant mass is clearly observed, and the lower separation between the hypothesis templates in the high invariant-mass region is apparent.

The results of the fits in all of the individual channels for each region of $t\bar{t}$ invariant mass are presented in Fig. 8.18. The lower statistical power of the e^+e^- and $\mu^+\mu^-$ channels manifests as much larger statistical uncertainties in these channels. The $e^\pm\mu^\mp$ channel dominates the result of the combined fit in all cases. In general, the high invariant-mass regime preferred a spin-correlation slightly higher than is predicted by the SM. In the low invariant-mass region, where this variable is expected to have high sensitivity, the data agrees with the SM prediction very well. In the inclusive selection, the data also agrees with the SM prediction.

Systematic uncertainties on the f_{SM} parameter are presented in Table 8.1 for the inclusive observable, 8.2 for the observable in the low invariant-mass region, and 8.3 for the high mass region. Systematic uncertainties on the $n_{t\bar{t}}$ parameter are presented in Tables 8.4, 8.5, and 8.6 for the inclusive, low, and high invariant-mass regions respectively. Systematic uncertainties dominated over statistical uncertainties in all results. In the inclusive observable, the dominant systematic sources are from ISR/FSR, underlying-event modelling, and renormalisation and factorisation scales. The ISR/FSR is expected to be a large contribution as the $\Delta\phi$ angle is measured in the laboratory frame and is therefore sensitive to jet recoil. In the low and high mass regions, the uncertainties due to jet modelling become large. Unlike the inclusive $\Delta\phi$, the observable in the different mass regions requires full $t\bar{t}$ reconstruction and uncertainties due to jet modelling become important.

All results for the $\Delta\phi$ variable in all channels and invariant-mass regimes agree with the SM hypothesis to within one standard deviation of their uncertainties for both the f_{SM} and $n_{t\bar{t}}$ parameters. The most sensitive result for the f_{SM} parameter is the combined channel in the inclusive invariant-mass regime.

These results represent a large improvement over the systematic uncertainties of the previous result [27]. The data used in these results has twice the integrated luminosity than the previous. As such, the statistical uncertainty is reduced by a factor of $\sqrt{2}$. However, there are also significant improvements in the estimation of some of the sources of systematic uncertainty. The systematic uncertainties due to fake lepton modelling, jet energy scale and ISR/FSR are all improved for the result using the full 2011 data.
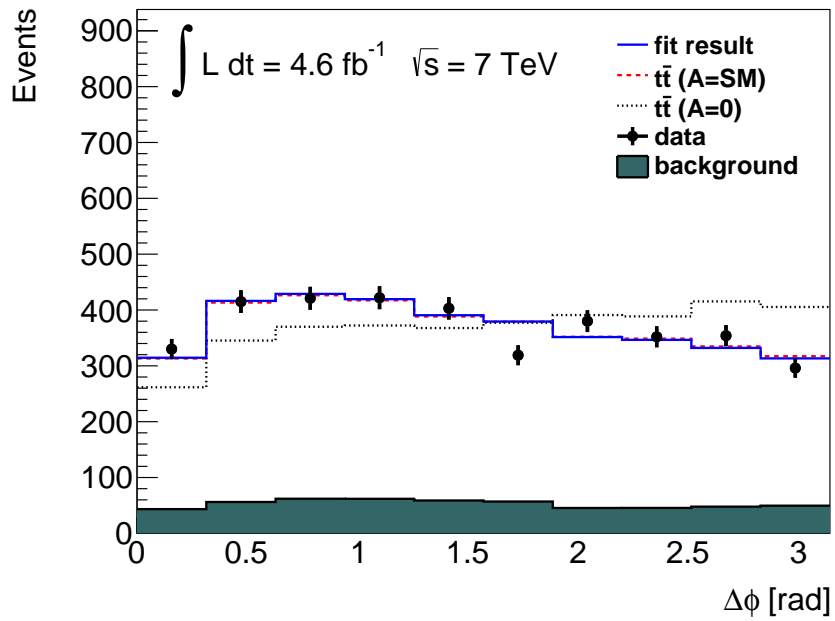
Figure 8.16: Fit results for the $\Delta\phi$ variable in the low $t\bar{t}$ invariant-mass region.
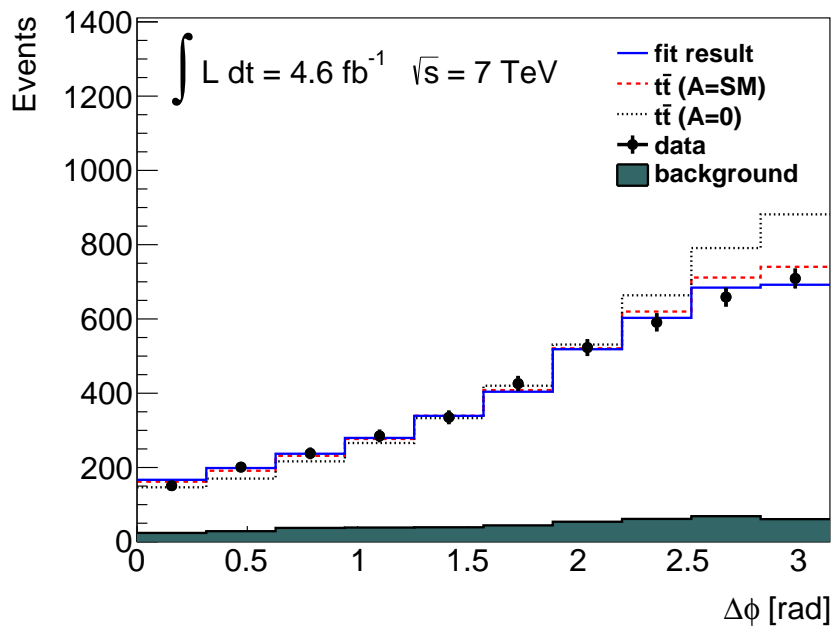
Figure 8.17: Fit results for the $\Delta\phi$ variable in the high $t\bar{t}$ invariant-mass region.
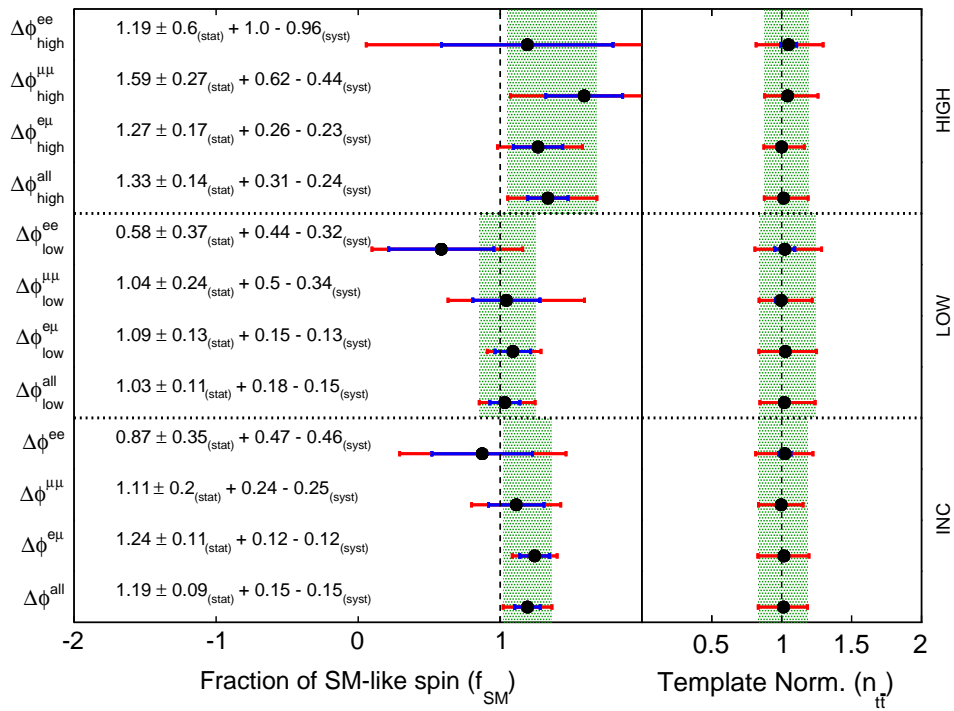
Figure 8.18: Summary of f_{SM} results for the $\Delta\phi$ variable in the inclusive, low, and high invariant-mass region. The left panel shows the results for the f_{SM} variable, the right shows results for the normalisation of the $t\bar{t}$ templates.

Source of uncertainty	e^+e^- channel	$\mu^+\mu^-$ channel	$e^\pm\mu^\mp$ channel	combination
Detector Modelling				
JES	0.081 / 0.120	0.021 / 0.034	0.020 / 0.021	0.015 / 0.023
Jet	0.041 / 0.037	0.018 / 0.018	0.003 / 0.003	0.003 / 0.003
Lepton	0.064 / 0.035	0.010 / 0.010	0.004 / 0.005	0.008 / 0.005
Fake	0.104 / 0.008	±0.006	0.021 / 0.018	0.028 / 0.014
MET	0.072 / 0.006	0.020 / 0.015	0.004 / 0.000	0.012 / 0.002
Background	0.087 / 0.089	0.091 / 0.094	0.023 / 0.023	0.041 / 0.042
Generator Modelling				
Renormalisation / Factorisation scale	±0.197	±0.157	±0.068	±0.085
ISR/FSR	±0.134	±0.127	±0.071	±0.089
Parton Shower and Fragmentation	±0.095	±0.010	±0.007	±0.000
MC Statistics	±0.179	±0.058	±0.032	±0.029
Top Mass	±0.017	±0.018	0.007 / 0.007	±0.000
PDF Uncertainty	±0.028	±0.015	±0.026	±0.022
Colour Reconnection	±0.200	±0.036	±0.008	±0.011
Underlying Event	±0.219	±0.063	±0.022	±0.044
top pT Reweighting	±0.001	±0.010	±0.020	±0.015
Total Systematics	0.472 / 0.460	0.245 / 0.247	0.118 / 0.117	0.147 / 0.146
Data Statistics	±0.354	±0.195	±0.105	±0.090

Table 8.1: Systematic uncertainties on the f_{SM} variable for $\Delta\phi$.

Source of uncertainty	e^+e^- channel	$\mu^+\mu^-$ channel	$e^\pm\mu^\mp$ channel	combination
Detector Modelling				
JES	0.143 / 0.095	0.314 / 0.224	0.082 / 0.039	0.123 / 0.064
Jet	0.286 / 0.045	0.298 / 0.075	0.043 / 0.008	0.049 / 0.020
Lepton	0.067 / 0.064	0.100 / 0.103	0.023 / 0.032	0.036 / 0.045
Fake	0.044 / 0.032	±0.031	0.075 / 0.076	0.046 / 0.047
MET	0.011 / 0.048	0.096 / 0.083	0.031 / 0.021	0.040 / 0.032
Background	0.065 / 0.067	0.044 / 0.045	0.007 / 0.007	0.008 / 0.009
Generator Modelling				
Renormalisation / Factorisation scale	±0.198	±0.128	±0.067	±0.079
ISR/FSR	±0.099	±0.090	±0.039	±0.059
Parton Shower and Fragmentation	±0.002	±0.012	±0.003	±0.004
MC Statistics	±0.131	±0.080	±0.040	±0.035
Top Mass	0.029 / 0.029	±0.020	±0.001	±0.008
Colour Reconnection	±0.061	±0.011	±0.006	±0.005
Underlying Event	±0.083	±0.063	±0.009	±0.014
top pT Reweighting	±0.021	±0.032	±0.011	±0.002
Total Systematics	0.437 / 0.318	0.496 / 0.336	0.153 / 0.129	0.185 / 0.146
Data Statistics	±0.370	±0.236	±0.125	±0.106

Table 8.2: Systematic uncertainties on the f_{SM} variable for $\Delta\phi_{low}$.

Source of uncertainty	e^+e^- channel	$\mu^+\mu^-$ channel	$e^\pm\mu^\mp$ channel	combination
Detector Modelling				
JES	0.202 / 0.238	0.275 / 0.130	0.083 / 0.068	0.114 / 0.069
Jet	0.275 / 0.071	0.344 / 0.032	0.100 / 0.003	0.160 / 0.005
Lepton	0.098 / 0.095	0.104 / 0.106	0.041 / 0.034	0.052 / 0.042
Fake	0.132 / 0.060	±0.034	0.070 / 0.062	0.071 / 0.067
MET	0.089 / 0.038	0.114 / 0.028	0.050 / 0.021	0.064 / 0.013
Background	0.095 / 0.095	0.092 / 0.096	0.041 / 0.042	0.053 / 0.054
Generator Modelling				
Renormalisation / Factorisation scale	±0.235	±0.169	±0.067	±0.095
ISR/FSR	±0.255	±0.156	±0.128	±0.138
Parton Shower and Fragmentation	±0.262	±0.179	±0.114	±0.095
MC Statistics	±0.666	±0.173	±0.062	±0.067
Top Mass	0.030 / 0.030	±0.014	0.022 / 0.022	0.019 / 0.019
Colour Reconnection	±0.343	±0.154	±0.002	±0.021
Underlying Event	±0.290	±0.030	±0.036	±0.049
top pT Reweighting	±0.016	±0.128	±0.009	±0.026
Total Systematics	0.997 / 0.959	0.619 / 0.443	0.260 / 0.227	0.314 / 0.244
Data Statistics	±0.604	±0.271	±0.173	±0.142

Table 8.3: Systematic uncertainties on the f_{SM} variable for $\Delta\phi_{high}$.

Source of uncertainty	e^+e^- channel	$\mu^+\mu^-$ channel	$e^\pm\mu^\mp$ channel	combination
Detector Modelling				
JES	0.030 / 0.068	0.013 / 0.045	0.020 / 0.059	0.019 / 0.056
Jet	0.015 / 0.012	0.010 / 0.009	0.012 / 0.011	0.012 / 0.010
Lepton	0.013 / 0.020	0.005 / 0.005	0.010 / 0.012	0.009 / 0.011
Fake	0.033 / 0.019	±0.002	0.013 / 0.012	0.006 / 0.015
MET	0.009 / 0.017	0.005 / 0.009	0.013 / 0.009	0.011 / 0.010
Background	0.017 / 0.017	0.021 / 0.021	0.015 / 0.015	0.016 / 0.016
Generator Modelling				
Renormalisation / Factorisation scale	±0.007	±0.005	±0.002	±0.003
ISR/FSR	±0.069	±0.010	±0.040	±0.036
Parton Shower and Fragmentation	±0.104	±0.072	±0.091	±0.087
MC Statistics	±0.008	±0.002	±0.002	±0.002
Top Mass	±0.023	±0.024	±0.028	±0.027
PDF Uncertainty	±0.110	±0.112	±0.112	±0.112
Colour Reconnection	±0.062	±0.005	±0.037	±0.030
Underlying Event	±0.027	±0.003	±0.019	±0.016
top pT Reweighting	±0.052	±0.066	±0.074	±0.071
Total Systematics	0.196 / 0.204	0.154 / 0.160	0.178 / 0.186	0.172 / 0.180
Data Statistics	±0.044	±0.026	±0.016	±0.013

Table 8.4: Systematic uncertainties on the $t\bar{t}$ normalisation for $\Delta\phi$.

174

Source of uncertainty	e^+e^- channel	$\mu^+\mu^-$ channel	$e^\pm\mu^\mp$ channel	combination
Detector Modelling				
JES	0.023 / 0.065	0.039 / 0.069	0.050 / 0.086	0.044 / 0.079
Jet	0.167 / 0.011	0.169 / 0.015	0.141 / 0.027	0.152 / 0.023
Lepton	0.017 / 0.019	0.015 / 0.016	0.023 / 0.023	0.020 / 0.021
Fake	0.026 / 0.025	±0.010	0.023 / 0.023	0.017 / 0.025
MET	0.011 / 0.019	0.006 / 0.013	0.021 / 0.018	0.017 / 0.017
Background	0.022 / 0.022	0.017 / 0.017	0.017 / 0.017	0.017 / 0.016
Generator Modelling				
Renormalisation / Factorisation scale	±0.005	±0.003	±0.000	±0.000
ISR/FSR	±0.084	±0.015	±0.054	±0.048
Parton Shower and Fragmentation	±0.152	±0.105	±0.118	±0.117
MC Statistics	±0.005	±0.002	±0.000	±0.000
Top Mass	±0.023	0.023 / 0.023	±0.039	0.028 / 0.028
Colour Reconnection	±0.046	±0.032	±0.043	±0.027
Underlying Event	±0.008	±0.020	±0.026	±0.015
top pT Reweighting	±0.037	±0.064	±0.065	±0.062
Total Systematics	0.254 / 0.201	0.219 / 0.152	0.223 / 0.187	0.219 / 0.174
Data Statistics	±0.071	±0.040	±0.024	±0.020

Table 8.5: Systematic uncertainties on the $t\bar{t}$ normalisation for $\Delta\phi_{low}$.

Source of uncertainty	e^+e^- channel	$\mu^+\mu^-$ channel	$e^\pm\mu^\mp$ channel	combination
Detector Modelling				
JES	0.084 / 0.124	0.037 / 0.060	0.021 / 0.059	0.028 / 0.064
Jet	0.123 / 0.023	0.153 / 0.023	0.115 / 0.007	0.125 / 0.011
Lepton	0.032 / 0.045	0.016 / 0.010	0.009 / 0.013	0.011 / 0.016
Fake	0.051 / 0.010	±0.019	0.028 / 0.028	0.027 / 0.028
MET	0.024 / 0.032	0.015 / 0.025	0.012 / 0.011	0.014 / 0.016
Background	0.013 / 0.013	0.023 / 0.023	0.013 / 0.013	0.015 / 0.015
Generator Modelling				
Renormalisation / Factorisation scale	±0.010	±0.012	±0.004	±0.006
ISR/FSR	±0.083	±0.049	±0.016	±0.030
Parton Shower and Fragmentation	±0.076	±0.030	±0.060	±0.054
MC Statistics	±0.024	±0.013	±0.004	±0.004
Top Mass	±0.020	±0.031	±0.025	±0.023
Colour Reconnection	±0.092	±0.064	±0.024	±0.040
Underlying Event	±0.057	±0.059	±0.004	±0.022
top pT Reweighting	±0.074	±0.088	±0.076	±0.080
Total Systematics	0.240 / 0.225	0.215 / 0.160	0.161 / 0.125	0.175 / 0.137
Data Statistics	±0.058	±0.036	±0.022	±0.018

Table 8.6: Systematic uncertainties on the $t\bar{t}$ normalisation for $\Delta\phi_{high}$.
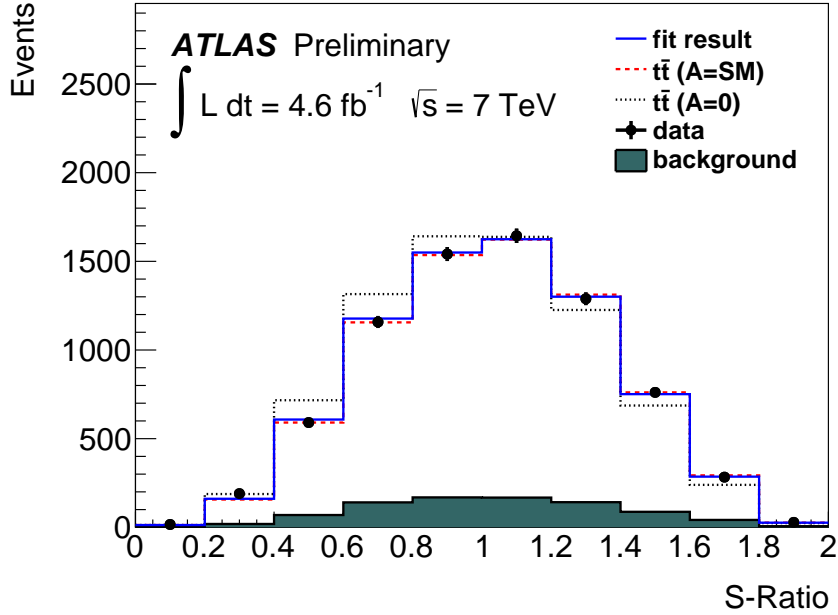
Figure 8.19: Fit results for the S-Ratio variable in the inclusive $t\bar{t}$ invariant-mass region.

8.4.2 S-Ratio Results

The results for the extraction of f_{SM} in the S-Ratio variable for the inclusive, low and high $t\bar{t}$ invariant-mass regimes are presented. The result of the fit, described in Section 7.1, for the inclusive result in the combined channel is shown in Fig. 8.19. Similarly to the $\Delta\phi$ observable, it is clear that the data favour the correlated hypothesis rather than the uncorrelated hypothesis. The results for the low and high invariant-mass regimes in the combined channel are shown in Fig. 8.20 and Fig. 8.21, respectively. In the low invariant mass case, the data clearly tend toward the spin-correlated hypothesis. In the high invariant-mass region this is less apparent bye eye, but can be observed in the numerical results of the fit. In both of these figures, the expected behaviour of the observable in different regions of invariant mass is clearly observed. As with the $\Delta\phi$ observable, the lower separation between the hypothesis templates in the high invariant-mass region is apparent.

The results of the fits in all of the individual channels for each region of $t\bar{t}$ invariant mass are presented in Fig. 8.22. The $e^{\pm}\mu^{\mp}$ channel dominates the result of the combined fit in all cases. Unlike the $\Delta\phi$ result, all invariant-mass regions preferred a spin correlation slightly lower than is predicted by the SM but within one standard deviation of the SM prediction. The low statistics and poor separation of the hypothesis templates in the high invariant-mass region results in large uncertainties in the $e^{+}e^{-}$ and $\mu^{+}\mu^{-}$ channels.

Systematic uncertainties on the f_{SM} parameter are presented in Table 8.7 for the inclusive observable, 8.9 for the observable in the low invariant-mass region, and 8.8 for the high mass region. Systematic uncertainties on the $n_{t\bar{t}}$ parameter are presented in Tables 8.10, 8.11, and 8.12 for the inclusive, low, and high invariant-mass regions respectively.

Systematic uncertainties dominated over statistical uncertainties in the e^+e^- and $\mu^+\mu^-$ channels and were of similar magnitude in the $e^\pm\mu^\mp$ channel. Renormalisation and factorisation scale and underlying-event modelling systematics are dominant sources of systematic uncertainty for the inclusive measurement. In the low invariant-mass regime, uncertainties due to parton shower and hadronisation are also a dominant effect. In the high invariant-mass regime all reconstructed objects, not only jets, have large associated uncertainties as well as a much larger effect due fake lepton estimates.

All results for the S-Ratio observable in all channels and invariant-mass regimes agree with the SM hypothesis to within approximately one standard deviation of their uncertainties for both the f_{SM} and $n_{t\bar{t}}$ parameters. In some cases the disagreement is slightly more than one standard deviation, but always much less than two. The most sensitive result for the f_{SM} parameter is the combined channel in the inclusive invariant-mass regime.
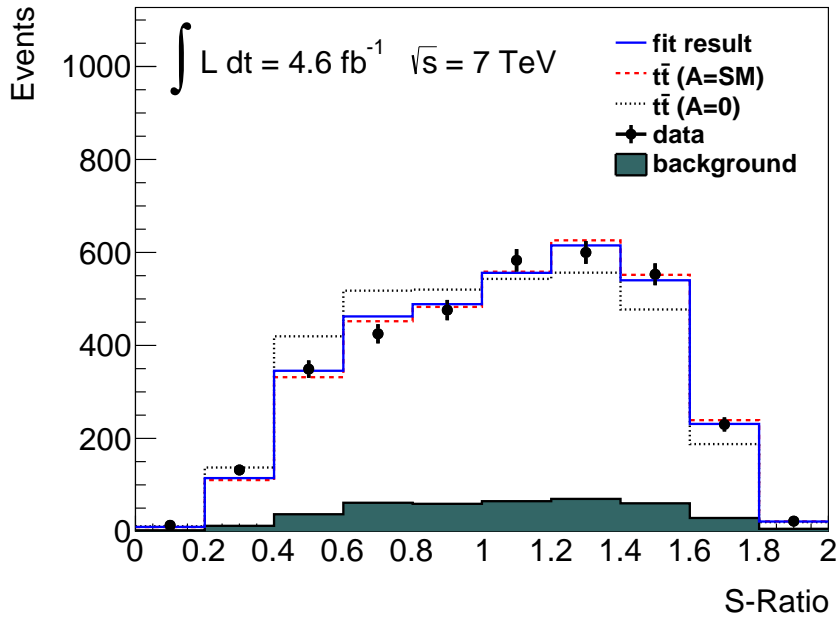
Figure 8.20: Fit results for the S-Ratio variable in the low $t\bar{t}$ invariant-mass region.
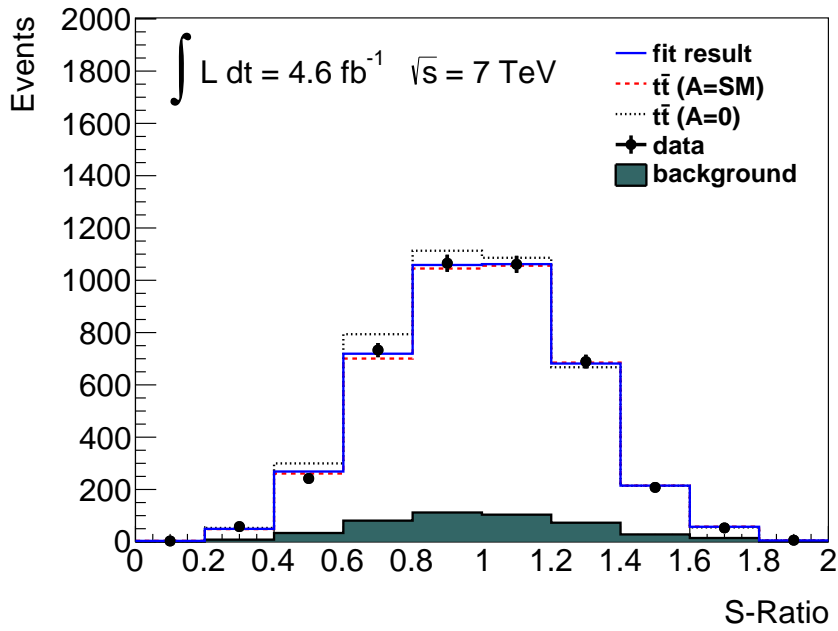
Figure 8.21: Fit results for the S-Ratio variable in the high $t\bar{t}$ invariant-mass region.
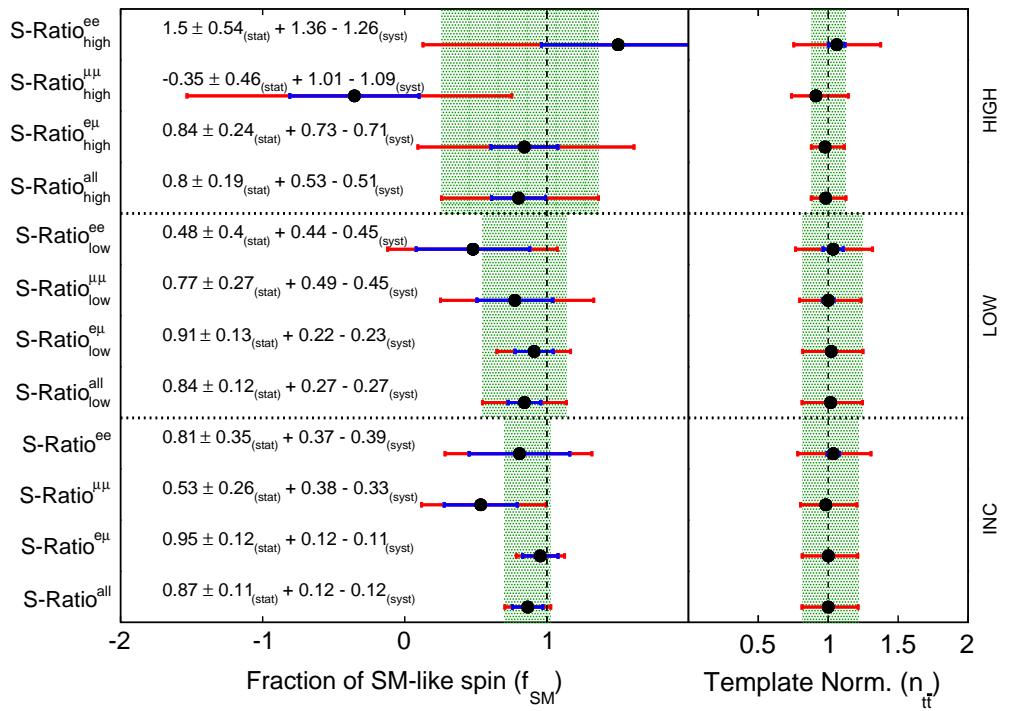
Figure 8.22: Summary of f_{SM} results for the S-Ratio variable in the inclusive, low, and high invariant-mass regions. The left panel shows the results for the f_{SM} variable, the right shows results for the normalisation of the $t\bar{t}$ templates.

Source of uncertainty	e^+e^- channel	$\mu^+\mu^-$ channel	$e^\pm\mu^\mp$ channel	combination
Detector Modelling				
JES	0.212 / 0.244	0.085 / 0.083	0.027 / 0.036	0.037 / 0.041
Jet	0.087 / 0.051	0.200 / 0.024	0.028 / 0.015	0.027 / 0.013
Lepton	0.050 / 0.035	0.030 / 0.037	0.026 / 0.013	0.017 / 0.011
Fake	0.031 / 0.079	±0.030	0.017 / 0.011	0.026 / 0.022
MET	0.013 / 0.021	0.008 / 0.035	0.012 / 0.005	0.006 / 0.009
Background	0.061 / 0.061	0.018 / 0.018	0.018 / 0.018	0.013 / 0.014
Generator Modelling				
Renormalisation / Factorisation scale	±0.095	±0.174	±0.066	±0.076
ISR/FSR	±0.078	±0.047	±0.006	±0.020
Parton Shower and Fragmentation	±0.084	±0.188	±0.060	±0.004
MC Statistics	±0.127	±0.095	±0.034	±0.033
Top Mass	±0.044	±0.037	0.004 / 0.004	0.015 / 0.015
PDF Uncertainty	±0.047	±0.050	±0.016	±0.012
Colour Reconnection	±0.101	±0.002	±0.012	±0.019
Underlying Event	±0.148	±0.123	±0.035	±0.059
top pT Reweighting	±0.010	±0.009	±0.002	±0.004
Total Systematics	0.367 / 0.386	0.382 / 0.328	0.117 / 0.113	0.122 / 0.119
Data Statistics	±0.354	±0.257	±0.125	±0.107

Table 8.7: Systematic uncertainties on the f_{SM} variable for S-Ratio.

Source of uncertainty	e^+e^- channel	$\mu^+\mu^-$ channel	$e^\pm\mu^\mp$ channel	combination
Detector Modelling				
JES	1.110 / 1.032	0.553 / 0.755	0.534 / 0.519	0.337 / 0.323
Jet	0.342 / 0.301	0.333 / 0.117	0.190 / 0.143	0.134 / 0.109
Lepton	0.267 / 0.286	0.202 / 0.176	0.214 / 0.216	0.169 / 0.150
Fake	0.080 / 0.090	±0.060	0.079 / 0.080	0.167 / 0.165
MET	0.280 / 0.047	0.055 / 0.088	0.171 / 0.165	0.120 / 0.125
Background	0.085 / 0.085	0.130 / 0.130	0.020 / 0.020	0.028 / 0.028
Generator Modelling				
Renormalisation / Factorisation scale	±0.228	±0.454	±0.175	±0.126
ISR/FSR	±0.136	±0.108	±0.038	±0.049
Parton Shower and Fragmentation	±0.149	±0.159	±0.297	±0.173
MC Statistics	±0.334	±0.515	±0.092	±0.102
Top Mass	0.021 / 0.021	±0.099	0.020 / 0.020	±0.034
Colour Reconnection	±0.240	±0.026	±0.077	±0.111
Underlying Event	±0.258	±0.090	±0.029	±0.067
top pT Reweighting	±0.111	±0.104	±0.002	±0.008
Total Systematics	1.362 / 1.263	1.009 / 1.087	0.734 / 0.712	0.529 / 0.509
Data Statistics	±0.539	±0.455	±0.235	±0.190

Table 8.8: Systematic uncertainties on the f_{SM} variable for S-Ratio$_{high}$.

Source of uncertainty	e^+e^- channel	$\mu^+\mu^-$ channel	emu channel	combination
Detector Modelling				
JES	0.137 / 0.169	0.354 / 0.318	0.179 / 0.186	0.216 / 0.214
Jet	0.070 / 0.019	0.164 / 0.106	0.060 / 0.057	0.077 / 0.062
Lepton	0.050 / 0.021	0.126 / 0.117	0.043 / 0.059	0.055 / 0.065
Fake	0.045 / 0.089	±0.044	0.021 / 0.020	0.013 / 0.007
MET	0.039 / 0.019	0.096 / 0.129	0.052 / 0.049	0.051 / 0.062
Background	0.053 / 0.053	0.021 / 0.021	0.015 / 0.015	0.013 / 0.014
Generator Modelling				
Renormalisation / Factorisation scale	±0.136	±0.111	±0.019	±0.042
ISR/FSR	±0.058	±0.064	±0.009	±0.015
Parton Shower and Fragmentation	±0.009	±0.071	±0.003	±0.008
MC Statistics	±0.117	±0.097	±0.036	±0.035
Top Mass	±0.053	0.028 / 0.028	0.007 / 0.007	0.005 / 0.005
Colour Reconnection	±0.204	±0.012	±0.041	±0.055
Underlying Event	±0.283	±0.158	±0.056	±0.097
top pT Reweighting	±0.003	±0.009	±0.006	±0.006
Total Systematics	0.439 / 0.448	0.487 / 0.450	0.218 / 0.226	0.273 / 0.272
Data Statistics	±0.400	±0.267	±0.135	±0.115

Table 8.9: Systematic uncertainties on the f_{SM} variable for S-Ratio$_{low}$.

Source of uncertainty	ee channel	mumu channel	emu channel	combination
Detector Modelling				
JES	0.100 / 0.132	0.075 / 0.096	0.051 / 0.084	0.062 / 0.092
Jet	0.127 / 0.034	0.147 / 0.030	0.119 / 0.023	0.127 / 0.026
Lepton	0.036 / 0.047	0.031 / 0.031	0.023 / 0.025	0.026 / 0.028
Fake	0.033 / 0.002	±0.001	0.014 / 0.012	0.007 / 0.014
MET	0.031 / 0.035	0.023 / 0.029	0.022 / 0.020	0.024 / 0.024
Background	0.013 / 0.013	0.015 / 0.015	0.012 / 0.012	0.012 / 0.012
Generator Modelling				
Renormalisation / Factorisation scale	±0.005	±0.005	±0.002	±0.003
ISR/FSR	±0.088	±0.000	±0.028	±0.028
Parton Shower and Fragmentation	±0.105	±0.075	±0.089	±0.086
MC Statistics	±0.005	±0.003	±0.002	±0.002
Top Mass	0.023 / 0.023	0.022 / 0.022	0.028 / 0.028	0.026 / 0.026
PDF Uncertainty	±0.111	±0.110	±0.112	±0.111
Colour Reconnection	±0.074	±0.022	±0.022	±0.017
Underlying Event	±0.033	±0.017	±0.004	±0.002
top pT Reweighting	±0.050	±0.033	±0.058	±0.052
Total Systematics	0.265 / 0.251	0.221 / 0.179	0.210 / 0.186	0.213 / 0.187
Data Statistics	±0.045	±0.026	±0.016	±0.013

Table 8.10: Systematic uncertainties on the $t\bar{t}$ normalisation for S-Ratio.

Source of uncertainty	e^+e^- channel	$\mu^+\mu^-$ channel	$e^\pm\mu^\mp$ channel	combination
Detector Modelling				
JES	0.107 / 0.144	0.111 / 0.134	0.082 / 0.113	0.091 / 0.120
Jet	0.136 / 0.039	0.147 / 0.040	0.132 / 0.038	0.137 / 0.038
Lepton	0.049 / 0.051	0.043 / 0.044	0.037 / 0.037	0.039 / 0.039
Fake	0.028 / 0.007	±0.013	0.026 / 0.025	0.022 / 0.027
MET	0.037 / 0.045	0.027 / 0.039	0.030 / 0.029	0.030 / 0.033
Background	0.012 / 0.012	0.013 / 0.013	0.015 / 0.015	0.014 / 0.014
Generator Modelling				
Renormalisation / Factorisation scale	±0.004	±0.003	±0.000	±0.000
ISR/FSR	±0.101	±0.021	±0.055	±0.049
Parton Shower and Fragmentation	±0.161	±0.111	±0.122	±0.123
MC Statistics	±0.003	±0.003	±0.002	±0.002
Top Mass	0.021 / 0.021	±0.021	±0.029	±0.027
Colour Reconnection	±0.043	±0.028	±0.039	±0.024
Underlying Event	±0.004	±0.014	±0.023	±0.011
top pT Reweighting	±0.034	±0.049	±0.054	±0.051
Total Systematics	0.273 / 0.258	0.231 / 0.200	0.226 / 0.202	0.228 / 0.203
Data Statistics	±0.072	±0.040	±0.024	±0.020

Table 8.11: Systematic uncertainties on the $t\bar{t}$ normalisation for S-Ratio$_{low}$.

Source of uncertainty	e^+e^- channel	$\mu^+\mu^-$ channel	$e^\pm\mu^\mp$ channel	combination
Detector Modelling				
JES	0.145 / 0.187	0.056 / 0.060	0.013 / 0.043	0.025 / 0.057
Jet	0.125 / 0.040	0.154 / 0.017	0.105 / 0.004	0.114 / 0.010
Lepton	0.043 / 0.056	0.021 / 0.021	0.003 / 0.006	0.007 / 0.012
Fake	0.068 / 0.007	±0.019	0.031 / 0.030	0.033 / 0.033
MET	0.043 / 0.030	0.015 / 0.013	0.009 / 0.005	0.013 / 0.010
Background	0.016 / 0.016	0.023 / 0.023	0.011 / 0.011	0.013 / 0.013
Generator Modelling				
Renormalisation / Factorisation scale	±0.011	±0.030	±0.010	±0.007
ISR/FSR	±0.100	±0.085	±0.002	±0.003
Parton Shower and Fragmentation	±0.074	±0.050	±0.048	±0.047
MC Statistics	±0.015	±0.027	±0.005	±0.006
Top Mass	0.022 / 0.022	0.025 / 0.025	0.027 / 0.027	±0.026
Colour Reconnection	±0.129	±0.082	±0.005	±0.013
Underlying Event	±0.093	±0.071	±0.015	±0.003
top pT Reweighting	±0.092	±0.007	±0.053	±0.049
Total Systematics	0.309 / 0.301	0.229 / 0.171	0.136 / 0.096	0.143 / 0.102
Data Statistics	±0.059	±0.032	±0.021	±0.017

Table 8.12: Systematic uncertainties on the $t\bar{t}$ normalisation for S-Ratio$_{high}$.

Figure 8.23: Fit results for the $\cos(\theta_+)\cos(\theta_-)_{Maximal}$ variable in the inclusive $t\bar{t}$ invariant-mass region.

8.4.3 $\quad cos(\theta_+)cos(\theta_-)_{Maximal}$ Results

The result of the fit for the combined channel in the inclusive invariant-mass regime for the $cos(\theta_+)cos(\theta_-)$ in the Maximal basis is shown in Fig. 8.23. The data, by eye, appears to favour the SM spin-correlation hypothesis despite the poor separation between the two hypothesis templates when compared to the $\Delta\phi$ and S-Ratio observables. The fit results for the low and high invariant-mass regions are presented in Fig. 8.24 and Fig. 8.25, respectively. In both figures, the data also appears to favour the SM hypothesis. The fit results for f_{SM} and $n_{t\bar{t}}$ for all channels in all regions of invariant mass are presented in Fig. 8.26. The results in all regions of invariant mass agree with the SM hypothesis to within approximately one standard deviation. A slight preference towards a lower value is observed; however, the significance of this trend is not as dramatic as it first appears as the combined channel fits are statistically correlated with the individual channels and the inclusive region results are statistically correlated with the high and low mass region results.

The systematics uncertainties on the f_{SM} parameter are shown in Table 8.13, Table 8.15, and Table 8.17 for the inclusive, low, and high invariant-mass regions, respectively. Similar tables are presented for the $n_{t\bar{t}}$ parameter in Table 8.14, Table 8.16, and Table 8.18, again for inclusive, low, and high, respectively. Systematic uncertainties are either greater than, or comparable to, the statistical uncertainties in all results. Uncertainties due to jets, parton shower and fragmentation, and renormalisation and
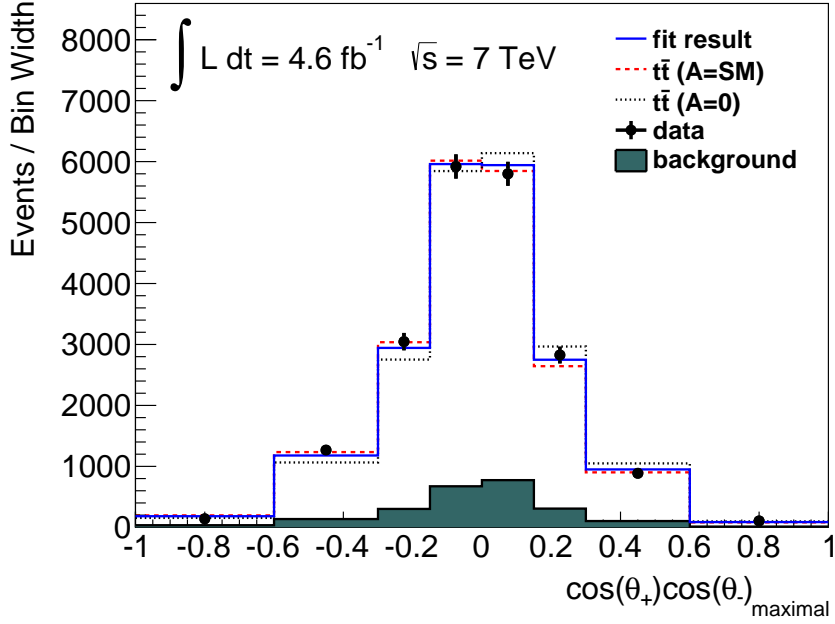
Figure 8.24: Fit results for the $\cos(\theta_+)\cos(\theta_-)_{Maximal}$ variable in the low $t\bar{t}$ invariant-mass region.

factorisation scale are the dominant source of systematic uncertainty in all invariant-mass regimes.

The Maximal basis shows the best performance of the two bases used for the $\cos(\theta_+)\cos(\theta_-)$ observable. This is to some degree expected from the truth level studies, where the maximal basis is shown to have slightly better separation between the spin-correlated and uncorrelated hypotheses.

All results for the $\cos(\theta_+)\cos(\theta_-)_{Maximal}$ variable in all channels and invariant-mass regimes agree with the SM hypothesis to within approximately one standard deviation of their uncertainties for both the f_{SM} and $n_{t\bar{t}}$ parameters. The most sensitive result for the f_{SM} parameter is the combined channel in the inclusive invariant-mass regime. In statistically independent samples, all results converging to the SM value within one standard deviation of their uncertainties would indicate an over-estimation of the un-certainties. One would naively expect that only 68% of results should agree within one standard deviation. However, as stated previously, a high degree of statistical correlation occurs between the individual observables and between the analysis channels and invariant-mass regimes. In addition, the effect of statistical and systematic uncertainties are not uniform amongst the results and can affect some observables and channels more than others. It is therefore consistent that more than 68% of results agree with the SM hypothesis to within one standard deviation.

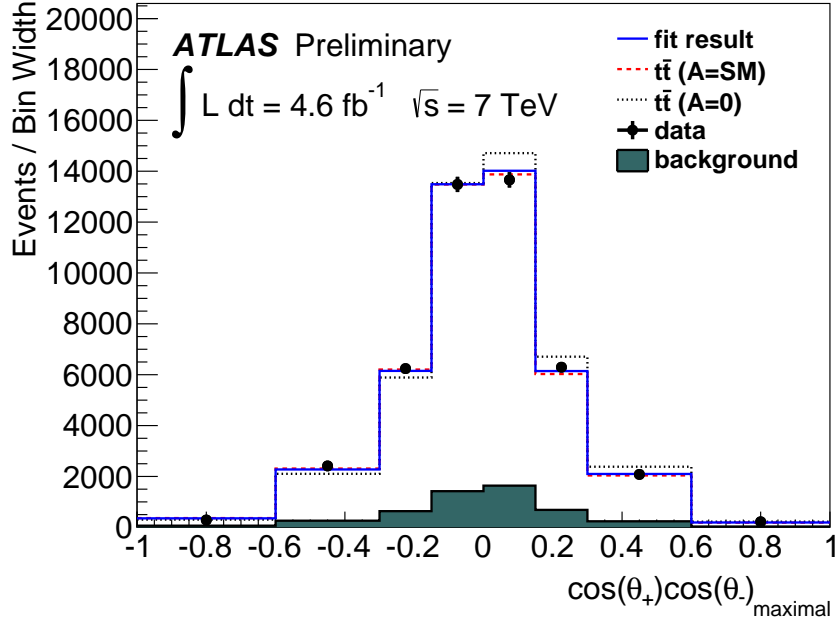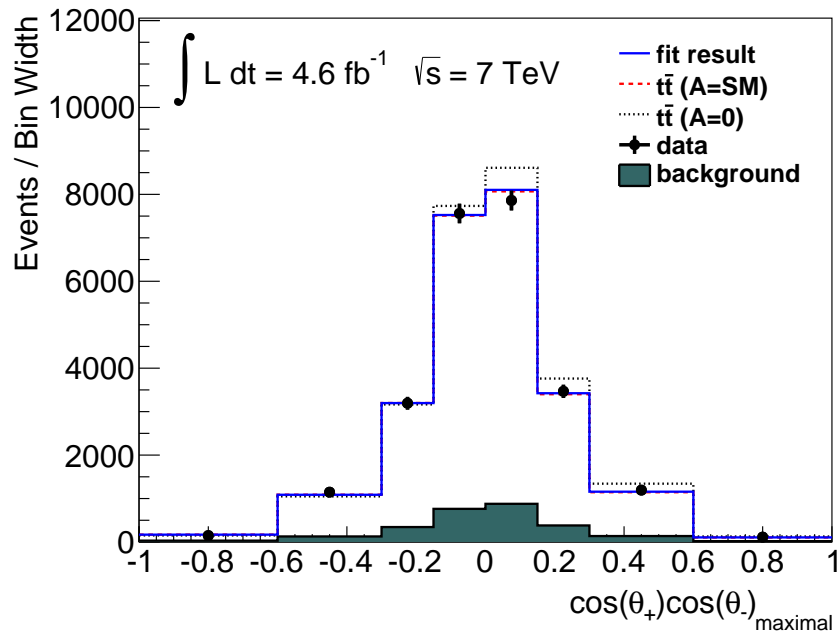**Figure 8.25:** Fit results for the $\cos(\theta_+)\cos(\theta_-)_{Maximal}$ variable in the high $t\bar{t}$ invariant-mass region.
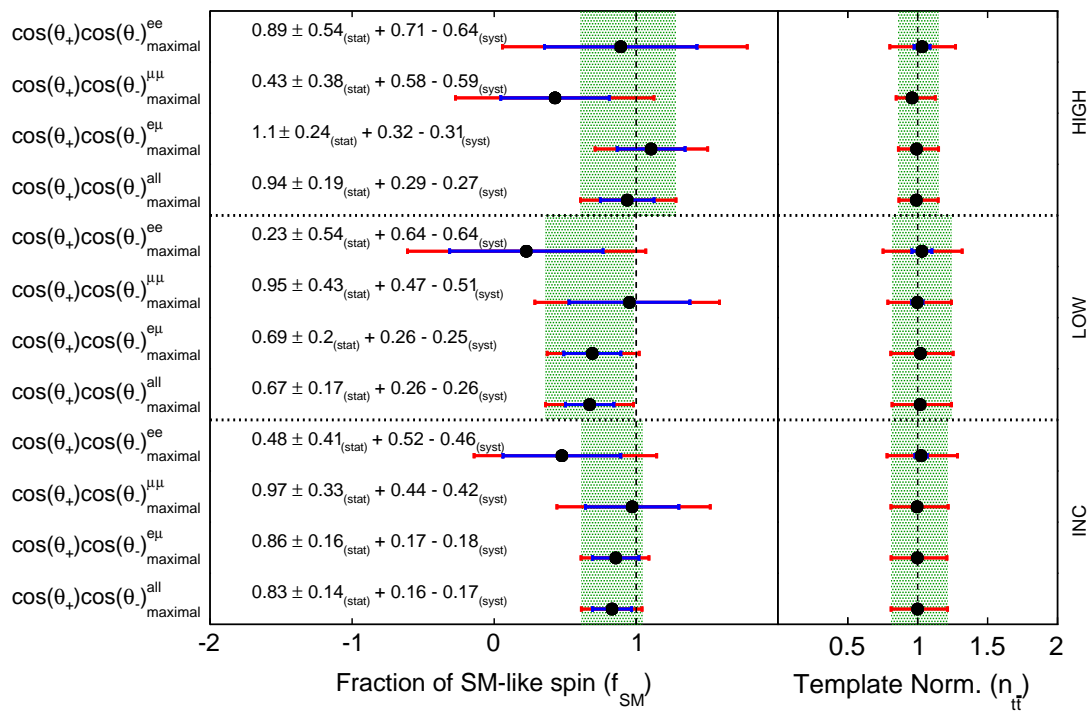
Figure 8.26: Summary of f_{SM} results for the $\cos(\theta_+)\cos(\theta_-)$ variable in the Maximal basis in the inclusive, low, and high invariant-mass regions. The left panel shows the results for the f_{SM} parameter, the right shows results for the $n_{t\bar{t}}$ parameter.

Source of uncertainty	e^+e^- channel	$\mu^+\mu^-$ channel	$e^\pm\mu^\mp$ channel	combination
Detector Modelling				
JES	0.260 / 0.213	0.173 / 0.126	0.093 / 0.116	0.058 / 0.077
Jet	0.093 / 0.051	0.140 / 0.116	0.022 / 0.020	0.010 / 0.008
Lepton	0.053 / 0.036	0.080 / 0.057	0.027 / 0.047	0.020 / 0.025
Fake	0.196 / 0.066	±0.012	0.059 / 0.056	0.041 / 0.038
MET	0.023 / 0.034	0.042 / 0.057	0.040 / 0.028	0.020 / 0.012
Background	0.025 / 0.025	0.036 / 0.036	0.012 / 0.012	0.016 / 0.017
Generator Modelling				
Renormalisation / Factorisation scale	±0.141	±0.321	±0.027	±0.071
ISR/FSR	±0.011	±0.061	±0.010	±0.008
Parton Shower and Fragmentation	±0.322	±0.119	±0.038	±0.081
MC Statistics	±0.135	±0.106	±0.045	±0.039
Top Mass	±0.019	0.020 / 0.020	0.032 / 0.032	±0.023
PDF Uncertainty	±0.050	±0.020	±0.021	±0.030
Colour Reconnection	±0.069	±0.041	±0.081	±0.066
Underlying Event	±0.047	±0.019	±0.013	±0.001
top pT Reweighting	±0.048	±0.013	±0.017	±0.017
Total Systematics	0.522 / 0.458	0.441 / 0.415	0.167 / 0.182	0.160 / 0.166
Data Statistics	±0.415	±0.329	±0.163	±0.138

Table 8.13: Systematic uncertainties on the f_{SM} variable for $\cos(\theta_+)\cos(\theta_-)$ Maximal.

Source of uncertainty	e^+e^- channel	$\mu^+\mu^-$ channel	$e^\pm\mu^\mp$ channel	combination
Detector Modelling				
JES	0.093 / 0.123	0.073 / 0.098	0.055 / 0.088	0.063 / 0.093
Jet	0.128 / 0.034	0.140 / 0.027	0.121 / 0.023	0.126 / 0.025
Lepton	0.038 / 0.047	0.028 / 0.029	0.024 / 0.027	0.026 / 0.029
Fake	0.029 / 0.009	±0.000	0.015 / 0.012	0.007 / 0.014
MET	0.032 / 0.037	0.023 / 0.028	0.024 / 0.021	0.024 / 0.024
Background	0.011 / 0.011	0.014 / 0.014	0.013 / 0.012	0.012 / 0.012
Generator Modelling				
Renormalisation / Factorisation scale	±0.005	±0.009	±0.001	±0.002
ISR/FSR	±0.079	±0.014	±0.026	±0.027
Parton Shower and Fragmentation	±0.112	±0.074	±0.091	±0.089
MC Statistics	±0.005	±0.004	±0.002	±0.002
Top Mass	±0.022	0.022 / 0.022	0.026 / 0.026	±0.025
PDF Uncertainty	±0.108	±0.112	±0.111	±0.111
Colour Reconnection	±0.069	±0.007	±0.022	±0.019
Underlying Event	±0.025	±0.001	±0.003	±0.003
top pT Reweighting	±0.032	±0.059	±0.052	±0.051
Total Systematics	0.256 / 0.240	0.220 / 0.185	0.210 / 0.187	0.214 / 0.189
Data Statistics	±0.044	±0.026	±0.016	±0.013

Table 8.14: Systematic uncertainties on the $t\bar{t}$ normalisation for $\cos(\theta_+)\cos(\theta_-)$ Maximal.

Source of uncertainty	e^+e^- channel	$\mu^+\mu^-$ channel	$e^\pm\mu^\mp$ channel	combination
Detector Modelling				
JES	0.188 / 0.224	0.227 / 0.308	0.198 / 0.179	0.153 / 0.165
Jet	0.157 / 0.138	0.092 / 0.089	0.063 / 0.048	0.056 / 0.033
Lepton	0.072 / 0.035	0.065 / 0.066	0.038 / 0.058	0.040 / 0.047
Fake	0.115 / 0.034	±0.061	0.050 / 0.051	0.030 / 0.025
MET	0.047 / 0.047	0.049 / 0.022	0.057 / 0.040	0.040 / 0.030
Background	0.027 / 0.027	0.043 / 0.044	0.018 / 0.018	0.018 / 0.018
Generator Modelling				
Renormalisation / Factorisation scale	±0.089	±0.015	±0.059	±0.039
ISR/FSR	±0.025	±0.054	±0.008	±0.020
Parton Shower and Fragmentation	±0.428	±0.226	±0.102	±0.173
MC Statistics	±0.160	±0.228	±0.054	±0.053
Top Mass	0.039 / 0.039	±0.014	±0.011	0.001 / 0.001
Colour Reconnection	±0.083	±0.165	±0.021	±0.008
Underlying Event	±0.324	±0.107	±0.024	±0.007
top pT Reweighting	±0.043	±0.058	±0.011	±0.007
Total Systematics	0.644 / 0.638	0.470 / 0.512	0.262 / 0.246	0.257 / 0.259
Data Statistics	±0.540	±0.425	±0.201	±0.171

Table 8.15: Systematic uncertainties on the f_{SM} variable for $\cos(\theta_+)\cos(\theta_-)_{low}$ Maximal.

Source of uncertainty	e^+e^- channel	$\mu^+\mu^-$ channel	$e^\pm\mu^\mp$ channel	combination
Detector Modelling				
JES	0.116 / 0.155	0.119 / 0.137	0.080 / 0.113	0.089 / 0.120
Jet	0.136 / 0.038	0.150 / 0.041	0.132 / 0.036	0.137 / 0.037
Lepton	0.054 / 0.054	0.046 / 0.048	0.036 / 0.036	0.039 / 0.039
Fake	0.015 / 0.013	±0.013	0.026 / 0.026	0.023 / 0.028
MET	0.041 / 0.048	0.029 / 0.043	0.030 / 0.029	0.030 / 0.033
Background	0.011 / 0.011	0.014 / 0.014	0.015 / 0.015	0.014 / 0.014
Generator Modelling				
Renormalisation / Factorisation scale	±0.001	±0.000	±0.001	±0.000
ISR/FSR	±0.096	±0.019	±0.053	±0.050
Parton Shower and Fragmentation	±0.170	±0.107	±0.122	±0.122
MC Statistics	±0.004	±0.007	±0.000	±0.002
Top Mass	0.021 / 0.021	±0.020	0.077 / 0.077	0.027 / 0.027
Colour Reconnection	±0.043	±0.034	±0.038	±0.025
Underlying Event	±0.007	±0.024	±0.022	±0.012
top pT Reweighting	±0.016	±0.061	±0.041	±0.040
Total Systematics	0.279 / 0.268	0.240 / 0.207	0.233 / 0.210	0.224 / 0.200
Data Statistics	±0.072	±0.040	±0.024	±0.020

Table 8.16: Systematic uncertainties on the $t\bar{t}$ normalisation for $\cos(\theta_+)\cos(\theta_-)_{low}$ Maximal.

Source of uncertainty	e^+e^- channel	$\mu^+\mu^-$ channel	$e^\pm\mu^\mp$ channel	combination
Detector Modelling				
JES	0.334 / 0.251	0.256 / 0.280	0.126 / 0.112	0.120 / 0.084
Jet	0.129 / 0.127	0.078 / 0.076	0.073 / 0.049	0.075 / 0.056
Lepton	0.075 / 0.085	0.177 / 0.158	0.054 / 0.069	0.038 / 0.029
Fake	0.285 / 0.166	±0.003	0.172 / 0.172	0.113 / 0.113
MET	0.048 / 0.058	0.067 / 0.064	0.023 / 0.047	0.011 / 0.028
Background	0.061 / 0.061	0.035 / 0.036	0.023 / 0.023	0.018 / 0.018
Generator Modelling				
Renormalisation / Factorisation scale	±0.055	±0.393	±0.089	±0.129
ISR/FSR	±0.001	±0.038	±0.002	±0.000
Parton Shower and Fragmentation	±0.145	±0.119	±0.047	±0.014
MC Statistics	±0.311	±0.206	±0.089	±0.087
Top Mass	0.003 / 0.003	±0.021	±0.046	±0.032
Colour Reconnection	±0.221	±0.054	±0.161	±0.142
Underlying Event	±0.335	±0.102	±0.007	±0.018
top pT Reweighting	±0.042	±0.061	±0.019	±0.036
Total Systematics	0.711 / 0.636	0.582 / 0.587	0.318 / 0.314	0.286 / 0.269
Data Statistics	±0.537	±0.382	±0.239	±0.189

Table 8.17: Systematic uncertainties on the f_{SM} variable for $\cos(\theta_+)\cos(\theta_-)_{high}$ Maximal.

Source of uncertainty	e^+e^- channel	$\mu^+\mu^-$ channel	$e^\pm\mu^\mp$ channel	combination
Detector Modelling				
JES	0.090 / 0.127	0.039 / 0.069	0.028 / 0.066	0.036 / 0.072
Jet	0.117 / 0.032	0.136 / 0.016	0.108 / 0.009	0.115 / 0.012
Lepton	0.032 / 0.045	0.011 / 0.013	0.013 / 0.020	0.015 / 0.021
Fake	0.025 / 0.014	±0.016	0.037 / 0.035	0.030 / 0.031
MET	0.032 / 0.030	0.015 / 0.016	0.017 / 0.015	0.019 / 0.017
Background	0.011 / 0.010	0.018 / 0.018	0.011 / 0.011	0.012 / 0.012
Generator Modelling				
Renormalisation / Factorisation scale	±0.002	±0.027	±0.005	±0.007
ISR/FSR	±0.078	±0.026	±0.014	±0.014
Parton Shower and Fragmentation	±0.072	±0.031	±0.062	±0.057
MC Statistics	±0.015	±0.014	±0.005	±0.005
Top Mass	±0.020	±0.020	±0.024	±0.023
Colour Reconnection	±0.100	±0.033	±0.025	±0.023
Underlying Event	±0.068	±0.029	±0.002	±0.003
top pT Reweighting	±0.054	±0.028	±0.068	±0.058
Total Systematics	0.232 / 0.223	0.163 / 0.108	0.156 / 0.128	0.155 / 0.123
Data Statistics	±0.057	±0.033	±0.022	±0.017

Table 8.18: Systematic uncertainties on the $t\bar{t}$ normalisation for $\cos(\theta_+)\cos(\theta_-)_{high}$ Maximal.

Figure 8.27: Fit results for the $\cos(\theta_+)\cos(\theta_-)_{Helicity}$ variable in the inclusive $t\bar{t}$ invariant-mass region.

8.4.4 $cos(\theta_+)cos(\theta_-)_{Helicity}$ **Results**

The result of the fit for the $cos(\theta_+)cos(\theta_-)$ is shown in Fig. 8.27. The separation between the spin-correlated and uncorrelated hypothesis templates is not as pronounced as with the other analysis observables. As such, it is not possible to discern the agreement with either template using the distributions observed directly from the data. The effect of allowing the normalisation of the templates to vary also makes it difficult to judge the agreement without using the log-likelihood fit. The results for the low and high invariant-mass regions are presented in Fig. 8.28 and Fig. 8.29, respectively. The fit results for f_{SM} and $n_{t\bar{t}}$ for all channels in all regions of invariant mass are presented in Fig. 8.30. The low statistics and separation power between the hypothesis templates in the e^+e^- and $\mu^+\mu^-$ channels is such that it is not possible to distinguish spin correlated from uncorrelated in the fit, resulting in uncertainty bands that are consistent with both $f_{SM} = 1$ and $f_{SM} = 0$. In the $e^{\pm}\mu^{\mp}$ channel, in the inclusive selection, the data appear to favour the spin-correlated hypothesis over the uncorrelated hypothesis.

The systematics uncertainties on the f_{SM} parameter are shown in Table 8.13, Table 8.15, and Table 8.17 for the inclusive, low, and high invariant-mass regions, respectively. Similar tables are presented for the $n_{t\bar{t}}$ parameter in Table 8.14, Table 8.16, and Table 8.18, again for inclusive, low, and high, respectively. Systematic uncertainties are either greater than, or comparable to, the statistical uncertainties in all results, with the exception of the high invariant-mass regime where systematic uncertainties

dominate completely. Uncertainties due to jets are the dominant source of systematic uncertainty in all invariant-mass regimes. In the inclusive result uncertainties due to fake leptons and parton shower are also dominant. In the low invariant-mass regime uncertainties due to parton shower and renormalisation and factorisation scales are a dominant effect in addition to jet modelling. In the high invariant-mass regime jet, lepton and $E_{\mathrm{T}}^{\mathrm{miss}}$ modelling are among the largest.

The Helicity basis shows the poorest performance of all analysis observables. This was expected from the truth level studies, where the helicity basis is shown to have the poorest separation between the spin-correlated and uncorrelated hypotheses before any detector acceptance and resolution effects are considered. The most sensitive result for the f_{SM} parameter is the combined channel in the inclusive invariant-mass regime.
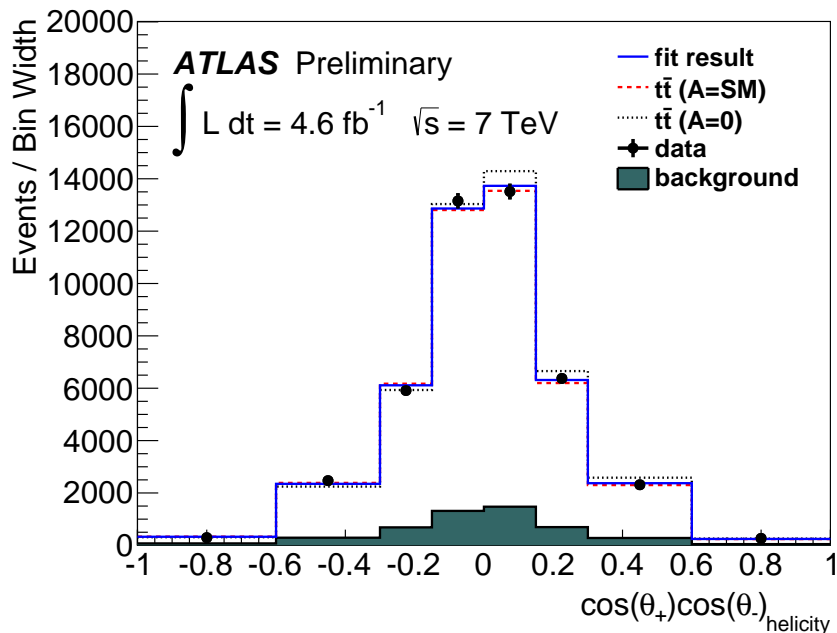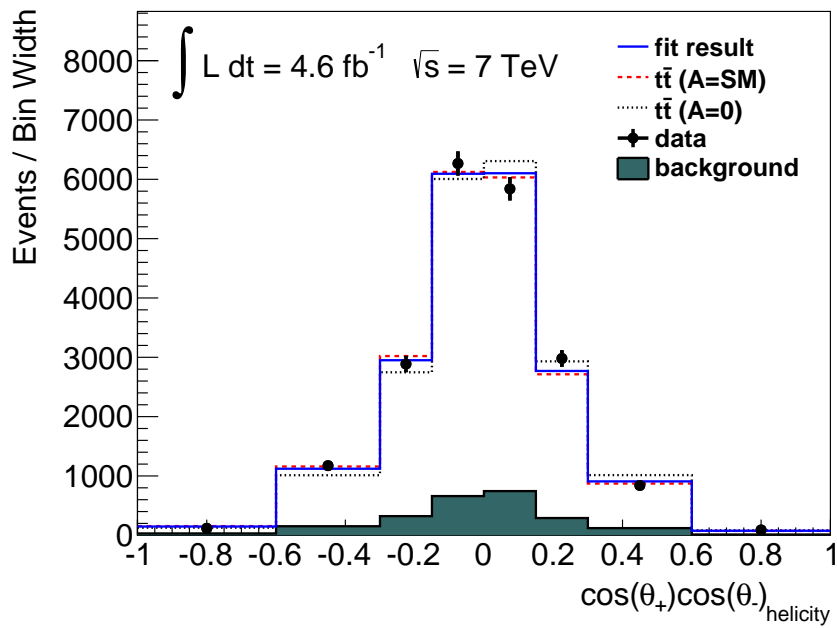
Figure 8.28: Fit results for the $\cos(\theta_+)\cos(\theta_-)_{Helicity}$ variable in the low $t\bar{t}$ invariant-mass region.

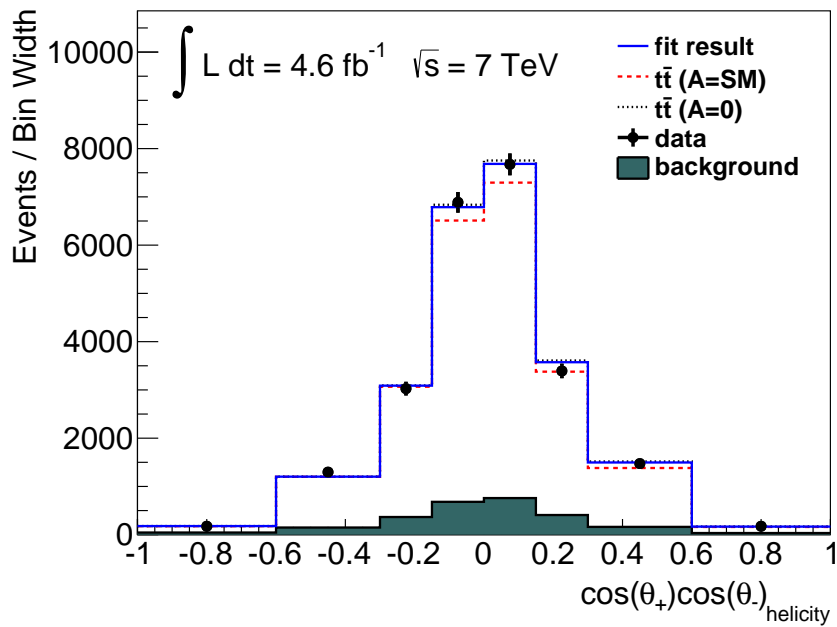**Figure 8.29:** Fit results for the $\cos(\theta_+)\cos(\theta_-)_{Helicity}$ variable in the high $t\bar{t}$ invariant-mass region.
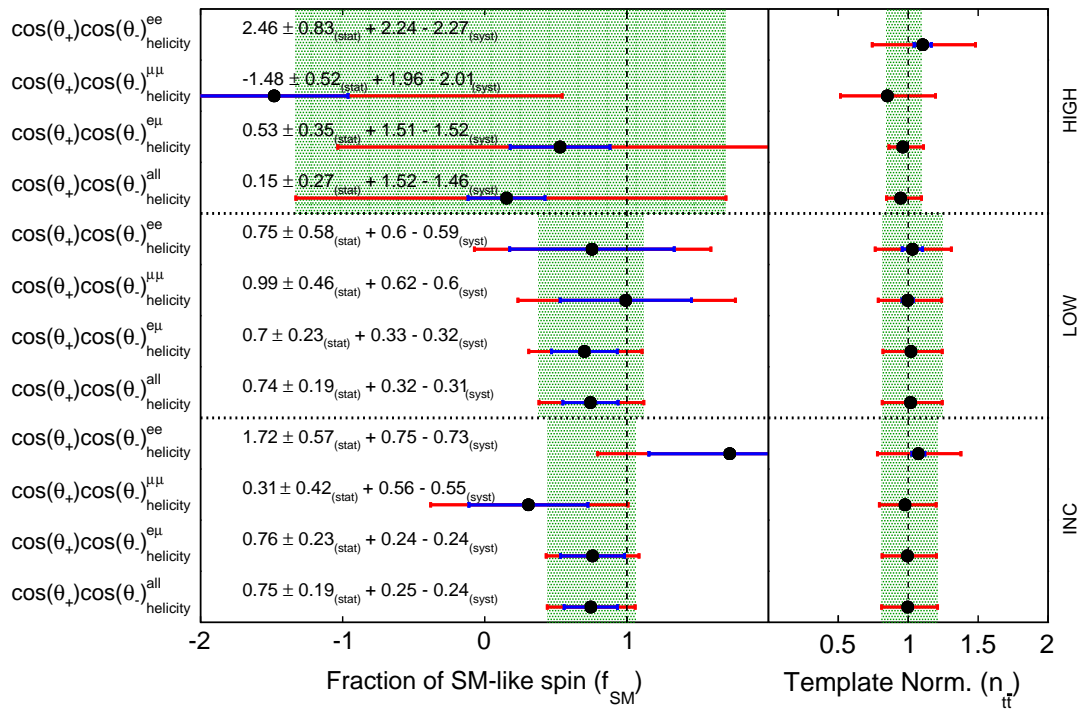
Figure 8.30: Summary of f_{SM} results for the $\cos(\theta_+)\cos(\theta_-)$ variable in the Helicity basis in the inclusive, low, and high invariant-mass regions. The left panel shows the results for the f_{SM} parameter, the right shows results for the $n_{t\bar{t}}$ parameter.

Source of uncertainty	e^+e^- channel	$\mu^+\mu^-$ channel	$e^\pm\mu^\mp$ channel	combination
Detector Modelling				
JES	0.364 / 0.454	0.142 / 0.155	0.141 / 0.145	0.119 / 0.121
Jet	0.165 / 0.164	0.159 / 0.070	0.062 / 0.056	0.082 / 0.063
Lepton	0.124 / 0.101	0.085 / 0.086	0.081 / 0.069	0.046 / 0.032
Fake	0.276 / 0.116	±0.040	0.065 / 0.065	0.063 / 0.058
MET	0.200 / 0.131	0.070 / 0.055	0.036 / 0.048	0.021 / 0.025
Background	0.058 / 0.059	0.053 / 0.055	0.014 / 0.015	0.022 / 0.022
Generator Modelling				
Renormalisation / Factorisation scale	±0.326	±0.197	±0.062	±0.075
ISR/FSR	±0.057	±0.037	±0.011	±0.007
Parton Shower and Fragmentation	±0.133	±0.384	±0.040	±0.130
MC Statistics	±0.299	±0.192	±0.072	±0.076
Top Mass	0.036 / 0.036	0.005 / 0.005	0.029 / 0.029	±0.021
PDF Uncertainty	±0.094	±0.107	±0.031	±0.036
Colour Reconnection	±0.150	±0.125	±0.087	±0.065
Underlying Event	±0.115	±0.006	±0.003	±0.013
top pT Reweighting	±0.001	±0.051	±0.003	±0.007
Total Systematics	0.746 / 0.735	0.562 / 0.546	0.237 / 0.236	0.250 / 0.242
Data Statistics	±0.569	±0.419	±0.225	±0.188

Table 8.19: Systematic uncertainties on the f_{SM} variable for $\cos(\theta_+)\cos(\theta_-)$ Helicity.

Source of uncertainty	e^+e^- channel	$\mu^+\mu^-$ channel	$e^\pm\mu^\mp$ channel	combination
Detector Modelling				
JES	0.071 / 0.110	0.075 / 0.098	0.049 / 0.082	0.060 / 0.090
Jet	0.119 / 0.023	0.146 / 0.030	0.121 / 0.021	0.127 / 0.024
Lepton	0.030 / 0.043	0.033 / 0.033	0.021 / 0.024	0.026 / 0.028
Fake	0.042 / 0.014	±0.001	0.014 / 0.012	0.008 / 0.015
MET	0.019 / 0.027	0.025 / 0.030	0.023 / 0.019	0.024 / 0.023
Background	0.012 / 0.012	0.014 / 0.014	0.013 / 0.012	0.012 / 0.012
Generator Modelling				
Renormalisation / Factorisation scale	±0.012	±0.005	±0.002	±0.002
ISR/FSR	±0.121	±0.005	±0.023	±0.024
Parton Shower and Fragmentation	±0.115	±0.079	±0.091	±0.090
MC Statistics	±0.011	±0.006	±0.003	±0.003
Top Mass	0.021 / 0.021	±0.022	0.026 / 0.026	0.025 / 0.025
PDF Uncertainty	±0.114	±0.110	±0.111	±0.112
Colour Reconnection	±0.105	±0.024	±0.019	±0.016
Underlying Event	±0.066	±0.020	±0.001	±0.000
top pT Reweighting	±0.106	±0.020	±0.046	±0.044
Total Systematics	0.301 / 0.289	0.221 / 0.181	0.206 / 0.181	0.213 / 0.186
Data Statistics	±0.046	±0.026	±0.016	±0.013

Table 8.20: Systematic uncertainties on the $t\bar{t}$ normalisation for $\cos(\theta_+)\cos(\theta_-)$ Helicity.

Source of uncertainty	e^+e^- channel	$\mu^+\mu^-$ channel	$e^\pm\mu^\mp$ channel	combination
Detector Modelling				
JES	0.176 / 0.142	0.388 / 0.386	0.212 / 0.195	0.218 / 0.209
Jet	0.113 / 0.100	0.073 / 0.056	0.095 / 0.064	0.097 / 0.058
Lepton	0.113 / 0.086	0.132 / 0.125	0.045 / 0.056	0.065 / 0.070
Fake	0.057 / 0.132	±0.061	0.110 / 0.111	0.083 / 0.082
MET	0.109 / 0.025	0.155 / 0.105	0.066 / 0.060	0.062 / 0.059
Background	0.045 / 0.046	0.044 / 0.045	0.025 / 0.025	0.028 / 0.029
Generator Modelling				
Renormalisation / Factorisation scale	±0.095	±0.075	±0.124	±0.064
ISR/FSR	±0.039	±0.107	±0.011	±0.030
Parton Shower and Fragmentation	±0.297	±0.160	±0.125	±0.135
MC Statistics	±0.346	±0.229	±0.066	±0.070
Top Mass	0.019 / 0.019	0.019 / 0.019	±0.016	0.009 / 0.009
Colour Reconnection	±0.192	±0.247	±0.017	±0.022
Underlying Event	±0.188	±0.142	±0.044	±0.038
top pT Reweighting	±0.019	±0.036	±0.009	±0.013
Total Systematics	0.604 / 0.591	0.618 / 0.602	0.333 / 0.316	0.321 / 0.305
Data Statistics	±0.579	±0.462	±0.232	±0.195

Table 8.21: Systematic uncertainties on the f_{SM} variable for $\cos(\theta_+)\cos(\theta_-)_{low}$ Helicity.

Source of uncertainty	e^+e^- channel	$\mu^+\mu^-$ channel	$e^\pm\mu^\mp$ channel	combination
Detector Modelling				
JES	0.098 / 0.133	0.118 / 0.137	0.081 / 0.114	0.090 / 0.121
Jet	0.134 / 0.037	0.149 / 0.042	0.132 / 0.036	0.137 / 0.038
Lepton	0.046 / 0.049	0.044 / 0.045	0.037 / 0.036	0.039 / 0.040
Fake	0.008 / 0.025	±0.013	0.027 / 0.027	0.022 / 0.028
MET	0.032 / 0.042	0.027 / 0.041	0.030 / 0.030	0.030 / 0.033
Background	0.011 / 0.011	0.014 / 0.014	0.015 / 0.015	0.014 / 0.014
Generator Modelling				
Renormalisation / Factorisation scale	±0.001	±0.002	±0.002	±0.000
ISR/FSR	±0.096	±0.019	±0.053	±0.049
Parton Shower and Fragmentation	±0.167	±0.107	±0.122	±0.123
MC Statistics	±0.007	±0.006	±0.002	±0.000
Top Mass	0.021 / 0.021	0.021 / 0.021	±0.028	0.027 / 0.027
Colour Reconnection	±0.041	±0.038	±0.038	±0.024
Underlying Event	±0.006	±0.026	±0.021	±0.011
top pT Reweighting	±0.046	±0.061	±0.041	±0.043
Total Systematics	0.269 / 0.256	0.239 / 0.207	0.222 / 0.199	0.226 / 0.201
Data Statistics	±0.073	±0.040	±0.024	±0.020

Table 8.22: Systematic uncertainties on the $t\bar{t}$ normalisation for $\cos(\theta_+)\cos(\theta_-)_{low}$ Helicity.

Source of uncertainty	e^+e^- channel	$\mu^+\mu^-$ channel	$e^\pm\mu^\mp$ channel	combination
Detector Modelling				
JES	0.323 / 0.331	1.008 / 1.076	1.116 / 1.129	1.227 / 1.153
Jet	0.134 / 0.052	0.362 / 0.310	0.334 / 0.330	0.423 / 0.406
Lepton	0.155 / 0.152	0.422 / 0.449	0.481 / 0.465	0.452 / 0.436
Fake	0.714 / 0.780	±0.158	0.267 / 0.265	0.273 / 0.243
MET	0.016 / 0.123	0.308 / 0.408	0.345 / 0.392	0.349 / 0.393
Background	0.135 / 0.135	0.130 / 0.131	0.046 / 0.046	0.051 / 0.051
Generator Modelling				
Renormalisation / Factorisation scale	±0.375	±0.334	±0.408	±0.269
ISR/FSR	±0.110	±0.045	±0.002	±0.066
Parton Shower and Fragmentation	±1.585	±1.324	±0.228	±0.030
MC Statistics	±1.178	±0.693	±0.419	±0.290
Top Mass	±0.458	0.081 / 0.081	±0.051	0.023 / 0.023
Colour Reconnection	±0.210	±0.011	±0.271	±0.238
Underlying Event	±0.168	±0.072	±0.143	±0.042
top pT Reweighting	±0.160	±0.130	±0.091	±0.057
Total Systematics	2.244 / 2.267	1.959 / 2.010	1.510 / 1.525	1.520 / 1.458
Data Statistics	±0.829	±0.520	±0.352	±0.271

Table 8.23: Systematic uncertainties on the f_{SM} variable for $\cos(\theta_+)\cos(\theta_-)_{high}$ Helicity.

Source of uncertainty	e^+e^- channel	$\mu^+\mu^-$ channel	$e^\pm\mu^\mp$ channel	combination
Detector Modelling				
JES	0.147 / 0.170	0.125 / 0.143	0.037 / 0.038	0.029 / 0.037
Jet	0.131 / 0.030	0.115 / 0.014	0.110 / 0.014	0.112 / 0.005
Lepton	0.032 / 0.047	0.035 / 0.041	0.013 / 0.007	0.009 / 0.003
Fake	0.086 / 0.057	±0.025	0.040 / 0.041	0.037 / 0.038
MET	0.025 / 0.017	0.026 / 0.051	0.007 / 0.008	0.006 / 0.005
Background	0.019 / 0.019	0.023 / 0.023	0.013 / 0.013	0.014 / 0.014
Generator Modelling				
Renormalisation / Factorisation scale	±0.018	±0.020	±0.022	±0.015
ISR/FSR	±0.147	±0.153	±0.017	±0.029
Parton Shower and Fragmentation	±0.070	±0.043	±0.051	±0.054
MC Statistics	±0.032	±0.036	±0.020	±0.015
Top Mass	0.015 / 0.015	0.020 / 0.020	0.022 / 0.022	±0.022
Colour Reconnection	±0.162	±0.163	±0.001	±0.019
Underlying Event	±0.124	±0.160	±0.026	±0.043
top pT Reweighting	±0.143	±0.078	±0.030	±0.008
Total Systematics	0.372 / 0.355	0.343 / 0.334	0.146 / 0.097	0.148 / 0.100
Data Statistics	±0.062	±0.029	±0.021	±0.017

Table 8.24: Systematic uncertainties on the $t\bar{t}$ normalisation for $\cos(\theta_+)\cos(\theta_-)_{high}$ Helicity.
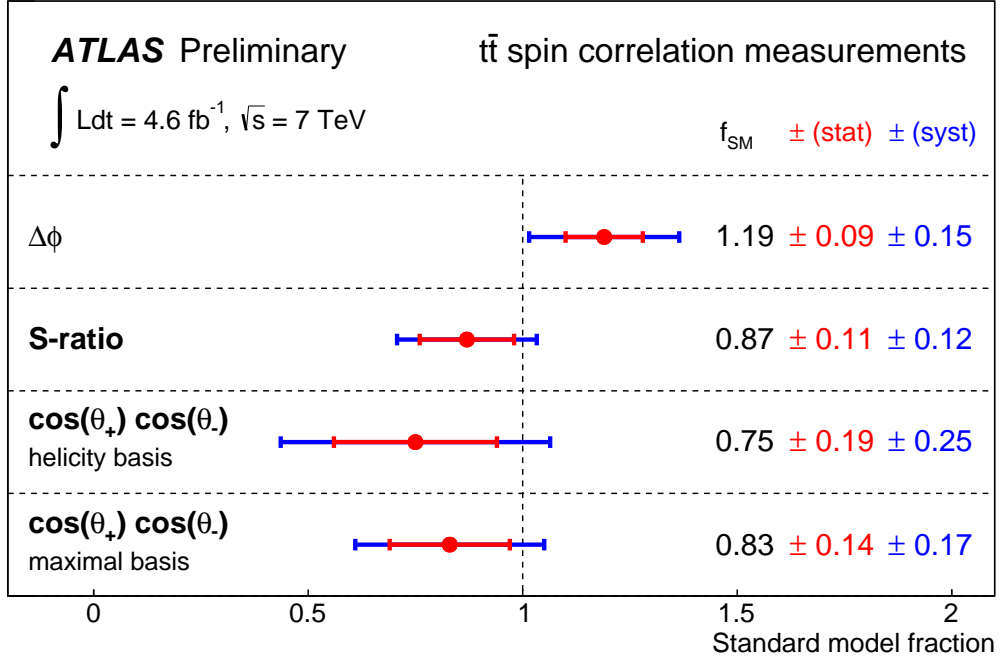
Figure 8.31: Summary of the extracted spin correlation strength f_{SM} in the combined channel for the inclusive $t\bar{t}$ invariant-mass regime.

8.5 Summary of Results

An analysis of spin correlation in dileptonic $t\bar{t}$ final states has been performed using the full 7 TeV LHC run 1 dataset, corresponding to an integrated luminosity of 4.6 fb^{-1}, using the ATLAS detector. Four analysis variables, each with a different sensitivity to the initial state production, have been used to extract the fraction of standard model like spin correlation. In addition these variables have been investigated in three regions of $t\bar{t}$ invariant mass; low (less than 450 GeV), high (greater than 450 GeV), and inclusive in order to enhance or suppress different initial state production mechanisms and maximise each variable's sensitivity. All results in all variables and channels are consistent with the SM prediction of $f_{SM} = 1$ and no deviations from this prediction are observed. A summary of the e^+e^-, $\mu^+\mu^-$, $e^\pm\mu^\mp$, and combined channels in the inclusive $t\bar{t}$ region is shown in Table. 8.25. A summary of the combined channel results in the inclusive $t\bar{t}$ mass region is presented in Fig. 8.31.

Results of observables most sensitive in $g_L g_L$, $g_R g_R \rightarrow t\bar{t}$ events

The $\Delta\phi$ result is sensitive to spin correlation arising from coefficients c_1^a and c_2^a of the spin-density matrix and has the highest separation between the correlated and

channel	$\Delta\phi$	S-Ratio	Maximal	Helicity
e^+e^-	$0.87 \pm 0.35 \pm 0.47$	$0.81 \pm 0.35 \pm 0.39$	$0.48 \pm 0.41 \pm 0.52$	$1.72 \pm 0.57 \pm 0.75$
$e^\pm\mu^\mp$	$1.24 \pm 0.11 \pm 0.12$	$0.95 \pm 0.12 \pm 0.12$	$0.86 \pm 0.16 \pm 0.18$	$0.76 \pm 0.23 \pm 0.24$
$\mu^+\mu^-$	$1.11 \pm 0.20 \pm 0.25$	$0.53 \pm 0.26 \pm 0.38$	$0.97 \pm 0.33 \pm 0.44$	$0.31 \pm 0.42 \pm 0.56$
Dilepton	$1.19 \pm 0.09 \pm 0.15$	$0.87 \pm 0.11 \pm 0.12$	$0.83 \pm 0.14 \pm 0.17$	$0.75 \pm 0.19 \pm 0.25$

Table 8.25: Summary of f_{SM} measurements in the individual channels and in the combined dilepton channel for the four different observables. The uncertainties quoted are first statistical and then systematic. The Maximal column are the results for the $\cos(\theta_+)\cos(\theta_-)_{\mathrm{maximal}}$ variable and the Helicity column are the results for the $\cos(\theta_+)\cos(\theta_-)_{\mathrm{helicity}}$ variable.

uncorrelated hypothesis in like helicity gluon-gluon fusion produced $t\bar{t}$ pairs. The fit extracted a value of $f_{SM} = 1.19 \pm 0.09$ (stat.) ± 0.15 (syst.) in the combined channel using the $\Delta\phi$ variable in the inclusive mass regime, in agreement with the SM prediction of $f_{SM} = 1$. This result has the highest expected sensitivity and is also overall the most sensitive of the combined fit results of all variables in any $t\bar{t}$ invariant-mass regime. This result is consistent with an earlier ATLAS result, measured using a subset of this data, but surpasses the previous result in its treatment and estimation of systematic uncertainties.

Results of observables most sensitive in $\mathrm{gg} \rightarrow t\bar{t}$ events

The Maximal basis result is sensitive to a linear combination of c_1^g, c_2^g, c_3^g, and c_4^g since it uses the gluon-gluon matrix elements directly in it's construction. The result extracted a value of $f_{SM} = 0.83 \pm 0.14$ (stat.) $^{+0.16}_{-0.17}$ (syst.) in the combined channel using the $\cos(\theta_+)\cos(\theta_-)$ in the Maximal basis in agreement with the SM prediction. This is the first time that a variable of this type has been explored by ATLAS, and the first time that the Maximal basis has been used to extract spin correlation in any experiment.

Results of observables most sensitive in $\mathrm{q_L\bar{q}_R, g_R g_L, g_L g_R} \rightarrow t\bar{t}$ events

The Helicity basis result is also sensitive to a linear combination of c_1^a, c_2^a, c_3^a, and c_4^a. The fit extracted a value of $f_{SM} = 0.75 \pm 0.19$ (stat.) $^{+0.25}_{-0.24}$ (syst.) in the combined channel using the $\cos(\theta_+)\cos(\theta_-)$ in the Helicity basis, in agreement with the SM prediction. This result represents the first measurement by ATLAS using the $\cos(\theta_+)\cos(\theta_-)$ in the Helicity basis and is in agreement with a previous preliminary result from the CMS collaboration [66].

Comparisons to theory predictions

It is possible to compare the results for the Helicity basis and Maximal basis to theory predictions. The $\Delta\phi$ and S-Ratio variables only allow an indirect extraction of A, because A is only defined according to the $\cos(\theta_+)\cos(\theta_-)$ distribution as shown in Eq. 2.5. The f_{SM} value corresponds to a sample containing a fraction of $t\bar{t}$ events with correlated spins as predicted in the SM and $t\bar{t}$ events with no spin correlation. This represents the strength of the SM spin correlation and can be translated into any spin quantisation basis using:

$$A_{\text{basis}}^{\text{measured}} = f_{\text{SM}}\, A_{\text{basis}}^{SM}, \tag{8.1}$$

where $A_{\text{basis}}^{\text{measured}}$ is the measured value extrapolated into a particular basis and A_{basis}^{SM} is the theory prediction in that same basis. This is therefore considered an indirect measurement of spin correlation, whilst those extracted using the $\cos\theta_+\cos\theta_-$ distributions are called direct measurements. For the Helicity basis, the theory predictions are taken from the source given for Table. 5.5.

The $\Delta\phi$ variable, when extrapolated into the helicity and maximal bases, gives a result of:

$$A_{\text{helicity}}^{\text{measured}} = 0.37 \pm 0.03\ (\text{stat})\ {}^{+0.04}_{-0.05}\ (\text{syst}) \tag{8.2}$$

$$A_{\text{maximal}}^{\text{measured}} = 0.52 \pm 0.04\ (\text{stat})\ {}^{+0.06}_{-0.07}\ (\text{syst}), \tag{8.3}$$

which is the most precise measurement of spin correlation to date. The result is limited by systematic uncertainties and are in agreement with a previous result from ATLAS [27]. In the same way the S-Ratio result may also be extrapolated as:

$$A_{\text{helicity}}^{\text{measured}} = 0.27 \pm 0.03\ (\text{stat})\ {}^{+0.04}_{-0.04}\ (\text{syst}) \tag{8.4}$$

$$A_{\text{maximal}}^{\text{measured}} = 0.38 \pm 0.05\ (\text{stat})\ {}^{+0.05}_{-0.06}\ (\text{syst}). \tag{8.5}$$

The two $\cos\theta_+\cos\theta_-$ allow for direct measurements of the spin correlation strength A. Measuring A with these variables is equivalent to extracting the number of events where the spins of the top and the anti-top are parallel minus the number of events where they are anti-parallel, normalised by the total number of events. The extraction of spin correlation using a template method with this distribution is equivalent to extracting the spin correlation in the respective quantisation axis using the relation given in Eq. 8.1. The extraction in the Helicity basis gives:

$$A_{\text{helicity}}^{\text{measured}} = 0.23 \pm 0.06\ (\text{stat})\ {}^{+0.08}_{-0.08}\ (\text{syst}) \tag{8.6}$$

which is in good agreement with the SM value of $A_{\text{helicity}}^{SM} = 0.31$ [12], and using the Maximal basis:

$$A_{\text{maximal}}^{\text{measured}} = 0.36 \pm 0.06\ (\text{stat})\ {}^{+0.07}_{-0.07}\ (\text{syst}) \tag{8.7}$$

which is also in agreement with the SM prediction of $A^{SM}_{\text{maximal}} = 0.44$ derived using MC@NLO. The result in the Maximal basis is the most precise, direct measurement of A currently available.

All of these measurements are summarised in Tab. 8.26. All values are in agreement with the predictions from the SM and with each other within their uncertainties.

dilepton	$\Delta\phi$	S-Ratio	Maximal	Helicity
$A^{\text{measured}}_{\text{helicity}}$	$0.37 \pm 0.03 \pm 0.05$	$0.27 \pm 0.03 \pm 0.04$	—	$0.23 \pm 0.06 \pm 0.10$
$A^{\text{measured}}_{\text{maximal}}$	$0.52 \pm 0.04 \pm 0.07$	$0.38 \pm 0.05 \pm 0.06$	$0.36 \pm 0.06 \pm 0.09$	—

Table 8.26: Summary of measurements of A in the Helicity and Maximal bases in the combined dilepton channel for the four different observables. For the indirect extractions using $\Delta\phi$ and the S-ratio, A is presented in both the Helicity and Maximal bases. For the direct measurements using $\cos(\theta_+)\cos(\theta_-)$, results are quoted for the basis utilised for the measurement only. The Maximal column are the results for the $\cos(\theta_+)\cos(\theta_-)_{\text{maximal}}$ variable and the Helicity column are the results for the $\cos(\theta_+)\cos(\theta_-)_{\text{helicity}}$ variable. The uncertainties quoted are first statistical followed by systematic.

Chapter 9

Conclusions

The spin correlation in dileptonic $t\bar{t}$ events has been measured using ATLAS data recorded during 2011 in proton-proton collisions at the LHC with a center-of-mass energy of 7 TeV. Four observables were used, each with different sensitivities to the non-zero coefficients of the spin-density matrix.

Events were selected by requiring two opposite charge leptons and two high p_T jets. In events where both leptons are either electrons or muons, addition cuts were required on the invariant mass of the lepton pair and on the transverse missing energy in order to suppress Drell-Yan contributions. Signal $t\bar{t}$ events were generated for MC@NLO using for a case with SM spin correlations and uncorrelated $t\bar{t}$ pairs. Background events due to the diboson, single top quarks in association with a W boson and $Z \to \tau\tau$ processes were estimated using MC. Backgrounds due to Drell-Yan and non-prompt leptons were estimated using data driven techniques.

The $t\bar{t}$ final state was reconstructed using the Neutrino Weighting algorithm. This algorithm was improved from a previous version, and optimised for high performance on 7 TeV ATLAS data. The reconstruction algorithm performed extremely well and was instrumental in the final sensitivity of the analysis observables that required full $t\bar{t}$ reconstruction.

The spin correlation strength was extracted using four observables that are sensitive to spin correlation: the $\Delta\phi$ observable, which is sensitive to spin-correlations arising from a linear combination of the c_1^a and c_2^a coefficients of the spin-density matrix for either gluon-gluon fusion or $q\bar{q}$ annihilation; the S-Ratio observable, which is sensitive to a linear combination of the c_1^a, c_2^a, c_3^a, and c_4^a coefficients; the $cos(\theta_+)\cos(\theta_-)$ observable in the Maximal basis, which is sensitive to a linear combination of the c_1^g, c_2^g, c_3^g, and c_4^g coefficients from the gluon-gluon fusion spin-density matrix; and the $cos(\theta_+)\cos(\theta_-)$ observable in the Helicity basis, which is also sensitive to a linear combination of the c_1^a, c_2^a, c_3^a, and c_4^a coefficients. Many of these observables have never been investigated in real data and some are used for the first time at ATLAS. These observables were probed in three regions of $t\bar{t}$ invariant mass to enhance their sensitivity and in all cases,

no significant deviation form the SM expectation is observed. These results, taken together, represent the most comprehensive probe of spin correlation in $t\bar{t}$ events ever performed on data at any experiment.

References

[1] ATLAS Collaboration, *Observation of a new particle in the search for the Standard Model Higgs boson with the ATLAS detector at the LHC*, Phys.Lett. **B716** (2012) 1–29, arXiv:1207.7214 [hep-ex].

[2] ATLAS Collaboration, *Combined measurements of the mass and signal strength of the Higgs-like boson with the ATLAS detector using up to 25 fb^{-1} of proton-proton collision data*, Tech. Rep. ATLAS-CONF-2013-014, Mar, 2013.

[3] Particle Data Group Collaboration, *Review of Particle Physics*, Phys. Rev. D **86** (2012) 010001.

[4] M. Kobayashi and T. Maskawa, *CP Violation in the Renormalizable Theory of Weak Interaction*, Prog.Theor.Phys. **49** (1973) 652–657.

[5] S. Herb, D. Hom, L. Lederman, J. Sens, H. Snyder, et al., *Observation of a Dimuon Resonance at 9.5-GeV in 400-GeV Proton-Nucleus Collisions*, Phys.Rev.Lett. **39** (1977) 252–255.

[6] D0 Collaboration, *Observation of the top quark*, Phys.Rev.Lett. **74** (1995) 2632–2637, arXiv:hep-ex/9503003 [hep-ex].

[7] CDF Collaboration, *Observation of top quark production in $\bar{p}p$ collisions*, Phys.Rev.Lett. **74** (1995) 2626–2631, arXiv:hep-ex/9503002 [hep-ex].

[8] Tevatron Electroweak Working Group, D0 Collaboration, CDF Collaboration, *Combination of CDF and DO results on the mass of the top quark using up to 8.7 fb^{-1} at the Tevatron*, arXiv:1305.3929 [hep-ex].

[9] CDF Collaboration, D0 Collaboration, *Combination of the top-quark mass measurements from the Tevatron collider*, Phys.Rev. **D86** (2012) 092003, arXiv:1207.1069 [hep-ex].

[10] A. Heinson, "Feynman Diagrams for Top Physics Talks and Notes." http://www-d0.fnal.gov/Run2Physics/top/top_public_web_pages/top_feynman_diagrams.html. [Online; accessed 05-September-2013].

[11] W. Bernreuther and Z.-G. Si, *Distributions and correlations for top quark pair production and decay at the Tevatron and LHC.*, Nucl.Phys. **B837** (2010) 90–121, `arXiv:1003.3926 [hep-ph]`.

[12] W. Bernreuther and Z.-G. Si, *Top quark spin correlations and polarization at the LHC: standard model predictions and effects of anomalous top chromo moments*, `arXiv:1305.2066 [hep-ph]`.

[13] P. Uwer, *Maximizing the spin correlation of top quark pairs produced at the Large Hadron Collider*, Phys.Lett. **B609** (2005) 271–276, `arXiv:hep-ph/0412097 [hep-ph]`.

[14] CMS Collaboration, *Measurement of the top polarization in the dilepton final state*, Tech. Rep. CMS-PAS-TOP-12-016, 2012.

[15] ATLAS Collaboration, S. Borroni, F. Deliot, C. Deterre, A. Grohsjean, S. Hamilton, L. Mijovic, R. Peters, M. Rudolph, and R. Schaefer, *Measurement of top quark polarisation in $t\bar{t}$ events with the ATLAS detector in proton-proton collisions at $\sqrt{s} = 7$ TeV*, Tech. Rep. ATL-COM-PHYS-2013-367, Mar, 2013.

[16] W. Bernreuther, "Memo on spin correlation and polarisation interpretations." Private communication.

[17] G. Mahlon and S. J. Parke, *Spin Correlation Effects in Top Quark Pair Production at the LHC*, Phys.Rev. **D81** (2010) 074024, `arXiv:1001.3422 [hep-ph]`.

[18] CDF Collaboration, *Evidence for a Mass Dependent Forward-Backward Asymmetry in Top Quark Pair Production*, Phys.Rev. **D83** (2011) 112003, `arXiv:1101.0034 [hep-ex]`.

[19] D0 Collaboration, *Forward-backward asymmetry in top quark-antiquark production*, Phys.Rev. **D84** (2011) 112005, `arXiv:1107.4995 [hep-ex]`.

[20] ATLAS Collaboration, *Measurement of the charge asymmetry in top quark pair production in pp collisions at $\sqrt{s} = 7$ TeV using the ATLAS detector*, Eur.Phys.J. **C72** (2012) 2039, `arXiv:1203.4211 [hep-ex]`.

[21] F. Hubaut, *Top physics at LHC with $t\bar{t}$ events*, `arXiv:hep-ex/0605029`.

[22] A. Czarnecki, M. Jezabek, and J. H. Kuhn, *LEPTON SPECTRA FROM DECAYS OF POLARIZED TOP QUARKS*, Nucl.Phys. **B351** (1991) 70–80.

[23] A. Brandenburg, Z. Si, and P. Uwer, *QCD corrected spin analyzing power of jets in decays of polarized top quarks*, Phys.Lett. **B539** (2002) 235–241, `arXiv:hep-ph/0205023 [hep-ph]`.

[24] F. Hubaut, E. Monnier, P. Pralavorio, K. Smolek, and V. Simak, *ATLAS sensitivity to top quark and W boson polarization in $t\bar{t}$ events*, Eur.Phys.J. **C44S2** (2005) 13–33, `arXiv:hep-ex/0508061 [hep-ex]`.

[25] ATLAS Collaboration, *Top Quark Properties*, Tech. Rep. ATL-PHYS-PUB-2009-044. ATL-COM-PHYS-2009-112, Mar, 2009.

[26] W. Bernreuther, A. Brandenburg, Z. Si, and P. Uwer, *Investigation of top quark spin correlations at hadron collider*, `arXiv:hep-ph/0410197 [hep-ph]`.

[27] ATLAS Collaboration, *Observation of spin correlation in $t\bar{t}$ events from pp collisions at sqrt(s) = 7 TeV using the ATLAS detector*, Phys.Rev.Lett. **108** (2012) 212001, `arXiv:1203.4081 [hep-ex]`.

[28] M. Czakon, P. Fiedler, and A. Mitov, *The total top quark pair production cross-section at hadron colliders through $O(\alpha_S^4)$*, Phys.Rev.Lett. **110** (2013) 252004, `arXiv:1303.6254 [hep-ph]`.

[29] T. Sjöstrand, *Jet fragmentation of multiparton configurations in a string framework*, Nuclear Physics B **248** (1984) 469 – 502.

[30] M. S. Jon Butterworth, Jeff Forshaw and R. Walker, "JIMMY Generator, Multiparton Interactions in HERWIG." `https://jimmy.hepforge.org/`. [Online; accessed 09-September-2013].

[31] H.-L. Lai, M. Guzzi, J. Huston, Z. Li, P. M. Nadolsky, et al., *New parton distributions for collider physics*, Phys.Rev. **D82** (2010) 074024, `arXiv:1007.2241 [hep-ph]`.

[32] M. L. Mangano, M. Moretti, F. Piccinini, R. Pittau, and A. D. Polosa, *ALPGEN, a generator for hard multiparton processes in hadronic collisions*, JHEP **0307** (2003) 001, `arXiv:hep-ph/0206293 [hep-ph]`.

[33] T. Gleisberg, S. Hoeche, F. Krauss, M. Schonherr, S. Schumann, et al., *Event generation with SHERPA 1.1*, JHEP **0902** (2009) 007, `arXiv:0811.4622 [hep-ph]`.

[34] G. Corcella, I. Knowles, G. Marchesini, S. Moretti, K. Odagiri, et al., *HERWIG 6: An Event generator for hadron emission reactions with interfering gluons (including supersymmetric processes)*, JHEP **0101** (2001) 010, `arXiv:hep-ph/0011363 [hep-ph]`.

[35] B. P. Kersevan and E. Richter-Was, *The Monte Carlo event generator AcerMC version 2.0 with interfaces to PYTHIA 6.2 and HERWIG 6.5*, `arXiv:hep-ph/0405247 [hep-ph]`.

[36] S. Frixione and B. R. Webber, *Matching NLO QCD computations and parton shower simulations*, JHEP **0206** (2002) 029, `arXiv:hep-ph/0204244 [hep-ph]`.

[37] P. Nason, *A New method for combining NLO QCD with shower Monte Carlo algorithms*, JHEP **0411** (2004) 040, `arXiv:hep-ph/0409146 [hep-ph]`.

[38] O. S. Brning, P. Collier, P. Lebrun, S. Myers, R. Ostojic, J. Poole, and P. Proudlock, *LHC Design Report; Volume 1*. CERN, 2004.

[39] O. S. Brning, P. Collier, P. Lebrun, S. Myers, R. Ostojic, J. Poole, and P. Proudlock, *LHC Design Report; Volume 2*. CERN, 2004.

[40] M. Benedikt, P. Collier, V. Mertens, J. Poole, and K. Schindl, *LHC Design Report; Volume 3*. CERN, 2004.

[41] CERN, "The accelerator complex." `http://home.web.cern.ch/about/accelerators`. [Online; accessed 05-September-2013].

[42] CERN, "CERN Accelerator Complex." `http://bigscience.web.cern.ch/bigscience/Objects/LHC/accelerator.jpg`. [Online; accessed 05-September-2013].

[43] ATLAS Collaboration, "Luminosity public results." `https://twiki.cern.ch/twiki/bin/view/AtlasPublic/LuminosityPublicResults#2011_pp_Collisions`. [Online; accessed 05-September-2013].

[44] J. Pequenao, "Computer generated image of the whole ATLAS detector." Mar, 2008.

[45] ATLAS Collaboration, *The ATLAS Experiment at the CERN Large Hadron Collider*, JINST **3** (2008) S08003.

[46] C. Nellist, "Illustration of the ATLAS coordinate system", howpublished =.".

[47] J. Pequenao, "Computer generated image of the ATLAS inner detector." Mar, 2008.

[48] J. Pequenao, "Computer Generated image of the ATLAS calorimeter." Mar, 2008.

[49] J. Pequenao, "Computer generated image of the ATLAS Muons subsystem." Mar, 2008.

[50] ATLAS Collaboration, *A Fast Hardware Tracker for the ATLAS Trigger System*, `arXiv:1110.1910 [hep-ex]`.

[51] ATLAS Collaboration, *Object selection and calibration, background estimation and MC samples for the Winter 2012 Top Quark analyses with 2011 data.*,.

[52] ATLAS Collaboration, "Top Common Objects for Winter 2012 Analyses." `https://twiki.cern.ch/twiki/bin/viewauth/AtlasProtected/TopCommonObjects2011`. [Online; accessed 23-August-2013].

[53] ATLAS Collaboration, "Top Common Scale Prescritpions for Winter 2012 Analyses." `https://twiki.cern.ch/twiki/bin/viewauth/AtlasProtected/TopCommonScales2011`. [Online; accessed 23-August-2013].

[54] M. Cacciari, G. P. Salam, and G. Soyez, *The Anti-k(t) jet clustering algorithm*, JHEP **0804** (2008) 063, `arXiv:0802.1189 [hep-ph]`.

[55] ATLAS Collaboration, "How To Clean Jets." `https://twiki.cern.ch/twiki/bin/viewauth/AtlasProtected/HowToCleanJets`. [Online; accessed 05-September-2013].

[56] ATLAS Collaboration, *Electron performance measurements with the ATLAS detector using the 2010 LHC proton-proton collision data*, Eur.Phys.J. **C72** (2012) 1909, `arXiv:1110.3174 [hep-ex]`.

[57] ATLAS Collaboration, *Expected electron performance in the ATLAS experiment*, Tech. Rep. ATL-PHYS-PUB-2011-006, Apr, 2011.

[58] ATLAS Collaboration, "The MuID Muon Collection." `https://twiki.cern.ch/twiki/bin/viewauth/AtlasProtected/MuidMuonCollection`. [Online; accessed 05-September-2013].

[59] ATLAS Collaboration, "Muon Combined Performance Guidlines Twiki." `https://twiki.cern.ch/twiki/bin/viewauth/AtlasProtected/MCPAnalysisGuidelinesRel17MC11a`. [Online; accessed 23-August-2013].

[60] ATLAS Collaboration, *Performance of Missing Transverse Momentum Reconstruction in Proton-Proton Collisions at 7 TeV with ATLAS*, Eur.Phys.J. **C72** (2012) 1844, `arXiv:1108.5602 [hep-ex]`.

[61] ATLAS Collaboration, *Measurement of the cross section for top-quark pair production in pp collisions at $\sqrt{s} = 7$ TeV with the ATLAS detector using final states with two high-pt leptons*, JHEP **1205** (2012) 059, `arXiv:1202.4892 [hep-ex]`.

[62] CTEQ Collaboration, "CT10 NLO and NNLO parton distribution functions." `http://hep.pa.msu.edu/cteq/public/index.html`. [Online; accessed 25-August-2013].

[63] T. Sjostrand, S. Mrenna, and P. Z. Skands, *PYTHIA 6.4 Physics and Manual*, JHEP **0605** (2006) 026, `arXiv:hep-ph/0603175 [hep-ph]`.

[64] P. Z. Skands, *Tuning Monte Carlo Generators: The Perugia Tunes*, Phys.Rev. **D82** (2010) 074018, `arXiv:1005.3457 [hep-ph]`.

[65] S. Jadach, Z. Was, R. Decker, and J. H. Kuhn, *The tau decay library TAUOLA: Version 2.4*, Comput.Phys.Commun. **76** (1993) 361–380.

[66] CMS Collaboration, *Measurement of Spin Correlations in ttbar production*, Tech. Rep. CMS-PAS-TOP-12-004, 2012.

[67] ATLAS Collaboration, B. Abi, et al., *Mis-identified lepton backgrounds to top quark pair production for moriond 2011 analysis.,*.

[68] J. M. Meyer, *Measurement of the Top Quark Mass using Dilepton Events and a Neutrino Weighting Algorithm with the D0 Experiment at the Tevatron (Run II),*.

[69] V. M. A. et al. Phys. Rev. D **80** (2009) 092006.

[70] ATLAS Collaboration, *Performance of Missing Transverse Momentum Reconstruction in ATLAS with 2011 Proton-Proton Collisions at sqrts = 7 TeV,*.

[71] ATLAS Collaboration, *Jet energy resolution in proton-proton collisions at $\sqrt{s} = 7$ TeV recorded in 2010 with the ATLAS detector*, Eur.Phys.J. **C73** (2013) 2306, `arXiv:1210.6210 [hep-ex]`.

[72] ATLAS Collaboration, *Measurement of the W boson polarisation in top quark decays in 0.70 fb?1 of pp collisions at $\sqrt{s} = 7$ TeV with the ATLAS detector*, Tech. Rep. ATL-CONF-2011-122, August, 2011.

[73] ATLAS Collaboration, *Measurements of top quark pair relative differential cross-sections with ATLAS in pp collisions at $\sqrt{s} = 7$ TeV*, Eur.Phys.J. **C73** (2013) 2261, `arXiv:1207.5644 [hep-ex]`.

[74] F. James and M. Roos Comput. Phys. Commun. **10** (1975) 343.

[75] ATLAS Collaboration, "Top Systematic Prescritpions for 2011 Analyses." `https://twiki.cern.ch/twiki/bin/viewauth/AtlasProtected/ TopSystematicUncertainties2011`. [Online; accessed 14-July-2013].

[76] ATLAS Collaboration, *Improved luminosity determination in pp collisions at sqrt(s) = 7 TeV using the ATLAS detector at the LHC*, `arXiv:1302.4393 [hep-ex]`.

[77] ATLAS Collaboration, "Electron energy scale recommendations twiki." `https://twiki.cern.ch/twiki/bin/viewauth/AtlasProtected/ EnergyScaleResolutionRecommendations`. [Online; accessed 23-August-2013].

[78] ATLAS Collaboration, *Performance of the ATLAS Electron and Photon Trigger in p-p Collisions at $\sqrt{s} = 7$ TeV in 2011*, Tech. Rep. ATLAS-CONF-2012-048, 2012.

[79] ATLAS Collaboration, "Electron Efficiency Recommendations Twiki." `https://twiki.cern.ch/twiki/bin/viewauth/AtlasProtected/` `EfficiencyMeasurements#Trigger`. [Online; accessed 23-August-2013].

[80] ATLAS Collaboration, *Muon Momentum Resolution in First Pass Reconstruction of pp Collision Data Recorded by ATLAS in 2010*, Tech. Rep. ATLAS-CONF-2011-046, Mar, 2011.

[81] ATLAS Collaboration, *Muon reconstruction efficiency in reprocessed 2010 LHC proton-proton collision data recorded with the ATLAS detector*, Tech. Rep. ATLAS-CONF-2011-063, Apr, 2011.

[82] ATLAS Collaboration, T. Barillari, *Jet Energy Scale Uncertainties in ATLAS*, Tech. Rep. ATL-PHYS-PROC-2012-137, Aug, 2012.

[83] ATLAS Collaboration, "Jet Uncertainties Twiki." `https://twiki.cern.ch/` `twiki/bin/viewauth/AtlasProtected/JetUncertainties2011`. [Online; accessed 23-August-2013].

[84] ATLAS Collaboration, G. Romeo, A. Schwartzman, R. Piegaia, T. Carli, and R. Teuscher, *Jet Energy Resolution from In-situ Techniques with the ATLAS Detector Using Proton-Proton Collisions at a Center of Mass Energy $\sqrt{s} = 7$ TeV*, Tech. Rep. ATL-COM-PHYS-2011-240, Mar, 2011.

[85] ATLAS Collaboration, *Jet energy resolution and selection efficiency relative to track jets from in-situ techniques with the ATLAS Detector Using Proton-Proton Collisions at a Center of Mass Energy sqrts = 7 TeV*, Tech. Rep. ATLAS-CONF-2010-054, Jul, 2010.

[86] N. Kidonakis, *Two-loop soft anomalous dimensions for single top quark associated production with a W- or H-*, Phys.Rev. **D82** (2010) 054018, `arXiv:1005.4451 [hep-ph]`.

[87] S. Frixione, E. Laenen, P. Motylinski, B. R. Webber, and C. D. White, *Single-top hadroproduction in association with a W boson*, JHEP **0807** (2008) 029, `arXiv:0805.3067 [hep-ph]`.

[88] ATLAS Collaboration, J. Butterworth, E. Dobson, U. Klein, B. Mellado Garcia, T. Nunnemann, J. Qian, D. Rebuzzi, and R. Tanaka, *Single Boson and Diboson Production Cross Sections in pp Collisions at sqrts=7 TeV*, Tech. Rep. ATL-COM-PHYS-2010-695, Aug, 2010.

[89] ATLAS Collaboration, *Measurement of $t\bar{t}$ production with a veto on additional central jet activity in pp collisions at sqrt(s) = 7 TeV using the ATLAS detector*, Eur.Phys.J. **C72** (2012) 2043, `arXiv:1203.5015 [hep-ex]`.

[90] ATLAS Collaboration, *Measurement of top quark pair differential cross section with ATLAS in pp collisions at sqrt(s)=7 TeV: Measurement of top quark pair differential cross section with ATLAS using 5/fb of data collected in 2011 and the rel.17 version of the Atlas software*, Tech. Rep. ATL-COM-PHYS-2012-1137, Jul, 2012.